Engineering Economical and Sustainable Solutions for the Abatement of Volatile Organic Compounds

by

Adarsh Bhat

A dissertation submitted in partial fulfilment
of the requirements for the degree of
Doctor of Philosophy
(Chemical Engineering)
in the University of Michigan
2021

Doctoral Committee:

Professor Johannes W. Schwank, Chair
Assistant Professor Andrej Lenert
Assistant Professor Charles McCrory
Assistant Professor Nirala Singh

Adarsh Bhat

bhatada@umich.edu

ORCID iD: 0000-0002-1142-6731

Acknowledgments

I am profoundly thankful to my advisor, Prof. Johannes Schwank, for giving me an opportunity to work on this project and helping me in developing my scientific acumen and critical thinking skills. The successful completion of this work could not have been possible without his continuous guidance, encouragement, and great enthusiasm to experiment with new ideas. I am extremely thankful to my committee members Prof. Andrej Lenert, Prof. Nirala Singh, and Prof. Charles McCrory, for their insights and valuable suggestions throughout my research. I would also like to express my gratitude to Prof. Galen Fisher and Dr. Xiaoyin Chen for their mentorship, ideas, and encouragement during my research.

The research presented in this dissertation was a part of UM – Ford Alliance project. The project funded my research and provided me with a platform to pursue collaborative multi-disciplinary work. I thank Dr. Hiroko Ohtani and Dr. Kevin Ellwood for their guidance, valuable inputs and for allowing me to conduct my experiments at Ford research labs at Dearborn.

I am grateful to Dr. Mohit Nahata and Dr. Chang Yup Seo for their support, assistance, and advice in exploring new research tools and skills, especially during my initial phase as a graduate student. A special thanks to Alexander Hill, who has been a constant friend, motivator, and a guide throughout the completion of this dissertation. I couldn't have asked for a better colleague. I would like to acknowledge Schwank lab's current and past members, Dr. Lei Ma, Dr. Ping Li, Dr. Huawang Zhao, Anna Hayden, Pradeep Krishnakumar, Maithri Venkat, Pallav Jani, and Raghav Kaushik Siddavaram. They have been instrumental in this journey in one way or the other.

Now on a personal level, I am incredibly fortunate to have met some fantastic people and made wonderful friends along this journey. This is a long list, and I cannot possibly elaborate on everyone's role in my life, as this section wouldn't end! Bhuvan Neema, Samhita Shiledar, Rubin Sagar, Ayush Awadhiya, Julian Olivares, Lovlesh Kaushik, Abdulla Alqubati, Luis Rivera, Akshay Sarin, Harsh Agarwal, Harit Bhargava, Sarayu Rao, Sanjana Chandrashekar, Christine Thomas, Bolívar Aponte Rolón, Ariana Mohnke, Austin George the list goes on! All have had a profound influence on my life, and this journey wouldn't have been possible without them.

Most importantly, I would like to thank Appa and Amma for all their scarifies to ensure that I have a solid foundation to build upon, without which this journey wouldn't have been possible. All my accomplishments are in large part a reflection of their efforts. I am extremely grateful to everyone in the Karasulli, Kanmoole, and Kalluraya families for their tremendous support throughout my graduate school, especially during the unprecedented COVID times. A special note of thanks to Kanti Akka and Chikkappa for their constant encouragement that helped me to stay motivated. I am thankful to Sindhoor anna, Survarnakka and Sharath anna, Sumakka for all the help and for making me feel at home away from home in the US. I would like to convey immense gratitude to Ajja, Aayi, Rekhakka, Vinayak Maava, Sahanatte and all the cousins for being my pillar of strength and supporting me throughout my journey. Lastly, Swathi, I can't thank you enough for being an amazing friend, mentor, companion, and constant source of motivation throughout this journey. I have and will continue to look to her for inspiration.

There can be no overstating the contributions of so many people, so my fear is of sinning by omission or under-representation. Simply put, I could not have done it on my own!

Table of Contents

Acknowledgments ii

List of Tables ix

List of Figures x

Abstract xiii

Chapter 1: Introduction **1**

1.1. Volatile organic compounds - a class of primary air pollutants 2
1.2. Major types of VOCs and their sources 3
  1.2.1. Oxygen-containing VOCs 3
  1.2.2. Halogenated VOCs 5
  1.2.3. Aromatic VOCs 5
  1.2.4. Miscellaneous VOCs 6
1.3. Current VOC abatement technologies 6
1.4. Challenges associated with industrial VOC abatement system 9
  1.4.1. Heel accumulation 10
    1.4.1.1. Role of adsorption conditions 13
    1.4.1.2. Role of regeneration conditions 14
    1.4.1.3. Role of adsorbate and adsorbent properties 15
  1.4.2. Inefficiency of destruction unit 16
  1.4.3. Catalytic oxidation of VOCs - an energy efficient solution 17
    1.4.3.1. Metal nanoparticles encapsulated in mesoporous support 19
1.5. Thesis layout 21
1.6. References 23

Chapter 2: Chemical Surface Modification of Beaded Activated Carbon: A Strategy to Inhibit Heel Accumulation from VOCs **34**

2.1. Introduction 34
2.2. Experimental 38
2.2.1. Materials 38
2.2.2. Surface modification of BAC 38
2.2.3. Characterization of BAC 39
2.2.4. Experimental setup and procedure 40
2.2.4.1. Adsorption of target VOCs onto BAC samples 40
2.2.4.2. Thermal desorption of VOCs from saturated BAC 41
2.2.5. *In-situ* desorption studies in thermogravimetric analyzer 42
2.2.6. Diffusive reflectance infrared Fourier transform spectroscopy of heel accumulated BAC samples 42
2.3. Results and discussion 43
2.3.1. Factors influencing desorption characteristics of VOCs and heel accumulation 43
2.3.2. Impact of surface modification on textural properties of BAC 46
2.3.3. Adsorption and desorption characteristics of VOCs on surface modified BAC 51
2.3.3.1. Impact of surface modification on adsorption capacity 51
2.3.3.2. Impact of surface modification on desorption characteristics 52
2.3.4. Analysis of surface functional groups of heel formed in BAC 54
2.3.5. Effect of surface modification on total heel formation 56
2.4. Conclusion 58
2.5. References 60

Chapter 3: Recovering the Adsorption Capacity of Spent Beaded Activated Carbon via Solvent-based Regeneration Technique **67**

3.1. Introduction 67
3.2. Experimental 72

3.2.1. Materials 72
3.2.2. Batch regeneration experiments 72
3.2.2.1. Liquid phase solvent regeneration 72
3.2.2.2. Vapor phase solvent regeneration 73
3.2.3. Characterization of BAC samples 74
3.3. Results and discussion 74
3.3.1. Efficacy of solvents in liquid-phase solvent regeneration 75
3.3.2. Efficacy of solvents in vapor-phase solvent regeneration 76
3.4. Conclusion 79
3.5. References 80

Chapter 4: Self-assembly Directed Encapsulation of Noble Metal Nanoparticles in Mesoporous TiO_2 for Catalytic Oxidation of VOCs 83

4.1. Introduction 83
4.2. Experimental 86
4.2.1. Materials 86
4.2.2. Synthesis of metal encapsulated TiO_2 nanosphere 86
4.2.3. Catalyst Characterization 87
4.2.4. Catalytic activity evaluation 88
4.3. Results and discussion 90
4.3.1. Catalyst synthesis and characterization 90
4.3.2. Catalytic oxidation of n-butanol over metal encapsulated catalysts 95
4.4. Conclusion 97
4.5. References 98

Chapter 5: Improving the Thermal Stability and VOC Oxidation Activity of Ag-TiO_2 Catalysts by Controlling the Catalyst Architecture and Reaction Conditions 104

5.1. Introduction 104
5.2. Experimental 106

5.2.1. Materials 106

5.2.2. Catalyst synthesis 107

5.2.2.1. Synthesis of Ag encapsulated TiO_2 catalysts 107

5.2.2.2. Synthesis of surface impregnated Ag-TiO_2 catalysts 108

5.2.3. *Ex-situ* aging of catalysts in air 109

5.2.4. Catalyst characterization 109

5.2.5. Catalytic activity evaluation 110

5.2.5.1. Arrhenius experiments for evaluation of apparent activation energy 112

5.2.5.2. Repeated high-temperature aging of catalysts 112

5.2.5.3. Influence of water vapor on VOC oxidation efficacy 113

5.2.5.4. Saturating catalyst surface with hydroxyl ions 113

5.3. Results and discussion 113

5.3.1. Catalyst characterization 113

5.3.2. Catalytic performance of fresh catalysts 123

5.3.3. Effect of thermal aging on catalyst morphology and activity 127

5.3.4. Influence of water on oxidation efficacy 133

5.3.5. Effect of saturating the catalyst surface with hydroxyl ions 136

5.4. Conclusion 139

5.5. References 141

Chapter 6: Visible-light Enhanced Catalytic Oxidation of VOCs Over Ag-TiO_2 Core@Shell Catalysts 147

6.1. Introduction 147

6.2. Experimental 151

6.2.1. Materials 151

6.2.2. Synthesis of Ag@TiO_2 catalysts 151

6.2.3. Catalyst characterization 152

6.2.4. Thermal and photo-thermal VOC oxidation experiments 153

6.3. Results and discussion 155

6.3.1. Catalyst characterization 155

6.3.2. Thermal and photo-thermal catalytic oxidation of VOC 159

6.4. Conclusion 160

6.5. References 162

Chapter 7: Conclusions and Future Directions 166

7.1. Conclusion 166

7.2. Future directions 168

7.2.1. Optimizing vapor-phase solvent-based adsorbent regeneration 168

7.2.2. Evaluating the thermal stability of noble-metal encapsulated catalysts 169

7.2.3. Visible-light enhanced reactions over bimetallic encapsulated catalysts 170

7.3. References 172

List of Tables

Table

2.1 Boiling point, molecular weight, and corresponding peak desorption temperatures of individual VOC molecules from the surface of BAC-V 45

2.2 Change in textural properties of the BAC-V after multiple high temperature aging cycles 45

2.3 Textural properties of the BAC samples 47

2.4 VOC adsorption capacities of untreated and surface modified BAC samples 51

2.5 Textural properties of BAC samples after 10 adsorption-desorption cycles 58

3.1 Textural properties of BAC samples before and after different regeneration methods 77

4.1 Metal precursors and their corresponding weights to synthesize in encapsulated TiO_2 catalysts 87

4.2 Textural properties of the encapsulated catalysts 93

5.1 Summary of surface area, average pore size, and average crystallite size of TiO_2 support 119

5.2 Summary of activation energy and turnover frequency for n-butanol oxidation of fresh and aged Ag-TiO_2 catalysts 132

List of Figures

Figure

1.1 Schematic representation of a typical industrial hybrid VOC abatement system 10

2.1 Schematic representation of a typical VOC abatement setup in automotive painting industry 35

2.2 Temperature programmed desorption profile of individual VOCs from BAC-V (a), and cumulative heel accumulation of individual VOCs after 10 adsorption-desorption cycles (b). 43

2.3 Nitrogen adsorption isotherm and pore size distribution of BAC samples 47

2.4 High magnification SEM micrographs of untreated BAC (a), HNO_3 treated BAC (b), NaOH treated BAC (c), and NH_4OH treated BAC (d) 48

2.5 Decomposition of BAC samples in air flow (a), corresponding differential thermogravimetric (DTG) curves (b), and gas phase FTIR spectral snapshot of the decomposition of BAC samples at their respective peak temperatures of decomposition identified from DTG curves (c) 50

2.6 Change in average diameter of the bead and total surface area of surface modified BAC samples after exposing them to multiple heigh temperature cycles 50

2.7 Adsorption breakthrough curves and temperature programmed desorption profiles of VOCs from modified and untreated BAC samples; n-butanol [(a1), (a2)], n-butyl acetate [(b1), (b2)], and 1,2,4-trimethyl benzene [(c1), (c2)] 53

2.8 DRFITS of finely ground BAC samples after 10 adsorption-desorption cycles of different VOC samples [n-butanol (a), n-butyl acetate (b), and 1,2,4-trimethyl benzene (c)] 55

2.9 Percentage heel accumulation in BAC samples after 10 adsorption-desorption cycles of different VOCs [(a) n-butanol, (b) n-butyl acetate, and (c) 1,2,4 – trimethyl benzene] 57

3.1 Schematic representation of thermal regeneration of spent beaded activated carbon 69

3.2 Schematic representation of the experimental setup for liquid phase solvent regeneration (a), and vapor phase solvent regeneration (b) 73

3.3 SEM micrographs of BAC samples 75

3.4 Quantitative N_2 adsorption in different BAC samples obtained through nitrogen physisorption experiment at 77 K 78

4.1 Representation of the synthesis of metal encapsulated TiO_2 catalysts 91

4.2 Thermal decomposition of metal encapsulated TiO_2 catalysts after synthesis 92

4.3 Nitrogen adsorption and desorption isotherms of metal encapsulated TiO_2 catalysts 93

4.4 TEM and XEDS characterization of metal encapsulated TiO_2 catalysts 94

4.5 n-butanol oxidation profiles for metal encapsulated TiO_2 catalysts (a), and Arrhenius plots and corresponding activation energies of different metal encapsulated TiO_2 catalysts (b) 96

5.1 TEM images of the Ag-TiO_2 (E) catalysts immediately after synthesis (a, b), and corresponding SAED pattern taken from a single TiO_2 nanosphere, revealing the amorphous nature of the support (c) 114

5.2 Thermal decomposition of Ag-TiO_2 (E) and Ag-TiO_2 (ES) catalysts after synthesis prior to calcination 114

5.3 TEM images of fresh, post calcined 2% wt. Ag-TiO_2 (I) (a, b); XEDS map of fresh Ag-TiO_2 (I) catalyst ((c) - (f)) 116

5.4 TEM and XEDS characterization of fresh 2 wt. % Ag-TiO_2 (E) catalyst 117

5.5 TEM and XEDS characterization of fresh 2 wt. % Ag-TiO_2 (ES) catalyst 118

5.6 Nitrogen adsorption and desorption isotherms of fresh and aged Ag-TiO_2 catalysts 120

5.7 HRTEM image of the three different catalyst morphologies (Ag-TiO_2 (ES) (a), Ag-TiO_2 (E) (b), and Ag-TiO_2 (I) (c)) indicating the polycrystalline nature of TiO_2 support 121

5.8 XRD patterns of the fresh Ag-TiO_2 (a) and aged Ag-TiO_2 (b) catalyst samples 121

5.9 Normalized and deconvoluted XPS spectra in the Ag 3d scan region for fresh Ag-TiO_2 (a - c), and aged Ag-TiO_2 (d - f) catalysts 122

5.10 n-butanol oxidation profiles for fresh and *ex-situ* aged Ag-TiO_2 (I) (a), Ag-TiO_2 (E) (b), Ag-TiO_2 (ES) (c) catalysts, T_{90} of Ag-TiO_2 catalysts as a function aging cycle (d), and Arrhenius plots for fresh and *ex-situ* aged Ag-TiO_2 catalysts (e) and (f) 124

5.11 Products obtained during the n-butanol oxidation reaction over fresh Ag-TiO_2 (I) (a), Ag-TiO_2 (E) (b), and Ag-TiO_2 (ES) (c) catalysts under dry reaction conditions 125

5.12 Schematic representation of complete oxidation of n-butanol oxidation 126

5.13 STEM and XEDS images of Ag-TiO_2 (I) catalyst subjected to ex-situ high-temperature aging (550 °C for 10 hours) 128

5.14 Bright field and High-angle annular dark-field (HAADF) images of Ag-TiO_2 (E) (a, b) and Ag-TiO_2 (ES) (c, d) catalysts subjected to ex-situ high-temperature aging (550 °C for 10 hours) 130

5.15 n-butanol oxidation profiles for fresh Ag-TiO_2 (I), Ag-TiO_2 (E), and Ag-TiO_2 (ES) catalysts in the presence of 3% water vapor in the reaction feed 134

5.16 Products obtained during the n-butanol oxidation reaction over fresh Ag-TiO_2 (I) (a), Ag-TiO_2 (E) (b), and Ag-TiO_2 (ES) (c) catalysts in the presence of 3% water vapor in the reaction feed 135

5.17 The rate of n-butanol conversion over different Ag-TiO_2 catalysts; under dry oxidation conditions (a), and oxidation carried out after saturating the catalyst surface with hydroxyl ions (b) 136

5.18 Comparison between the n-butanol oxidation profiles over Ag-TiO_2 (I) (a), Ag-TiO_2 (E) (b), and Ag-TiO_2 (ES) (c) catalysts 138

6.1 Schematic illustration of the dynamics of an excited plasmonic nanoparticle 148

6.2 Photo-thermal reactor used to carryout VOC oxidation experiments 154

6.3 TEM images of Ag nanoparticles (a, b), and Ag@TiO_2 core@shell catalysts (c, d) 156

6.4 Analytical characterization of Ag@TiO_2 nanoparticles; Thermal decomposition profile Ag@TiO_2 nanoparticles after synthesis prior to calcination (a), nitrogen sorption isotherm of Ag@TiO_2 catalysts (b), XRD pattern of Ag@TiO_2 catalyst after calcination (c), and UV-Vis absorption spectrum of TiO_2, Ag, and Ag@TiO_2 nanoparticles (d) 157

6.5 Visible light enhanced n-butanol oxidation reaction; n-butanol oxidation profiles over Ag@TiO_2 catalysts in the in the dark and with visible illumination (a) and Rate enhancement of n-butanol oxidation (left axis, green triangles) under visible illumination 159

7.1 X-ray dispersive spectroscopic (a), and Transmission electron microscopy (b) characterization of Ag encapsulated TiO_2 catalysts aged at 800 °C for 4 hours under air 170

7.2 Schematic illustration of proposed bimetallic Ag-Ru encapsulated TiO_2 catalyst (a), and bimetallic hybrid Ru/Ag@TiO_2 catalyst (b) 171

Abstract

Over the last three decades, combined efforts of industries, the EPA, and automakers have helped reduce the emission of many harmful molecules such as carbon monoxide, sulfur dioxide, and particulate matter to improve air quality. However, rapid industrialization and urbanization have contributed to a significant rise in volatile organic compounds (VOCs), one of the primary air pollutants. Prolonged exposure to certain VOCs, even at concentrations as low as 0.25 ppm, is known to be carcinogenic. Therefore, the detrimental health impacts of VOCs and their increasingly stringent environmental regulations warrant continuous research to develop more effective, economical, and sustainable technologies to mitigate their emissions. In most industries, the VOCs are curtailed by combining an adsorption-desorption process using beaded activated carbon (BAC) with subsequent thermal incineration. This hybrid VOC abatement system suffers from two major limitations. First, the occurrence of strongly, or irreversibly adsorbed species in BAC, referred to as "heel", prevents complete regeneration of the sorbent, decreasing its capacity and lifetime. Second, the massive energy requirement of the thermal incinerator increases the carbon footprint of the operation and overall operational cost.

The research presented in this dissertation provides economical and sustainable strategies to address the limitations of the hybrid abatement process described above. Using spectroscopic and thermogravimetric techniques, we aimed at understanding the factors responsible for the heel accumulation mechanism in BAC during gas-phase adsorption-desorption operation. Addressing this, the dissertation provides a facile methodology to modify the surface of the BAC through a chemical treatment to impede heel formation. This modification protocol increases the porosity of BAC by up-to 55% without altering its structural integrity. Consequently, the adsorption capacity of the BAC increased by nearly 38% while decreasing the peak desorption temperature by as much as 50°C due to lowered adsorption strength. Furthermore, this thesis explored feasible methods of regenerating the spent BAC to improve the efficacy of the industrial VOC abatement technique. This effort resulted in the invention of a unique vapor-phase regeneration technique. The lab-scale studies demonstrated that dimethyl sulfoxide vapors could be effectively used to recover nearly 82% of the adsorption capacity of the spent BAC without compromising its structural integrity.

The second phase of this research investigated the feasibility of using energy-efficient catalytic oxidation to decompose or destroy VOCs into H_2O and CO_2 at low temperatures. As such, the dissertation provides a roadmap to the synthesis of a novel catalyst architecture of encapsulating catalytically active noble metals in porous TiO_2 support. Electron microscopic studies indicated that encapsulation helps maintain a uniform metal particle distribution (2-5 nm) and promotes metal-support interactions by maximizing interfacial sites, thereby improving catalytic activity. In addition, we discovered that subjecting the encapsulated catalyst to a post-synthesis solvothermal treatment step anchors the active metal more strongly to the support, which helps maintain superior activity under repeated uses. Finally, the thesis attempts to push the boundaries of catalytic VOC oxidation reactions via concurrent utilization of thermal energy and visible light to bring down the overall energy requirement of the VOC abatement. By encapsulating plasmonic silver nanostructures in a porous TiO_2 shell resembling a core@shell morphology, we created a multifunctional material capable of generating energetic electrons upon visible light illumination. These electrons can be used in tandem with thermal energy to decompose n-butanol at viable rates at significantly reduced temperatures as low as 200°C.

Chapter 1

Introduction

The air that we breathe is perceived as one of the four elemental compositions of creation. Recognizing its pivotal role in the proliferation of life on earth, for centuries, various civilizations and cultures around the globe have focused their efforts to keep it pristine. However, the advent of the industrial revolution in the 18th century brought forth a noticeable change in air quality around the globe. In 1867, troubled by the miasmatic tenements of America's burgeoning cities and their withering air quality, an engineer, Lewis W. Leeds, delivered a series of lectures under the title "Man's own breath is his greatest enemy". He warned that the foul air released to the atmosphere by anthropogenic activities would soon become of the most pressing challenges that humanity would face in the near future.

Almost a century later, in the 1950s, to address the deteriorating air quality, legislations to curb air pollution began appearing in the U.S. and other countries. After the passage of the Clean Air Act in 1963 and the creation of the Environmental Protection Agency (EPA) in 1970, the chemical composition of outdoor air became federally regulated, with penalties for polluters. Since the EPA's establishment, the emissions of many harmful gases, such as Carbon Monoxide (CO) and Sulfur dioxide (SO_2), and particulate matters have significantly reduced. However, this victory may be less significant than we assume.

The emission of volatile organic compounds (VOCs), one of the primary air pollutants from anthropogenic activities, has remained essentially unchanged for more than two decades. Even so, today, exposure to air pollution is regarded as the fifth ranking human health risk factor globally, following malnutrition, dietary risks, high blood pressure, and tobacco [1,2]. World Health Organization (WHO) estimates that exposure to air pollution accounts for almost 4.2 million deaths each year [2]. Therefore, further advancements in engineering sustainable, economic, and efficient technologies that regulate the components responsible for global air pollution are of paramount importance. In this thesis, an attempt has been made to optimize an industrial system designed for the abatement of VOCs. Additionally, a method for synthesizing a novel catalyst architecture, which can be used to destroy or decompose VOCs into harmless products in a more economical, energy-efficient, and sustainable way in industries, is illustrated.

1.1. Volatile organic compounds - a class of primary air pollutants

VOCs are a large group of odorous carbon-based chemicals that easily evaporate at room temperature and atmospheric pressure [3,4]. The EPA defines VOC as "any compound of carbon excluding carbon monoxide, carbon dioxide, carbonic acid, metallic carbides or carbonates, and ammonium carbonate, which participate in atmospheric photochemical reaction" [5]. VOCs are ubiquitous in our daily life. They are present in the naturally occurring scents of flowers to emissions resulting from anthropogenetic activities such as transportation, printing and coating, petroleum refining, food processing, textile manufacturing, and wastewater treatment [6,7]. In recent years, however, extraction and isolation of natural products and the use of organic chemicals on a massive scale have resulted in a substantial increase in VOC emissions around the globe.

A recent epidemiological study states that volatile chemical products are emerging as the largest petrochemical source of urban organic emissions [2]. VOCs negatively influence the climate through their involvement in producing organic aerosols, tropospheric ozone, and smog via photochemical reactions [8,9]. According to The Occupational Safety and Health Administration (OSHA) standards, certain VOCs such as formaldehyde, benzene, and toluene are known to cause health hazards to humans and animals even when inhaled at a concentration as low as 0.25 ppm [9]. Some of the reported ill effects from long-term exposure to VOCs include headaches, eye, nose, throat irritations, nausea, dizziness, memory loss, and damage to the liver, central nervous system, and lungs [10–15]. In 2020, a total of 12.1 million metric tons of VOCs were emitted in the USA, with the oil and gas sector, industries handling paints and solvents, and agricultural activities being the most prominent contributors [16]. Due to their harmful impact on the environment, human health, and tremendous growth in the extent of VOCs emitted, the release of VOCs into the environment is strictly being controlled to meet the stringent emission regulations worldwide [1].

1.2. Major types of VOCs and their sources

Understanding the molecular structure of VOCs is essential for engineering an appropriate abatement method. Often, abatement methods depend on the VOCs' structure, heteroatom content, toxicity, and concentration. This section gives a high-level overview of the VOC classifications based on their molecular structure and discusses the most common sources of their emissions.

1.2.1. Oxygen-containing VOCs

Oxygen-containing VOCs are the most abundant in both indoor and outdoor settings as they contain many common functional groups such as aldehydes, ketones, and alcohols. Some oxygen-containing function groups, such as carbonyls, are particularly harmful. This is due to their ability to form free radicals, which results in the formation of tropospheric ozone [17]. Some of these oxygen-containing VOCs are abundant in indoor environments and are responsible for health effects such as allergies, respiratory illnesses, and even cancer [18]. For example, formaldehyde has been identified as one of the most harmful carbonyl compounds due to its toxicity and abundance in the indoor environment [19]. Partial degradation or incomplete destruction of larger VOC molecules often results in the formation of formaldehyde. The EPA and the American Lung Association recommend a maximum threshold concentration of 0.1 ppm in the air to maintain acceptable indoor air quality. While ambient concentrations are around 0.03 ppm, industrial workers are commonly exposed to much higher levels of formaldehyde for extended durations, which can cause adverse health effects [20]. In a study done by Jordan et al., formaldehyde levels of 30 ppm or more caused allergic reactions in patients even when exposed for short durations [21]. Ethyl acetate and acetone are two ketone-based VOCs that are the most emitted VOCs from anthropogenic activities. Ketone-based VOCs are dangerous and can cause depression and damage to the nervous system. They are present in smaller concentrations compared to their aldehyde counterparts [22]. Although recently acetone has gained VOC exempt status from the EPA, its deleterious effect on human health is still being studied. Alcohols are commonly used in paints, cosmetics, and personal care products such as nail polish removers, perfumes, colognes, and hair sprays. Some of the common alcohol-based VOCs include ethyl alcohol, isopropyl alcohol, butanol, and benzyl alcohol. Alcohols increase the formation of aldehydes by secondary reactions, which cause throat and eye irritation, shortness of breath, and chest tightness. Long-term exposure to short-chain alcohols (ethanol, propanol, and butanol) may cause harm to the central nervous system [15].

1.2.2. Halogenated VOCs

Halogenated VOCs (X-VOCs, where X is the halogen) are hazardous compounds due to their strong bioaccumulation potential, acute toxicity, and resistance to degradation. They are very stable, leading to slower degradation rates, and have been shown to contaminate both ambient air and groundwater systems. Compared to other VOCs, X-VOCs are challenging to remediate due to their ability to deactivate catalysts and form harmful byproducts. More importantly, the remediation process requires much higher energy to destroy or decompose X-VOCs effectively [23]. Polychloromethanes (PCMs) such as chloroform, dichloromethane, trichloromethane, and carbon tetrachloride, are the most widely used compounds among X-VOCs. Formulations and processing of chemical extractants, paints and adhesives, drugs, and polymers use excessive PCMs. Humans can be exposed to X-VOCs by drinking water, inhalation, and adsorption during swimming [24]. These compounds significantly impact the destruction of the ozone layer and are known to contribute to global warming substantially. Compared to CO_2, which has a global warming potential (GWP) index of 1, it is reported that one kg of X-VOCs can cause 10 to 1800 times more warming than CO_2 over 100 years, making the GWP index of X-VOCs between 10 - 1800 [25].

1.2.3. Aromatic VOCs

Aromatic compounds such as benzene, ethylbenzene, and toluene occur naturally in petroleum products, including gasoline and other fuels produced from crude oil. Consequently, the incomplete combustion of liquid fuels in automobiles releases significant amounts of aromatic compounds into the atmosphere. Compounds such as 1,2,4-trimethylbenzene are also used in various products and formulations such as petrochemicals, paint, medicine, and detergents [26]. Aromatic VOCs are responsible for a large portion of groundwater and soil contamination through vapor sorption. Aromatic compounds are toxic and carcinogenic, cause severe damage to the ozone layer, produce photochemical smog, and pose mutagenic hazards [27]. At low-level exposure, aromatic VOCs can cause weakness, nausea, tiredness and loss of appetite, sight, and memory. Inhalation of a high level of aromatic compounds can cause unconsciousness, dizziness, and even death. The safe limit of aromatic compounds is 1 mg/L in drinking water and 200 ppm in air [22].

1.2.4. Miscellaneous VOCs

Some alkenes also belong in the category of VOCs. Propylene is considered to be extremely polluting due to its ability to create ozone photochemically. Ethylene is of considerable importance as it is used as a raw material in many petrochemical syntheses [28]. Ethylene released during the storage of agricultural products can induce physical and chemical changes in vegetables and fruits. Furthermore, ethylene is also extensively used to produce varnishes, synthetic resins, adhesives, printing ink, pharmaceutical products, and perfumes due to good solubility and volatility [29]. Methyl tert-butyl ether (MTBE) is another example of semi-volatile VOC used as a fuel enhancer to improve octane ratings and oxidation ability of fuel [30]. Improper storage of MTBE in underground tanks and watercraft has resulted in leakages. Their presence in drinking water has become a significant issue in the U.S and Europe. MTBE is potentially carcinogenic and adversely affects the odor and taste of drinking water [31].

1.3. Current VOC abatement technologies

Broadly, industrial VOC emission treatment operations can be divided into non-destructive and destructive abatement techniques. The former involves capturing or trapping VOC molecules at the point of exhaust in a process. On the other hand, destruction operations are an “end-of-pipe” solution strategy, where VOCs are decomposed or converted to comparatively less harmful products like CO_2 and water vapor.

Absorption, condensation, membrane separation, biofiltration, and adsorption are extensively used non-destructive methods of VOC removal [32]. Absorption is used to remove VOCs from gas streams by contacting the VOC-laden effluent gas with a liquid solvent. As a result, any soluble VOCs will be transferred to the liquid phase. In effect, the air stream is scrubbed of VOCs. This operation generally occurs in an absorption tower consisting of packings, trays, and liquid atomizer (spray nozzle) designed to provide the liquid-vapor contact area to facilitate the mass transfer. However, it usually comes with challenging subsequent treatment of spent solvent and high maintenance costs [33]. Condensation, also referred to as cryogenic separation, is an alternative unit operation used in several industrial processes to capture VOCs. It can recover VOCs by transforming them into liquid at lower temperatures or higher pressures. Nonetheless, due to the increased processing cost, condensation usually deals with valuable VOCs at high concentrations and is limited by the disposal of spent coolant during the condensation process [34]. Membrane separation is one of the emerging technologies for VOC reduction. The principle of membrane separation capitalizes the difference in the permeability of VOC molecules to achieve separation effectively. Generally, the pressure, concentration, and electric potential difference acts as the driving force for the separation. However, the high expense, poor stability, and low flux of membranes have limited their use in industry [35]. Biofiltration technology utilizes microorganisms for VOC abatement. The process comprises of a filter bed attached with microbes that remove VOC molecules by metabolizing them. Although biofiltration comes with the advantages of low operational and maintenance costs, several studies have reported bioaerosol emissions, filter bed clogging, and low abatement efficiency [36–38]. Among all the non-destructive VOC abatement techniques, adsorption is recognized as one of the most effective methods for removing VOCs, especially at low concentration (<1000 mg/m^3) due to high selectivity, low energy consumption, and facile operation [39,40]. Undoubtedly, the choice of adsorbent plays a critical role in achieving an effective adsorption process. Textural properties (surface area and porosity) and surface physicochemical properties of adsorbents determine their capability of VOC removal.

Methods such as thermal incineration and catalytic oxidation are among the most commonly used destructive technologies for VOC abatement [41]. Thermal incineration involves burning the VOCs at extremely high temperatures (900 - 1200 °C), resulting in CO_2 and H_2O [42]. This process is suitable for removing medium to high concentrations (≥ 2000 mg/m^3) of VOCs. However, as the incinerators need to be maintained at high operational temperatures, their energy requirement is extremely high. However, the catalytic oxidation of VOCs is similar to thermal incineration. It involves using a catalyst in the form of a packed column to reduce the energy of the otherwise high-temperature operation. In general, the catalytic oxidation of VOCs follows the deep oxidation pathway, which is the complete conversion of the VOC to CO_2 and H_2O [41].

Although numerous studies have been devoted to developing VOC control technologies, the complicated emissions characteristics of VOCs impose many practical limitations. The wide variety of VOCs composition and differences in their stability make their treatment very difficult and non-universal. For example, exhaust from printing industries commonly emits alcohols, ketones, and aromatics, while acidic gas is the major pollutant among the prominent families of VOCs emitted from pharmaceutical industries. Besides, the distinction between emission conditions of VOCs is another challenge for VOCs control. For instance, effluent gas emitted from painting or spraying processes generally exit at ambient temperatures. However, the effluent gas from the chemical and pharmaceutical industries exits at a much higher temperature with significantly higher relative humidity. As a result, the effectiveness of abatement processes such as adsorption or catalytic oxidation gets reduced substantially. Therefore, it is imperative to consider the concentration, composition, temperature, pressure, and humidity of the effluent streams while designing and implementing an effective VOC abatement system.

1.4. Challenges associated with industrial VOC abatement system

With continuous development and optimization over industrial front-end processes, most operations tend to emit low-concentration VOCs. Therefore, deploying traditional technologies (combustion and absorption) is inapplicable due to their high-energy consumption, significant capital investment but limited efficiency under low exhaust concentrations. Additionally, owing to the diversity and complexity of VOCs in the stream, it is unrealistic to get rid of them all using one single technology. Therefore, scientists and engineers realized that hybrid treatments combining adsorptive concentration with those of thermal incineration, catalytic oxidation, or ozonation are more effective and appropriate than individual ones. A typical industrial hybrid VOC treatment process with a combination of non-destructive (adsorption-desorption and condensation) and destructive (thermal incinerator) technologies is shown in Figure 1.1.

The hybrid adsorptive concentration-thermal incineration technology is a well-designed solution to abate low concentrations of VOCs. Generally, a porous adsorbent with a high surface area, such as activated carbon, adsorbs low concentrations of VOCs from the inlet exhaust in a fluidized adsorption column. As a result, treated gas (clean gas) is released into the atmosphere. As the adsorbent gets saturated by VOCs and loses its adsorption capacity, it is regenerated by desorbing the VOCs at elevated temperatures (300 - 500 °C) in a desorption column. The adsorption-desorption process is carried out cyclically to reuse the adsorbent. Employing continuous adsorption and desorption, higher concentration (10 - 30 times of inlet) VOCs flow is obtained, making the post-treatment more energy efficient. Subsequently, the concentrated stream with VOCs exiting the desorption column is condensed and sent to an incinerator, where the VOCs are combusted at 900 - 1200 °C.

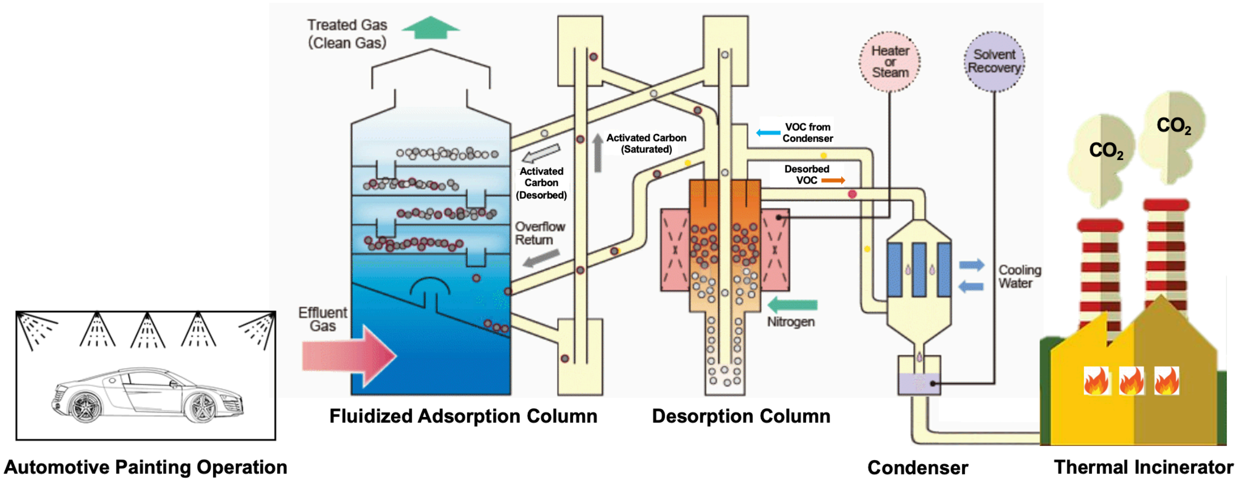

Figure 1.1 *- Schematic representation of a typical industrial hybrid VOC abatement system.*

1.4.1. Heel accumulation

While the hybrid VOC treatment system described in Figure 1.1 is very effective for VOC abatement, the cyclic VOC adsorption-desorption process is not entirely reversible [43]. The occurrence of strongly, or even permanently, adsorbed VOC molecules results in irreversible adsorption of carbonaceous material. This irreversible adsorption also termed "heel formation," prevents the complete regeneration of the adsorbent, decreasing its capacity and operational lifetime [44,45]. As a result, the operation and maintenance costs increase due to more frequent adsorbent replacement to maintain a high column adsorption capacity. Therefore, understanding the factors contributing to irreversible adsorption and finding solutions to limit heel accumulation is instructive in increasing the adsorbent's functional life.

Adsorption can be reversible or irreversible. Reversible adsorption is often attributed to weak physical interactions, such as van der Waals forces, between the adsorbate and the adsorbent. In most cases, physisorption is reversible due to its low heat of adsorption (20 - 70 kJ/mol) [46]. However, Van der Waals forces may be strong enough to prevent the desorption of VOC molecules under few circumstances. For example, when VOC molecules with a similar molecular diameter as the adsorbent's pore width are being desorbed, strong dispersive forces make the desorption difficult due to overlapping forces from opposing pore walls [47]. The presence of these non-desorbed species (heel) decrease the capacity of the adsorbent in subsequent adsorption cycles.

The occurrence of irreversible adsorption is predominantly reported during the removal of organic compounds in aqueous solutions. Generally, adsorption of phenol or other aromatics occurs in the aqueous phase by displacing the water molecule, resulting in a relatively higher adsorption heat (≥ 100 kJ/mol) [48,49]. However, from a qualitative perspective, the adsorption fundamentals are similar in gas and aqueous phases. Thus, the outcomes of irreversible aqueous phase adsorption of organic compounds can be reviewed to identify the relevant operational parameters in gas phase capture of VOCs. Furthermore, studies carried out to understand the irreversible adsorption of gas phase VOC molecules in activated carbon are very limited. Broadly, three scenarios can result in irreversible adsorption:

i. Strong interactions between adsorbent and adsorbate, resulting in chemisorption.
ii. High desorption temperatures leading to oxidative coupling, forming molecules that have higher molecular weight or boiling point within the pores of the adsorbent.

iii. Decomposition of adsorbate during regeneration, resulting in coke formation inside the adsorbent's pores.

Chemisorption is a kind of adsorption involving a chemical linkage between the adsorbent and the adsorbate [48]. As such, the heat of adsorption is high (~ 400 kJ/mol), approaching the energy of chemical bonds [49]. Unlike physical adsorption, which relies on the accessible pore volume of the adsorbent, chemisorption relies on accessible adsorption sites. As chemisorption involves surface reactions, adsorbates can only form a monolayer on the adsorbent. The increased surface area only enhances chemisorption if there is an associated increase in the adsorption sites accessible to the contaminant [50]. As chemisorption results in some sort of bond formation, a shear increase in regeneration temperatures or pressures may not be sufficient to break the bonds between the adsorbent and the adsorbate [51]. This can increase operational costs but may also increase selectivity [47–49,51]. While there are benefits of investigating chemisorption for environmental pollution remediation purposes, it generally diminishes adsorption capacity in successive adsorption cycles and a shorter lifetime of the adsorbent [52,53].

Researchers have reported the formation of polymeric compounds in the pores of the adsorbent due to the oxidative coupling of phenolic compounds in the aqueous phase [54] . Several studies show that irreversible adsorption of phenols can be attributed to oxidative coupling [55–59]. Upon losing a hydrogen atom, a phenol molecule is converted to a phenoxy radical that can oligomerize with others. The reaction can occur at room temperature in an activated carbon pore. Oxidative coupling promotes irreversible adsorption as it results in the formation of larger compounds with higher boiling points [60,61]. Additionally, if coupling occurs in a larger void space accessible only through narrow channels, the oligomers can become trapped. Several factors, including the chemical properties and pore size distribution of the adsorbent, the presence of oxygen in adsorption medium and, to a lesser extent, the presence of metals or metal oxides on adsorbent's surface can affect oxidative coupling.

Organic adsorbates may decompose during regeneration due to exposure to high temperatures, resulting in the formation of amorphous, carbonaceous deposits, also known as coke, inside the pores of the adsorbent, which subsequently decreases their adsorption capacity [44]. Suzuki et al. performed one of the first comprehensive studies on the behavior of adsorbates during thermal regeneration. Using thermogravimetric analysis, they showed that adsorbed phenols decompose to form carbon deposits inside the pores of the activated carbon adsorbent, which remain there even when heated to 800 °C [62]. The carbon deposits may be removed when the adsorbent is reactivated at temperatures greater than 600 °C under oxidizing environments such as steam [63]. However, reactivation results in adsorbate decomposition, diminishing the adsorption capacity during successive adsorption-desorption cycles and a shorter lifetime of the adsorbent.

1.4.1.1. Role of adsorption conditions

Adsorption conditions, including adsorption environment and temperature, have a remarkable effect on the heel formation and accumulation [64]. Identifying the conditions that promote or hinder irreversible adsorption can help us better design the industrial VOC abatement.

The oxidative environment during adsorption-desorption operation can initiate oxidative coupling which can promote heel accumulation [65]. Such occurrences have been extensively reported in aqueous adsorption systems [8,66,67]. A study conducted by Vidic et al. shows a linear relationship between the consumption of dissolved oxygen (DO) and irreversibly adsorbed phenol molecules [59]. Nakhla et al. confirmed these results, showing regeneration efficiencies for phenol-loaded carbon of 80% and 25% in anoxic and oxic conditions, respectively [68].

Adsorption of organic compounds onto activated carbon is exothermic. Hence, adsorption capacity decreases with an increase in adsorption temperature [48,49]. Furthermore, providing additional thermal energy increases the likelihood of polymerization reactions and bond-forming chemisorption and adsorbent desorption. Several researchers have studied the impact of temperature on the polymerization of adsorbed phenols. Most studies reported a greater extent of irreversible adsorption at higher adsorption temperatures due to increased polymerization and chemisorption [69–71].

1.4.1.2. Role of regeneration conditions

Conditions such as regeneration environment, regeneration temperature, desorption gas flow rate, and heating rate can influence heel formation and accumulation. Alvarez et al. found that high-temperature regeneration in an oxidizing environment achieved almost 90% recovery of adsorption capacity of activated carbon. In contrast, regeneration in an inert environment could only recover nearly 50% of the initial adsorption capacity of the spent activated carbon [65].

The type of regeneration plays a major role in heel formation. For instance, during conductive heating regeneration of activated carbon saturated with a mixture of VOC adsorbates, increasing regeneration temperature from 288 to 400 °C facilitated VOC desorption and decreased heel formation by 61% [69]. However, in the case of electrothermal regeneration of activated carbon saturated with trimethylbenzene (TMB), a higher heel was observed in samples regenerated at 400 °C than samples regenerated at 288 °C. Decomposition of TMB due to high-temperature exposure could have caused higher heel formation on microporous activated carbon [44]. Additionally, the flow rate of regeneration gas and its constituents can affect irreversible adsorption. Low flow rates may cause high adsorbate concentration inside carbon pores, particularly for highly microporous carbons. Conversely, the combination of elevated regeneration temperatures with high concentration of adsorbates, caused by low flow rates, can increase the prevalence of coke [72]. Fayaz et al. investigated the effects of regeneration heating rate on irreversible adsorption of VOCs from two different kinds of activated carbon with varying microporosity. For higher regeneration temperature (400 °C), a higher heating rate increased heel accumulation by 92% in predominantly microporous activated carbon and by 169% in partially microporous activated carbon. Conversely, lower regeneration temperature (288 °C) showed no significant effect on heel accumulation. Therefore, high regeneration and high heating rates can contribute to adsorbate decomposition, leading to coke formation inside the carbon pores resulting in irreversible adsorption [73].

1.4.1.3. Role of adsorbate and adsorbent properties

The pore size distribution of adsorbent affects the reversibility of adsorption [74]. Narrow pore size distribution hinders the oligomerization of phenolic compounds and therefore decrease irreversible adsorption [75]. However, contradictions were also found where adsorbents' narrow pore size increased irreversible adsorption by enhancing adsorption energy [76]. Several studies have shown a correlation between the amount of heel and pore structure of activated carbon, confirming that micropores contribute more to heel formation due to plausible transport limitations [64].

The properties of the adsorbate, including molecular weight, kinetic diameter, boiling point, functional group identity and density, and thermal stability can influence irreversible adsorption on activated carbon adsorbents. Phenols have clearly shown irreversible adsorption in the aqueous phase [49,69,71]. Adsorbates' critical oxidation potential (COP), the amount of energy required to add or remove electrons to or from an element or compound, essentially controls the potential of oxidative coupling on activated carbon and consequent heel formation. Therefore, adsorbates with electron-donating groups reduce COP and increase irreversible adsorption. In contrast, electron-withdrawing groups can increase the COP and hinder the dehydrogenation of adsorbates, minimizing irreversible adsorption. Aqueous phase adsorption of both electron-donating and electron attracting compounds on activated carbon were compared, and results showed irreversible adsorption in the presence of electron-donating groups. In contrast, electron-attracting groups adsorbed reversibly [77,78]. However, these factors are not very well evaluated and understood during gas-phase adsorption-desorption operations.

1.4.2. Inefficiency of destruction unit

While the VOC pre-concentrator unit (adsorption-desorption) suffers from perpetual heel accumulation, the VOC destruction unit (thermal incinerator) is extremely energy-intensive [79]. Thermal incineration is a chemical process arising from the rapid combustion of VOC molecules with oxygen resulting in the release of heat. The combustion reaction is initiated when the bonds between the heteroatoms of VOCs and the diatomic oxygen molecule are broken. This process requires a certain energy, referred to as activation energy. As such, thermal incinerators are maintained at very high temperatures to provide the activation energy required for decomposition.

In the setup described in Figure 1.1, the exhaust stream from the desorption column enters the combustion chamber of the thermal incinerator, where the VOCs are combusted with natural gas. The temperature in the combustion chamber is typically between 900 - 1200 °C [15]. Even though thermal incinerators have a high VOC destruction efficiency, the energy required to operate them is exceptionally high. Due to the low fuel cost, natural gas is often supplemented to maintain the high operating temperatures of the thermal incinerator [80]. However, this auxiliary fuel consumption makes the VOC destruction process expensive and increases the overall carbon footprint. For example, the life cycle impact analysis conducted by Tomatis et al. showed that a single thermal incinerator used for the abatement of benzene, toluene, ethylbenzene, and xylene resulted in an enormous amount of CO_2 (160 tons/day) [81]. Additionally, thermal incinerators can result in partial oxidation of VOCs, leading to the formation of CO or toxic hydrocarbons along with excessive CO_2 production. Furthermore, combustion of VOC-natural gas mixture in the air at high temperatures results in NO_x formation, which is another class of air pollutant. Therefore, the exhaust from thermal incinerators often requires an additional setup of treatment [82].

1.4.3. Catalytic oxidation of VOCs - an energy efficient solution

Catalysts are materials that accelerate the rates of chemical reactions without undergoing any permanent chemical change [83]. An efficient catalyst allows the desired reactions to occur at lower temperatures than non-catalytic chemical transformations, reducing the overall energy requirement of the process. They do so by providing new reaction pathways for the reactants to form the product via the formation of chemical intermediates stabilized by the catalyst surface. Additionally, catalytic reactions are often highly selective, converting reactants to the desired products [84].

The catalytic properties of metal nanoparticles mostly emerge from the relatively high energy of metal surface atoms. Additionally, metal nanoparticles hold great promise in catalysis due to their high surface-to-volume ratio and distinctive electronic structures compared with their bulk counterparts [85]. Generally, there are two types of metal atoms in any arbitrary structure.

1) *bulk metal atoms that are totally surrounded by other metal atoms (i.e., highly coordinated)*, and 2) *surface metal atoms bonded with underlying metal atoms but lack bonds at the surface (i.e., under-coordinated)*. This deficiency of chemical bonds renders the metal surface atoms higher in energy. As a result, the likelihood of seeking other atoms to share electron density and create chemical bonds increases. As such, when metal surface atoms form a chemical bond with a molecule, the molecules' bonds become weaker, making it easier for reactions to occur. As the molecule's bond breaks, adjacent metal surface atoms chemically bond with the resulting fragments, thereby stabilizing those fragments. These chemical fragments then react with the other chemical fragments on the metal surface and eventually desorb, forming a new molecule. Hence, metal surface atoms or catalysts facilitate the making and breaking of chemical bonds, resulting in chemical reactions.

The catalytic oxidation of VOCs follows a similar reaction pathway as that of thermal incineration. However, it involves using a catalyst in the form of a packed column to reduce the activation energy of the otherwise high-temperature operation and alter the reaction kinetics of the thermal combustion of a VOC. In general, the catalytic oxidation of VOCs usually follows the deep oxidation pathway, which is the complete conversion of the VOC to CO_2 and water [7]. Owing to their superior ability in making and breaking bonds with complex molecules, nanoparticles of noble metals (Pt, Pd, Au, Ag) are generally used as catalysts to achieve complete oxidation of VOCs at low temperatures [86]. Nevertheless, widespread utilization of these metals coupled with their scarcity has appreciably increased their cost over the last decade.

Given the importance of metal surface atoms for catalysis, their scarcity, and increasing costs, the synthesis of catalysts has been aimed at maximizing the availability of metal surface atoms per mass of the metal. Generally, metal nanoparticle catalysts are synthesized using a technique known as surface impregnation. This method involves physically mixing a metal precursor (solvated metal ions or transition metal complexes) with a metal oxide support (SiO_2, Al_2O_3, ZrO_2, TiO_2, etc.). Thus, the metal precursor anchors onto the oxide support [87]. The result is a catalyst of small metal nanoparticles which provides the most significant metal surface sites per mass of metal for reactions. These catalysts are often referred to as “supported metal catalysts”. However, this synthesis approach comes with an associated drawback. Because of their high surface energy, metal nanoparticles are thermodynamically unstable and are prone to migration and coalescence, especially at high reaction temperatures [87]. Subsequently, these thermally induced structural changes, also known as sintering, result in a dramatic decrease in catalytic activity and selectivity, thereby reducing the efficiency of catalytic oxidation. Therefore, it is imperative to design catalysts that are resistant to the aforementioned adverse thermal restructuring and maintain their activity for a prolonged period of operation.

1.4.3.1. Metal nanoparticles encapsulated in mesoporous support

Researchers have developed several strategies such as strengthening the metal-support interactions, stabilizing the dispersed active metal nanoparticles through atom trapping to address adverse thermal restructuring and subsequent catalyst deactivation [88,89]. However, some of these methods require complex post-synthesis treatments, while others, due to the specificity of the synthesis methodology, exhibit difficulties in scale-up. Notably, a new architecture of encapsulating metal nanoparticles encapsulated in a mesoporous matrix has received substantial attention in recent years [85,90].

Mesoporous materials possess nanopores with a size of 2-50 nm, usually synthesized by cooperative self-assembly of surfactants and framework precursors. The high surface area of this porous matrix contributes to a better spatial dispersion of metal nanoparticles, provides enhanced stability against migration and coalescence during reactions at elevated temperatures, and allows convenient mass transfer even for large-molecule reactants. Jongh et al. demonstrated that the wet impregnation synthesis method could be used to encapsulate Cu-Zn nanoparticles of 4 nm in mesoporous SBA-15 silica support. The capillary force draws the metals salt solution into the mesopores during the catalyst synthesis and helps in synthesizing spatially separated Cu-Zn nanoclusters. They also showed that the agglomeration of the nanoparticles could be minimized when they were uniformly distributed in mesopores with large interparticle distances [91]. Xiao et al. also demonstrated similar encapsulation strategies. They delineated a method to encapsulate nanoparticles of Pt, Pd, Rh, and Ag in various kinds of zeolite supports such as BEA, MOR, and MFI. Compared to supported metal catalysts, these encapsulated metal nanoparticles showed better stability against agglomeration in a series of high-temperature catalytic reactions, such as water-gas shift, CO oxidation, and oxidative reforming of methane [92]. Strong metal-support interactions could also be established when the metal nanoparticles are encapsulated in metal oxides. As a typical example, Bae et al. synthesized Cu nanoparticles in mesoporous γ-Al_2O_3 for dimethyl ether synthesis from syngas. Formation of stable copper aluminate was observed between the Cu nanoparticles and the γ-Al_2O_3 support, leading to strong metal-support interactions. Benefiting from the spatial confinement by the γ-Al_2O_3 and formation of copper aluminate, the catalyst showed not only enhanced catalytic activity but significantly suppressed aggregation of the Cu nanoparticles [93]. Another fascinating feature of the encapsulated metal nanoparticles is their ability to drive tandem catalysis as they can integrate different interfaces in one nanostructure in a controllable manner. For example, Yang et al. presented the fabrication of Pt-CeO_2 nanoparticles encapsulated in mesoporous silica for tandem alkene hydroformylation [94]. Here, the Pt-CeO_2 interface was active for the production of CO and H_2 from methanol decomposition, while the Pt/SiO_2 interface could catalyze the hydroformylation of ethylene with CO and H_2. Compared with the single step hydroformylation of ethylene with CO and H_2, the tandem hydroformylation of ethylene with methanol showed greatly enhanced selectivity.

Apart from the methods mentioned above, several other facile methods to encapsulate active metal nanoparticles in porous supports have been elucidated in literature [85]. Depending upon the end-use and specificity of catalytic reactions, one may choose to adopt one or more of the aforementioned methods to synthesize thermally stable catalysts.

1.5. Thesis layout

Given the context discussed in Section 1.4, a plan of study was implemented to address the limitations of industrial VOC abatement systems. Chapter 2 focuses on understanding the primary factors that affect the heel accumulation mechanism in activated carbon during gas-phase adsorption-desorption operation. Additionally, the chapter provides a simple methodology to modify the surface of the activated carbon (adsorbent) through a chemical treatment to impede heel accumulation. Finally, through comprehensive material characterization and analytical studies, the chapter attempts to shed light on how the surface modification limits heel formation during the cyclic adsorption-desorption process.

While surface modification slows down the formation and accumulation of the heel, it does not completely eliminate it. Recognizing this phenomenon, in Chapter 3, details of a novel gas-phase solvent regeneration method are discussed. The results indicate that this regeneration method can be implemented *in-situ* during VOC abatement operation to recover the adsorption capacity of spent activated carbon effectively. Combined, Chapters 2 and 3 can address the limitations of the VOC pre-concentrator unit and make the process more economical.

Chapters 4,5, and 6, discuss different facile techniques to synthesize sinter-resistant metal encapsulated catalysts. Specifically, Chapter 4 describes the details of synthesizing a novel catalyst architecture of encapsulating and dispersing catalytically active noble metal (Pt, Pd, Au, Ag) nanoparticles inside a porous TiO_2 nanosphere. Microscopic studies show that this synthesis approach helps achieve a high dispersion of noble metal nanoparticles and promotes metal-support interactions, which are critical in enhancing the overall catalytic activity of the material. Chapters 5 and 6 comprehensively elucidate methodologies of improving the thermal stability, and VOC oxidation activity of silver encapsulated TiO_2 catalysts by controlling the catalyst architecture and reaction conditions to design an economical and sustainable catalytic VOC abatement system. Overall, these chapters evaluate the feasibility of using catalytic oxidation to destroy or decompose the VOCs as an alternative to the energy-intensive thermal incineration process.

Finally, Chapter 7 enlists different natural pathways that emerge for future work. First, in the context of optimizing solvent-based regeneration studies, and second, generalizing the methods for synthesizing thermally stable encapsulated catalysts and leveraging the concurrent visible light utilization capability of silver encapsulated TiO_2 catalysts to improve the reaction efficiencies. Preliminary data on improving the thermal stability of encapsulated catalysts is provided, and avenues for more long-term studies are discussed.

1.6. References

(1) Lewis, A. C. The Changing Face of Urban Air Pollution. *Science* **2018**, *359* (6377), 744 – 745. https://doi.org/10.1126/science.aar4925.

(2) McDonald, B. C.; de Gouw, J. A.; Gilman, J. B.; Jathar, S. H.; Akherati, A.; Cappa, C. D.; Jimenez, J. L.; Lee-Taylor, J.; Hayes, P. L.; McKeen, S. A.; Cui, Y. Y.; Kim, S.-W.; Gentner, D. R.; Isaacman-VanWertz, G.; Goldstein, A. H.; Harley, R. A.; Frost, G. J.; Roberts, J. M.; Ryerson, T. B.; Trainer, M. Volatile Chemical Products Emerging as Largest Petrochemical Source of Urban Organic Emissions. *Science* **2018**, *359* (6377), 760 – 764. https://doi.org/10.1126/science.aaq0524.

(3) Baur, G. B.; Yuranov, I.; Renken, A.; Kiwi-Minsker, L. Activated Carbon Fibers for Efficient VOC Removal from Diluted Streams: The Role of Surface Morphology. *Adsorption* **2015**, *21* (6), 479–488. https://doi.org/10.1007/s10450-015-9685-5.

(4) Xian, S.; Yu, Y.; Xiao, J.; Zhang, Z.; Xia, Q.; Wang, H.; Li, Z. Competitive Adsorption of Water Vapor with VOCs Dichloroethane, Ethyl Acetate and Benzene on MIL-101(Cr) in Humid Atmosphere. *RSC Advances* **2015**, *5* (3), 1827–1834. https://doi.org/10.1039/C4RA10463C.

(5) What is the definition of VOC? | Air Emissions Inventories | US EPA https://www.epa.gov/air-emissions-inventories/what-definition-voc (accessed Apr 22, 2021).

(6) Zhang, G.; Liu, Y.; Zheng, S.; Hashisho, Z. Adsorption of Volatile Organic Compounds onto Natural Porous Minerals. *Journal of Hazardous Materials* **2019**, *364*, 317–324. https://doi.org/https://doi.org/10.1016/j.jhazmat.2018.10.031.

(7) Krishnamurthy, A.; Adebayo, B.; Gelles, T.; Rownaghi, A.; Rezaei, F. Abatement of Gaseous Volatile Organic Compounds: A Process Perspective. *Catalysis Today* **2020**, *350*, 100–119. https://doi.org/https://doi.org/10.1016/j.cattod.2019.05.069.

(8) Zhang, X.; Gao, B.; Creamer, A. E.; Cao, C.; Li, Y. Adsorption of VOCs onto Engineered Carbon Materials: A Review. *Journal of Hazardous Materials* **2017**, *338*, 102–123. https://doi.org/https://doi.org/10.1016/j.jhazmat.2017.05.013.

(9) Permissible Exposure Limits – OSHA Annotated Table Z-1 | Occupational Safety and Health Administration https://www.osha.gov/annotated-pels/table-z-1 (accessed Mar 30, 2021).

(10) Organization, W. H. WHO Guidelines for Indoor Air Quality: Selected Pollutants. **2010**.

(11) Gupta, K. N.; Rao, N. J.; Agarwal, G. K. Adsorption of Toluene on Granular Activated Carbon. *International Journal of Chemical Engineering and Applications* **2011**, *2* (5), 310.

(12) Gironi, F.; Piemonte, V. VOCs Removal from Dilute Vapour Streams by Adsorption onto Activated Carbon. *Chemical Engineering Journal* **2011**, *172* (2), 671–677. https://doi.org/https://doi.org/10.1016/j.cej.2011.06.034.

(13) le Cloirec, P. Adsorption onto Activated Carbon Fiber Cloth and Electrothermal Desorption of Volatile Organic Compound (VOCs): A Specific Review. *Chinese Journal of Chemical Engineering* **2012**, *20* (3), 461–468. https://doi.org/https://doi.org/10.1016/S1004-9541(11)60207-3.

(14) Churkina, G.; Kuik, F.; Bonn, B.; Lauer, A.; Grote, R.; Tomiak, K.; Butler, T. M. Effect of VOC Emissions from Vegetation on Air Quality in Berlin during a Heatwave. *Environmental Science & Technology* **2017**, *51* (11), 6120–6130. https://doi.org/10.1021/acs.est.6b06514.

(15) He, C.; Cheng, J.; Zhang, X.; Douthwaite, M.; Pattisson, S.; Hao, Z. Recent Advances in the Catalytic Oxidation of Volatile Organic Compounds: A Review Based on Pollutant Sorts and Sources. *Chemical Reviews* **2019**, *119* (7), 4471–4568. https://doi.org/10.1021/acs.chemrev.8b00408.

(16) Air Pollutant Emissions Trends Data | Air Emissions Inventories | US EPA https://www.epa.gov/air-emissions-inventories/air-pollutant-emissions-trends-data (accessed Apr 3, 2021).

(17) Toro, M. V.; Cremades, L. v; Calbó, J. Relationship between VOC and NOx Emissions and Chemical Production of Tropospheric Ozone in the Aburrá Valley (Colombia). *Chemosphere* **2006**, *65* (5), 881–888. https://doi.org/https://doi.org/10.1016/j.chemosphere.2006.03.013.

(18) Guerra, F. D.; Campbell, M. L.; Attia, M. F.; Whitehead, Daniel. C.; Alexis, F. Capture of Aldehyde VOCs Using a Series of Amine-Functionalized Cellulose Nanocrystals.

ChemistrySelect **2018**, *3* (20), 5495–5501. https://doi.org/https://doi.org/10.1002/slct.201703149.

(19) Nomura, A.; Jones, C. W. Enhanced Formaldehyde-Vapor Adsorption Capacity of Polymeric Amine-Incorporated Aminosilicas. *Chemistry – A European Journal* **2014**, *20* (21), 6381–6390. https://doi.org/https://doi.org/10.1002/chem.201304954.

(20) Checkoway, H.; Dell, L. D.; Boffetta, P.; Gallagher, A. E.; Crawford, L.; Lees, P. S.; Mundt, K. A. Formaldehyde Exposure and Mortality Risks From Acute Myeloid Leukemia and Other Lymphohematopoietic Malignancies in the US National Cancer Institute Cohort Study of Workers in Formaldehyde Industries. *Journal of occupational and environmental medicine* **2015**, *57* (7), 785–794. https://doi.org/10.1097/JOM.0000000000000466.

(21) Jordan, W. P.; Sherman, W. T.; King, S. E. Threshold Responses in Formaldehyde-Sensitive Subjects. *Journal of the American Academy of Dermatology* **1979**, *1* (1), 44–48. https://doi.org/https://doi.org/10.1016/S0190-9622(79)70003-X.

(22) Kamal, M. S.; Razzak, S. A.; Hossain, M. M. Catalytic Oxidation of Volatile Organic Compounds (VOCs) – A Review. *Atmospheric Environment* **2016**, *140*, 117–134. https://doi.org/https://doi.org/10.1016/j.atmosenv.2016.05.031.

(23) Aranzabal, A.; Pereda-Ayo, B.; González-Marcos, M. P.; González-Marcos, J. A.; López-Fonseca, R.; González-Velasco, J. R. State of the Art in Catalytic Oxidation of Chlorinated Volatile Organic Compounds. *Chemical Papers* **2014**, *68* (9), 1169–1186. https://doi.org/10.2478/s11696-013-0505-7.

(24) Huang, B.; Lei, C.; Wei, C.; Zeng, G. Chlorinated Volatile Organic Compounds (Cl-VOCs) in Environment — Sources, Potential Human Health Impacts, and Current Remediation Technologies. *Environment International* **2014**, *71*, 118–138. https://doi.org/https://doi.org/10.1016/j.envint.2014.06.013.

(25) Rajabi, H.; Hadi Mosleh, M.; Mandal, P.; Lea-Langton, A.; Sedighi, M. Emissions of Volatile Organic Compounds from Crude Oil Processing – Global Emission Inventory and Environmental Release. *Science of The Total Environment* **2020**, *727*, 138654. https://doi.org/https://doi.org/10.1016/j.scitotenv.2020.138654.

(26) Li, S.; Wang, H.; Li, W.; Wu, X.; Tang, W.; Chen, Y. Effect of Cu Substitution on Promoted Benzene Oxidation over Porous CuCo-Based Catalysts Derived from Layered

Double Hydroxide with Resistance of Water Vapor. *Applied Catalysis B: Environmental* **2015**, *166–167*, 260–269. https://doi.org/https://doi.org/10.1016/j.apcatb.2014.11.040.

(27) Lamprea Pineda, P. A.; Demeestere, K.; Toledo, M.; van Langenhove, H.; Walgraeve, C. Enhanced Removal of Hydrophobic Volatile Organic Compounds in Biofilters and Biotrickling Filters: A Review on the Use of Surfactants and the Addition of Hydrophilic Compounds. *Chemosphere* **2021**, *279*, 130757. https://doi.org/https://doi.org/10.1016/j.chemosphere.2021.130757.

(28) Patdhanagul, N.; Rangsriwatananon, K.; Siriwong, K.; Hengrasmee, S. Combined Modification of Zeolite NaY by Phenyl Trimethyl Ammonium Bromide and Potassium for Ethylene Gas Adsorption. *Microporous and Mesoporous Materials* **2012**, *153*, 30–34. https://doi.org/https://doi.org/10.1016/j.micromeso.2011.12.007.

(29) Trinh, Q. H.; Lee, S. B.; Mok, Y. S. Removal of Ethylene from Air Stream by Adsorption and Plasma-Catalytic Oxidation Using Silver-Based Bimetallic Catalysts Supported on Zeolite. *Journal of Hazardous Materials* **2015**, *285*, 525–534. https://doi.org/https://doi.org/10.1016/j.jhazmat.2014.12.019.

(30) Kujawa, J.; Cerneaux, S.; Kujawski, W. Removal of Hazardous Volatile Organic Compounds from Water by Vacuum Pervaporation with Hydrophobic Ceramic Membranes. *Journal of Membrane Science* **2015**, *474*, 11–19. https://doi.org/https://doi.org/10.1016/j.memsci.2014.08.054.

(31) Zadaka-Amir, D.; Nasser, A.; Nir, S.; Mishael, Y. G. Removal of Methyl Tertiary-Butyl Ether (MTBE) from Water by Polymer–Zeolite Composites. *Microporous and Mesoporous Materials* **2012**, *151*, 216–222. https://doi.org/https://doi.org/10.1016/j.micromeso.2011.10.033.

(32) Son, Y.-S. Decomposition of VOCs and Odorous Compounds by Radiolysis: A Critical Review. *Chemical Engineering Journal* **2017**, *316*, 609–622. https://doi.org/https://doi.org/10.1016/j.cej.2017.01.063.

(33) Dumont, E.; Darracq, G.; Couvert, A.; Couriol, C.; Amrane, A.; Thomas, D.; Andrès, Y.; le Cloirec, P. VOC Absorption in a Countercurrent Packed-Bed Column Using Water/Silicone Oil Mixtures: Influence of Silicone Oil Volume Fraction. *Chemical Engineering Journal* **2011**, *168* (1), 241–248. https://doi.org/https://doi.org/10.1016/j.cej.2010.12.073.

(34) Dwivedi, P.; Gaur, V.; Sharma, A.; Verma, N. Comparative Study of Removal of Volatile Organic Compounds by Cryogenic Condensation and Adsorption by Activated Carbon Fiber. *Separation and Purification Technology* **2004**, *39* (1), 23–37. https://doi.org/https://doi.org/10.1016/j.seppur.2003.12.016.

(35) Teimoori, S.; Hassani, A. H.; Panahi, M.; Mansouri, N. A Review: Methods for Removal and Adsorption of Volatile Organic Compounds from Environmental Matrixes. *Analytical Methods in Environmental Chemistry Journal* **2020**, *3* (02 SE-Review Article). https://doi.org/10.24200/amecj.v3.i02.100.

(36) Dorado, A. D.; Baeza, J. A.; Lafuente, J.; Gabriel, D.; Gamisans, X. Biomass Accumulation in a Biofilter Treating Toluene at High Loads – Part 1: Experimental Performance from Inoculation to Clogging. *Chemical Engineering Journal* **2012**, *209*, 661–669. https://doi.org/https://doi.org/10.1016/j.cej.2012.08.018.

(37) Han, M.-F.; Hu, X.-R.; Wang, Y.-C.; Tong, Z.; Wang, C.; Cheng, Z.-W.; Feng, K.; Qu, M.-M.; Chen, J.-M.; Deng, J.-G.; Hsi, H.-C. Comparison of Separated and Combined Photodegradation and Biofiltration Technology for the Treatment of Volatile Organic Compounds: A Critical Review. *Critical Reviews in Environmental Science and Technology* **2020**, 1–31. https://doi.org/10.1080/10643389.2020.1854566.

(38) Wu, H.; Guo, C.; Yin, Z.; Quan, Y.; Yin, C. Performance and Bacterial Diversity of Biotrickling Filters Filled with Conductive Packing Material for the Treatment of Toluene. *Bioresource Technology* **2018**, *257*, 201–209. https://doi.org/https://doi.org/10.1016/j.biortech.2018.02.108.

(39) Mohamad Nor, N.; Lau, L. C.; Lee, K. T.; Mohamed, A. R. Synthesis of Activated Carbon from Lignocellulosic Biomass and Its Applications in Air Pollution Control—a Review. *Journal of Environmental Chemical Engineering* **2013**, *1* (4), 658–666. https://doi.org/https://doi.org/10.1016/j.jece.2013.09.017.

(40) Bhargavi, R.; Kadirvelu, K.; Kumar, N. S. Vapor Phase Adsorption of Homologous Aliphatic Ketones on Activated Spherical Carbon. *International Journal of Environmental Sciences* **2011**, *1* (5), 938.

(41) Zhang, Z.; Jiang, Z.; Shangguan, W. Low-Temperature Catalysis for VOCs Removal in Technology and Application: A State-of-the-Art Review. *Catalysis Today* **2016**, *264*, 270–278. https://doi.org/https://doi.org/10.1016/j.cattod.2015.10.040.

(42) Lewandowski, D. A. *Design of Thermal Oxidation Systems for Volatile Organic Compounds*; CRC Press, 2017.

(43) Gong, H.; Zhou, S.; Chen, Z.; Chen, L. Effect of Volatile Organic Compounds on Carbon Dioxide Adsorption Performance via Pressure Swing Adsorption for Landfill Gas Upgrading. *Renewable Energy* **2019**, *135*, 811–818. https://doi.org/https://doi.org/10.1016/j.renene.2018.12.068.

(44) Niknaddaf, S.; Atkinson, J. D.; Shariaty, P.; Jahandar Lashaki, M.; Hashisho, Z.; Phillips, J. H.; Anderson, J. E.; Nichols, M. Heel Formation during Volatile Organic Compound Desorption from Activated Carbon Fiber Cloth. *Carbon* **2016**, *96*, 131–138. https://doi.org/https://doi.org/10.1016/j.carbon.2015.09.049.

(45) Ohtani, H.; Ellwood, K. R. J.; Venkat, M.; Bhat, A.; Schwank, J. Recovery of Adsorption Capacity of Beaded Activated Carbon Using Gas-Phase Organic Solvents. *U.S. Patent Application No.* 16/569,914., 2020.

(46) Aktaş, Ö.; Çeçen, F. Bioregeneration of Activated Carbon: A Review. *International Biodeterioration & Biodegradation* **2007**, *59* (4), 257–272. https://doi.org/https://doi.org/10.1016/j.ibiod.2007.01.003.

(47) Khan, F. I.; Kr. Ghoshal, A. Removal of Volatile Organic Compounds from Polluted Air. *Journal of Loss Prevention in the Process Industries* **2000**, *13* (6), 527–545. https://doi.org/https://doi.org/10.1016/S0950-4230(00)00007-3.

(48) Yang, R. T. *Adsorbents: Fundamentals and Applications*; John Wiley & Sons, 2003.

(49) Marsh, H.; Reinoso, F. R. *Activated Carbon*; Elsevier, 2006.

(50) Langmuir, I. The Adsorption of Gases on Plane Surfaces of Glass, Mica and Platinum. *Journal of the American Chemical society* **1918**, *40* (9), 1361–1403.

(51) Liu, W.; Vidić, R. D.; Brown, T. D. Optimization of Sulfur Impregnation Protocol for Fixed-Bed Application of Activated Carbon-Based Sorbents for Gas-Phase Mercury Removal. *Environmental Science & Technology* **1998**, *32* (4), 531–538. https://doi.org/10.1021/es970630+.

(52) Dutta, T.; Kim, T.; Vellingiri, K.; Tsang, D. C. W.; Shon, J. R.; Kim, K.-H.; Kumar, S. Recycling and Regeneration of Carbonaceous and Porous Materials through Thermal or Solvent Treatment. *Chemical Engineering Journal* **2019**, *364*, 514–529. https://doi.org/https://doi.org/10.1016/j.cej.2019.01.049.

(53) Shah, I. K.; Pre, P.; Alappat, B. J. Effect of Thermal Regeneration of Spent Activated Carbon on Volatile Organic Compound Adsorption Performances. *Journal of the Taiwan Institute of Chemical Engineers* **2014**, *45* (4), 1733–1738. https://doi.org/https://doi.org/10.1016/j.jtice.2014.01.006.

(54) de Jonge, R. J.; Breure, A. M.; van Andel, J. G. Reversibility of Adsorption of Aromatic Compounds onto Powdered Activated Carbon (PAC). *Water Research* **1996**, *30* (4), 883–892. https://doi.org/https://doi.org/10.1016/0043-1354(95)00248-0.

(55) Soto, M. L.; Moure, A.; Domínguez, H.; Parajó, J. C. Recovery, Concentration and Purification of Phenolic Compounds by Adsorption: A Review. *Journal of Food Engineering* **2011**, *105* (1), 1–27. https://doi.org/https://doi.org/10.1016/j.jfoodeng.2011.02.010.

(56) Li, J.; Li, Q.; Steinberg, C. E. W.; Zhao, Q.; Pan, B.; Pignatello, J. J.; Xing, B. Reaction of Substituted Phenols with Lignin Char: Dual Oxidative and Reductive Pathways Depending on Substituents and Conditions. *Environmental Science & Technology* **2020**, *54* (24), 15811–15820. https://doi.org/10.1021/acs.est.0c04991.

(57) Mu'azu, N. D.; Jarrah, N.; Zubair, M.; Alagha, O. Removal of Phenolic Compounds from Water Using Sewage Sludge-Based Activated Carbon Adsorption: A Review. *International Journal of Environmental Research and Public Health* . 2017. https://doi.org/10.3390/ijerph14101094.

(58) Vidic, R. D.; Tessmer, C. H.; Uranowski, L. J. Impact of Surface Properties of Activated Carbons on Oxidative Coupling of Phenolic Compounds. *Carbon* **1997**, *35* (9), 1349–1359. https://doi.org/https://doi.org/10.1016/S0008-6223(97)00071-7.

(59) Vidic, R. D.; Suidan, M. T.; Brenner, R. C. Oxidative Coupling of Phenols on Activated Carbon: Impact on Adsorption Equilibrium. *Environmental science & technology* **1993**, *27* (10), 2079–2085.

(60) Tessmer, C. H.; Vidic, R. D.; Uranowski, L. J. Impact of Oxygen-Containing Surface Functional Groups on Activated Carbon Adsorption of Phenols. *Environmental Science & Technology* **1997**, *31* (7), 1872–1878. https://doi.org/10.1021/es960474r.

(61) Humayun, R.; Karakas, G.; Dahlstrom, P. R.; Ozkan, U. S.; Tomasko, D. L. Supercritical Fluid Extraction and Temperature-Programmed Desorption of Phenol and Its Oxidative

Coupling Products from Activated Carbon. *Industrial & Engineering Chemistry Research* **1998**, *37* (8), 3089–3097. https://doi.org/10.1021/ie970936p.

(62) Suzuki, M.; Misic, D. M.; Koyama, O.; Kawazoe, K. Study of Thermal Regeneration of Spent Activated Carbons: Thermogravimetric Measurement of Various Single Component Organics Loaded on Activated Carbons. *Chemical Engineering Science* **1978**, *33* (3), 271–279. https://doi.org/https://doi.org/10.1016/0009-2509(78)80085-2.

(63) Salvador, F.; Jiménez, C. S. A New Method for Regenerating Activated Carbon by Thermal Desorption with Liquid Water under Subcritical Conditions. *Carbon* **1996**, *34* (4), 511–516. https://doi.org/https://doi.org/10.1016/0008-6223(95)00211-1.

(64) Li, X.; Zhang, L.; Yang, Z.; Wang, P.; Yan, Y.; Ran, J. Adsorption Materials for Volatile Organic Compounds (VOCs) and the Key Factors for VOCs Adsorption Process: A Review. *Separation and Purification Technology* **2020**, *235*, 116213. https://doi.org/https://doi.org/10.1016/j.seppur.2019.116213.

(65) Álvarez, P. M.; Beltrán, F. J.; Gómez-Serrano, V.; Jaramillo, J.; Rodríguez, E. M. Comparison between Thermal and Ozone Regenerations of Spent Activated Carbon Exhausted with Phenol. *Water Research* **2004**, *38* (8), 2155–2165. https://doi.org/https://doi.org/10.1016/j.watres.2004.01.030.

(66) Zou, W.; Gao, B.; Ok, Y. S.; Dong, L. Integrated Adsorption and Photocatalytic Degradation of Volatile Organic Compounds (VOCs) Using Carbon-Based Nanocomposites: A Critical Review. *Chemosphere* **2019**, *218*, 845–859. https://doi.org/https://doi.org/10.1016/j.chemosphere.2018.11.175.

(67) Yang, X.; Wan, Y.; Zheng, Y.; He, F.; Yu, Z.; Huang, J.; Wang, H.; Ok, Y. S.; Jiang, Y.; Gao, B. Surface Functional Groups of Carbon-Based Adsorbents and Their Roles in the Removal of Heavy Metals from Aqueous Solutions: A Critical Review. *Chemical Engineering Journal* **2019**, *366*, 608–621. https://doi.org/https://doi.org/10.1016/j.cej.2019.02.119.

(68) Nakhla, G.; Abuzaid, N.; Farooq, S. Activated Carbon Adsorption of Phenolics in Oxic Systems: Effect of PH and Temperature Variations. *Water Environment Research* **1994**, *66* (6), 842–850. https://doi.org/https://doi.org/10.2175/WER.66.6.12.

(69) Lashaki, M. J.; Fayaz, M.; Wang, H. (Helena); Hashisho, Z.; Philips, J. H.; Anderson, J. E.; Nichols, M. Effect of Adsorption and Regeneration Temperature on Irreversible

Adsorption of Organic Vapors on Beaded Activated Carbon. *Environmental Science & Technology* **2012**, *46* (7), 4083–4090. https://doi.org/10.1021/es3000195.

(70) Dąbrowski, A.; Podkościelny, P.; Hubicki, Z.; Barczak, M. Adsorption of Phenolic Compounds by Activated Carbon—a Critical Review. *Chemosphere* **2005**, *58* (8), 1049–1070. https://doi.org/https://doi.org/10.1016/j.chemosphere.2004.09.067.

(71) Wang, H.; Jahandar Lashaki, M.; Fayaz, M.; Hashisho, Z.; Philips, J. H.; Anderson, J. E.; Nichols, M. Adsorption and Desorption of Mixtures of Organic Vapors on Beaded Activated Carbon. *Environmental Science & Technology* **2012**, *46* (15), 8341–8350. https://doi.org/10.1021/es3013062.

(72) Jahandar Lashaki, M.; Atkinson, J. D.; Hashisho, Z.; Phillips, J. H.; Anderson, J. E.; Nichols, M.; Misovski, T. Effect of Desorption Purge Gas Oxygen Impurity on Irreversible Adsorption of Organic Vapors. *Carbon* **2016**, *99*, 310–317. https://doi.org/https://doi.org/10.1016/j.carbon.2015.12.037.

(73) Fayaz, M.; Shariaty, P.; Atkinson, J. D.; Hashisho, Z.; Phillips, J. H.; Anderson, J. E.; Nichols, M. Using Microwave Heating To Improve the Desorption Efficiency of High Molecular Weight VOC from Beaded Activated Carbon. *Environmental Science & Technology* **2015**, *49* (7), 4536–4542. https://doi.org/10.1021/es505953c.

(74) Scida, K.; Stege, P. W.; Haby, G.; Messina, G. A.; García, C. D. Recent Applications of Carbon-Based Nanomaterials in Analytical Chemistry: Critical Review. *Analytica Chimica Acta* **2011**, *691* (1), 6–17. https://doi.org/https://doi.org/10.1016/j.aca.2011.02.025.

(75) Yan, L.; Sorial, G. A. Chemical Activation of Bituminous Coal for Hampering Oligomerization of Organic Contaminants. *Journal of Hazardous Materials* **2011**, *197*, 311–319. https://doi.org/https://doi.org/10.1016/j.jhazmat.2011.09.093.

(76) Wang, Q.; Liang, X.; ZhanG, R.; Liu, C.; Liu, X.; Qiao, W.; Zhan, L.; Ling, L. Preparation of Polystyrene-Based Activated Carbon Spheres and Their Adsorption of Dibenzothiophene. *New Carbon Materials* **2009**, *24* (1), 55–60. https://doi.org/https://doi.org/10.1016/S1872-5805(08)60036-0.

(77) Tamon, H.; Saito, T.; Kishimura, M.; Okazaki, M.; Toei, R. Solvent Regeneration of Spent Activated Carbon in Wastewater Treatment. *Journal of chemical engineering of Japan* **1990**, *23* (4), 426–432.

(78) Grant, T. M.; King, C. J. Mechanism of Irreversible Adsorption of Phenolic Compounds by Activated Carbons. *Industrial & engineering chemistry research* **1990**, *29* (2), 264–271.

(79) Kong, W.; Lv, B.; Yang, S.; Shen, H.; Jing, G.; Zhou, Z. Case Study on Environmental Safety and Sustainability of Pharmaceutical Production Based on Life Cycle Assessment of Enrofloxacin. *Journal of Environmental Chemical Engineering* **2021**, *9* (4), 105734. https://doi.org/https://doi.org/10.1016/j.jece.2021.105734.

(80) Kim, B. R. VOC Emissions from Automotive Painting and Their Control: A Review. *Environmental Engineering Research* **2011**, *16* (1), 1–9. https://doi.org/10.4491/eer.2011.16.1.001.

(81) Tomatis, M.; Moreira, M. T.; Xu, H.; Deng, W.; He, J.; Parvez, A. M. Removal of VOCs from Waste Gases Using Various Thermal Oxidizers: A Comparative Study Based on Life Cycle Assessment and Cost Analysis in China. *Journal of Cleaner Production* **2019**, *233*, 808–818. https://doi.org/https://doi.org/10.1016/j.jclepro.2019.06.131.

(82) Chou, M.-S.; Hei, C.-M.; Huang, Y.-W. Regenerative Thermal Oxidation of Airborne N, N-Dimethylformamide and Its Associated Nitrogen Oxides Formation Characteristics. *Journal of the Air & Waste Management Association* **2007**, *57* (8), 991–999. https://doi.org/10.3155/1047-3289.57.8.991.

(83) Thomas, J. M.; Thomas, W. J. *Principles and Practice of Heterogeneous Catalysis*; John Wiley & Sons, 2014.

(84) Somorjai, G. A.; McCrea, K. R.; Zhu, J. Active Sites in Heterogeneous Catalysis: Development of Molecular Concepts and Future Challenges. *Topics in Catalysis* **2002**, *18* (3), 157–166. https://doi.org/10.1023/A:1013874202404.

(85) Gao, C.; Lyu, F.; Yin, Y. Encapsulated Metal Nanoparticles for Catalysis. *Chemical Reviews* **2020**. https://doi.org/10.1021/acs.chemrev.0c00237.

(86) Du, R.; Jin, X.; Hübner, R.; Fan, X.; Hu, Y.; Eychmüller, A. Engineering Self-Supported Noble Metal Foams Toward Electrocatalysis and Beyond. *Advanced Energy Materials* **2020**, *10* (11), 1901945. https://doi.org/https://doi.org/10.1002/aenm.201901945.

(87) Lu, J.; Fu, B.; Kung, M. C.; Xiao, G.; Elam, J. W.; Kung, H. H.; Stair, P. C. Coking- and Sintering-Resistant Palladium Catalysts Achieved Through Atomic Layer Deposition. *Science* **2012**, *335* (6073), 1205 – 1208. https://doi.org/10.1126/science.1212906.

(88) Jones, J.; Xiong, H.; DeLaRiva, A. T.; Peterson, E. J.; Pham, H.; Challa, S. R.; Qi, G.; Oh, S.; Wiebenga, M. H.; Pereira Hernández, X. I.; Wang, Y.; Datye, A. K. Thermally Stable Single-Atom Platinum-on-Ceria Catalysts via Atom Trapping. *Science* **2016**, *353* (6295), 150 – 154. https://doi.org/10.1126/science.aaf8800.

(89) Tang, H.; Wei, J.; Liu, F.; Qiao, B.; Pan, X.; Li, L.; Liu, J.; Wang, J.; Zhang, T. Strong Metal–Support Interactions between Gold Nanoparticles and Nonoxides. *Journal of the American Chemical Society* **2016**, *138* (1), 56–59. https://doi.org/10.1021/jacs.5b11306.

(90) Otto, T.; Zones, S. I.; Iglesia, E. Challenges and Strategies in the Encapsulation and Stabilization of Monodisperse Au Clusters within Zeolites. *Journal of Catalysis* **2016**, *339*, 195–208. https://doi.org/https://doi.org/10.1016/j.jcat.2016.04.015.

(91) Prieto, G.; Zečević, J.; Friedrich, H.; de Jong, K. P.; de Jongh, P. E. Towards Stable Catalysts by Controlling Collective Properties of Supported Metal Nanoparticles. *Nature Materials* **2013**, *12* (1), 34–39. https://doi.org/10.1038/nmat3471.

(92) Zhang, J.; Wang, L.; Zhang, B.; Zhao, H.; Kolb, U.; Zhu, Y.; Liu, L.; Han, Y.; Wang, G.; Wang, C.; Su, D. S.; Gates, B. C.; Xiao, F.-S. Sinter-Resistant Metal Nanoparticle Catalysts Achieved by Immobilization within Zeolite Crystals via Seed-Directed Growth. *Nature Catalysis* **2018**, *1* (7), 540–546. https://doi.org/10.1038/s41929-018-0098-1.

(93) Ham, H.; Kim, J.; Cho, S. J.; Choi, J.-H.; Moon, D. J.; Bae, J. W. Enhanced Stability of Spatially Confined Copper Nanoparticles in an Ordered Mesoporous Alumina for Dimethyl Ether Synthesis from Syngas. *ACS Catalysis* **2016**, *6* (9), 5629–5640. https://doi.org/10.1021/acscatal.6b00882.

(94) Su, J.; Xie, C.; Chen, C.; Yu, Y.; Kennedy, G.; Somorjai, G. A.; Yang, P. Insights into the Mechanism of Tandem Alkene Hydroformylation over a Nanostructured Catalyst with Multiple Interfaces. *Journal of the American Chemical Society* **2016**, *138* (36), 11568–11574. https://doi.org/10.1021/jacs.6b03915.

Chapter 2

Chemical Surface Modification of Beaded Activated Carbon: A Strategy to Inhibit Heel Accumulation from VOCs *

2.1. Introduction

Surface coating and painting operations in automotive industries are among the largest sources of global VOC emitters. These emissions consist of several low and high molecular weight hydrocarbons with hetero-atoms like oxygen, sulfur, nitrogen, and halogens. On average, 6.58 kg of VOCs is used as paint solvents per vehicle in typical automotive plants in North America [1]. As discussed in chapter 1, most VOC emissions are of concern due to their detrimental health effects, aerosols, ozone, and photochemical smog formation in the troposphere [2]. Hence, the gaseous emission from automotive industries needs to be treated before discharging into the atmosphere.

As previously mentioned, methods to control the emission of VOCs include adsorption, absorption, oxidation, biofiltration, condensation, and membrane separation. Among these, adsorption is often used to control the emission of volatile organic compounds from a wide range of industrial gas streams. This is due to several advantages such as low operational cost, high efficiency at low effluent concentrations, and ability to recover the adsorbate for reuse [3–5].

---

* A version of this chapter has been published in the Journal of Industrial and Engineering Chemistry.
https://doi.org/10.1016/j.jiec.2021.07.035

In most large-scale adsorption processes, activated carbon is one of the most frequently used adsorbents due to its cost-effectiveness and large surface area. Structurally, activated carbon is an assembly of defective sheets of graphene having high porosity. Activated carbon is also available in many physical forms, including fibers, powders, beads, monoliths, and granules, implying that it can be used in nearly any shape or size reactor. It is resistant to acidic and basic conditions, can have tailored physical and chemical properties, can be regenerable, is thermally stable in anoxic conditions, and is inexpensive.

A schematic representation of VOC abatement operation in automotive painting process is shown in Figure 2.1. Generally, a porous adsorbent with a high surface area, such as beaded activated carbon (BAC), adsorbs low concentrations of VOCs from the inlet exhaust in a fluidized adsorption column. As a result, treated gas is released into the atmosphere. As the adsorbent gets saturated by VOC and loses its adsorption capacity, it is regenerated by desorbing the adsorbed VOCs at elevated temperatures (300 - 500 °C) in a desorption column. The adsorption-desorption process is carried out cyclically to reuse the adsorbent in the process. By employing continuous adsorption and desorption, higher concentration VOCs flow is obtained, making the post-treatment more energy efficient. Subsequently, the concentrated stream of VOC exiting the desorption column is condensed and sent to an incinerator, where the VOCs are combusted at 900 - 1200 °C.

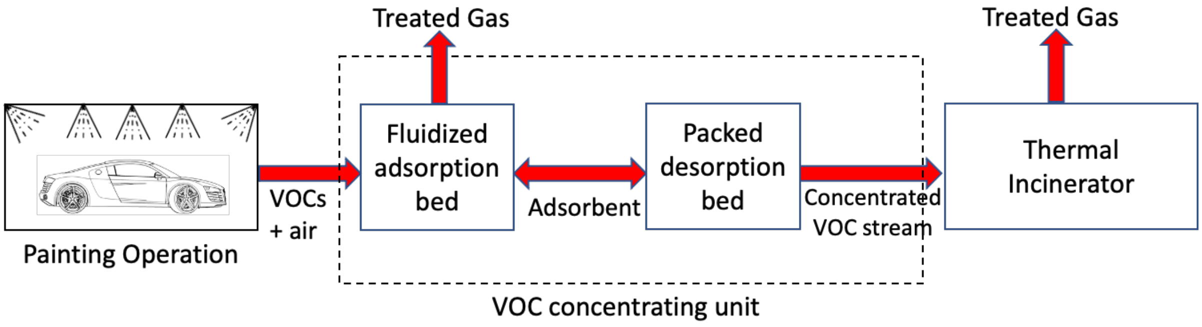

Figure 2.1 *- Schematic representation of a typical VOC abatement setup in automotive painting industry.*

The adsorption-desorption process of VOCs is not entirely reversible [6]. During each desorption operation, trace amounts of VOCs are retained in the pores of the adsorbent as heel (non-desorbable polymeric complex) [7,8]. Over prolonged operation, heel accumulation becomes so severe that the adsorbent loses its ability to adsorb VOCs. This results in periodic replacement of spent BAC and substantial material wastage [9,10].

Several researchers have evaluated the factors that contribute to heel accumulation. Lashaki *et al.* found that heel accumulation depends strongly on the pore structure of the adsorbent. They reported that activated carbon with higher micropore volume suffered from higher heel accumulation [11]. A study done by Kamravaei *et al.* found that uniformity of adsorbate distribution and competitive adsorption in a multicomponent system influences heel accumulation [12]. They also reported that an increase in the desorption heating rate results in elevated heel accumulation [13]. While several studies have reported such irreversible adsorption of organic compounds on activated carbon, work done to address these challenges is minimal. Furthermore, identifying and addressing the factors responsible for the heel accumulation phenomenon can greatly benefit industrially implemented cyclic adsorption systems and minimize performance losses.

Techniques such as laser heating, microwave-assisted desorption, electron-stimulated desorption have been investigated to increase the desorption efficiency and avoid heel accumulation [14]. However, these techniques require substantial modification of the existing infrastructure or relatively high energy requirements in industries [15]. An alternative to this is to introduce surface functional groups on the activated carbon. The presence of surface functionality on an adsorbent can alter the strength of adsorption, which in turn, facilitates easier and complete desorption [16]. For instance, oxygen functional groups on the activated carbon surface are known to decrease the occurrence of irreversible adsorption of organics due to oxidative coupling [17–19]. However, such modifications also reduce the adsorption capacity of activated carbon [20,21]. Introducing nitrogen functionality on activated carbon's surface can increase the adsorption capacity of organic compounds and CO_2 due to enhanced dipole-dipole interactions [22,23]. This was demonstrated by Li *et al.* who modified the surface of activated carbon by introducing nitrogen functional groups and observed that this promotes the affinity between acetone molecules and the activated carbon [24]. Although several studies have evaluated the effect of surface functionalization of activated carbon on VOC adsorption, effect of surface modification on irreversible VOC adsorption and heel accumulation are not very well understood. Besides, to the best of our knowledge, no previous work has been done to inhibit or avoid heel accumulation via surface modification of activated carbon while maintaining high adsorption capacity.

This chapter sheds light on the factors that play a significant role in forming the heel by understanding and evaluating the desorption mechanism of VOCs from the surface of the beaded activated carbon (BAC). Furthermore, a simple and scalable method to modify the surface of BAC using acidic and alkaline solutions is presented in this chapter with the goal of enhancing adsorption capacity and desorption characteristics. As n-butanol, butyl acetate, and 1,2,4-trimethylbenzene are among the most common VOC molecules emitted from automotive painting, experiments using these VOC molecules are discussed to understand the role of surface modification on adsorption-desorption characteristics. In sum, this chapter elucidates how surface modification can be successfully utilized to impede heel accumulation during periodic adsorption-desorption operation using a set of material characterization and analytical techniques. Finally, by conducting cyclic adsorption-desorption studies in a pilot plant, the efficacy of surface modification in reducing heel accumulation in an industrial setup is evaluated.

2.2. Experimental

2.2.1. Materials

The adsorbent, beaded activated carbon (BAC), used in this study was obtained from Kureha Corporation. For synthesizing BAC, a mixture of pitch obtained from thermal cracking of naphtha and coconut shell-charcoal was fluidified by heating at a temperature of 210 °C. This fluidified mixture was extruded into beads and was further activated in an atmosphere of water vapor and nitrogen at 800 °C or higher for 3 hours [25]. Nitric acid (HNO_3, 70 wt. %), ammonium hydroxide (NH_4OH, 28-30% NH_3 basis), and sodium hydroxide (NaOH) pellets (ACS reagent, ≥ 97%), all of which were used for surface modification, were purchased from Sigma-Aldrich.

2.2.2. Surface modification of BAC

The surface modification was carried out in an acidic or alkaline solution. Prior to the modification, the BAC samples were washed in deionized water and dried at 120 °C for 3 hours. Acidic functionalization was performed by modifying the liquid phase oxidation method that has been previously reported in the literature [26]. 4.0 g of BAC was soaked in 150 mL of 1 M HNO_3 solution while placing on a reciprocating shaker for 24 hours at room temperature. Surface modification by the alkaline solution was done by slightly modifying the method that has been previously reported in the literature [27]. 4.0 g of BAC was refluxed in 150 mL of boiling 1 M NaOH or 1 M NH_4OH for 4 hours. The mixture of alkaline solution and BAC was then ambiently cooled down to room temperature and kept undisturbed for 20 hours. These chemically modified BAC samples were separated from the reaction mixture by filtration. The surface-modified BAC samples were then washed in deionized water until no further change in pH was detected. Next, the washed BAC samples were dried in an oven at 120 °C for 3 hours. Post drying, modified samples were activated by treating at 800 °C in a tube furnace for 3 hours under nitrogen flow (100 mL/min). Finally, the samples were denoted as BAC-N (modified by HNO_3), BAC-S (modified by NaOH), and BAC-A (modified by NH_4OH), while the untreated (Virgin) BAC sample was denoted as BAC-V.

2.2.3. Characterization of BAC samples

An integrated gas sorption apparatus (Micromeritics ASAP 2020) was used to determine the textural properties of the BAC samples. All the samples were degassed for 24 hours under vacuum at 350 °C, and nitrogen adsorption-desorption experiments were carried out at 77 K. The BET equation in the relative pressure (P/P_0) range from 0.06 to 0.32 were used to calculate the surface area from the isotherm data. The micropore volume of the BAC samples was determined from the Dubinin-Astakhov equation [28]. The micropore size distribution was obtained from the Horvath-Kawazoe model using slit pore geometry [29].

In-situ thermochemical decomposition studies were used to evaluate the change in the carbon content in BAC samples due to surface modification. Approximately 20 mg of BAC samples were heated to a temperature of 750 °C, at a ramp rate of 5 °C/min in TA Instrument Q 500 analyzer. The total airflow (100 mL/min) in the TGA system was diluted by adding balance N_2 gas, lowering the actual O_2 concentration to 16 %. Specifically, a heating rate of 5 °C/min was chosen to facilitate slow pyrolysis. The vapors and gases released in the TGA were swept immediately to a transfer line, connected to a Nicolet 380 FTIR spectrometer for qualitative analysis. The transfer line was heated to an internal temperature of 150 °C to avoid condensation of semi-volatile products. The gas-phase IR spectrum was obtained for every 1 °C rise in temperature, and the scanning range was from 4000 to 500 cm^{-1}.

Furthermore, a Philips XL 30 FEG scanning electron microscope (SEM) was used to observe and understand the resultant changes of surface modification pertaining to the morphology and topography of the BAC samples.

2.2.4. Experimental setup and procedure

2.2.4.1. Adsorption of target VOCs onto BAC samples

Adsorption studies in the present work were carried out in a lab-scale setup and an industrial-scale pilot setup.

The lab-scale setup consisted of two separate sections. The first section was for the generation of the carrier gas and VOC mixture. The second section was comprised of saturation analysis. The VOC feed used for adsorption was generated by passing nitrogen carrier gas through a bubbler containing target VOC species at a rate of 150 mL/min. The carrier gas and VOC mixture generated from the bubbler was fed at the top of the adsorption column made of a quartz tube (ID = 1.27 cm) containing 1 g of BAC. The carbon bead's size varied between 700 to 800 μm in diameter, and the overall volume of the adsorption bed was ~ 6.81 cm^3.

The industrial-scale adsorption experiments were carried out at Research and Innovation Center - Ford Motor Company, Dearborn. This study tried to mimic actual (plant) adsorption and conditions with few scaled-down parameters. The experimental setup consisted of 1 g of BAC sample in a fluidized bed. A fuel injector was used to produce the target VOC vapor and nitrogen was used as a carrier gas during adsorption. The inlet concentration of VOC was estimated to be 3000 ppm with a total flow of 3500 mL/min.

The outlet concentration of VOC from the adsorption column was monitored by a downstream Fourier transform infrared analyzer (FTIR) to obtain the breakthrough curve indicating the saturation of adsorbent. The adsorption was continued until the BAC bed was saturated with VOC. After obtaining a breakthrough curve, the quantitative VOC uptake (adsorption capacity) was determined by calculating the difference in the initial and final weight of the adsorption bed according to equation (1), defined below.

$$Adsorption\ Capacity\ (\%) = \left(\frac{W_{BAC,\ after\,adsorption} - W_{BAC,\ initial}}{W_{BAC,\ initial}}\right) \times 100 \qquad (1)$$

2.2.4.2. Thermal desorption of VOCs from saturated BAC

After the BAC samples were saturated, the adsorption column was purged with nitrogen gas (50 mL/min) for 30 min to remove any weakly bonded VOC molecules from the surface of BAC samples. Thereafter, VOCs were desorbed from the BAC by heating the column to 400 °C under the flow of either pure nitrogen or nitrogen containing 100 ppm oxygen at 200 mL/min. The difference in the column weight before the adsorption and after the desorption represents the amount of irreversible adsorption or heel built up during a given cycle and is calculated by equation (2) below.

$$Heel\ accumulated\ (\%) = \left(\frac{W_{BAC,\ after\,desorption} - W_{BAC,\ initial}}{W_{BAC,\ initial}}\right) \times 100 \qquad (2)$$

Adsorption, purging and desorption operations, combined, were considered as one cycle. As such, a total of ten cycles were carried out to investigate the extent of heel accumulated under different desorption streams.

2.2.5. *In-situ* desorption studies in thermogravimetric analyzer

The desorption profile and the peak desorption temperature of individual VOCs from the surface of the BAC samples were obtained by thermogravimetric analysis. In a typical experiment, roughly 10 - 15 mg of BAC samples saturated with different VOC vapors (obtained from the adsorption bed) were placed in a TGA (TA Instrument Q 500). The sample was heated to 400 °C at a rate of 5 °C /min under a flow of pure nitrogen gas (100 mL/min). The peak desorption temperature was obtained from the TA Universal software coupled with the TGA.

2.2.6. Diffusive reflectance infrared Fourier transform spectroscopy of heel accumulated BAC samples

DRIFTS analysis of powdered BAC samples was conducted after completing ten cycles of adsorption-desorption operation (carried out at Research and Innovation Center - Ford Motor Company, Dearborn), to understand the effect of surface modification on heel accumulation. Roughly, 50 mg of BAC samples (BAC-V, BAC-A, BAC-N, BAC-S) were finely ground and transferred to into a Harrick Praying Mantis diffuse reflection infrared cell. DRIFTS analysis was performed on a Bruker Tensor 27 FTIR using an OPUS data collection program. Finely ground BAC samples that had not been subjected to any VOC adsorption were used as a background, and FTIR spectra were recorded. The resolution and the number of scans were set to 2.5 cm^{-1} and 256 respectively. The IR scanning range was from 4000 to 600 cm^{-1}.

2.3. Results and discussion

2.3.1. Factors influencing desorption characteristics of VOCs and heel accumulation

Temperature-programmed desorption profiles of individual VOCs from thermogravimetric analysis of BAC-V are shown in Figure 2.2 (a). The symmetric shape of the desorption curve indicates first-order desorption characteristics, which are independent of initial surface coverage [30]. It can be seen from Figure 2.2 (a) and Table 2.1 that the VOC molecules with a lower boiling point were desorbed at a lower temperature from the surface of the BAC compared to the VOC molecules with a higher boiling point. The experimental results show a direct correlation between the boiling point of the VOC and the peak desorption temperature (Table 2.1).

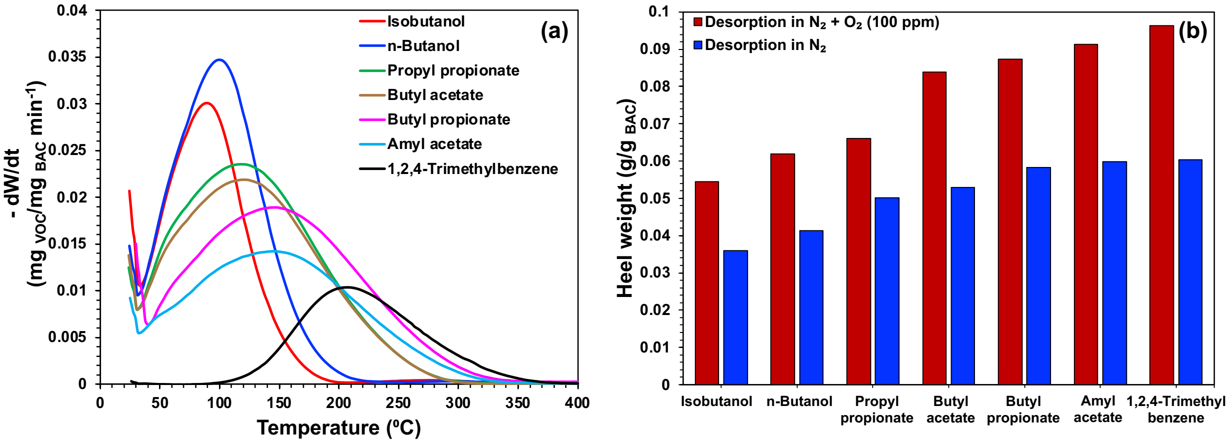

Figure 2.2 *- Temperature programmed desorption profile of individual VOCs from BAC-V (a), and cumulative heel accumulation of individual VOCs after 10 adsorption-desorption cycles (b).*

Two solvents, iso-butanol, and n-butanol, having identical molecular weights and similar structures but different boiling points were chosen for a desorption study to further probe this trend. The boiling point of n-butanol is 20 °C higher than iso-butanol. It can be seen from Table 2.1 that the peak desorption temperature of n-butanol was 14 °C higher than that of iso-butanol. Similar results were observed in the case of 1,2,4-trimethylbenzene and cumene. Despite having similar molecular weight and kinetic diameter, the peak desorption temperature of 1,2,4-trimethylbenzene was 47 °C higher than that of cumene (Table 2.1). Our experimental findings indicate that the boiling point of VOC molecules plays a significant role in determining the ease of desorption from the surface of the adsorbent. Similar results are reported by Lashaki and co-workers [31].

Ideally, a typical thermal desorption process is carried out under an inert gas flow (high purity nitrogen). However, impurities such as O_2, CO_2, and H_2O exist in the desorption gas flow in most practical conditions. We observed that the presence of oxygen in desorption gas contributes to increased heel accumulation. Figure 2.2 (b) shows the heel accumulation profile on BAC-V in two different scenarios (desorption was carried out under pure N_2 and N_2 containing 100 ppm oxygen). In the presence of trace amounts (100 ppm) of oxygen, we observed up to 51% increase in the heel accumulation compared to the desorption carried out under pure nitrogen flow. Researchers have shown that the presence of high oxygen content in desorption gas stream can result in irreversible adsorption of organic vapors, shorter breakthrough time, greater loss of adsorption capacity, and more significant cumulative heel accumulation [32].

Along with contributing to heel accumulation, the presence of oxygen in the desorption purge gas stream also altered the textural properties of BAC. Repetitive exposure of BAC-V to high temperature (400 °C) under the nitrogen flow containing trace amounts of oxygen (100 ppm), in the absence of VOCs, resulted in shrinkage of the overall size of the BAC. Evaluation of textural properties after 50 of these cycles revealed that along with the shrinkage of BAC diameter, the total surface area and median micropore size also decreased by 4.97 % and 6.29%, respectively (Table 2.2). This reduction in surface area and micropore size can be attributed to the gradual thermal decomposition and subsequent collapse of the internal pore structure of the activated carbon under oxidative environment and temperatures above ~ 280 °C [33–35]. Although further study is warranted, it is possible that the gradual thermal decomposition and subsequent collapse of microporous structures in BAC-V would result in a substantial decrease in its overall VOC adsorption capacity.

Table 2.1 *- Boiling point, molecular weight, and corresponding peak desorption temperatures of individual VOC molecules from the surface of BAC-V*

Volatile organic compound	**Boiling point (°C)**	**Molecular weight (g/mol)**	**Peak desorption temperature (°C)**
iso-butanol	108	74.12	92.4
n-butanol	118	74.12	106.1
n-propyl propionate	123	116.16	122.1
n-butyl acetate	126	116.16	124.5
n-butyl propionate	146	130.2	146.4
n-amyl acetate	149	130.19	148.7
cumene	152	120.19	158.3
1,2,4-trimethylbenzene	171	120.19	205.3

Table 2.2 *- Change in textural properties of the BAC-V after multiple high temperature aging cycles*

Number of high temperature cycles	**BET S.A (m^2/g)**	**Median micropore size (nm)**	**Average diameter of the BAC (µm)**
10	1007	0.525	746.3
20	994	0.521	740.7
30	981	0.513	731.9
40	969	0.507	723.4
50	957	0.492	704.4

It is conceivable that the adsorbed VOCs can condense in the microporous structures of BAC-V due to capillary effects. However, at high desorption temperatures, these condensed VOCs can oligomerize in the presence of oxygen. This phenomenon can result in the formation of non-desorbable polymeric complexes such as methyl naphthalene, poly-phenyl species, and benzaldehydes in the microporous structures of BAC-V [31]. Coupled with this, shrinkage of the beads and the resultant decrease in the pore size can trap the polymeric complexes in the micropores, resulting in persistent heel accumulation. Additionally, high desorption temperatures (≥ 350 °C) can result in possible interactions of VOC molecules with dangling C–C bonds present in the basal plane of BAC and form strong bonds between VOC and the BAC, which can be challenging to break during desorption attempts [36]. Over time the combination of these processes results in the loss of adsorption capacity of the BAC, and thus it becomes unusable.

2.3.2. Impact of surface modification on textural properties of BAC

As the presence of oxygen and subsequent thermal decomposition contributes to heel accumulation, we sought to impede the formation of heel by modifying the surface of BAC. The N_2 adsorption isotherms and pore size distributions of untreated and surface modified BAC samples are shown in Figure 2.3.

In all four BAC samples, we observed a type I isotherm, with most nitrogen adsorption occurring at relative pressures lower than 0.1 along with minimal additional adsorption at higher relative pressures. The large adsorption capacity at low relative pressures and a narrow pore size distribution is a characteristic indication of microporous adsorbents [37,38]. The surface area, pore width, and pore volume of BAC samples are listed in Table 2.3. For comparison purposes, one part of the BAC sample was subjected to heat treatment without additional modification. As the activation of beaded activated carbon is carried out in an atmosphere of water vapor and nitrogen at 800 °C or higher for 3 hours, plain heat treatment without acidic or alkaline modification had no overall effect on textural and sorption properties of BAC. Contrary to this, the acidic surface modification followed by heat treatment at 800 °C increased the surface area of BAC-N by nearly 13% compared to BAC-V. Similarly, alkaline modification and subsequent heat treatment at 800 °C resulted in an almost 45% and 36% increase in the surface area of BAC-S and BAC-A, respectively (Table 2.3). The increase in the surface area would consequently increase the monolayer adsorption of N_2. Therefore, we observed a substantial increase in the quantity of N_2 adsorbed on the surface-modified BAC sample compared to BAC-V (Figure 2.3).

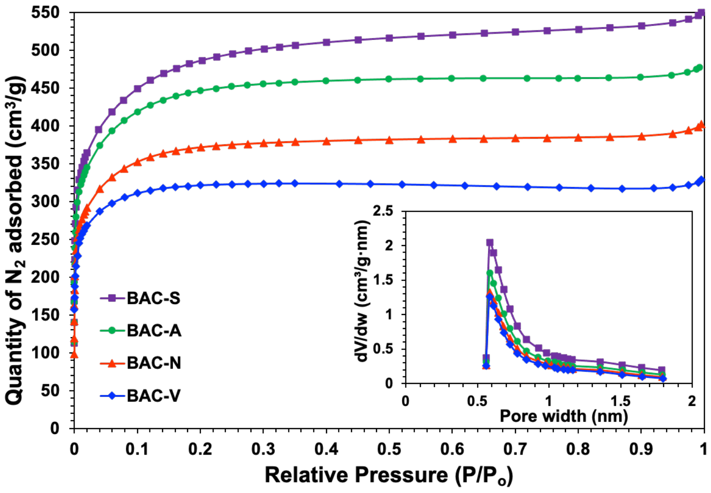

Figure 2.3 *- Nitrogen adsorption isotherm and pore size distribution (in-set) of BAC samples*

Table 2.3 *- Textural properties of the BAC samples*

Sample	**Heat treatment**	**BET S.A. (m^2/g)**	**Total pore volume (cm^3/g)**	**Micropore volume (cm^3/g)**	**Average pore width (nm)**
BAC-V	N/A	1013 ± 34	0.566 ± 0.017	0.525 ± 0.069	2.128
BAC-V	800 °C	1021 ± 11	0.569 ± 0.024	0.527 ± 0.009	2.148
BAC-N	800 °C	1139 ± 26	0.770 ± 0.046	0.614 ± 0.091	2.484
BAC-S	800 °C	1526 ± 31	0.879 ± 0.013	0.686 ± 0.103	2.428
BAC-A	800 °C	1382 ± 28	0.851 ± 0.073	0.758 ± 0.097	2.637

Figure 4 shows the SEM images of untreated and surface-modified BAC samples. There are considerable differences in the surface morphologies of the untreated and surface-modified

BAC samples. The surface of the BAC appeared considerably rougher after surface modification. It is known that activated carbon usually contains a networked pore structure where macropores (≥ 50 nm pore size) and mesopores (pore size between 2 nm and 50 nm) lead to the eventual micropores (< 2 nm) [39]. SEM images show evidence of chemical surface modification and heat treatment resulting in possible enlargement of these pore openings in BAC. The textural analysis presented in Table 2.3 provides conclusive evidence of pore widening as a result of surface modification. It can be seen that the average pore width and median micropore width increased by up to 23.91% and 24.01% after surface modification.

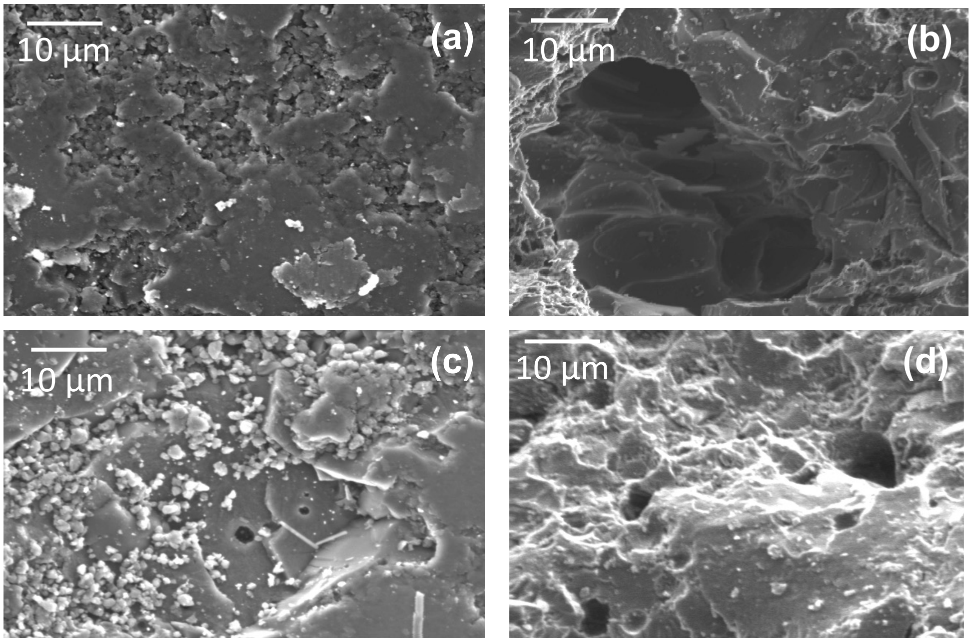

Figure 2.4 *- High magnification SEM micrographs of untreated BAC (a),* HNO_3 *treated BAC (b), NaOH treated BAC (c), and* NH_4OH *treated BAC (d).*

Subjecting the BAC to acidic and alkaline surface modification alters its overall surface chemistry. HNO_3, being a strong oxidizing acid, modifies the surface of BAC by creating carboxylic, phenolic, and carbonyl functional groups [40–42]. In addition, acidification of the surface gives the activated carbon a higher ion exchange capacity and amphoteric character due to the introduction of various functional groups [43]. Furthermore, subjecting the nitric acid-treated BAC at 800 °C under N_2 flow can potentially reactivate the carbon and increase the microporosity and the total surface area [44]. As shown in Figure 4 (b), the surface of the HNO_3 treated BAC appears to be rougher, while the overall shape, size, and structure of the BAC remaining intact. Refluxing BAC in an alkaline solution (NaOH, or NH_4OH) results in the formation of CO_2 and corresponding carbonate crystals (Na_2CO_3 and $(NH_4)_2CO_3$) [45]. While Na_2CO_3 is readily soluble in water, $(NH_4)_2CO_3$ easily decomposes into ammonia and carbon dioxide upon heating. Therefore, repetitive washing and heat treatment of alkaline-modified BAC samples at 800 °C under N_2 flow removes the carbonate crystals from the surface of modified BAC. Similar to acid-treated BAC, subsequent heat treatment of alkaline modified BAC samples at 800 °C under N_2, after repetitive washing, reactivates the sample and increases its microporosity and total surface area [44].

It should be noted that BAC loses a portion of its carbon content due to the carbonate crystal formation. This is evidenced by the in-situ thermochemical decomposition studies (Figure 2.5). We can see that the alkaline treatment resulted in a significantly lower decomposition temperature. BAC-A and BAC-S almost entirely decomposed at around 570 °C, while BAC-V and BAC-N required a higher temperature to burn off (640 °C) due to their higher carbon content. Figure 2.5 (c) is an FTIR spectral snapshot of the gas phase at the peak decomposition temperature, as seen in the differential thermogravimetric curves in Figure 2.5 (b). Besides CO_2 and H_2O, no other signals were observed in FTIR, indicating complete combustion of BAC samples. The decrease in burn-off temperature is caused by a reduction in carbon content and the degree of graphitization. It is plausible that the loss of carbon content during alkaline treatment combined with activation might be the reason for increase in porosity and surface area.

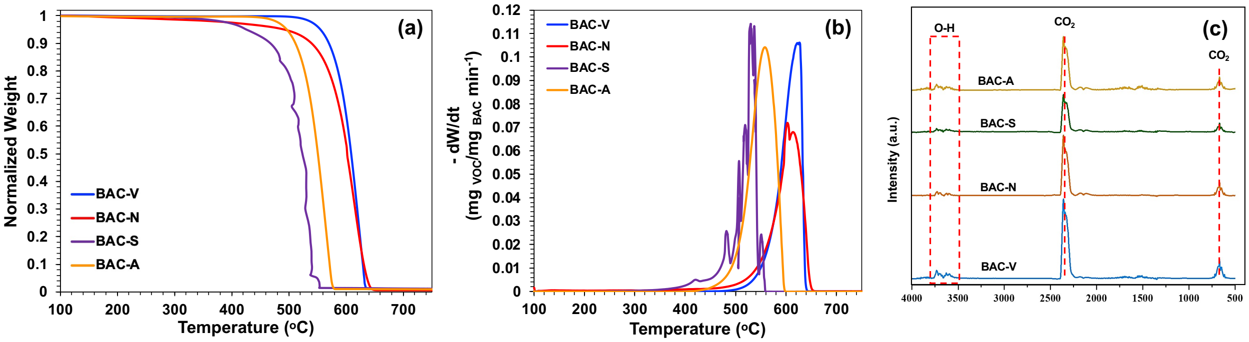

Figure 2.5 *- Decomposition of BAC samples in air flow (a), corresponding differential thermogravimetric (DTG) curves (b), and Gas phase FTIR spectral snapshot of the decomposition of BAC samples at their respective peak temperatures of decomposition identified from DTG curves (c).*

While acidic and alkaline surface modification enhanced the porosity of the BAC, we noticed that surface modification also improved its thermal stability. As described in Section 3.1, surface-modified samples were also repeatedly exposed to high temperature (400 °C) under nitrogen containing 100 ppm oxygen flow. We observed that, contrary to BAC-V, surface-modified samples had little to no change in the surface area, and average diameter (Figure 2.6). It is possible that thermal treatment at 800 °C might have annealed the BAC, reinforcing their structural integrity, retaining the pore structure and the overall shape of the BAC intact.

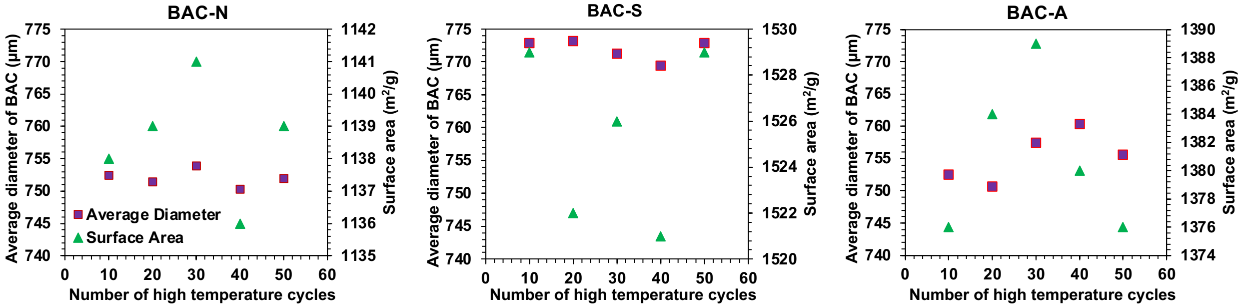

Figure 2.6 *- Change in average diameter of the bead and total surface area of surface-modified BAC samples after exposing them to multiple heigh temperature cycles.*

2.3.3. Adsorption and desorption characteristics of VOCs on surface-modified BAC

2.3.3.1. Impact of surface modification on adsorption capacity

The overall VOC adsorption capacity of untreated and surface-modified BAC samples was evaluated using n-butanol, butyl acetate, and 1,2,4-trimethylbenzene adsorption. Quantitative VOC uptake capacity reported in Table 2.4 was calculated using Equation 1. Experimental breakthrough curves of the VOC adsorption on BAC samples are shown in Figure 2.7 (a1), (b1), and (c1). Surface-modified BAC samples showed greater adsorption capacity than untreated BAC. Specifically, we found that nitric acid treatment increased the VOC uptake capacity by 17% - 29%. Congruently, we also observed a substantial increase in breakthrough time. The presence of functional groups on the surface of BAC can influence the affinity and the extent of adsorption of VOC molecules [22,46]. Several studies have shown that the dipole moment of oxygenated functional groups on the surface of activated carbon can increase the uptake of certain VOC molecules [47,48]. The oxidizing nature of HNO_3, acidic surface modification results in the creation of carboxylic, phenolic, and carbonyl functional groups on the basal planes of BAC. Due to their strong electron donating nature, carbonyl groups exhibit a high dipole moment [49]. As a result, electron donor-acceptor interactions increase, and this would exert a promoting effect on VOC adsorption [50].

Table 2.4 *- VOC adsorption capacities of untreated and surface-modified BAC samples*

Sample	**VOC amount adsorbed (g_{VOC} / g_{BAC})**		
	n-butanol	**n-butyl acetate**	**1,2,4-trimethylbenzene**
BAC-V	0.298	0.351	0.342
BAC-N	0.378	0.454	0.401
BAC-S	0.320	0.487	0.386
BAC-A	0.361	0.459	0.473

Alkaline-treated BAC samples (BAC-S and BAC-A) showed even higher VOC uptake capacity than BAC-N and longer breakthrough times. We observed an increase of approximately 38% in VOC uptake capacity in BAC-S and BAC-A compared to BAC-V. This increase in VOC uptake capacity can be attributed to the substantial increase in total pore volume and surface area of BAC-S and BAC-A [51]. We also observed a steeper slope of the breakthrough curve for alkaline-treated BAC samples. This indicates that the length of the unused bed is substantially shorter in the case of BAC-A and BAC-S than the other BAC samples [52]. Overall, both acidic and alkaline modified BAC samples showed significantly higher VOC uptake capacity compared to BAC-V.

2.3.3.2. Impact of surface modification on desorption characteristics

We used thermogravimetric analysis to study the desorption characteristics of VOC in order to complement our breakthrough analyses, which showed increased uptake capacity of surface-modified BAC samples. Figure 2.7 (a2), (b2), and (c2) shows the characteristic desorption curves of n-butanol, butyl acetate, and 1,2,4-trimethylbenzene, respectively, from different BAC samples. Compared to BAC-V, the peak desorption temperature for n-butanol and butyl acetate desorption dropped by nearly 10 °C in surface modified BAC samples. However, we observed a 50 - 60 °C decrease in peak desorption temperature of 1,2,4-trimethylbenzene from surface-modified BAC samples compared to the peak desorption temperature from BAC-V. Surface modification and subsequent heat treatment increased median micropore width and average pore width (Table 2.4). While further study is warranted, it appears that the relative widening of micropores in surface-modified BAC samples may have reduced potential diffusion and transport limitations, thereby decreasing the temperature required to achieve complete desorption [35]. Among all the modified BAC samples, BAC-N showed a significant decrease in peak desorption temperature. Generally, dispersion interactions during adsorption are related to the π-electrons of aromatic rings of VOC molecules and delocalized π-electrons of basal planes of the BAC [53].

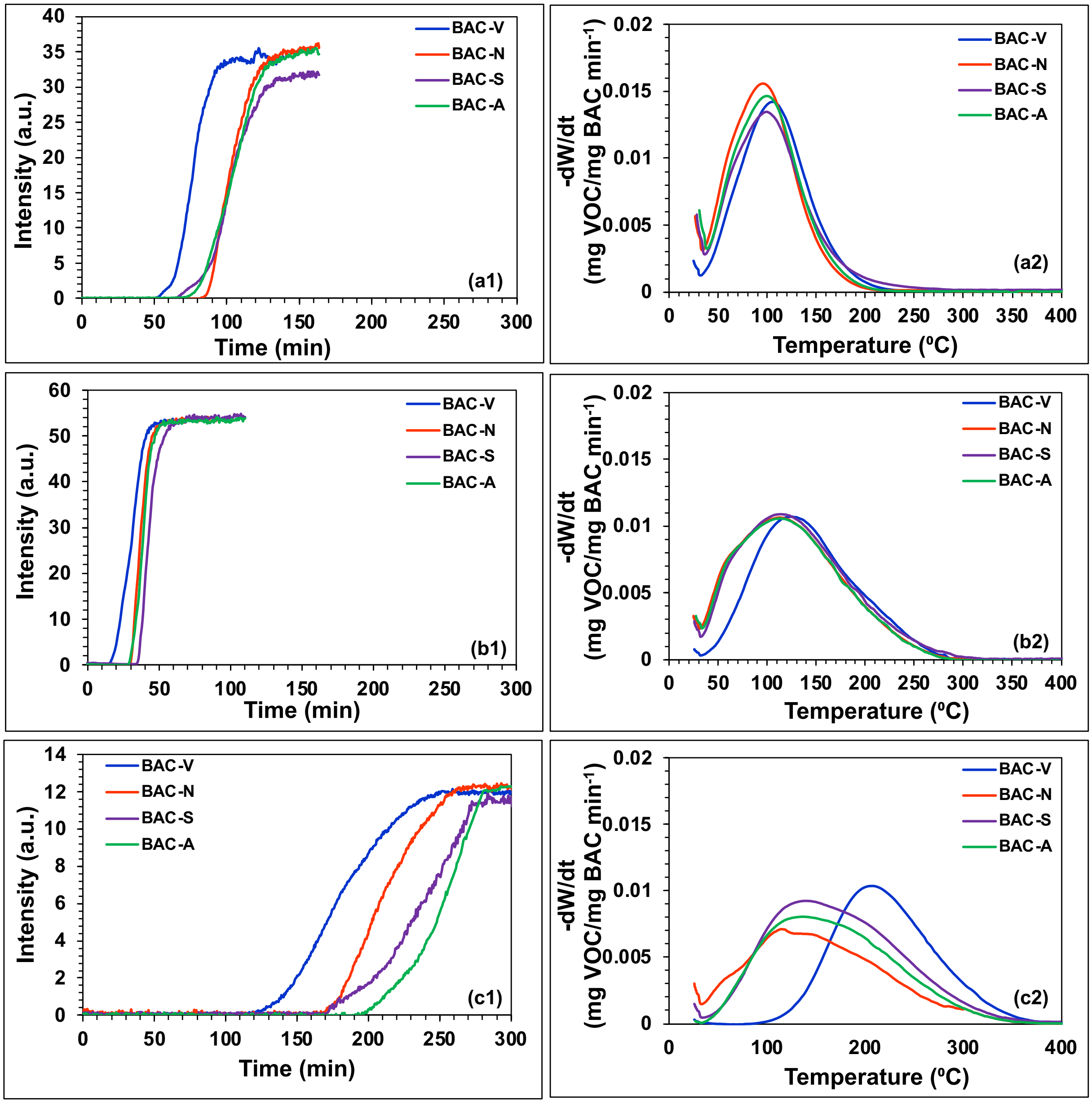

Figure 2.7 *- Adsorption breakthrough curves and temperature programmed desorption profiles of VOCs from modified and untreated BAC samples; n-butanol [(a1), (a2)], n-butyl acetate [(b1), (b2)], and 1,2,4-trimethyl benzene [(c1), (c2)].*

The presence of oxygen-containing functionalities removes the electrons from the π band of the BAC and weakens the dispersion forces between VOC and BAC. Thus, the increasing oxygen content of the BAC by HNO_3 treatment may be responsible for weakening the dispersion interaction.

Despite having a higher adsorption capacity, surface-modified BAC showed superior desorption characteristics compared to unmodified BAC. The diminished diffusion and transport limitations due to pore widening combined with weakly adsorbed VOC molecules on the surface of the BAC, due to the presence of delocalized π-electrons of basal planes, resulted in a significant reduction (50 - 60 °C) in the peak desorption temperature and overall temperature required for complete desorption of VOCs. This can bring down the operation cost of VOC abatement process due to a reduction in the thermal input required to achieve complete desorption. Additionally, operating desorption columns at lower temperatures (~ 350 °C) can reduce the thermal attrition of BAC samples and increase the operational life of the adsorbent.

2.3.4. Analysis of surface functional groups of heel formed in BAC

DRIFTS experiments were carried out after 10 adsorption-desorption cycles to better understand the variability in heel accumulation characteristics among the different BAC samples. Figure 2.8 (a) shows the DRIFTS spectra of powdered BAC samples after 10 n-butanol adsorption-desorption cycles. The broad peaks centered roughly at 3250 cm^{-1}, 1080 cm^{-1}, and 3000 cm^{-1} - 2840 cm^{-1} can be attributed to O–H vibrations, C–O stretching, and C–H stretching (alkane), respectively. The appearance of these peaks indicate the presence of residual n-butanol in BAC-V [40]. However, these peaks are almost negligible in surface-modified BAC samples. Furthermore, we observed multiple peaks between 1400 cm^{-1} - 1700 cm^{-1} in BAC-V, BAC-A, and BAC-S, which can be attributed to C=O stretches and C=C stretching vibrations (both conjugated and non-conjugated). These peaks are characteristics of aldehydes [54]. It is possible that in a high temperature oxidative desorption environment, n-butanol could have undergone conversion, forming butyraldehyde and butene [55,56]. This explains the appearance of C=O and C=C stretches in the

DRIFTS spectra of BAC-V, BAC-S, and BAC-A samples. However, except for a very small C–H stretch (alkane), we saw no other vibrations on BAC-N. As mentioned earlier, the presence of oxygen functionality on the surface of BAC-N prevents the occurrence of strong adsorption on the surface. Consequently, we observe a lower heel accumulation on BAC-N samples.

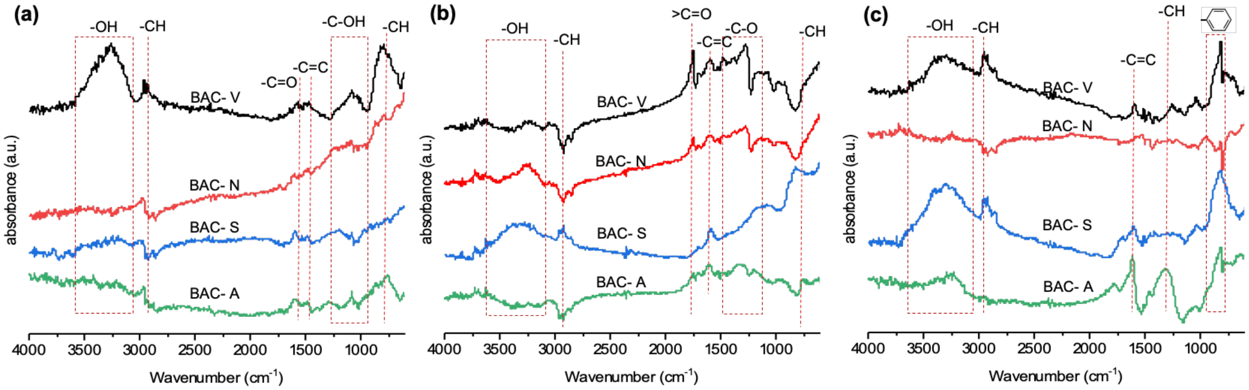

Figure 2.8 *- DRFITS of finely ground BAC samples after 10 adsorption-desorption cycles of different VOC samples [n-butanol (a), n-butyl acetate (b), and 1,2,4-trimethyl benzene (c)].*

Figure 2.8 (b) shows the DRIFTS spectra of BAC samples exposed to 10 butyl acetate adsorption-desorption cycles. The broad peak centered roughly at 3250 cm^{-1} and the peak at 2350 cm^{-1} are possibly due to water vapor and CO_2 adsorption from the atmosphere [57]. The sharp peaks at 2950 cm^{-1} and 1750 cm^{-1} can be attributed to C–H stretching and C=O stretching in esters. Appearance of several smaller peaks between 1500 cm^{-1} to 1050 cm^{-1} are due to the C–O stretching vibrations of the esters. Interestingly, we see C=C peaks in BAC-N, BAC-S, and BAC-A, roughly around 1600 cm^{-1}. This could be due to dehydrogenation reactions at high temperatures.

Figure 2.8 (c) shows the DRIFTS spectra of BAC samples after 10 adsorption-desorption cycles of 1,2,4-trimethylbenzene. Except for BAC-N, all three BAC samples had a broad peak centered at 3250 cm^{-1}, indicating the presence of water vapor on the surface. The sharp peak between 800 cm^{-1} - 900 cm^{-1} is due to aromatic substituted benzene [54]. Interestingly, this peak is absent in BAC-N (Figure 2.8 (c)). Except for C–H stretching centered at 2890 cm^{-1} and C=C bending centered at 960 cm^{-1}, we did not observe any other peaks in BAC-N. However, in the rest of the BAC samples, we see multiple peaks between 1700 cm^{-1} to 900 cm^{-1} that could have possibly come from partial oligomerization or polymeric complex formation in the presence of trace oxygen. Although the assignment of individual spectral peaks can be differently interpreted and diverse conclusions could be drawn regarding polymeric complex formation, it is clear that chemical surface modification significantly influences the interaction of VOCs with the surface of the BAC and limits the formation and accumulation of heel in the pore structures of BAC.

2.3.5. Effect of surface modification on total heel formation

In most practical scenarios, VOC abatement is carried out in a cyclic adsorption-desorption process. The surface area of the saturated adsorbent is regenerated by thermal desorption. However, the regeneration process is not entirely reversible and results in heel accumulation. To evaluate the cumulative percentage of heel accumulated in untreated and surface-modified BAC samples, 10 cycles of adsorption-desorption experiments were carried out in a pilot industrial setup. The experiments were conducted by mimicking the actual plant adsorption and desorption conditions, albeit with a few scaled-down parameters in a pilot plant.

The cumulative percentage of heel accumulated in untreated and surface-modified BAC samples for n-butanol, n-butyl acetate, and 1,2,4-trimethylbenzene after 10 adsorption-desorption cycles are shown in Figure 2.9. We observed a heel accumulation of approximately 6% - 10% on BAC-V when desorption was carried out nitrogen containing 100 ppm oxygen. However, when using surface-modified BAC samples, the extent of heel accumulation was significantly lower than that of BAC-V. As seen in Section 2.3.3, the presence of oxygen-containing functionalities removes the electrons from the π band of the BAC and weakens the dispersion forces between VOC and BAC. As a result of this weakened physisorption, BAC-N showed the lowest percentage of heel accumulation among all four BAC samples (≤ 3%). The textural properties of BAC samples after 10 adsorption-desorption cycles are given in Table 2.5. As a result of heel accumulation, the surface area and micropore pore volume of BAC-V decreased by nearly 10.67% and 39.9%, respectively. However, the textural properties of surface-modified carbon remained largely unaltered.

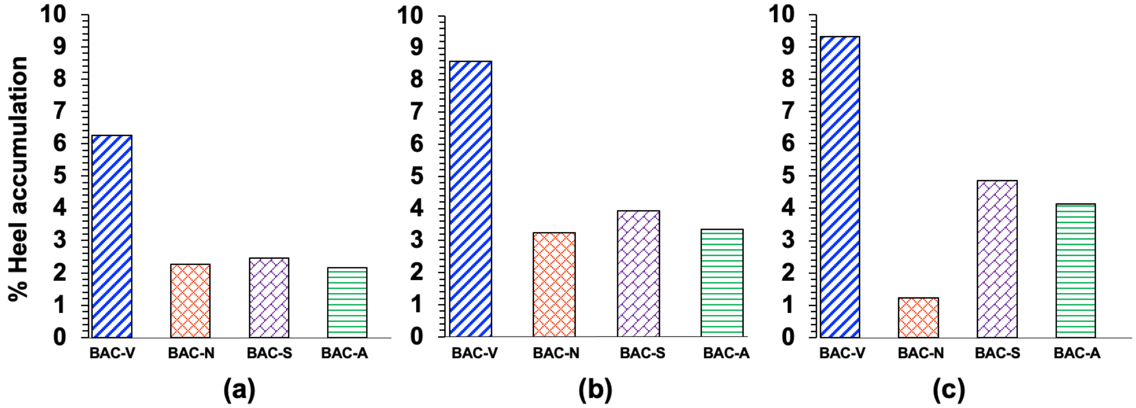

Figure 2.9 *- Percentage heel accumulation in BAC samples after 10 adsorption-desorption cycles of different VOCs [(a) n-butanol, (b) n-butyl acetate, and (c) 1,2,4 – trimethyl benzene].*

Overall, it can be interpreted that the presence of functional groups and changes in the degree of graphitization improved the desorption characteristics of surface-modified BAC samples. Thus, the surface modification methodology can act as a simple technique to inhibit heel formation even in practical industrial settings. Furthermore, it is evident from the results that the chemical modification process described here not only increases the VOC uptake but also prolongs the usable lifetime of the activated carbon beads by suppressing heel formation.

Table 2.5 *- Textural properties of BAC samples after 10 adsorption-desorption cycles*

BAC Sample	BET S.A. (m^2/g)	Total pore volume (cm^3/g)	Micropore volume (cm^3/g)	Average pore width (nm)
BAC-V	905.34	0.494	0.326	2.104
BAC-N	1133.43	0.689	0.588	2.502
BAC-S	1505.96	0.789	0.594	2.453
BAC-A	1361.27	0.695	0.562	2.631

2.4. Conclusion

From a practical standpoint, the desorption studies described here reveal that the ease of desorbing VOC molecules and the extent of heel accumulation are primarily dependent on the boiling point of the respective VOC. Additionally, the presence of oxygen, the resultant shrinkage of activated carbon beads and the collapse of micropores during high-temperature desorption processes largely influence the formation and accumulation of heel in BAC. This chapter has delineated a simple and promising strategy for increasing the surface area and pore volume of the BAC by chemical surface modifications. Furthermore, the introduction of oxygen-containing functionalities onto the surface of the BAC by acidic surface modification, followed by heat treatment, can be used as an effective strategy for suppressing heel accumulation and prolonging the useful life of the BAC in industrial applications. The cyclic adsorption-desorption experiments mimicking actual plant operating conditions demonstrate that this method is promising for large-scale industrial applications to improve the lifetime and efficiency of adsorbent materials.

In summary, the results indicate that the surface modification of BAC improves the adsorption-desorption characteristics in several ways. First, the modifications increase the surface area and pore volume of the BAC while keeping the pore size distribution the same, thereby increasing the VOC uptake capacity. Second, the introduction of functional groups on the surface of the BAC is responsible for the weaker physisorption of VOC molecules, thereby reducing the peak desorption temperature. Finally, the surface modifications inhibit the conversion of VOCs to polymeric complexes at high desorption temperatures, resulting in lower heel accumulation and prolonging the life of the adsorbent.

2.5. References

(1) Kim, B. R. VOC Emissions from Automotive Painting and Their Control: A Review. *Environmental Engineering Research* **2011**, *16* (1), 1–9. https://doi.org/10.4491/eer.2011.16.1.001.

(2) McDonald, B. C.; de Gouw, J. A.; Gilman, J. B.; Jathar, S. H.; Akherati, A.; Cappa, C. D.; Jimenez, J. L.; Lee-Taylor, J.; Hayes, P. L.; McKeen, S. A.; Cui, Y. Y.; Kim, S.-W.; Gentner, D. R.; Isaacman-VanWertz, G.; Goldstein, A. H.; Harley, R. A.; Frost, G. J.; Roberts, J. M.; Ryerson, T. B.; Trainer, M. Volatile Chemical Products Emerging as Largest Petrochemical Source of Urban Organic Emissions. *Science* **2018**, *359* (6377), 760 – 764. https://doi.org/10.1126/science.aaq0524.

(3) Yang, C.; Miao, G.; Pi, Y.; Xia, Q.; Wu, J.; Li, Z.; Xiao, J. Abatement of Various Types of VOCs by Adsorption/Catalytic Oxidation: A Review. *Chemical Engineering Journal* **2019**, *370*, 1128–1153. https://doi.org/https://doi.org/10.1016/j.cej.2019.03.232.

(4) Lee, J. E.; Ok, Y. S.; Tsang, D. C. W.; Song, J.; Jung, S.-C.; Park, Y.-K. Recent Advances in Volatile Organic Compounds Abatement by Catalysis and Catalytic Hybrid Processes: A Critical Review. *Science of The Total Environment* **2020**, *719*, 137405. https://doi.org/https://doi.org/10.1016/j.scitotenv.2020.137405.

(5) Krishnamurthy, A.; Adebayo, B.; Gelles, T.; Rownaghi, A.; Rezaei, F. Abatement of Gaseous Volatile Organic Compounds: A Process Perspective. *Catalysis Today* **2020**, *350*, 100–119. https://doi.org/https://doi.org/10.1016/j.cattod.2019.05.069.

(6) Gong, H.; Zhou, S.; Chen, Z.; Chen, L. Effect of Volatile Organic Compounds on Carbon Dioxide Adsorption Performance via Pressure Swing Adsorption for Landfill Gas Upgrading. *Renewable Energy* **2019**, *135*, 811–818. https://doi.org/https://doi.org/10.1016/j.renene.2018.12.068.

(7) Ohtani, H.; Ellwood, K. R. J.; Venkat, M.; Bhat, A.; Schwank, J. Recovery of Adsorption Capacity of Beaded Activated Carbon Using Gas-Phase Organic Solvents. *U.S. Patent Application No.,* 16/569,914 **2020**.

(8) Niknaddaf, S.; Atkinson, J. D.; Shariaty, P.; Jahandar Lashaki, M.; Hashisho, Z.; Phillips, J. H.; Anderson, J. E.; Nichols, M. Heel Formation during Volatile Organic Compound

Desorption from Activated Carbon Fiber Cloth. *Carbon* **2016**, *96*, 131–138. https://doi.org/https://doi.org/10.1016/j.carbon.2015.09.049.

(9) Wang, H.; Jahandar Lashaki, M.; Fayaz, M.; Hashisho, Z.; Philips, J. H.; Anderson, J. E.; Nichols, M. Adsorption and Desorption of Mixtures of Organic Vapors on Beaded Activated Carbon. *Environmental Science & Technology* **2012**, *46* (15), 8341–8350. https://doi.org/10.1021/es3013062.

(10) Lashaki, M. J.; Fayaz, M.; Wang, H. (Helena); Hashisho, Z.; Philips, J. H.; Anderson, J. E.; Nichols, M. Effect of Adsorption and Regeneration Temperature on Irreversible Adsorption of Organic Vapors on Beaded Activated Carbon. *Environmental Science & Technology* **2012**, *46* (7), 4083–4090. https://doi.org/10.1021/es3000195.

(11) Jahandar Lashaki, M.; Atkinson, J. D.; Hashisho, Z.; Phillips, J. H.; Anderson, J. E.; Nichols, M. The Role of Beaded Activated Carbon's Pore Size Distribution on Heel Formation during Cyclic Adsorption/Desorption of Organic Vapors. *Journal of Hazardous Materials* **2016**, *315*, 42–51. https://doi.org/https://doi.org/10.1016/j.jhazmat.2016.04.071.

(12) Kamravaei, S.; Shariaty, P.; Jahandar Lashaki, M.; Atkinson, J. D.; Hashisho, Z.; Phillips, J. H.; Anderson, J. E.; Nichols, M. Effect of Beaded Activated Carbon Fluidization on Adsorption of Volatile Organic Compounds. *Industrial & Engineering Chemistry Research* **2017**, *56* (5), 1297–1305. https://doi.org/10.1021/acs.iecr.6b04165.

(13) Niknaddaf, S.; Atkinson, J. D.; Gholidoust, A.; Fayaz, M.; Awad, R.; Hashisho, Z.; Phillips, J. H.; Anderson, J. E.; Nichols, M. Influence of Purge Gas Flow and Heating Rates on Volatile Organic Compound Decomposition during Regeneration of an Activated Carbon Fiber Cloth. *Industrial & Engineering Chemistry Research* **2020**, *59* (8), 3521–3530. https://doi.org/10.1021/acs.iecr.9b06070.

(14) Fayaz, M.; Shariaty, P.; Atkinson, J. D.; Hashisho, Z.; Phillips, J. H.; Anderson, J. E.; Nichols, M. Using microwave heating to improve the desorption efficiency of high molecular weight VOC from beaded activated carbon. *Environmental Science & Technology* **2015**, *49* (7), 4536–4542. https://doi.org/10.1021/es505953c.

(15) Cherbański, R.; Molga, E. Intensification of desorption processes by use of microwaves - an overview of possible applications and industrial perspectives. *Chemical Engineering and Processing: Process Intensification* **2009**, *48* (1), 48–58. https://doi.org/https://doi.org/10.1016/j.cep.2008.01.004.

(16) Zhang, X.; Gao, B.; Creamer, A. E.; Cao, C.; Li, Y. Adsorption of VOCs onto Engineered Carbon Materials: A Review. *Journal of Hazardous Materials* **2017**, *338*, 102–123. https://doi.org/https://doi.org/10.1016/j.jhazmat.2017.05.013.

(17) Terzyk, A. P.; Wiśniewski, M.; Gauden, P. A.; Rychlicki, G.; Furmaniak, S. Carbon Surface Chemical Composition in Para-Nitrophenol Adsorption Determined under Real Oxic and Anoxic Conditions. *Journal of Colloid and Interface Science* **2008**, *320* (1), 40–51. https://doi.org/https://doi.org/10.1016/j.jcis.2007.12.037.

(18) Álvarez, P. M.; Beltrán, F. J.; Gómez-Serrano, V.; Jaramillo, J.; Rodríguez, E. M. Comparison between Thermal and Ozone Regenerations of Spent Activated Carbon Exhausted with Phenol. *Water Research* **2004**, *38* (8), 2155–2165. https://doi.org/https://doi.org/10.1016/j.watres.2004.01.030.

(19) Leng, C.-C.; Pinto, N. G. Effects of Surface Properties of Activated Carbons on Adsorption Behavior of Selected Aromatics. *Carbon* **1997**, *35* (9), 1375–1385. https://doi.org/https://doi.org/10.1016/S0008-6223(97)00091-2.

(20) Jahandar Lashaki, M.; Atkinson, J. D.; Hashisho, Z.; Phillips, J. H.; Anderson, J. E.; Nichols, M. The Role of Beaded Activated Carbon's Surface Oxygen Groups on Irreversible Adsorption of Organic Vapors. *Journal of Hazardous Materials* **2016**, *317*, 284–294. https://doi.org/https://doi.org/10.1016/j.jhazmat.2016.05.087.

(21) Li, L.; Liu, S.; Liu, J. Surface Modification of Coconut Shell Based Activated Carbon for the Improvement of Hydrophobic VOC Removal. *Journal of Hazardous Materials* **2011**, *192* (2), 683–690. https://doi.org/https://doi.org/10.1016/j.jhazmat.2011.05.069.

(22) Scida, K.; Stege, P. W.; Haby, G.; Messina, G. A.; García, C. D. Recent Applications of Carbon-Based Nanomaterials in Analytical Chemistry: Critical Review. *Analytica Chimica Acta* **2011**, *691* (1), 6–17. https://doi.org/https://doi.org/10.1016/j.aca.2011.02.025.

(23) Plaza, M. G.; Pevida, C.; Arias, B.; Fermoso, J.; Casal, M. D.; Martín, C. F.; Rubiera, F.; Pis, J. J. Development of Low-Cost Biomass-Based Adsorbents for Postcombustion CO2 Capture. *Fuel* **2009**, *88* (12), 2442–2447. https://doi.org/https://doi.org/10.1016/j.fuel.2009.02.025.

(24) Li, L.; Ma, X.; Chen, R.; Wang, C.; Lu, M. Nitrogen-Containing Functional Groups-Facilitated Acetone Adsorption by ZIF-8-Derived Porous Carbon. *Materials* . 2018. https://doi.org/10.3390/ma11010159.

(25) Hisatsugu, K.; Watanabe, K. Process for Preparing Spherical Carbon Material and Spherical Activated Carbon. *U.S. Patent No.,* 4,371,454, **1983**.

(26) Liu, X.; LIang, X.; Liu, C.; Zhan, L.; Qiao, W.; Ling, L. Pitch Spheres Stabilized by HNO3 Oxidation and Their Carbonization Behavior. *New Carbon Materials* **2010**, *25* (1), 29–34. https://doi.org/https://doi.org/10.1016/S1872-5805(09)60013-5.

(27) Jana, S.; Sarkar, U. Alkaline Functionalization of Granular Activated Carbon for the Removal of Volatile Organo Sulphur Compounds (VOSCs) Generated in Sewage Treatment Plants. *Journal of Environmental Chemical Engineering* **2018**, *6* (2), 3510–3519. https://doi.org/https://doi.org/10.1016/j.jece.2018.05.022.

(28) Gil, A.; Grange, P. Application of the Dubinin-Radushkevich and Dubinin-Astakhov Equations in the Characterization of Microporous Solids. *Colloids and Surfaces A: Physicochemical and Engineering Aspects* **1996**, *113* (1), 39–50. https://doi.org/https://doi.org/10.1016/0927-7757(96)81455-5.

(29) Dombrowski, R. J.; Lastoskie, C. M.; Hyduke, D. R. The Horvath–Kawazoe Method Revisited. *Colloids and Surfaces A: Physicochemical and Engineering Aspects* **2001**, *187–188*, 23–39. https://doi.org/https://doi.org/10.1016/S0927-7757(01)00618-5.

(30) Redhead, P. A. Thermal Desorption of Gases. *vacuum* **1962**, *12* (4), 203–211.

(31) Jahandar Lashaki, M.; Hashisho, Z.; Phillips, J. H.; Crompton, D.; Anderson, J. E.; Nichols, M. Mechanisms of Heel Buildup during Cyclic Adsorption-Desorption of Volatile Organic Compounds in a Full-Scale Adsorber-Desorber. *Chemical Engineering Journal* **2020**, *400*, 124937. https://doi.org/https://doi.org/10.1016/j.cej.2020.124937.

(32) Jahandar Lashaki, M.; Atkinson, J. D.; Hashisho, Z.; Phillips, J. H.; Anderson, J. E.; Nichols, M.; Misovski, T. Effect of Desorption Purge Gas Oxygen Impurity on Irreversible Adsorption of Organic Vapors. *Carbon* **2016**, *99*, 310–317. https://doi.org/https://doi.org/10.1016/j.carbon.2015.12.037.

(33) Szymański, G. S.; Karpiński, Z.; Biniak, S.; Świątkowski, A. The Effect of the Gradual Thermal Decomposition of Surface Oxygen Species on the Chemical and Catalytic

Properties of Oxidized Activated Carbon. *Carbon* **2002**, *40* (14), 2627–2639. https://doi.org/https://doi.org/10.1016/S0008-6223(02)00188-4.

(34) Li, H.; Liu, L.; Cui, J.; Cui, J.; Wang, F.; Zhang, F. High-Efficiency Adsorption and Regeneration of Methylene Blue and Aniline onto Activated Carbon from Waste Edible Fungus Residue and Its Possible Mechanism. *RSC Advances* **2020**, *10* (24), 14262–14273. https://doi.org/10.1039/D0RA01245A.

(35) Li, X.; Zhang, L.; Yang, Z.; Wang, P.; Yan, Y.; Ran, J. Adsorption Materials for Volatile Organic Compounds (VOCs) and the Key Factors for VOCs Adsorption Process: A Review. *Separation and Purification Technology* **2020**, *235*, 116213. https://doi.org/https://doi.org/10.1016/j.seppur.2019.116213.

(36) Mojtaba Hashemi, S.; Jahandar Lashaki, M.; Hashisho, Z.; Phillips, J. H.; Anderson, J. E.; Nichols, M. Oxygen Impurity in Nitrogen Desorption Purge Gas Can Increase Heel Buildup on Activated Carbon. *Separation and Purification Technology* **2019**, *210*, 497–503. https://doi.org/https://doi.org/10.1016/j.seppur.2018.08.035.

(37) Lillo-Ródenas, M. A.; Cazorla-Amorós, D.; Linares-Solano, A. Benzene and Toluene Adsorption at Low Concentration on Activated Carbon Fibres. *Adsorption* **2011**, *17* (3), 473–481. https://doi.org/10.1007/s10450-010-9301-7.

(38) Lin, C.-L.; Cheng, Y.-H.; Liu, Z.-S.; Chen, J.-Y. Adsorption and Oxidation of High Concentration Toluene with Activated Carbon Fibers. *Journal of Porous Materials* **2013**, *20* (4), 883–889. https://doi.org/10.1007/s10934-012-9665-z.

(39) Marsh, H.; Reinoso, F. R. *Activated Carbon*; Elsevier, 2006.

(40) Shafeeyan, M. S.; Daud, W. M. A. W.; Houshmand, A.; Shamiri, A. A Review on Surface Modification of Activated Carbon for Carbon Dioxide Adsorption. *Journal of Analytical and Applied Pyrolysis* **2010**, *89* (2), 143–151. https://doi.org/https://doi.org/10.1016/j.jaap.2010.07.006.

(41) Jia, Y. F.; Xiao, B.; Thomas, K. M. Adsorption of Metal Ions on Nitrogen Surface Functional Groups in Activated Carbons. *Langmuir* **2002**, *18* (2), 470–478. https://doi.org/10.1021/la011161z.

(42) Pereira, M. F. R.; Soares, S. F.; Órfão, J. J. M.; Figueiredo, J. L. Adsorption of Dyes on Activated Carbons: Influence of Surface Chemical Groups. *Carbon* **2003**, *41* (4), 811–821. https://doi.org/https://doi.org/10.1016/S0008-6223(02)00406-2.

(43) Swiatkowski, A.; Pakula, M.; Biniak, S.; Walczyk, M. Influence of the Surface Chemistry of Modified Activated Carbon on Its Electrochemical Behaviour in the Presence of Lead(II) Ions. *Carbon* **2004**, *42* (15), 3057–3069. https://doi.org/https://doi.org/10.1016/j.carbon.2004.06.043.

(44) Treeweranuwat, P.; Boonyoung, P.; Chareonpanich, M.; Nueangnoraj, K. Role of Nitrogen on the Porosity, Surface, and Electrochemical Characteristics of Activated Carbon. *ACS Omega* **2020**, *5* (4), 1911–1918. https://doi.org/10.1021/acsomega.9b03586.

(45) Montes-Morán, M. A.; Suárez, D.; Menéndez, J. A.; Fuente, E. On the Nature of Basic Sites on Carbon Surfaces: An Overview. *Carbon* **2004**, *42* (7), 1219–1225. https://doi.org/https://doi.org/10.1016/j.carbon.2004.01.023.

(46) Jaramillo, J.; Álvarez, P. M.; Gómez-Serrano, V. Oxidation of Activated Carbon by Dry and Wet Methods: Surface Chemistry and Textural Modifications. *Fuel Processing Technology* **2010**, *91* (11), 1768–1775. https://doi.org/https://doi.org/10.1016/j.fuproc.2010.07.018.

(47) Daifullah, A. A. M.; Girgis, B. S. Impact of Surface Characteristics of Activated Carbon on Adsorption of BTEX. *Colloids and Surfaces A: Physicochemical and Engineering Aspects* **2003**, *214* (1), 181–193. https://doi.org/https://doi.org/10.1016/S0927-7757(02)00392-8.

(48) Li, L.; Sun, Z.; Li, H.; Keener, T. C. Effects of Activated Carbon Surface Properties on the Adsorption of Volatile Organic Compounds. *Journal of the Air & Waste Management Association* **2012**, *62* (10), 1196–1202. https://doi.org/10.1080/10962247.2012.700633.

(49) Zhu, D.; Pignatello, J. J. Characterization of Aromatic Compound Sorptive Interactions with Black Carbon (Charcoal) Assisted by Graphite as a Model. *Environmental Science & Technology* **2005**, *39* (7), 2033–2041. https://doi.org/10.1021/es0491376.

(50) Gokce, Y.; Aktas, Z. Nitric Acid Modification of Activated Carbon Produced from Waste Tea and Adsorption of Methylene Blue and Phenol. *Applied Surface Science* **2014**, *313*, 352–359. https://doi.org/https://doi.org/10.1016/j.apsusc.2014.05.214.

(51) Tseng, R.-L. Mesopore Control of High Surface Area NaOH-Activated Carbon. *Journal of Colloid and Interface Science* **2006**, *303* (2), 494–502. https://doi.org/https://doi.org/10.1016/j.jcis.2006.08.024.

(52) Yang, R. T. *Adsorbents: Fundamentals and Applications*; John Wiley & Sons, 2003.

(53) Derylo-Marczewska, A.; Swiatkowski, A.; Biniak, S.; Walczyk, M. Effect of Properties of Chemically Modified Activated Carbon and Aromatic Adsorbate Molecule on Adsorption from Liquid Phase. *Colloids and Surfaces A: Physicochemical and Engineering Aspects* **2008**, *327* (1), 1–8. https://doi.org/https://doi.org/10.1016/j.colsurfa.2008.05.026.

(54) Wang, X.; Liu, Y.; Zhang, T.; Luo, Y.; Lan, Z.; Zhang, K.; Zuo, J.; Jiang, L.; Wang, R. Geometrical-Site-Dependent Catalytic Activity of Ordered Mesoporous Co-Based Spinel for Benzene Oxidation: In Situ DRIFTS Study Coupled with Raman and XAFS Spectroscopy. *ACS Catalysis* **2017**, *7* (3), 1626–1636. https://doi.org/10.1021/acscatal.6b03547.

(55) Gandarias, I.; Nowicka, E.; May, B. J.; Alghareed, S.; Armstrong, R. D.; Miedziak, P. J.; Taylor, S. H. The Selective Oxidation of N-Butanol to Butyraldehyde by Oxygen Using Stable Pt-Based Nanoparticulate Catalysts: An Efficient Route for Upgrading Aqueous Biobutanol. *Catalysis Science & Technology* **2016**, *6* (12), 4201–4209. https://doi.org/10.1039/C5CY01726B.

(56) Sedjame, H.-J.; Lafaye, G.; Barbier, J. N-Butanol Removal over Alumina Supported Platinum Catalysts. *Applied Catalysis B: Environmental* **2013**, *132–133*, 132–141. https://doi.org/https://doi.org/10.1016/j.apcatb.2012.11.032.

(57) Nahata, M.; Seo, C. Y.; Krishnakumar, P.; Schwank, J. New Approaches to Water Purification for Resource-Constrained Settings: Production of Activated Biochar by Chemical Activation with Diammonium Hydrogenphosphate. *Frontiers of Chemical Science and Engineering* **2018**, *12* (1), 194–208. https://doi.org/10.1007/s11705-017-1647-x.

Chapter 3

Recovering the Adsorption Capacity of Spent Beaded Activated Carbon via Solvent-based Regeneration Technique *

3.1. Introduction

Automotive paint formulations generally involve 35-40 different kinds of organic solvents. VOC emissions that stem from this process commonly consist of low and high molecular weight compounds from different organic groups, including aromatic hydrocarbons, aliphatic hydrocarbons, alcohols, ketones, esters, and ethers [1]. A unique abatement operation, known as fluidized carbon bed system (FCBS), is implemented within the automotive industry for adsorbing the VOCs to avoid their detrimental environmental impact [2]. This system is described in detail in Chapter One. A significant challenge associated with the FCBS system is the accumulation of strongly or permanently adsorbed VOC species, commonly referred to as a heel [2,3]. Heel accumulation prevents the complete desorption of the VOC from the adsorbent, decreasing its adsorption capacity and operational lifetime.

It was demonstrated in Chapter Two that the introduction of surface functional groups onto the beaded activated carbon (BAC), specifically through nitric acid treatment, could significantly inhibit the heel accumulation, thereby prolonging the functional life of the BAC. While the

---

* A version of this chapter has been submitted for US Patent application publication. Pub. No.: US 2020/0086298 A1, Mar. 19, 2020.

presence of carbonyl and amine groups results in weak physisorption of VOC on the surface of the adsorbent and facilitates desorption at relatively lower temperatures, it does not completely eliminate the heel formation. As a result, at a certain point during VOC abatement, due to the inevitability of heel accumulation, the BAC loses its capacity to adsorb VOCs.

As a consequence of heel accumulation, the density of the BAC increases. Consequently, measuring the apparent density (AD) of BAC is a straightforward way of qualitatively assessing heel. The AD of virgin BAC often varies between 0.55 to 0.6 g/cm^3. Generally, 100 cm^3 of the BAC sample is obtained from the desorption column in a graduated cylinder, and its weight is recorded. Then, the AD is reported in g/cm^3. BAC is periodically characterized by measuring the AD during a typical VOC abatement operation to ensure effective capture [4]. As such, when the value of AD crosses a certain threshold (0.8 g/cm^3), it is suggestive of substantial heel accumulation. In other words, it indicates that the BAC can no longer be effectively used to capture VOCs. To address this issue, automakers generally suspend the painting operation temporarily and ship the BAC off-site for regeneration.

Thermal regeneration, wet-oxidation regeneration, electrochemical regeneration, supercritical fluid regeneration, microwave irradiation regeneration, and solvent-based regeneration are some of the methods that have been developed to regenerate spent adsorbents [5–7]. Among these, thermal regeneration under a steam or nitrogen environment has an efficiency of 80-90%. It is most widely used due to its cost-effectiveness and ability to regenerate a large capacity of spent adsorbents [8]. While this process can differ based on the adsorbent and the adsorbed components, in general, it is done in four consecutive stages, as shown in Figure 3.1. First, the spent BAC is dried in a furnace at temperatures between 100 °C - 200 °C to remove adsorbed water or moisture content. Drying is followed by vaporizing the volatile organic adsorbates by heating the furnace to 500 °C. Next, the temperature of the furnace is raised from 500 °C to 700 °C, where the absorbates remaining in the porous structures of BAC undergo pyrolysis and subsequent volatilization. Finally, after pyrolysis, the pores of BAC regenerated by reactivating it in steam between 700 - 900 °C [9].

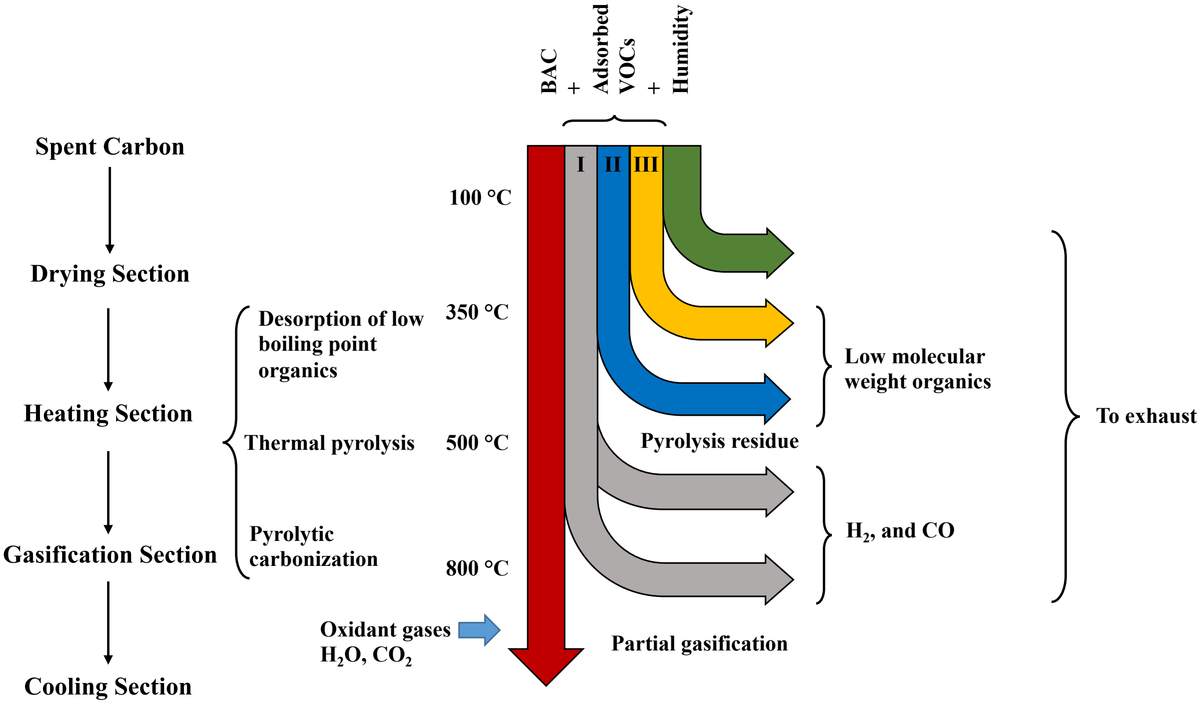

Figure 3.1 *- Schematic representation of thermal regeneration of spent beaded activated carbon; I - Organics that are originally present or formed during the pyrolysis stages and that are volatilized following reaction with steam or carbon dioxide during the gasification stages; II - Organics that volatilize during pyrolysis stages of BAC regeneration; III - Organics that volatilize upon heating.*

The off-site thermal regeneration of spent BACs has several disadvantages. First, the automotive painting process must be temporarily suspended as the spent BAC must be unloaded from FCBS and shipped to a regeneration facility. This inversely impacts the efficiency of the painting operation. Second, during the off-site regeneration process, it is common to lose 10-12%

of the total mass of carbon due to thermal degradation and attrition. Furthermore, attrition during regeneration can also gradually destroy the structural integrity of the BAC. As a result, after 3-4 cycles of the regeneration process, the bulk of the regenerated BAC used in VOC abatement ends up being replaced by virgin BAC [10]. Hence, this process creates substantial material wastage.

Recognizing the limitations of the thermal regeneration process, solvent-based regeneration of spent adsorbents has been receiving substantial attention in recent years. The solvent-based regeneration approach has several other advantages, namely,

i. Regeneration of the spent adsorbent can be done *in-situ*.
ii. No carbon attrition: thus, the cost of replacing adsorbent is avoided.
iii. No carbon surface or pore structure degradation; only a modest loss of adsorption capacity over the first few cycles occurs due to irreversible solvent adsorption.
iv. Using appropriate unit operation, the solvent used for adsorbent regeneration can be recovered.

Researchers have shown that a solvent-based regeneration system could be used to recover the adsorption capacity of spent adsorbent with an efficiency up to 80% or higher [11]. For instance, Tamon et al. used ethanol and toluene to regenerate activated carbon saturated with an organic compound. They found that both ethanol and toluene showed high regeneration efficiency, close to 80%, after five regeneration cycles [12]. Sutikno and Himmelstein used acetone followed by low pressure to regenerate activated carbon saturated with phenol and developed a mathematical model to characterize the phenol desorption during the extraction [13]. Ferro-Garcia et al. regenerated activated carbon prepared from olive stones saturated by chlorophenol using acetone, methanol, ethanol, and benzene. Their experiments revealed that ethanol was the best solvent among the ones they had chosen [14]. Kim and Kim developed a desorption kinetic model of phenol from activated carbon by acetone, N,N-dimethylformamide (DMF), and methanol; the desorption efficiencies attained by acetone and DMF were close to each other but greater than that obtained by methanol [15]. Guo et al. regenerated spent carbon used in the treatment of coking wastewaters with different solvents. Their results indicated that n-pentane could be used effectively and repetitively to recover the adsorption capacity of activated carbon that has irreversibly adsorbed the organic compounds which stem from the cooking wastewater [12].

Among all the studies summarized above, the spent activated carbon is suspended in the desired solvent liquid for a stipulated time under specific pressure and temperature to facilitate the extraction of the irreversibly adsorbed molecule from the surface of the adsorbent [16]. Recognizing the stark advantages of solvent-based regeneration, in this chapter, we evaluate the feasibility of using four industrial solvents to remove the accumulated heel from the micropores of spent BAC samples. The effectiveness of solvent-based regeneration depends on two key factors. *1) The ability of the chosen solvent to dissolve the heel or weaken the bond between irreversibly adsorbed molecules and the adsorbent* and subsequently desorb from the surface of the adsorbent and *2) The extent of diffusion limitation that solvent encounters* in the adsorbent's pore structures. Specifically, when a liquid is used to regenerate microporous adsorbents, the resistance to diffusional mass transport in the pores often limits the solvent from reaching the accumulated heel. As a result, despite having very high miscibility or ability to dissolve heel, the overall efficiency of solvent regeneration can be substantially reduced [17–20]. In this chapter, addressing the transport limitations of liquid solvents, a novel vapor phase regeneration method is delineated to remove the accumulated heel from the pore structures of BAC. Additionally, the textural properties and the adsorption capacity of regenerated BAC are evaluated.

3.2. Experimental

3.2.1. Materials

The adsorbent, beaded activated carbon (BAC), used in this study was obtained from Kureha Corporation. Unused, fresh BAC in this study is referred to as virgin BAC (BAC-V). Spent (aged), unmodified BAC (BAC-Sp) was procured from FCBS that was designed to treat approximately 1700 m^3/min of VOC-laden air coming from automotive coating operations at Ford Motor Company, Dearborn. For comparison purposes, a small portion (~10 g) of thermally regenerated BAC (BAC-TR) was also obtained from Ford Motor Company, Dearborn. Organic solvents used in the regeneration study, benzene, acetone, acetonitrile, and dimethyl sulfoxide, were purchased from Sigma-Aldrich.

3.2.2. Batch regeneration experiments

3.2.2.1. Liquid phase solvent regeneration

About 150 mL of target organic solvent (benzene, acetone, acetonitrile, or dimethyl sulfoxide) was taken in a 500 mL round bottom flask. This was followed by the addition of nearly one gram of BAC-Sp. This mixture was placed in a heating mantle. A graham condenser was attached to the mouth of the round bottom flask, as shown in Figure 3.2 (a). The BAC-Sp was refluxed in boiling organic solvent for 3 hours. The solution was then ambiently cooled down to room temperature and kept undisturbed for five additional hours. Thereafter, the mixture was placed in an ultrasonic bath for 30 minutes to facilitate maximum heel extraction from the micropores of BAC-Sp. Post sonicating, the BAC samples were collected from the mixture by filtration, washed in deionized water and dried in an oven at 120 °C for 3 hours. Post drying, the BAC samples were characterized by measuring the surface area and pore-volume (Section 3.2.3).

3.2.2.2. Vapor phase solvent regeneration

A novel vapor phase regeneration system was designed to regenerate the BAC-Sp and recover its adsorption capacity. A schematic representation of the experimental setup is shown in Figure 3.2 (b). The organic solvent vapor used for extracting the heel was generated by flowing the carrier gas (N_2) through a bubbler containing the target organic solvent (benzene, acetone, acetonitrile, or dimethyl sulfoxide). The carrier gas flow rate was maintained at 200 mL/min using a mass flow controller. As such, the N_2 and Organic solvent vapor mixture were further fed to the top of a quartz tube for 12 hours. The quartz tube was housed in a vertical tube furnace whose temperature was set at 290 °C and consisted of a packed bed of 2g of BAC-Sp. Post regeneration, the quartz tube was ambiently cooled down to room temperature, and the textural properties of BAC samples were measured.

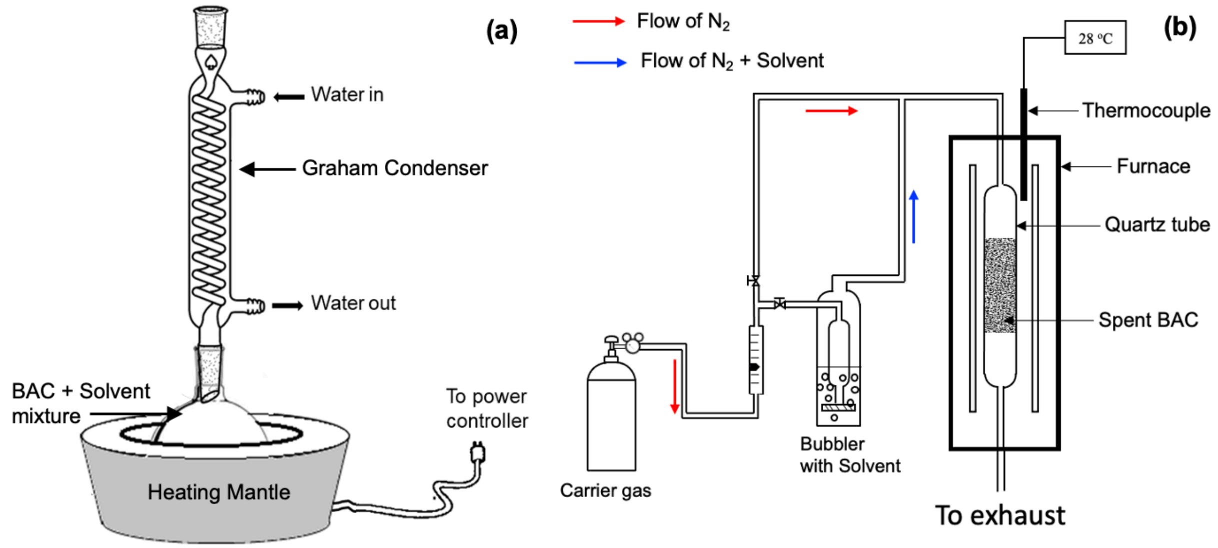

***Figure 3.2** - Schematic representation of the experimental setup for liquid phase solvent regeneration (a), and vapor phase solvent regeneration (b).*

3.2.3. Characterization of BAC samples

The changes in the texture and morphology of the BAC after different regeneration techniques were observed under a Philips XL 30 FEG scanning electron microscope (SEM). Furthermore, an integrated gas sorption apparatus (Micromeritics ASAP 2020) was used to measure the surface area and porosity of the BAC samples. All the samples were degassed for 24 hours under vacuum at 350 °C, and nitrogen adsorption-desorption experiments were carried out at 77 K. The BET equation in the relative pressure (P/P_0) range from 0.06 to 0.32 was used to calculate the surface area from the isotherm data. The micropore volume of the BAC samples was determined from the Dubinin-Astakhov equation [21].

3.3. Results and discussion

The representative SEM images of virgin BAC and BAC samples regenerated through different methods (thermal and solvent-based) are shown in Figure 3.3. Typically, BAC is synthesized by activating an extruded petroleum pitch and coconut shell-charcoal mixture in water vapor and nitrogen at 800 °C. The process of extrusion and activation gives the BAC a lustrous and smooth texture (Figure 3.3. (a)). However, thermal regeneration, which often occurs in a rotary kiln at temperatures as high as 900 °C, destroys the textural integrity of BAC. The associated loss of carbon and abrasion can evidently be observed in the SEM image below (Figure 3.3. (b)). Moreover, exposure to high temperature conditions during thermal regeneration can also change the physical and chemical properties of the BAC, which can affect its sorption behavior and capacity of the regenerated BAC [22]. Unlike thermal regeneration, which pyrolyzes the accumulated heel at very high temperatures, solvent regeneration requires an appropriate solvent with a high dielectric constant to be chosen to dissolve the heel or alter the nature of the bond between irreversibly adsorbed molecules and the porous adsorbent [23]. As such, contrary to thermal regeneration, we observed that both liquid and vapor phase solvent-based regeneration resulted in zero carbon attrition, preserving the structural integrity of BAC (Figure 3.3 (c,d)).

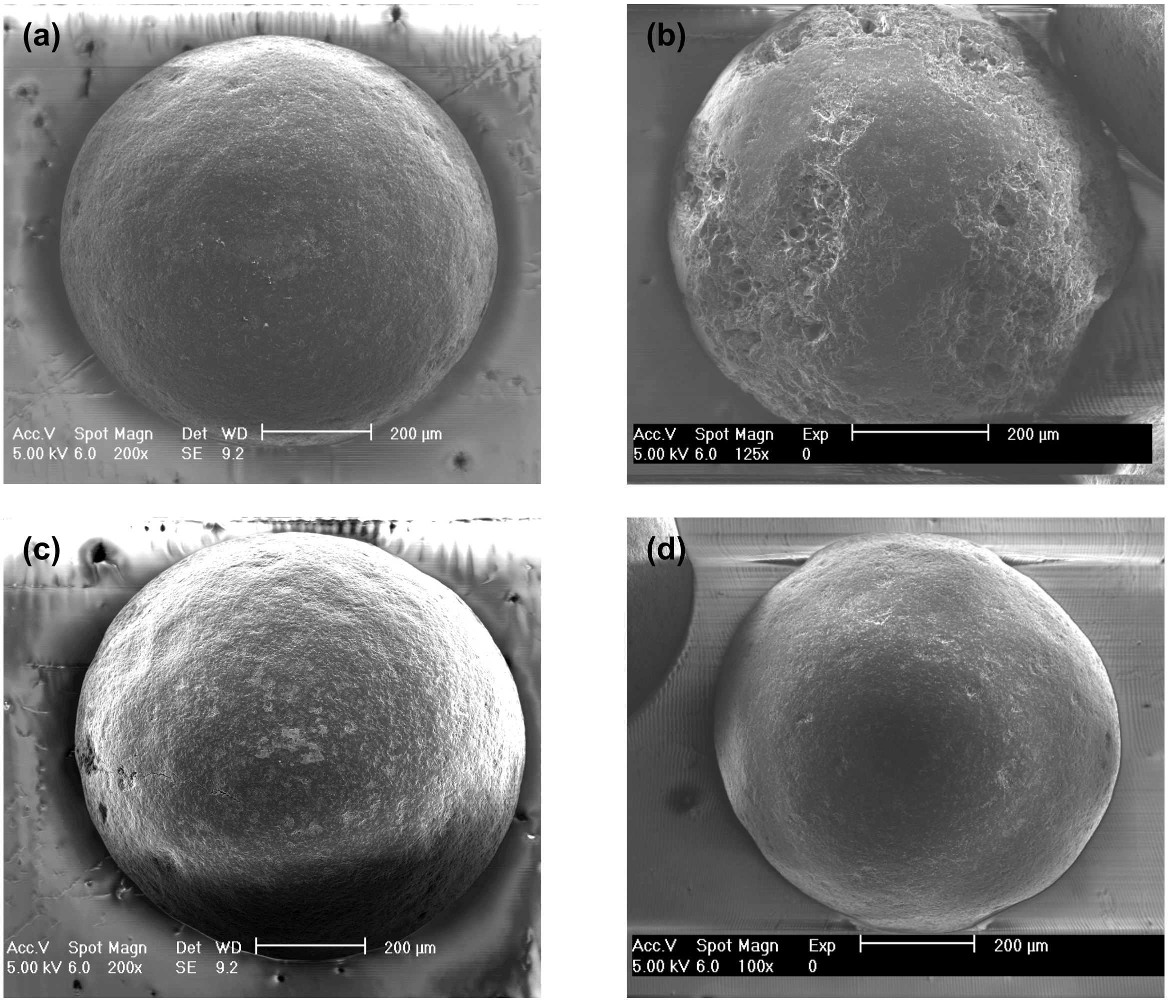

Figure 3.3 *- SEM micrographs of BAC samples; virgin BAC (a), thermally regenerated BAC (b), BAC after liquid-phase solvent regeneration (c), and BAC after vapor-phase solvent regeneration (d).*

3.3.1. Efficacy of solvents in liquid-phase solvent regeneration

A total of four different organic solvents were tested for extracting the accumulated heel from spent BAC (BAC-Sp). To evaluate the efficacy of the solvent, the surface area, and the pore volume of the BAC were measured post-regeneration and compared with the textural properties of virgin BAC, thermally regenerated BAC, and BAC-Sp (Table 3.1 and Figure 3.4). The virgin BAC (BAC-V), as expected, showed the highest pore volume and surface area of 0.582 cm^3/g and 1013 m^2/g respectively. In contrast, spent BAC (BAC-Sp) had the least available surface area and pore volume for adsorption due to cyclic operation and associated heel accumulation. Among the solvents used for liquid-phase regeneration, dimethyl sulfoxide (DMSO) resulted in the maximum surface area and pore volume recovery, amounting to nearly 51% of the adsorption capacity of BAC-V. In contrast, after regenerating the BAC-Sp in benzene, the textural analysis showed an even lower surface area of regenerated BAC compared to BAC-Sp, indicating the possible adsorption of benzene during regeneration. It should be noted that, although liquid-phase solvent regeneration resulted in little to no abrasion of the BAC, the overall efficiency of the regeneration was significantly lower than that of thermal regeneration (Table 3.1).

3.3.2. Efficacy of solvents in vapor-phase solvent regeneration

From a microscopic view, much of the gas phase adsorption in porous materials occurs in three steps. First, the VOC molecule enters the microporous structure of the adsorbent through pore diffusion. Second, VOC molecules adhere to the adsorbent's surface through intermolecular gravitation, namely Van der Waals or dispersion forces, forming a monolayer. Finally, as the adsorbent's pore fills up from diffusion, the VOC molecules condense and start to fill up the micropore due to the increased number of Van der Waals interactions [24]. As such, in solvent-based regeneration, the solvent diffuses into the adsorbent's micropores, weakening the dispersion forces between the adsorbent and VOC molecules, which facilitates desorption [19]. However, as the pores of the adsorbent get smaller, the diffusion of solvent becomes increasingly cumbersome. Hence, the ability of the solvent to weaken the dispersion force between the VOC and adsorbent gets compromised. While further study is warranted, it is possible that the liquid-phase solvent regeneration was ineffective in recovering the adsorption capacity of BAC-Sp due to the transport limitations encountered by the solvent. Therefore, we sought to carry out the regeneration experiments using solvent vapors to reduce the transport and diffusion limitations.

Table 3.1 *- Textural properties of BAC samples before and after different regeneration methods.*

		Liquid-phase regeneration		**Vapor-phase regeneration**	
Sample	**Solvent**	**BET surface area** (m^2/g)	**Total pore volume** (cm^3/g)	**BET surface area** (m^2/g)	**Total pore volume** (cm^3/g)
BAC-V	N/A	1013	0.582	1013	0.582
BAC-TR	N/A	983.2	0.502	983.2	0.502
BAC-Sp	N/A	285.1	0.119	285.1	0.119
	Dimethyl sulfoxide	592.3	0.291	955.6	0.473
	Acetonitrile	385.8	0.210	900.3	0.465
	Acetone	340.6	0.198	766.9	0.360
	Benzene	230.4	0.101	313.2	0.151

Figure 3.4 shows the quantity of N_2 adsorbed after regenerating the spent BAC using the vapor-phase solvent regeneration method. We can see that the amount of surface area recovered by the vapor-phase regeneration method was higher, corresponding to its liquid phase among the four solvents used. While it is difficult to state the regeneration mechanism conclusively, it is possible that the solvent vapors can more easily diffuse into the micropores of BAC compared to liquid solvents. Gradually, through capillary condensation, the solvent vapors condense and

subsequently dissolve the heel accumulated in the micropores. Upon heating, along with the dissolved heel, the solvent desorbs from the surface of BAC, consequently recovering its adsorption capacity.

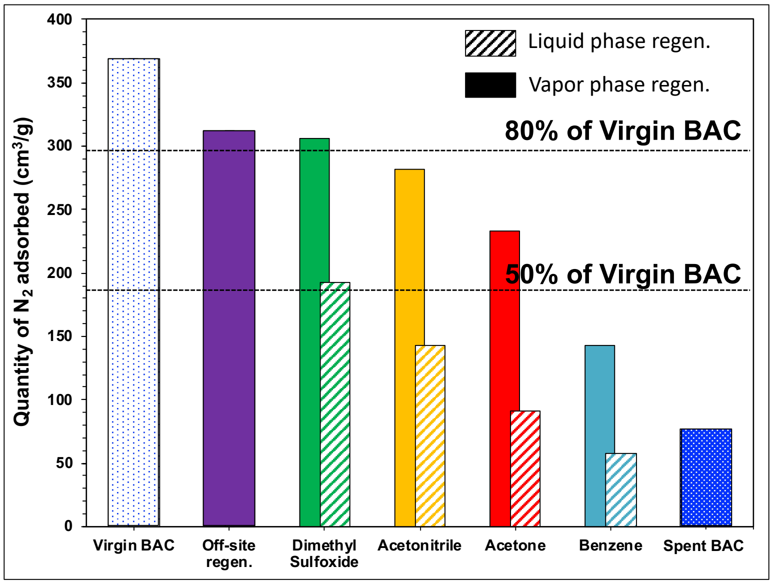

Figure 3.4 *- Quantitative N_2 adsorption in different BAC samples obtained through nitrogen physisorption experiment at 77 K.*

It should be noted that among the solvents used for vapor-phase regeneration, DMSO resulted in the maximum surface area and pore volume recovery, amounting to nearly 82% of the adsorption capacity of BAC-V (Table 3.1). The smaller kinetic diameter of the DMSO molecule, better miscibility in organic solvents, the ability to readily dissolve almost all organic solvents such as alcohols, esters, ketones, chlorinated solvents, and aromatic hydrocarbons, and a very high dielectric constant makes the DMSO a better heel extracting agent than other organic solvents. Additionally, the extent of surface area recovery using vapor-phase DMSO is almost equal to that of off-site thermal regeneration. As solvent-based regeneration results in little to no carbon attrition, the vapor-phase solvent-based regeneration could be an efficient, sustainable, and economical alternative to recover the adsorption capacity of spent BAC.

Operating the desorption column at 290 °C and concurrently passing an appropriate amount of DMSO vapor stream through the packed bed desorber, the accumulated heel from the BAC can be easily extracted. Thus, the adsorption capacity of BAC can be restored. Adding a distillation column to the FCBS and slightly altering the process can effectively assist in recovering the DMSO for reuse. For instance, the exit stream of the desorption unit containing a mixture of DMSO and VOC vapor is sent to a condenser where the mixture is liquified. The liquified mixture can be separated to obtain DMSO and the constituent VOCs using a distillation column operating at 180 °C. Since DMSO has a boiling point of 190 °C, the VOCs dissolved in DMSO evaporate and move to the overhead of the distillation column while DMSO remains liquid at the bottom of the distillation column. Thus, it can be recovered as the bottoms product and consequently can be reused multiple times, as the evaporation loss during phase separation is minimal. From a practical standpoint, the vapor-phase regeneration method described in this chapter can be easily integrated into the FCBS, making the VOC abatement process economical and efficient as it avoids the need for off-site regeneration.

3.4. Conclusion

This chapter outlines a novel method of recovering the adsorption capacity of spent BAC. The heel accumulated during the VOC abatement operation in the micropores of the BAC can be effectively removed using a vapor-phase, solvent-based regeneration method. Textural and morphological analysis of regenerated BAC confirmed that the novel regeneration method preserved the adsorptive nature of the BAC without altering its structural integrity. Of the four regeneration solvents tested, vapor-phase DMSO recovered the maximum surface area and pore volume, amounting to nearly 82% of the adsorption capacity of virgin BAC.

3.5. References

(1) Dinh, T.-V.; Choi, I.-Y.; Son, Y.-S.; Song, K.-Y.; Sunwoo, Y.; Kim, J.-C. Volatile Organic Compounds (VOCs) in Surface Coating Materials: Their Compositions and Potential as an Alternative Fuel. *Journal of Environmental Management* **2016**, *168*, 157–164. https://doi.org/https://doi.org/10.1016/j.jenvman.2015.11.059.

(2) Ohtani, H.; Ellwood, K. R. J.; Venkat, M.; Bhat, A.; Schwank, J. Recovery of Adsorption Capacity of Beaded Activated Carbon Using Gas-Phase Organic Solvents. *U.S. Patent Application No.,* 16/569,914 **2020**.

(3) Lashaki, M. J.; Fayaz, M.; Wang, H. (Helena); Hashisho, Z.; Philips, J. H.; Anderson, J. E.; Nichols, M. Effect of Adsorption and Regeneration Temperature on Irreversible Adsorption of Organic Vapors on Beaded Activated Carbon. *Environmental Science & Technology* **2012**, *46* (7), 4083–4090. https://doi.org/10.1021/es3000195.

(4) Jahandar Lashaki, M.; Hashisho, Z.; Phillips, J. H.; Crompton, D.; Anderson, J. E.; Nichols, M. Mechanisms of Heel Buildup during Cyclic Adsorption-Desorption of Volatile Organic Compounds in a Full-Scale Adsorber-Desorber. *Chemical Engineering Journal* **2020**, *400*, 124937. https://doi.org/https://doi.org/10.1016/j.cej.2020.124937.

(5) Dutta, T.; Kim, T.; Vellingiri, K.; Tsang, D. C. W.; Shon, J. R.; Kim, K.-H.; Kumar, S. Recycling and Regeneration of Carbonaceous and Porous Materials through Thermal or Solvent Treatment. *Chemical Engineering Journal* **2019**, *364*, 514–529. https://doi.org/https://doi.org/10.1016/j.cej.2019.01.049.

(6) Guo, D.; Shi, Q.; He, B.; Yuan, X. Different Solvents for the Regeneration of the Exhausted Activated Carbon Used in the Treatment of Coking Wastewater. *Journal of Hazardous Materials* **2011**, *186* (2), 1788–1793. https://doi.org/https://doi.org/10.1016/j.jhazmat.2010.12.068.

(7) Salvador, F.; Jiménez, C. S. A New Method for Regenerating Activated Carbon by Thermal Desorption with Liquid Water under Subcritical Conditions. *Carbon* **1996**, *34* (4), 511–516. https://doi.org/https://doi.org/10.1016/0008-6223(95)00211-1.

(8) Shah, I. K.; Pre, P.; Alappat, B. J. Effect of Thermal Regeneration of Spent Activated Carbon on Volatile Organic Compound Adsorption Performances. *Journal of the Taiwan*

Institute of Chemical Engineers **2014**, *45* (4), 1733–1738. https://doi.org/https://doi.org/10.1016/j.jtice.2014.01.006.

(9) Lambert, S. D.; Miguel, G. S.; Graham, N. J. D. Deleterious Effects of inorganic compounds during thermal regeneration of GAC: A Review. *Journal AWWA* **2002**, *94* (12), 109–119. https://doi.org/https://doi.org/10.1002/j.1551-8833.2002.tb10253.x.

(10) Sadi, M.; Zeboudj, S.; Azri, Y. M.; Tou, I. D-Limonene as a Green Solvent to Regenerate Granular-Activated Carbon Saturated with Phenol. *Separation Science and Technology* **2020**, *55* (10), 1776–1785. https://doi.org/10.1080/01496395.2019.1609513.

(11) Salvador, F.; Martin-Sanchez, N.; Sanchez-Hernandez, R.; Sanchez-Montero, M. J.; Izquierdo, C. Regeneration of Carbonaceous Adsorbents. Part II: Chemical, Microbiological and Vacuum Regeneration. *Microporous and Mesoporous Materials* **2015**, *202*, 277–296. https://doi.org/https://doi.org/10.1016/j.micromeso.2014.08.019.

(12) Tamon, H.; Saito, T.; Kishimura, M.; Okazaki, M.; Toei, R. Solvent Regeneration of Spent Activated Carbon in Wastewater Treatment. *Journal of chemical engineering of Japan* **1990**, *23* (4), 426–432.

(13) Sutikno, T.; Himmelstein, K. J. Desorption of Phenol from Activated Carbon by Solvent Regeneration. *Industrial & Engineering Chemistry Fundamentals* **1983**, *22* (4), 420–425. https://doi.org/10.1021/i100012a011.

(14) Ferro-García, M. A.; Utrera-Hidalgo, E.; Rivera-Utrilla, J.; Moreno-Castilla, C.; Joly, J. P. Regeneration of Activated Carbons Exhausted with Chlorophenols. *Carbon* **1993**, *31* (6), 857–863. https://doi.org/https://doi.org/10.1016/0008-6223(93)90185-D.

(15) Kim, S.; Kim, Y.-K. Apparent Desorption Kinetics of Phenol in Organic Solvents from Spent Activated Carbon Saturated with Phenol. *Chemical Engineering Journal* **2004**, *98* (3), 237–243. https://doi.org/https://doi.org/10.1016/j.cej.2003.10.006.

(16) Zanella, O.; Tessaro, I. C.; Féris, L. A. Desorption- and Decomposition-Based Techniques for the Regeneration of Activated Carbon. *Chemical Engineering & Technology* **2014**, *37* (9), 1447–1459. https://doi.org/https://doi.org/10.1002/ceat.201300808.

(17) Dong, H.; Wu, Z.; Liu, M. J.; Tarpeh, W. A. The Role of Intraparticle Diffusion Path Length during Electro-Assisted Regeneration of Ion Exchange Resins: Implications for Selective Adsorbent Design and Reverse Osmosis Pretreatment. *Chemical Engineering Journal* **2021**, *407*, 127821. https://doi.org/https://doi.org/10.1016/j.cej.2020.127821.

(18) Neubauer, R.; Weinlaender, C.; Kienzl, N.; Schroettner, H.; Hochenauer, C. Adsorptive Desulfurization: Fast On-Board Regeneration and the Influence of Fatty Acid Methyl Ester on Desulfurization and in Situ Regeneration Performance of a Silver-Based Adsorbent. *Energy & Fuels* **2016**, *30* (6), 5174–5182. https://doi.org/10.1021/acs.energyfuels.6b00519.

(19) Skibinski, B.; Götze, C.; Worch, E.; Uhl, W. Pore Diffusion Limits Removal of Monochloramine in Treatment of Swimming Pool Water Using Granular Activated Carbon. *Water Research* **2018**, *132*, 270–281. https://doi.org/https://doi.org/10.1016/j.watres.2017.12.060.

(20) Ndagijimana, P.; Liu, X.; Li, Z.; Yu, G.; Wang, Y. Optimized Synthesis of a Core-Shell Structure Activated Carbon and Its Adsorption Performance for Bisphenol A. *Science of The Total Environment* **2019**, *689*, 457–468. https://doi.org/https://doi.org/10.1016/j.scitotenv.2019.06.235.

(21) Gil, A.; Grange, P. Application of the Dubinin-Radushkevich and Dubinin-Astakhov Equations in the Characterization of Microporous Solids. *Colloids and Surfaces A: Physicochemical and Engineering Aspects* **1996**, *113* (1), 39–50. https://doi.org/https://doi.org/10.1016/0927-7757(96)81455-5.

(22) Matthis, J.; Carr, S. Reactivation of Spent Activated Carbon Used for PFAS Adsorption. In *Perfluoroalkyl Substances in the Environment*; CRC Press, 2018; pp 303–324.

(23) Busto, M.; Tarifa, E. E.; Vera, C. R. Coupling Solvent Extraction Units to Cyclic Adsorption Units. *International Journal of Chemical Engineering* **2018**, *2018*, 1620218. https://doi.org/10.1155/2018/1620218.

(24) Zhang, X.; Gao, B.; Creamer, A. E.; Cao, C.; Li, Y. Adsorption of VOCs onto Engineered Carbon Materials: A Review. *Journal of Hazardous Materials* **2017**, *338*, 102–123. https://doi.org/https://doi.org/10.1016/j.jhazmat.2017.05.013.

Chapter 4

Self-Assembly Directed Encapsulation of Noble Metal Nanoparticles in Mesoporous TiO_2 for Catalytic Oxidation of VOCs

4.1. Introduction

Thermal oxidation, a process of combusting or incinerating VOCs, is one of the most widely used operations to destroy VOCs in industries. This process involves burning the toxic VOCs at very high temperatures (900 - 1200 °C), which results in the formation of CO_2 and H_2O through a highly exothermic reaction [1]. In practice, these reactions are carried out in equipment called thermal incinerator [2,3]. Although incinerators have a very high VOC destruction efficiency (~ 90%), operating them is extremely energy-intensive [4]. Often, natural gas is supplemented to maintain the operating temperatures of the thermal incinerators [3]. Furthermore, the high operating temperatures of incinerators can form toxic dioxins and noxious products. Additionally, instead of readily decomposing into products like CO_2 and H_2O, VOCs sometimes partially oxidize in incinerators, resulting in CO or other undesirable by-products. Such instances would require additional post-operative treatments like NO_x trap or CO oxidizers [5]. In sum, the auxiliary fuel consumption, additional pollutant formation, and the associated increase in the total carbon footprint make the thermal incineration of VOC very inefficient.

To overcome the operational and financial constraints of thermal incinerators, several researchers have proposed the idea of replacing the incinerators with a low-temperature catalytic reactor that can completely oxidize the VOCs to CO_2 and H_2O [6]. In practice, noble metal based catalysts are the most extensively used materials in catalytic reactors to achieve complete oxidation of VOCs at low temperatures [7]. Specifically, platinum and palladium are the most widely used metal nanoparticles in catalytic applications due to their superior catalytic performance. However, widespread utilization of these metals coupled with their scarcity has appreciably increased their cost over the last decade [8]. This has motivated a significant interest in tailoring nanomaterials to maximize the extent of active metal utilization in catalytic applications [9–13]. Also, catalyst deactivation, which results from metal sintering and surface area loss, accompanied by the formation of surface-covering coke deposits, remains a significant challenge in heterogeneous catalysis [14,15]. Researchers have developed several strategies to address these issues, such as strengthening metal-support interactions, stabilizing high dispersion of active metal through atom trapping, and, alternatively, coating active metal species with shells of porous thermally robust metal oxides [16–21]. Some of these methods require complex post-synthesis treatments, while others, due to the specificity of the synthesis methodology, exhibit difficulties in scale-up and controlling the pore structure of the oxide shell coating, which renders many active sites inaccessible to gas-phase reactants.

In addressing these shortcomings, researchers have devised novel approaches of encapsulating metal catalysts in zeolites with small, stable, rigid, and uniform pores while maintaining a high dispersion throughout the support structure [22–29]. The high surface area of zeolite contributes to a better spatial dispersion of the metal nanoparticles and enhances active metal stability by preventing migration and coalescence [29–31]. Furthermore, the high porosity of zeolite materials facilitates better mass transfer, rendering the metal nanoparticles highly accessible to gas-phase reactants, which can improve reaction kinetics [32,33]. This has been demonstrated in recent work by Xiao *et al.,* who showed that immobilizing active metal species within zeolite crystals through a controllable, seed-directed growth technique can not only help in controlling the metal nanoparticle size but also results in a sinter-resistant structure that is capable of outperforming conventional supported metal catalysts [34].

While using zeolites is an excellent strategy, achieving a similar catalytic design using a reducible metal oxide support such as CeO_2 or TiO_2 can further enhance the collective performance of a catalyst [35–37]. Recent work from our lab demonstrated that encapsulating Pd metal in a CeO_2 shell, leading to a core@shell morphology, can facilitate enhanced catalytic performance through the increased use of lattice oxygen from the support and provides substantial resistance to sintering at high temperatures [38].

In this chapter, building upon the advancements mentioned above, a simple synthesis strategy is reported to encapsulate noble metal nanoparticles (Pt, Pd, Au, Ag) in a reducible TiO_2 nanosphere. The surfactant-mediated synthesis approach enables fine control over the nanoparticle size and the porosity of TiO_2 support. Additionally, the transmission electron microscopy and energy dispersive spectroscopy analysis demonstrates that this novel synthesis methodology achieves a high dispersion of noble metal nanoparticles in porous TiO_2 nanosphere and promotes metal-support interactions by maximizing interfacial sites. Finally, this chapter examines the VOC oxidation efficacy of the encapsulated catalysts by conducting catalytic oxidation of n-butanol, a common VOC encountered in many industrial processes such as automotive painting, to determine the most economical and sustainable catalyst for industrial VOC abatement.

4.2. Experimental

4.2.1. Materials

The metal precursors chloroplatinic acid (H_2PtCl_6, 99.9% trace metals basis), palladium (II) nitrate dihydrate ($PdNO_3•2H_2O$, 99 % trace metals basis), hydrogen tetrachloroaurate (III) hydrate ($H_3AuCl_4O•xH_2O$, 99.995% trace metals basis), silver nitrate ($AgNO_3$, ACS reagent ≥99.0%), and titanium (IV) butoxide (TBOT, 97%) were purchased from Sigma-Aldrich. The surfactants dodecylamine (DDA, 98%) and Pluronic F-127 triblock copolymer (MW = 12600) was procured from ACROS Organics™ and Sigma-Aldrich respectively. All the synthesis were carried out in deionized water and anhydrous ethanol.

4.2.2. Synthesis of metal encapsulated TiO_2 nanospheres

The metal (Pt, Pd, Au, Ag) encapsulated TiO_2 nanospheres were synthesized by a one-pot, two-step process. In a typical synthesis, 0.34 g of DDA and an appropriate amount of corresponding metal precursor (listed in Table 4.1) were added to a conical flask filled with 150 mL anhydrous ethanol. The ethanolic solution was placed on a magnetic stirrer. When the solution turned transparent, 0.79 g of Pluronic F-127 triblock copolymer was added to the conical flask. After 1 hour, 7.61 mL of deionized water was added to the ethanolic solution. This step was followed by the dropwise addition of 1.2 mL of TBOT. After the addition of TBOT, the solution was stirred for 90 additional minutes. The colloidal product obtained during the synthesis was left undisturbed for 12 hours. Upon completion of the synthesis, the encapsulated catalysts were collected by centrifugation, washed three times with ethanol, and dried at 80 °C in air. The as-prepared catalysts were denoted as encapsulated M-TiO_2 or M-TiO_2 (E), where M corresponds to Pt, Pd, Au, Ag.

Post drying, all the catalysts (Pt-TiO_2 (E), Pd-TiO_2 (E), Au-TiO_2, and Ag-TiO_2 (E)) were calcined at 450 °C for 3 hours in a muffle furnace to remove any residual surfactant. Once treated, all catalysts were subjected to characterization and catalytic experiments.

Table 4.1 *- Metal precursors and their corresponding weights to synthesize in encapsulated TiO_2 catalysts.*

Catalyst	**Precursor**	**Weight of metal precursor (g)**
Pt-TiO_2 (E)	H_2PtCl_6	0.0114
Pd-TiO_2 (E)	$PdNO_3.2H_2O$	0.0136
Au-TiO_2 (E)	H_3AuCl_4O	0.0098
Ag-TiO_2 (E)	$AgNO_3$	0.0086

4.2.3. Catalyst characterization

Characterization of the samples was done using a total of four different techniques: Thermogravimetric analysis (TGA), Brunauer – Emmett – Teller derived N_2 physisorption surface analysis (BET), transmission electron microscopy (TEM), and X-ray energy dispersive spectroscopy (XEDS).

In-situ thermal decomposition studies were carried out using TGA (TA Instrument Q 500). Roughly 15 mg of catalyst sample was placed in the TGA instrument and heated from 25 °C to 600 °C at a rate of 5 °C /min under the flow of air. The airflow in the TGA system was diluted by balance N_2 gas, lowering the actual O_2 concentration to 16 %.

Nitrogen physisorption experiments were carried out to measure the textural properties of encapsulated TiO_2 catalysts. Prior to physisorption analysis, all samples were pretreated at 350 °C for 24 hours under vacuum to remove adsorbed water as well as any potential volatiles. Surface area and porosity measurements were carried out with liquid nitrogen at 77K using a Micromeritics ASAP 2020 integrated gas sorption apparatus. The BET equation in the relative pressure (P/P_0) range from 0.06 to 0.32 was used to calculate the surface area from the isotherm data. The median pore width and the micropore size distribution were obtained from the Horvath-Kawazoe model using slit pore geometry and the BJH adsorption model.

The metal nanoparticle morphology was examined by TEM. Standard bright field TEM, High-angle annular dark-field scanning transmission electron microscopy and XEDS mapping of the catalyst sample was carried out using a Talos F200X G2 S/TEM at 200 kV. A typical TEM specimen was prepared by dispersing the washed M-TiO_2 (E) nanopowders in ethanol by sonication for 10 minutes. The suspended nanoparticles were supported on a 200-mesh copper grid with carbon film support.

4.2.4. Catalytic activity evaluation

The gaseous feed used for the catalytic tests was composed of 1000 ppmv of n-butanol in dry air. The required concentration of n-butanol was generated by bubbling an accurate amount of dry air through a saturator containing n-butanol at room temperature. The outlet flow from the saturator was mixed with a second stream of dry air to obtain 0.1% of n-butanol feed at the reactor inlet.

The catalyst samples were pressed into pellets and sieved to particles between 60 and 80 mesh. Catalytic reactions were carried out in a tubular quartz tube (ID = 4.0 mm), placed in a vertical electrical furnace equipped with a temperature programmer. A thermocouple was inserted in the reactor, embedded in the catalyst bed, to measure the exact reaction temperature. 50 mg of catalyst diluted with 100 mg of cordierite powder (also sieved to particles between 60−80 mesh) was used for the reaction. Before the catalytic tests, all samples were pretreated at 400 °C, for 1 hour under dry airflow (100 mL/min) with a ramping rate of 5 °C/min to clean the catalyst surface. The reaction products were analyzed by a gas chromatograph (Varian 450-GC). The GC was equipped with a 30 m long VF-5ms GC column (CP8944) and a 100 m long CP-Sil PONA CB column (CP7530). The column oven was maintained at 80 °C and the measurements were taken at 10 °C intervals between 40 °C and 350 °C. Each temperature point was stabilized for 30 min, with effluent gas analysis by downstream GC. The conversion of n-butanol ($X_{C_4H_{10}O}$) was calculated according to the equation:

$$X_{n-butanol}(\%) = \left[\frac{[C_4H_{10}O]_{in} - [C_4H_{10}O]_{out}}{[C_4H_{10}O]_{in}}\right] \times 100 \qquad (1)$$

where $[C_4H_{10}O]_{in}$ and $[C_4H_{10}O]_{out}$ are the n-butanol concentration in the feed gas and the outlet gas, respectively.

Apparent activation energies for n-butanol conversion were determined from an Arrhenius plot. Data points were collected using the experimental parameters described above with 25 mg of meshed but un-diluted catalyst. Temperatures points used for Arrhenius plotting were kept under 70 °C to ensure that n-butanol conversion was less than 20%. Each temperature point was stabilized for 30 min, with a constant effluent gas analysis by downstream GC. The rate of n-butanol conversion at a given temperature ($r_{n-butanol}$) was calculated by

$$r_{n-butanol} = \frac{[C_4H_{10}O]_{in} \times X_{C_4H_{10}O} \times V_f}{m_{cat}} \qquad (2)$$

where $[C_4H_{10}O]_{in}$ is the inlet concentration of n-butanol, $X_{C_4H_{10}O}$ is the n-butanol conversion at the given temperature, V_f is the test gas flow rate, and m_{cat} is the mass of the catalyst used in the experiment.

4.3. Results and discussion

4.3.1. Catalyst synthesis and characterization

The general synthesis of metal encapsulated TiO_2 catalysts (M-TiO_2 (E)) is illustrated in Figure 4.1. The addition of metal precursor to ethanolic solution results in dissociation of the metal salt into their corresponding anionic and cationic counterparts. The excessive ethanol, in the presence of dodecylamine (DDA) initiates a slow reduction of metal cation, resulting in the formation of M^0 seeds [39]. In an alcohol/water solution, non-ionic surfactant Pluronic F127 molecules form spherical micelles with their hydrophobic center, propylene oxide (PPO), attached towards M^0 seeds and the hydrophilic surface of polyethylene oxide (PEO) towards water. The hydrophobic alkyl groups of DDA can penetrate the hydrophobic center of PPO in the F127 spherical micelles, while the hydrophilic -NH_2 groups remain on the hydrophilic PEO surface in the micelle formation process [40]. Thus, F127, DDA, and reduced metal seeds assemble into cooperative spherical micelles in the alcohol/water solution at room temperature. When TBOT is added to this solution, it undergoes hydrolysis and results in the formation of $Ti(OCH_2CH_2CH_2CH_3)_{4-x}(OH)_x$ species, which interacts with the -NH_2 groups of the spherical micelle through hydrogen bonding and forms F127-DDA-M-TiO_2 composite oligomers [40–42]. As these composite Ti oligomers further polymerize, the concentration of the composite spherical micelles increases. To minimize the surface free energy, these composite spherical micelles aggregate and pack into large spheres [43–45].

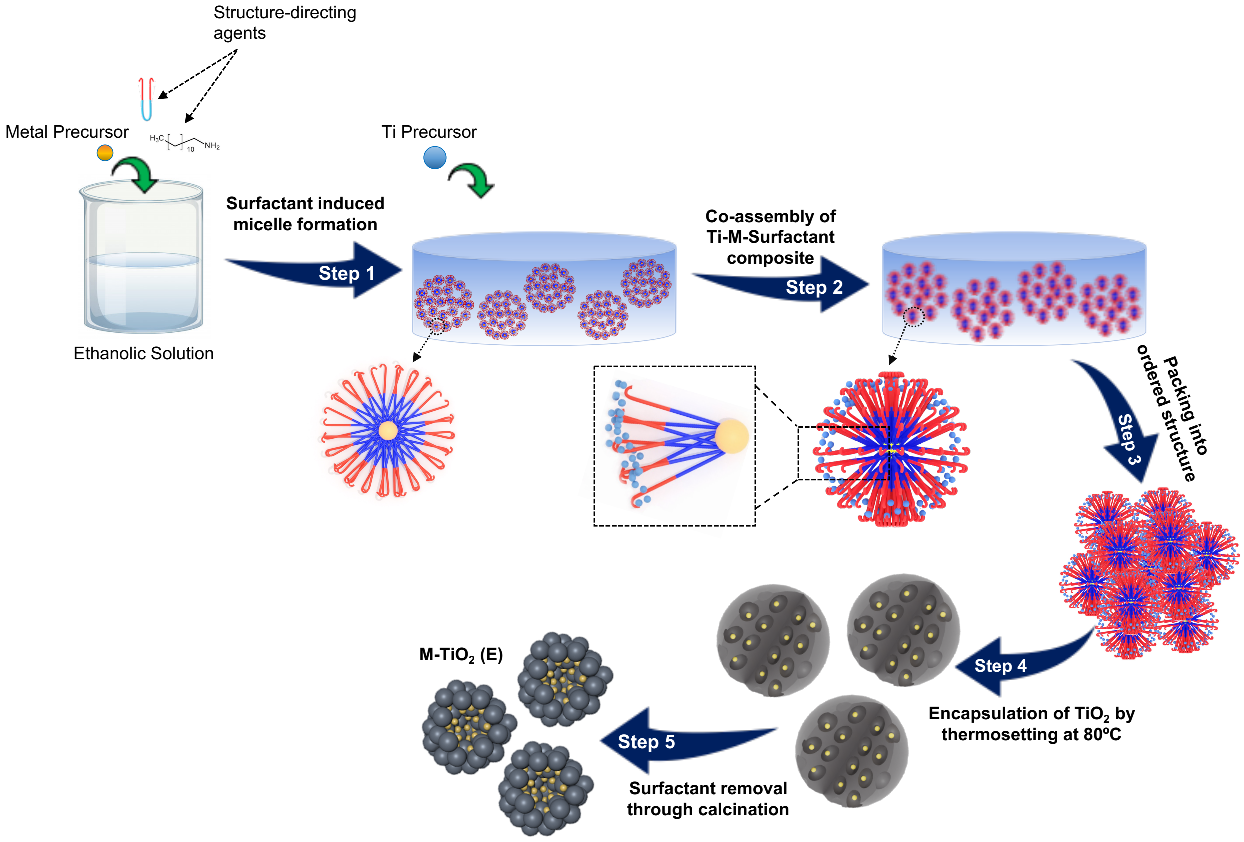

Figure 4.1 *- Representation of the synthesis of metal encapsulated TiO$_2$ catalysts.*
Step 1: *Formation of spherical micelles with metal nanoparticle core and hydrophobic polyethylene oxide shell.* ***Step 2:*** *Collaborative assembly with the Ti precursor to form F127-DDA-M-TiO$_2$ oligomer composite spherical micelles through hydrogen bond interactions.* ***Step 3:*** *Packing of the F127-DDA-M-TiO$_2$ oligomer composite spherical micelles into large spheres to minimize interface energy.* ***Step 4:*** *Encapsulation of Ag nanoparticles in amorphous TiO$_2$ nanosphere by thermosetting.* ***Step 5*** *Surfactant removal and crystallization of TiO$_2$ nanosphere through calcination.*

As the catalyst preparation uses surfactants to achieve the desired encapsulation morphology, it is very important to remove any remaining residual surfactants so that the catalyst can be utilized effectively. Hence, to determine the appropriate temperature for calcination, synthesized catalyst samples were thermally decomposed in TGA. Figure 4.2 shows change in the catalyst's weight as a function of temperature. The gradual weight loss between 100 to 450 °C can be attributed to the removal of both surfactants DDA and Pluronic F-127. Oxidation of the amorphous precursor with an inorganic/organic hybrid spherical structure can lead to a small incremental weight change at about 420 °C. Therefore, removal of organic surfactants and crystallization of the TiO_2 support can be best achieved by a calcination treatment at 450 °C.

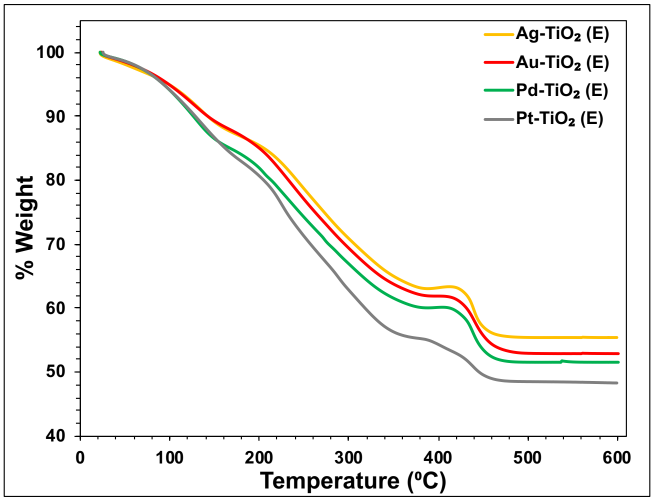

Figure 4.2 *- Thermal decomposition of metal encapsulated TiO_2 catalysts (M-TiO_2) after synthesis.*

Calcining the sample oxidizes the surfactant. Consequently, the exothermic reaction can increase the localized temperature surrounding active metals and result in sintering of the support during the crystallization. This process can lead to the subsequent collapse of the mesopore structure. This could prevent many active sites from participating in the reaction and also negatively affect the reaction due to potential transport limitations. Therefore, to probe the textural properties of encapsulated samples, nitrogen sorption experiments were carried out. The surface areas and average pore size distribution of metal encapsulated TiO_2 catalysts are reported in Table 4.1. Nitrogen adsorption-desorption isotherms shown in Figure 4.3 indicate that the encapsulated catalysts exhibit a type II isotherm. This suggests that the majority of the pores in TiO_2 support are macroporous in nature. It is possible that while calcination of the amorphous catalyst effectively removes the surfactants, the process may also result in collapse and closure of interconnected pores within the encapsulating TiO_2 support. Thus, in all the four synthesized catalysts, we observed a considerably smaller surface area.

Table 4.2 *- Textural properties of the encapsulated catalysts.*

Catalyst	**BET S.A (m^2/g)**	**Avg. pore size (nm)**
Pt-TiO_2 (E)	16.88	30.11
Pd-TiO_2 (E)	12.94	28.44
Au-TiO_2 (E)	18.71	25.59
Ag-TiO_2 (E)	18.68	24.24

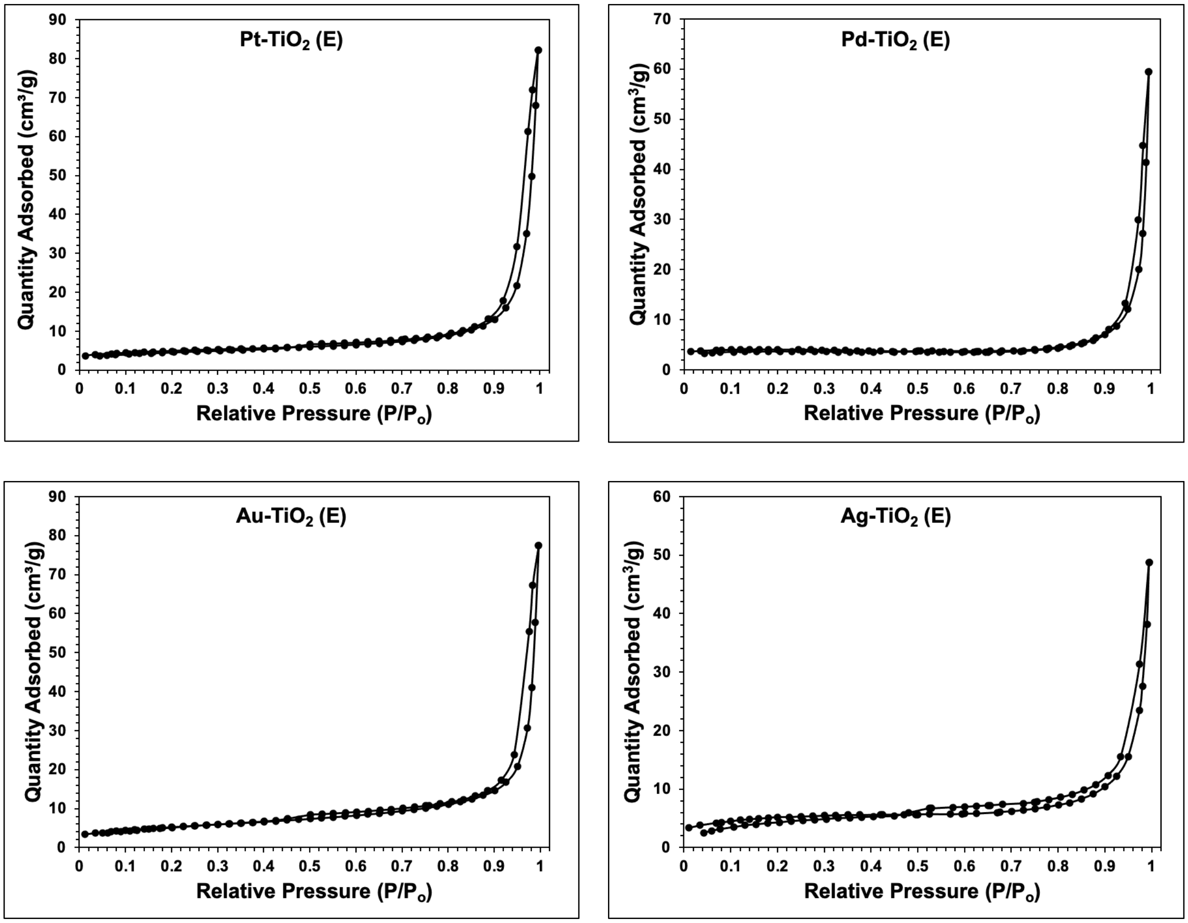

Figure 4.3 *- Nitrogen adsorption and desorption isotherms of metal encapsulated TiO_2 catalysts*

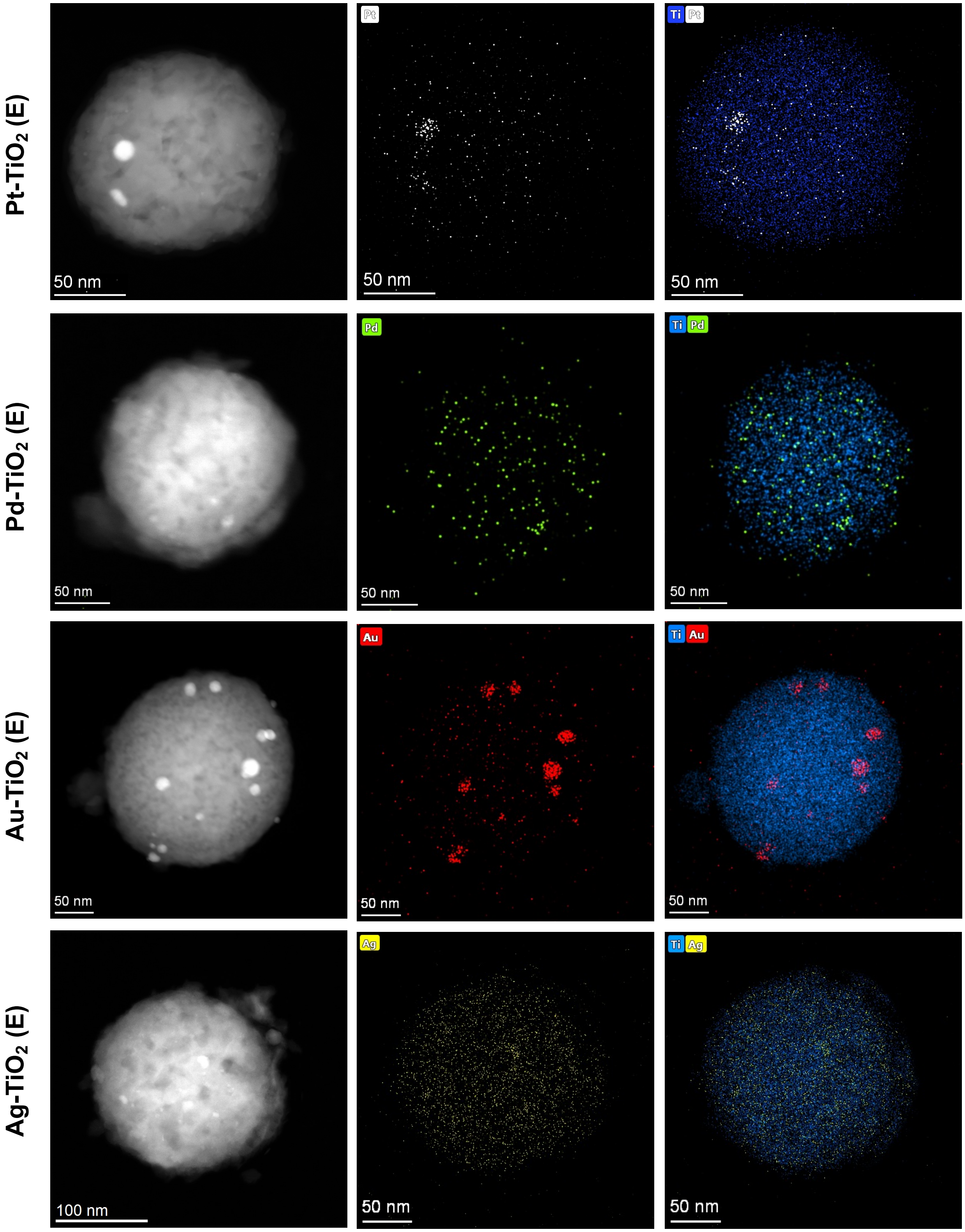

Figure 4.4 *- TEM and XEDS characterization of metal encapsulated TiO_2 catalysts.*

The representative TEM images and XEDS characterization of the metal encapsulated catalysts are shown in Figure 4.4. M-TiO_2 catalysts consist of metal nanoparticles (Pt, Pd, Au, and Ag) encapsulated in mesoporous TiO_2 nanosphere ranging between 100 - 150 nm. We also observed that the encapsulating TiO_2 support was made of randomly oriented polycrystalline TiO_2 nanoparticles stacked together in a spherical structure. While the size of Pt, Pd, and Ag nanoparticles had a narrow size range between 2-5 nm, we observed that the size of Au nanoparticles ranged between 2 - 20 nm. In the method described above (section 4.2.2), Au-TiO_2 (E) catalysts are synthesized using hydrogen tetrachloroaurate precursor. Several studies have reported that the presence of chloride is known to exacerbate metal sintering during calcination and thermal treatments on gold nanoparticles [46–48].

4.3.2. Catalytic oxidation of n-butanol over metal encapsulated catalysts

An elemental analysis conducted by Ford Motor Company reports that nearly 45% of the VOC exhaust that stems from automotive painting consists of n-butanol vapors. Thus, the oxidation of n-butanol was used to evaluate the catalytic activities of the M-TiO_2 catalysts. Figure 4.5 (a) shows the conversion of n-butanol as a function of temperature. Pt-TiO_2 (E) catalysts exhibited the best catalytic activity amongst all three catalytic systems, as evidenced by their having the lowest temperature required to reach 90% conversion of n-butanol (T_{90} ~ 160 °C). Furthermore, even at temperatures as low as 40 °C, we observed nearly 10% conversion of n-butanol over Pt-TiO_2 (E). Pd-TiO_2 (E) and Ag-TiO_2 (E), on the other hand, showed a similar conversion till 120 °C. However, as the reaction temperature increased, Pd-TiO_2 (E) showed a much higher rate of n-butanol conversion, achieving T_{90} ~ 190 °C, while the T_{90} for Ag-TiO_2 (E) was 210 °C. In comparison, Au-TiO_2 (E) was the least active catalyst for n-butanol oxidation, which exhibited a much higher T_{90} of 250 °C.

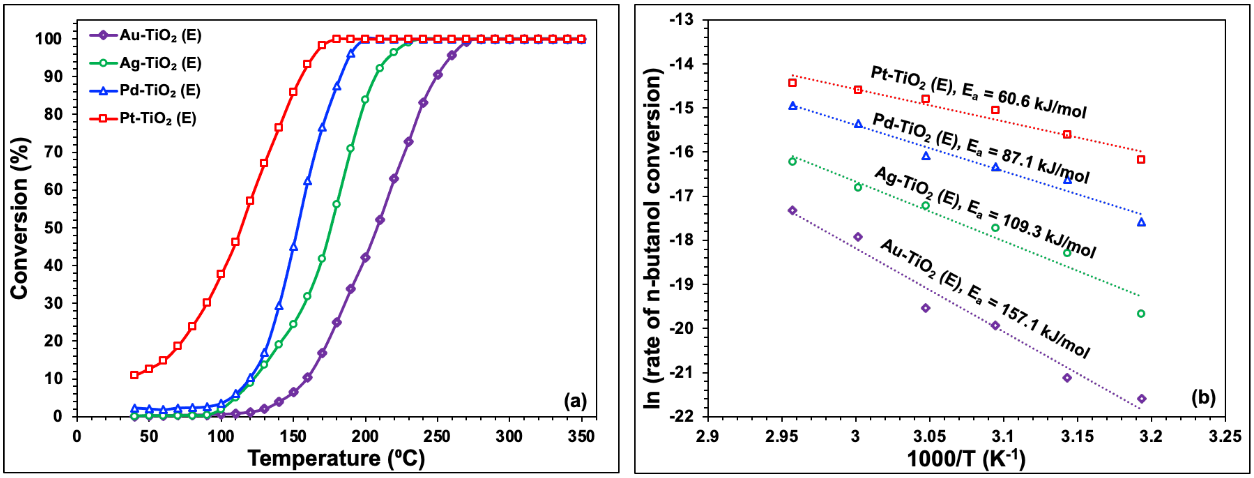

Figure 4.5 *- n-butanol oxidation profiles for metal encapsulated TiO_2 catalysts (a), and Arrhenius plots and corresponding activation energies of different metal encapsulated TiO_2 catalysts (b).*

By comparing the temperatures for 50, 90, and 100% conversion of n-butanol, the following performance trend was observed for the oxidation of n-butanol: Pt > Pd > Ag > Au. Often, catalytic oxidation of VOCs over noble metals involves dissociative adsorption of oxygen [49,50]. Metals that have lower adsorption energies can initiate reactions at relatively lower temperatures. Researchers have attempted to evaluate the intrinsic activity of noble metal catalysts at different temperatures for dissociative chemisorption energies of oxygen through first-principle and empirical studies. Among the four noble metals used, platinum nanoparticles require the lowest energy for dissociative chemisorption of oxygen. They were followed by palladium, silver, and gold nanoparticles [51]. The difference in intrinsic activities of each metal nanoparticle explains the variation in the n-butanol oxidation trend that we observed in Figure 4.5. Additionally, as seen in TEM and XEDS characterization, compared to Pt, Pd, and Ag, nanoparticles of Au showed significantly larger size distribution. Thus, the resultant decrease in the active sites available for adsorption could also have contributed to the higher light off profile exhibited by Au-TiO_2 (E).

4.4. Conclusion

This chapter elucidates the synthesis of a novel catalyst architecture of encapsulating and dispersing nanoparticles of noble metals inside a reducible, porous TiO_2 nanosphere. This surfactant mediated, self-assembly driven synthesis yields a uniform nanoparticle size distribution and promotes metal-support interactions by maximizing interfacial sites, thereby improving catalytic activity. Furthermore, the encapsulated TiO_2 catalysts proved to be very effective in oxidizing VOCs at temperatures as low as 160 °C, compared to the otherwise thermal incineration that requires temperatures above 900 °C for complete oxidation of VOCs.

4.5. References

(1) Krishnamurthy, A.; Adebayo, B.; Gelles, T.; Rownaghi, A.; Rezaei, F. Abatement of Gaseous Volatile Organic Compounds: A Process Perspective. *Catalysis Today* **2020**, *350*, 100–119. https://doi.org/https://doi.org/10.1016/j.cattod.2019.05.069.

(2) Cannon, B. J. Dual-Chamber RTO Oxidizers Provide Cost-Effective VOC Compliance for Metal Finishers and Coaters. *Metal Finishing* **2003**, *101* (1), 53–56. https://doi.org/https://doi.org/10.1016/S0026-0576(03)80022-3.

(3) Kim, B. R. VOC Emissions from Automotive Painting and Their Control: A Review. *Environmental Engineering Research* **2011**, *16* (1), 1–9. https://doi.org/10.4491/eer.2011.16.1.001.

(4) Zhang, Z.; Jiang, Z.; Shangguan, W. Low-Temperature Catalysis for VOCs Removal in Technology and Application: A State-of-the-Art Review. *Catalysis Today* **2016**, *264*, 270–278. https://doi.org/https://doi.org/10.1016/j.cattod.2015.10.040.

(5) Hu, Z.; Wang, Z.; Guo, Y.; Wang, L.; Guo, Y.; Zhang, J.; Zhan, W. Total Oxidation of Propane over a Ru/CeO2 Catalyst at Low Temperature. *Environmental Science & Technology* **2018**, *52* (16), 9531–9541. https://doi.org/10.1021/acs.est.8b03448.

(6) Kamal, M. S.; Razzak, S. A.; Hossain, M. M. Catalytic Oxidation of Volatile Organic Compounds (VOCs) – A Review. *Atmospheric Environment* **2016**, *140*, 117–134. https://doi.org/https://doi.org/10.1016/j.atmosenv.2016.05.031.

(7) Huang, H.; Xu, Y.; Feng, Q.; Leung, D. Y. C. Low Temperature Catalytic Oxidation of Volatile Organic Compounds: A Review. *Catalysis Science & Technology* **2015**, *5* (5), 2649–2669. https://doi.org/10.1039/C4CY01733A.

(8) Du, R.; Jin, X.; Hübner, R.; Fan, X.; Hu, Y.; Eychmüller, A. Engineering Self-Supported Noble Metal Foams Toward Electrocatalysis and Beyond. *Advanced Energy Materials* **2020**, *10* (11), 1901945. https://doi.org/https://doi.org/10.1002/aenm.201901945.

(9) Wang, L.; Wang, L.; Meng, X.; Xiao, F.-S. New Strategies for the Preparation of Sinter-Resistant Metal-Nanoparticle-Based Catalysts. *Advanced Materials* **2019**, *31* (50), 1901905. https://doi.org/https://doi.org/10.1002/adma.201901905.

(10) Lunkenbein, T.; Schumann, J.; Behrens, M.; Schlögl, R.; Willinger, M. G. Formation of a ZnO Overlayer in Industrial Cu/ZnO/Al2O3 Catalysts Induced by Strong Metal–Support

Interactions. *Angewandte Chemie International Edition* **2015**, *54* (15), 4544–4548. https://doi.org/https://doi.org/10.1002/anie.201411581.

(11) Qiao, B.; Wang, A.; Yang, X.; Allard, L. F.; Jiang, Z.; Cui, Y.; Liu, J.; Li, J.; Zhang, T. Single-Atom Catalysis of CO Oxidation Using Pt1/FeOx. *Nature Chemistry* **2011**, *3* (8), 634–641. https://doi.org/10.1038/nchem.1095.

(12) Gao, Z.; Qin, Y. Design and Properties of Confined Nanocatalysts by Atomic Layer Deposition. *Accounts of Chemical Research* **2017**, *50* (9), 2309–2316. https://doi.org/10.1021/acs.accounts.7b00266.

(13) Goel, S.; Wu, Z.; Zones, S. I.; Iglesia, E. Synthesis and Catalytic Properties of Metal Clusters Encapsulated within Small-Pore (SOD, GIS, ANA) Zeolites. *Journal of the American Chemical Society* **2012**, *134* (42), 17688–17695. https://doi.org/10.1021/ja307370z.

(14) Lu, J.; Fu, B.; Kung, M. C.; Xiao, G.; Elam, J. W.; Kung, H. H.; Stair, P. C. Coking- and Sintering-Resistant Palladium Catalysts Achieved Through Atomic Layer Deposition. *Science* **2012**, *335* (6073), 1205 – 1208. https://doi.org/10.1126/science.1212906.

(15) Tang, H.; Wei, J.; Liu, F.; Qiao, B.; Pan, X.; Li, L.; Liu, J.; Wang, J.; Zhang, T. Strong Metal–Support Interactions between Gold Nanoparticles and Nonoxides. *Journal of the American Chemical Society* **2016**, *138* (1), 56–59. https://doi.org/10.1021/jacs.5b11306.

(16) Tang, H.; Su, Y.; Zhang, B.; Lee, A. F.; Isaacs, M. A.; Wilson, K.; Li, L.; Ren, Y.; Huang, J.; Haruta, M.; Qiao, B.; Liu, X.; Jin, C.; Su, D.; Wang, J.; Zhang, T. Classical Strong Metal–Support Interactions between Gold Nanoparticles and Titanium Dioxide. *Science Advances* **2017**, *3* (10), e1700231. https://doi.org/10.1126/sciadv.1700231.

(17) Ta, N.; Liu, J. (Jimmy); Chenna, S.; Crozier, P. A.; Li, Y.; Chen, A.; Shen, W. Stabilized Gold Nanoparticles on Ceria Nanorods by Strong Interfacial Anchoring. *Journal of the American Chemical Society* **2012**, *134* (51), 20585–20588. https://doi.org/10.1021/ja310341j.

(18) Jones, J.; Xiong, H.; DeLaRiva, A. T.; Peterson, E. J.; Pham, H.; Challa, S. R.; Qi, G.; Oh, S.; Wiebenga, M. H.; Pereira Hernández, X. I.; Wang, Y.; Datye, A. K. Thermally Stable Single-Atom Platinum-on-Ceria Catalysts via Atom Trapping. *Science* **2016**, *353* (6295), 150 – 154. https://doi.org/10.1126/science.aaf8800.

(19) Seo, C.; Yi, E.; Nahata, M.; Laine, R. M.; Schwank, J. W. Facile, One-Pot Synthesis of Pd@CeO2 Core@shell Nanoparticles in Aqueous Environment by Controlled Hydrolysis of Metalloorganic Cerium Precursor. *Materials Letters* **2017**, *206*, 105–108. https://doi.org/https://doi.org/10.1016/j.matlet.2017.06.114.

(20) Seo, C. Y.; Chen, X.; Sun, K.; Allard, L. F.; Fisher, G. B.; Schwank, J. W. Palladium Redispersion at High Temperature within the Pd@SiO2 Core@shell Structure. *Catalysis Communications* **2018**, *108*, 73–76. https://doi.org/https://doi.org/10.1016/j.catcom.2018.01.027.

(21) Zhang, J.; Wang, H.; Wang, L.; Ali, S.; Wang, C.; Wang, L.; Meng, X.; Li, B.; Su, D. S.; Xiao, F.-S. Wet-Chemistry Strong Metal–Support Interactions in Titania-Supported Au Catalysts. *Journal of the American Chemical Society* **2019**, *141* (7), 2975–2983. https://doi.org/10.1021/jacs.8b10864.

(22) Choi, M.; Wu, Z.; Iglesia, E. Mercaptosilane-Assisted Synthesis of Metal Clusters within Zeolites and Catalytic Consequences of Encapsulation. *Journal of the American Chemical Society* **2010**, *132* (26), 9129–9137. https://doi.org/10.1021/ja102778e.

(23) Yang, X.; Li, Q.; Lu, E.; Wang, Z.; Gong, X.; Yu, Z.; Guo, Y.; Wang, L.; Guo, Y.; Zhan, W.; Zhang, J.; Dai, S. Taming the Stability of Pd Active Phases through a Compartmentalizing Strategy toward Nanostructured Catalyst Supports. *Nature Communications* **2019**, *10* (1), 1611. https://doi.org/10.1038/s41467-019-09662-4.

(24) Liu, S.; Xu, W.; Niu, Y.; Zhang, B.; Zheng, L.; Liu, W.; Li, L.; Wang, J. Ultrastable Au Nanoparticles on Titania through an Encapsulation Strategy under Oxidative Atmosphere. *Nature Communications* **2019**, *10* (1), 5790. https://doi.org/10.1038/s41467-019-13755-5.

(25) Shifa, T. A.; Vomiero, A. Confined Catalysis: Progress and Prospects in Energy Conversion. *Advanced Energy Materials* **2019**, *9* (40), 1902307. https://doi.org/https://doi.org/10.1002/aenm.201902307.

(26) Liu, L.; Corma, A. Confining Isolated Atoms and Clusters in Crystalline Porous Materials for Catalysis. *Nature Reviews Materials* **2020**. https://doi.org/10.1038/s41578-020-00250-3.

(27) Otto, T.; Ramallo-López, J. M.; Giovanetti, L. J.; Requejo, F. G.; Zones, S. I.; Iglesia, E. Synthesis of Stable Monodisperse AuPd, AuPt, and PdPt Bimetallic Clusters Encapsulated

within LTA-Zeolites. *Journal of Catalysis* **2016**, *342*, 125–137. https://doi.org/https://doi.org/10.1016/j.jcat.2016.07.017.

(28) Gao, C.; Lyu, F.; Yin, Y. Encapsulated Metal Nanoparticles for Catalysis. *Chemical Reviews* **2020**. https://doi.org/10.1021/acs.chemrev.0c00237.

(29) Cui, T.-L.; Ke, W.-Y.; Zhang, W.-B.; Wang, H.-H.; Li, X.-H.; Chen, J.-S. Encapsulating Palladium Nanoparticles Inside Mesoporous MFI Zeolite Nanocrystals for Shape-Selective Catalysis. *Angewandte Chemie International Edition* **2016**, *55* (32), 9178–9182. https://doi.org/10.1002/anie.201602429.

(30) Ma, J.; Ren, Y.; Zhou, X.; Liu, L.; Zhu, Y.; Cheng, X.; Xu, P.; Li, X.; Deng, Y.; Zhao, D. Pt Nanoparticles Sensitized Ordered Mesoporous WO3 Semiconductor: Gas Sensing Performance and Mechanism Study. *Advanced Functional Materials* **2018**, *28* (6), 1705268. https://doi.org/https://doi.org/10.1002/adfm.201705268.

(31) Wang, G.-H.; Cao, Z.; Gu, D.; Pfänder, N.; Swertz, A.-C.; Spliethoff, B.; Bongard, H.-J.; Weidenthaler, C.; Schmidt, W.; Rinaldi, R.; Schüth, F. Nitrogen-Doped Ordered Mesoporous Carbon Supported Bimetallic PtCo Nanoparticles for Upgrading of Biophenolics. *Angewandte Chemie International Edition* **2016**, *55* (31), 8850–8855. https://doi.org/https://doi.org/10.1002/anie.201511558.

(32) Chai, Y.; Liu, S.; Zhao, Z.-J.; Gong, J.; Dai, W.; Wu, G.; Guan, N.; Li, L. Selectivity Modulation of Encapsulated Palladium Nanoparticles by Zeolite Microenvironment for Biomass Catalytic Upgrading. *ACS Catalysis* **2018**, *8* (9), 8578–8589. https://doi.org/10.1021/acscatal.8b02276.

(33) Zhu, W.; Noureddine, A.; Howe, J. Y.; Guo, J.; Brinker, C. J. Conversion of Metal–Organic Cage to Ligand-Free Ultrasmall Noble Metal Nanocluster Catalysts Confined within Mesoporous Silica Nanoparticle Supports. *Nano Letters* **2019**, *19* (3), 1512–1519. https://doi.org/10.1021/acs.nanolett.8b04121.

(34) Zhang, J.; Wang, L.; Zhang, B.; Zhao, H.; Kolb, U.; Zhu, Y.; Liu, L.; Han, Y.; Wang, G.; Wang, C.; Su, D. S.; Gates, B. C.; Xiao, F.-S. Sinter-Resistant Metal Nanoparticle Catalysts Achieved by Immobilization within Zeolite Crystals via Seed-Directed Growth. *Nature Catalysis* **2018**, *1* (7), 540–546. https://doi.org/10.1038/s41929-018-0098-1.

(35) Mkhwanazi, T. P. O.; Farahani, M. D.; Mahomed, A. S.; Singh, S.; Friedrich, H. B. Engineering of Catalytic Sites of Pdx-Ce1-XO2-δ for Dehydrogenation, Oxygen Insertion

and Reverse Water Gas Shift Reactions during Methane Combustion. *Applied Catalysis B: Environmental* **2020**, *275*, 119118. https://doi.org/https://doi.org/10.1016/j.apcatb.2020.119118.

(36) Kim, H. J.; Lee, J. H.; Lee, M. W.; Seo, Y.; Choung, J. W.; Kim, C. H.; Lee, K.-Y. SiO2@Pd@CeO2 Catalyst with Improved Thermal Stability: Effect of Interaction between Pd and CeO2 on Activity for CO Oxidation. *Molecular Catalysis* **2020**, *492*, 111014. https://doi.org/https://doi.org/10.1016/j.mcat.2020.111014.

(37) Otto, T.; Zones, S. I.; Iglesia, E. Challenges and Strategies in the Encapsulation and Stabilization of Monodisperse Au Clusters within Zeolites. *Journal of Catalysis* **2016**, *339*, 195–208. https://doi.org/https://doi.org/10.1016/j.jcat.2016.04.015.

(38) Hill, A. J.; Seo, C. Y.; Chen, X.; Bhat, A.; Fisher, G. B.; Lenert, A.; Schwank, J. W. Thermally Induced Restructuring of Pd@CeO2 and Pd@SiO2 Nanoparticles as a Strategy for Enhancing Low-Temperature Catalytic Activity. *ACS Catalysis* **2020**, *10* (3), 1731–1741. https://doi.org/10.1021/acscatal.9b05224.

(39) JS, K. Reduction of Silver Nitrate in Ethanol by Poly(N-Vinylpyrrolidone). *Journal of Industrial and Engineering Chemistry* **2007**, *13* (4), 566–570.

(40) Chen, D.; Cao, L.; Huang, F.; Imperia, P.; Cheng, Y.-B.; Caruso, R. A. Synthesis of Monodisperse Mesoporous Titania Beads with Controllable Diameter, High Surface Areas, and Variable Pore Diameters (14−23 Nm). *Journal of the American Chemical Society* **2010**, *132* (12), 4438–4444. https://doi.org/10.1021/ja100040p.

(41) Sugimoto, T.; Kojima, T. Formation Mechanism of Amorphous TiO2 Spheres in Organic Solvents. 1. Roles of Ammonia. *The Journal of Physical Chemistry C* **2008**, *112* (48), 18760–18771. https://doi.org/10.1021/jp8029506.

(42) Liu, S.; Han, G.; Shu, M.; Han, L.; Che, S. Monodispersed Inorganic/Organic Hybrid Spherical Colloids: Versatile Synthesis and Their Gas-Triggered Reversibly Switchable Wettability. *Journal of Materials Chemistry* **2010**, *20* (44), 10001–10009. https://doi.org/10.1039/C0JM02101F.

(43) Zhu, H.; Shang, Y.; Jing, Y.; Liu, Y.; Liu, Y.; El-Toni, A. M.; Zhang, F.; Zhao, D. Synthesis of Monodisperse Mesoporous TiO2 Nanospheres from a Simple Double-Surfactant Assembly-Directed Method for Lithium Storage. *ACS Applied Materials & Interfaces* **2016**, *8* (38), 25586–25594. https://doi.org/10.1021/acsami.6b06534.

(44) Liao, J.-Y.; Lei, B.-X.; Kuang, D.-B.; Su, C.-Y. Tri-Functional Hierarchical TiO2 Spheres Consisting of Anatase Nanorods and Nanoparticles for High Efficiency Dye-Sensitized Solar Cells. *Energy & Environmental Science* **2011**, *4* (10), 4079–4085. https://doi.org/10.1039/C1EE01574E.

(45) Liu, H.; Deng, L.; Sun, C.; Li, J.; Zhu, Z. Titanium Dioxide Encapsulation of Supported Ag Nanoparticles on the Porous Silica Bead for Increased Photocatalytic Activity. *Applied Surface Science* **2015**, *326*, 82–90. https://doi.org/https://doi.org/10.1016/j.apsusc.2014.11.110.

(46) Bowker, M.; Nuhu, A.; Soares, J. High Activity Supported Gold Catalysts by Incipient Wetness Impregnation. *Catalysis Today* **2007**, *122* (3), 245–247. https://doi.org/https://doi.org/10.1016/j.cattod.2007.01.021.

(47) Hargittai, M.; Schulz, A.; Réffy, B.; Kolonits, M. Molecular Structure, Bonding, and Jahn−Teller Effect in Gold Chlorides: Quantum Chemical Study of AuCl3, Au2Cl6, AuCl4-, AuCl, and Au2Cl2 and Electron Diffraction Study of Au2Cl6. *Journal of the American Chemical Society* **2001**, *123* (7), 1449–1458. https://doi.org/10.1021/ja003038k.

(48) Carabineiro, S. A. C.; Silva, A. M. T.; Dražić, G.; Tavares, P. B.; Figueiredo, J. L. Effect of Chloride on the Sinterization of Au/CeO2 Catalysts. *Catalysis Today* **2010**, *154* (3), 293–302. https://doi.org/https://doi.org/10.1016/j.cattod.2009.12.017.

(49) Mallat, T.; Baiker, A. Oxidation of Alcohols with Molecular Oxygen on Solid Catalysts. *Chemical Reviews* **2004**, *104* (6), 3037–3058. https://doi.org/10.1021/cr0200116.

(50) Liotta, L. F. Catalytic Oxidation of Volatile Organic Compounds on Supported Noble Metals. *Applied Catalysis B: Environmental* **2010**, *100* (3), 403–412. https://doi.org/https://doi.org/10.1016/j.apcatb.2010.08.023.

(51) Bligaard, T.; Nørskov, J. K.; Dahl, S.; Matthiesen, J.; Christensen, C. H.; Sehested, J. The Brønsted–Evans–Polanyi Relation and the Volcano Curve in Heterogeneous Catalysis. *Journal of Catalysis* **2004**, *224* (1), 206–217. https://doi.org/https://doi.org/10.1016/j.jcat.2004.02.034.

Chapter 5

Improving the Thermal Stability and VOC Oxidation Activity of Ag-TiO_2 Catalysts by Controlling the Catalyst Architecture and Reaction Conditions *

5.1. Introduction

Sustainable technological development has become one of the cornerstones of the 21st century. Sustainability covers three pivotal elements: economic benefit, resource efficiency, environmental protection and social development. A just adaptation of technology can be achieved when all three aspects of sustainability are considered while designing. As such, Chapter 4 delineated a novel catalyst architecture capable of increasing the active metal utilization and oxidizing harmful VOCs at low temperatures in an energy-efficient way. Undoubtedly, platinum encapsulated in TiO_2 was the best performing catalyst among the noble metal catalysts investigated in Chapter 4. However, from a practical standpoint, platinum comes across as an unsustainable choice considering the economic benefit and resource efficiency as it is one of the rarest and most expensive metals in the Earth's crust, with less than a millionth of 1 percent in abundance.

Silver, although is a rare earth metal, is nearly 15 times more abundant than platinum, palladium, or gold. From a cost perception, silver is almost 100 times cheaper than platinum, palladium, or gold. Therefore, from an applications perspective, using silver encapsulated in TiO_2

---

* A version of this chapter has been published in Applied Catalysis B: Environmental journal. https://doi.org/10.1016/j.apcatb.2021.120476

catalysts to achieve low-temperature catalytic oxidation of VOCs is rather an economical, practical and more sustainable option. Considering the amicable performance of silver encapsulated in TiO_2 catalysts for VOC oxidation, this chapter extensively evaluates the influence of encapsulation morphology on the thermal stability, activity, selectivity, and overall efficacy of the catalyst.

To evaluate the effectiveness of the catalyst, two critical parameters are examined in this chapter, which are motivated by the proposed VOC oxidation application space: 1) *thermal aging at elevated temperatures (550 °C)*, which is used to remove carbonaceous deposits or coke from the catalyst surface and 2) *the presence of water vapor*, a common component in many industrial flue gases that can readily affect catalyst performance [1]. Similar to Chapter 4, catalytic oxidation of n-butanol, a common VOC encountered in many industrial processes such as automotive painting, was chosen as the probe reaction to examine VOC abatement efficacy in this chapter.

In recent years, nanoparticle synthesis by the solvothermal method has gained significant interest due to its exceptional ability to control nanoscale structure and particle size [2–8]. Generally, solvothermal synthesis takes place in a pressurized autoclave in the presence of a solvent at a temperature higher than the boiling point of the solvent [8]. By subjecting the Ag-TiO_2 catalysts prepared by our novel surfactant mediated synthesis to a post-synthesis solvothermal treatment, we demonstrate that solvothermal methods can be used to effectively anchor active metal to the support in addition to controlling active metal size, distribution, and support structure. This treatment leads to a catalyst with an improved activity that remains stable after repeated high-temperature (550 °C) aging cycles.

The performance of the encapsulated-solvothermally treated Ag catalyst (Ag-TiO_2 (ES)) was further compared with a catalyst prepared by Ag surface-impregnation on TiO_2 nanospheres

($Ag-TiO_2$ (I)), and also with a catalyst synthesized through the novel encapsulation morphology that was not exposed to a post-synthesis solvothermal treatment ($Ag-TiO_2$ (E)). This comparison provides insight into the role of encapsulation and solvothermal treatment on improved catalyst performance and enhanced stability.

Using a set of comprehensive material characterization techniques, collectively, this chapter demonstrates that the encapsulation strategy coupled with the post-synthesis solvothermal treatment allows us to drastically adjust the strength and abundance of $Ag-TiO_2$ metal-support interactions along with the size of the Ag nanoparticles. We find that this strategy changes reaction mechanisms to improve the selectivity towards desirable byproducts, enhancing the baseline catalytic performance. We also observe a significant improvement in the stability of the catalyst's performance under repeated high-temperature aging with water present in the reaction feed. Ultimately, we delineate a scalable synthesis method that can produce VOC oxidation catalysts with sustainable high catalytic activity.

5.2. Experimental

5.2.1. Materials

The metal precursors silver nitrate ($AgNO_3$, ACS reagent ≥99.0%) and titanium (IV) butoxide (TBOT, 97%) were purchased from Sigma-Aldrich. The surfactants dodecylamine (DDA, 98%) and Pluronic F-127 triblock copolymer (MW = 12600) was procured from ACROS Organics™ and Sigma-Aldrich respectively. All the synthesis were carried out in deionized water and anhydrous ethanol.

5.2.2. Catalyst synthesis

5.2.2.1. Synthesis of Ag encapsulated TiO_2 catalysts

Surfactant directed self-assembly method described in Chapter 4 was used to synthesize the Ag encapsulated TiO_2 catalysts used in this study. In a typical synthesis, 0.34 g of DDA and 0.0086 g of $AgNO_3$ were added to a conical flask filled with 150 mL anhydrous ethanol. The ethanolic solution was placed on a magnetic stirrer. When the solution turned transparent, 0.79 g of Pluronic F-127 triblock copolymer was added to the conical flask. After 1 hour, 7.61 mL of deionized water was added. This step was followed by the dropwise addition of 1.2 mL of TBOT. After the addition of TBOT, the solution was stirred for 90 additional minutes. The white colloidal product obtained during the synthesis was left undisturbed for 12 hours. Upon completion of the synthesis, the encapsulated catalysts were collected by centrifugation, washed three times with ethanol, and dried at 80 °C. The as-prepared catalysts were denoted as encapsulated Ag-TiO_2 or Ag-TiO_2 (E).

A mixture of ethanol and water was used to perform the solvothermal treatment of the catalysts. 1 g of Ag-TiO_2 (E) catalysts prepared by the protocol mentioned above were dispersed in a mixture of ethanol (35 mL) and water (35 mL). The solution was sealed within a Teflon-lined autoclave (90 mL capacity) and heated at 160 °C for 12 hours to complete the solvothermal treatment. Upon completion, the catalysts were collected by centrifugation, washed three times with ethanol and dried at 80 °C. These catalysts were denoted as encapsulated-solvothermally treated Ag-TiO_2 or Ag-TiO_2 (ES).

Post drying, both catalysts, Ag-TiO_2 (E) and Ag-TiO_2 (ES), were calcined at 450 °C for 3 hours in a muffle furnace to remove any residual surfactant. Once treated, all catalysts were subjected to characterization and catalytic experiments.

5.2.2.2. Synthesis of surface impregnated Ag-TiO_2 catalysts

TiO_2 nanospheres were prepared in the same method as mentioned above, however, in the absence of $AgNO_3$. 0.34 g of dodecylamine and 0.79 g of Pluronic F-127 triblock copolymer were added to 150 mL of anhydrous ethanol and placed on a magnetic stirrer. After 1 hour of stirring, 7.61 mL of deionized water was added to the solution, followed by the dropwise addition of 1.2 mL of TBOT. Upon adding TBOT, the solution was further stirred for 90 additional minutes and kept static for 12 hours to allow the TiO_2 nanospheres to form. The resulting solution was further centrifuged, washed in ethanol, and dried at 80 °C. After drying, 1 g of TiO_2 nanospheres were dispersed in a mixture of ethanol (35 mL) and water (35 mL). The solution was sealed within a Teflon-lined autoclave (90 mL capacity) and heated at 160 °C for 12 hours. Finally, the samples were further calcined at 450 °C for 3 hours in a muffle to obtain polycrystalline TiO_2 nanospheres.

The conventionally supported Ag-TiO_2 nanospheres were synthesized by the incipient wetness impregnation method. 0.5 g of previously made TiO_2 nanospheres were dispersed in 90 mL of deionized water under vigorous stirring. 10 mL of 14.6 mM $AgNO_3$ aqueous solution was added to this solution. The mixture was dried in an oven at 110 °C for 6 hours after 12 hours of vigorous stirring, followed by treatment in a muffle furnace at 450 °C for 3 hours. These samples were denoted as impregnated Ag-TiO_2 or Ag-TiO_2 (I). After calcination, the Ag-TiO_2 (I) catalysts were subjected to characterization and catalytic experiments.

5.2.3. *Ex-situ* aging of catalysts in air

Roughly 0.25g of each of the above synthesized three catalyst samples were put into separate ceramic crucibles, placed in a muffle furnace, and subjected to 550 °C aging for 10 hours in air. After that, these catalysts were left to cool in ambient conditions before additional characterization and catalytic experiments.

5.2.4. Catalyst characterization

Characterization of the samples was done using a total of seven different techniques: Thermogravimetric analysis (TGA), Brunauer – Emmett – Teller derived N_2 physisorption surface analysis (BET), Inductively coupled plasma mass spectrometry (ICP-MS), transmission electron microscopy (TEM), X-ray energy dispersive spectroscopy (XEDS), X-ray powder diffraction (XRD), and X-ray photoelectron spectroscopy (XPS).

In-situ thermal decomposition studies were carried out using TGA (TA Instrument Q 500). Roughly 15 mg of catalyst sample was placed in the TGA instrument and heated from 25 °C to 600 °C at a rate of 5 °C /min under the flow of air. The airflow in the TGA system was diluted by balance N_2 gas, lowering the actual O_2 concentration to 16 %. An integrated gas sorption apparatus (Micromeritics ASAP 2020) was used to determine the textural properties of the synthesized catalysts. The catalyst samples were degassed for 24 hours under vacuum at 350 °C, and nitrogen adsorption and desorption experiments were carried out at 77 K. The BET equation in the relative pressure (P/P_0) range from 0.06 to 0.32 was used to calculate the surface area from the isotherm data. The median pore width and the micropore size distribution were obtained from the Horvath-Kawazoe model using slit pore geometry and the BJH adsorption model.

The silver content (wt. %) in the Ag-TiO_2 catalyst samples were determined by a PerkinElmer Nexion 2000 ICP-MS, equipped with Syngistix data analysis software. Roughly 25 mg of Ag-TiO_2 samples were dispersed in 5 mL of deionized water, followed by the addition of 2 mL 48% hydrofluoric acid. This solution was kept undisturbed overnight to digest the Ag-TiO_2 catalyst samples. The solution was neutralized by adding 5 wt% boric acid solution making up to 100 mL in a volumetric flask, which were then analyzed by ICP-MS.

Standard bright field TEM and Selected Area Electron Diffraction (SAED) crystallography analysis were done using a Jeol 2010F Analytical Electron Microscope equipped with a zirconated tungsten (100) thermal field emission tip at 200 kV. High-angle annular dark-field scanning transmission electron microscopy and XEDS mapping of the catalyst sample was carried out using a Talos F200X G2 S/TEM at 200kV.

The XRD patterns of the samples were recorded on a Rigaku 600 Miniflex X-ray diffractometer instrument with Cu Kα radiation (λ=1.5406 Å). The wide-angle 2θ was scanned from 15 to 90° with a step size of 0.01 for all the measurements. Surface elemental analysis was performed using a Kratos Axis Ultra XPS with a monochromatic Al X-ray source operating at 10 mA and 15 kV and 1×10^{-9} torr.

5.2.5. Catalytic activity evaluation

The gaseous feed used for the catalytic tests was composed of 1000 ppmv of n-butanol. The required concentration of n-butanol was generated by bubbling an accurate amount of dry air through a saturator containing n-butanol at room temperature. The outlet flow from the saturator was mixed with a second stream of dry air to obtain 0.1% of n-butanol feed at the reactor inlet.

The catalyst samples were pressed into pellets and sieved to particles between 60 and 80 mesh (180–250 µm). Catalytic reactions were carried out in a tubular quartz tube (ID = 4.0 mm), placed in a vertical electrical furnace equipped with a temperature programmer. A thermocouple was inserted in the reactor, embedded in the catalyst bed, to measure the exact reaction temperature. 50 mg of catalyst diluted with 100 mg of SiO_2 (also sieved to particles between 60−80 mesh) was used for the reaction. The weight-hourly space velocity was estimated as 240,000 mL g^{-1} h^{-1}. Before the catalytic tests, all samples were pretreated at 400 °C, for 1 hour under dry airflow (100 mL/min) with a ramping rate of 5 °C/min to clean the catalyst surface. The reaction products were analyzed by a gas chromatograph (Varian 450-GC). The GC was equipped with a 30 m long VF-5ms GC column (CP8944) and a 100 m long CP-Sil PONA CB column (CP7530). The column oven was maintained at 80 °C and the measurements were taken at 10 °C intervals between 40 °C and 350 °C. Each temperature point was stabilized for 30 min, with effluent gas analysis by downstream GC. It is important to note that n-butanol adsorption was observed when the catalytic test began: the n-butanol amount at the reactor outlet slowly increased until it reached ~ 1000 ppmv. Therefore, the conversion curves presented in this study start when adsorption was no longer visible, that is, at 40 °C. The conversion of n-butanol ($X_{C_4H_{10}O}$) was calculated according to the equation:

$$X_{n-butanol}(\%) = \left[\frac{[C_4H_{10}O]_{in} - [C_4H_{10}O]_{out}}{[C_4H_{10}O]_{in}}\right] \times 100$$

where $[\mathrm{C_4H_{10}O}]_{\mathrm{in}}$ and $[\mathrm{C_4H_{10}O}]_{\mathrm{out}}$ are the n-butanol concentration in the feed gas and the outlet gas, respectively.

5.2.5.1. Arrhenius experiments for evaluation of apparent activation energy

Apparent activation energies for n-butanol conversion using the Ag-TiO$_2$ catalysts were determined from an Arrhenius plot. Data points were collected using the experimental parameters described above with 25 mg of meshed but un-diluted catalyst. Temperatures points used for Arrhenius plotting were kept under 70 °C to ensure that n-butanol conversion was less than 20%. Each temperature point was stabilized for 30 min, with a constant effluent gas analysis by downstream GC. Upon completing the Arrhenius experiment, the fresh Ag-TiO$_2$ catalysts were subjected to ex-situ aging in air (section 5.2.3), followed by an additional Arrhenius experiment. The rate of n-butanol conversion at a given temperature ($r_{n-butanol}$) was calculated by

$$r_{n-butanol} = \frac{[C_4H_{10}O]_{in} \times X_{C_4H_{10}O} \times \mathrm{V}_f}{m_{cat}}$$

where $[\mathrm{C_4H_{10}O}]_{\mathrm{in}}$ is the inlet concentration of n-butanol, $X_{C_4H_{10}O}$ is the n-butanol conversion at the given temperature, V_f is the test gas flow rate, and m_{cat} is the mass of the catalyst.

5.2.5.2. Repeated high-temperature aging of the catalysts

To validate the high-temperature stability of the catalyst samples, a cyclical high-temperature aging protocol was deployed. After collecting a complete light off profile for n-butanol oxidation (section 5.2.5), the reactor was cooled down to 40 °C under airflow (100 mL/min). Then the temperature of the reactor was raised to 550 °C at a rate of 5 °C/min and held for 1.5 hours under airflow (100 mL/min). The purpose of this high-temperature aging was to mimic the conditions used in coke removal processes from deactivated catalysts. The 550 °C treatment step was followed by cooling of the samples to ambient temperature in air. The sequence of these steps is considered as one cycle. To evaluate the durability of the catalysts, five such cycles were carried out.

5.2.5.3. Influence of water vapor on VOC oxidation efficacy

To examine the effect of water vapor on catalytic activity, 3% of water was added to the feed using a syringe pump. Transfer lines were heated at 110 °C to avoid condensation. The total flow rate was kept constant for all experiments at 200 mL/min using mass flow controllers.

5.2.5.4. Saturating catalyst surface with hydroxyl ions

One set of catalytic activity tests was carried out by saturating the catalyst surface with hydroxyl ions to evaluate the influence of these functional groups on VOC oxidation. Before introducing n-butanol, 100 mL/min of air mixed with 3% water vapor was fed to the catalyst bed for 2 hours at room temperature and atmospheric pressure conditions through a syringe pump into the feed line of the reactor. Thereafter, the syringe pump was turned off to suspend the flow of water vapor flow, and the reaction was carried out as mentioned above (section 5.2.5).

5.3. Results and discussion

5.3.1. Catalyst characterization

Representative TEM characterization and accompanying selected-area electron diffraction (SAED) pattern of the Ag-TiO_2 (E) catalysts immediately after synthesis are shown in Figure 5.1. Encapsulated Ag nanoparticles, which are very well dispersed throughout the TiO_2 nanosphere, can be clearly identified. Additionally, the wormhole-like mesopores of the encapsulating TiO_2

are very distinct and visible. The diffused rings observed by the SAED pattern illustrate the amorphous nature of the encapsulated TiO_2 nanosphere right after synthesis.

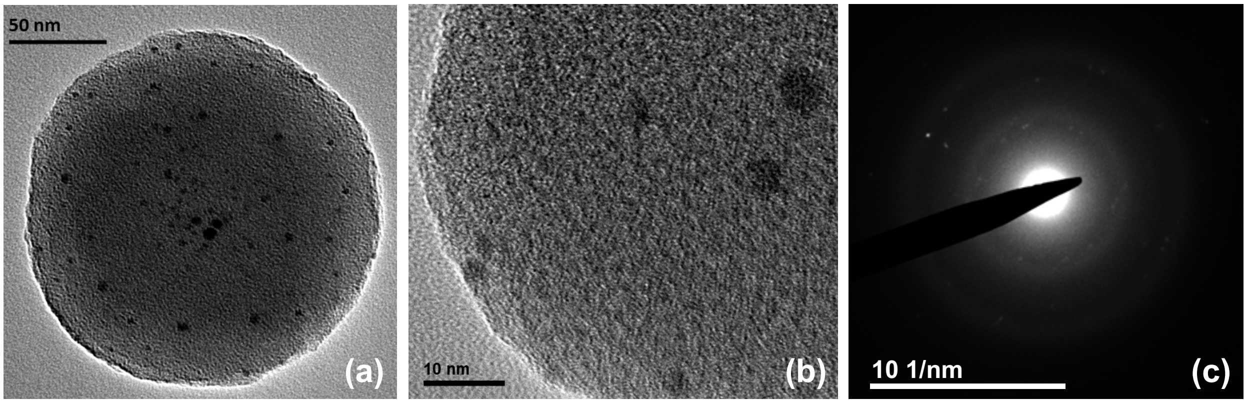

Figure 5.1 *- TEM images of the Ag-TiO_2 (E) catalysts immediately after synthesis (a, b), and corresponding SAED pattern taken from a single TiO_2 nanosphere, revealing the amorphous nature of the support (c).*

Thermal decomposition of the Ag-TiO_2 (E) catalysts prior to calcination and the associated surfactant removal is represented in Figure 5.2. The gradual weight loss between 100 to 450 °C can be attributed to the removal of both surfactants DDA and Pluronic F127. Oxidation of the amorphous precursor with an inorganic/organic hybrid spherical structure can lead to a small incremental weight change at about 420 °C. Therefore, removal of organic surfactants and crystallization of the TiO_2 support can be best achieved by a calcination treatment at 450 °C.

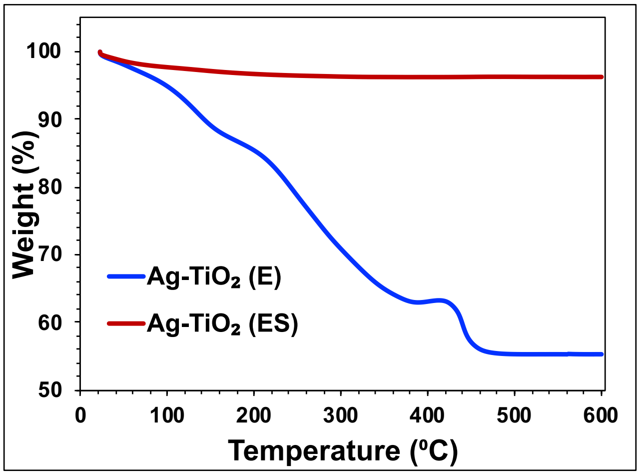

Figure 5.2 *- Thermal decomposition of Ag-TiO_2 (E) and Ag-TiO_2 (ES) catalysts after synthesis.*

Calcining the sample oxidizes the surfactant. Consequently, this exothermic reaction can increase the localized temperature surrounding active metals and result in sintering of the support during the crystallization. This process can lead to the subsequent collapse of the mesopore structure. This could prevent many active sites from participating in the reaction and also negatively affect the reaction due to potential transport limitations [9]. Therefore, as an alternative technique, solvothermal treatment was used to remove the surfactants. Although several aspects of solvothermal reactions are unknown, we hypothesize that the azeotropic mixture of water and ethanol can be very rapidly brought to temperatures above the critical point at which the dissolution of the surfactant takes place instantaneously while facilitating the crystallization of the TiO_2 support and subsequent precipitation of the encapsulated catalyst. Hence, it is believed that this process keeps the interconnected mesoporous network of the TiO_2 support intact while preventing the sintering of the polycrystalline TiO_2 [10]. The weight loss during the thermal decomposition of the catalyst after solvothermal treatment (Ag-TiO_2 (ES)) is shown in Figure 5.2. The absence of significant weight change during the thermal decomposition experiment of the Ag-TiO_2 (ES) sample confirms that the solvothermal process effectively removes the surfactants present.

Figure 5.3 provides representative TEM images and XEDS characterization of the three fresh catalyst morphologies post calcination. In this chapter, the term 'fresh' is used to address the catalysts that have been synthesized and subsequently calcined in air at 450 °C for 3 hours. The term 'aged' catalyst refers to the catalysts exposed to 550 °C for 10 hours in addition to calcining in air at 450 °C for 3 hours.

The conventionally supported Ag-TiO_2 (I) catalysts are comprised of Ag nanoparticles that decorate the surface of TiO_2 nanospheres. Most of the Ag nanoparticles on the TiO_2 surface were in the range of 5-10 nm, as shown in Figure 5.3. The support is made up of numerous packed crystallites of TiO_2 that form a structure on the order of 75-100 nm.

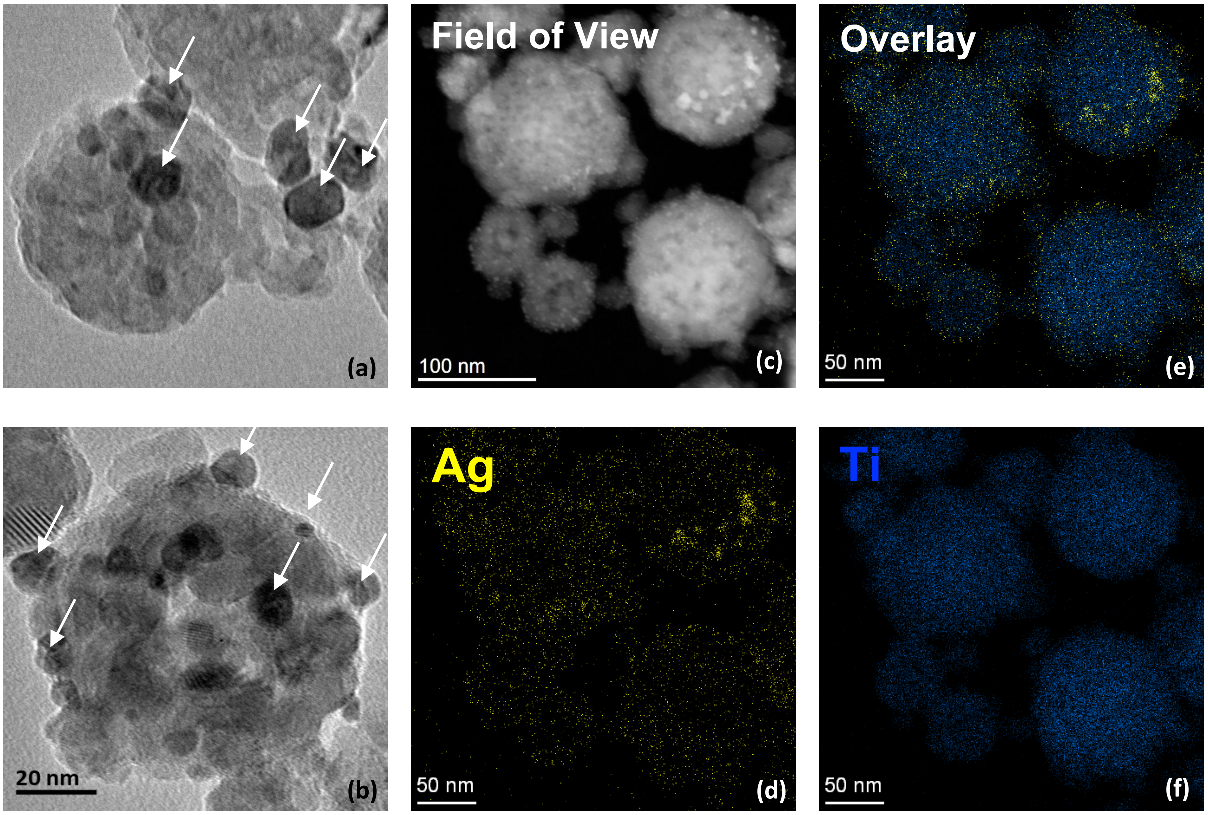

Figure 5.3 *- TEM images of fresh, post calcined 2% wt Ag-*TiO_2 *(I) (a, b); XEDS map of fresh Ag-*TiO_2 *(I) catalyst ((c) - (f)). Field of view used to collect the map and constituent elemental signals (Ag – yellow, Ti – blue). The nanospheres of* TiO_2 *appear on the order of 100 - 150 nm in diameter. Ag nanoparticles on the order of 5-10 nm appear to be dispersed along the surface of the supporting nanospheres.*

While all synthesized catalysts exhibited comparable Ag loading, as determined by ICP-MS (Table 1), encapsulation was found to readily affect the initial size of the active metal clusters. Ag-TiO_2 (E) catalyst consists of Ag nanoparticles, ranging from 2-5 nm in diameter, smaller than those observed on the fresh Ag-TiO_2 (I). Similar to the TiO_2 support in Ag-TiO_2 (I), the encapsulating TiO_2 shell appears to be made up of randomly oriented crystallites, which are packed together to form a nanosphere of 100-150 nm diameter, as seen in Figure 5.4. In contrast to the surface impregnated synthesis, encapsulation helps in obtaining relatively uniform active metal size distribution. Solvothermal treatment, however, resulted in a slight shrinkage of TiO_2 nanospheres (75-100 nm in diameter) and appears to have a reinforcing effect on the randomized packing of the polycrystalline TiO_2 shell without altering the particle size of Ag (Figure 5.5.)

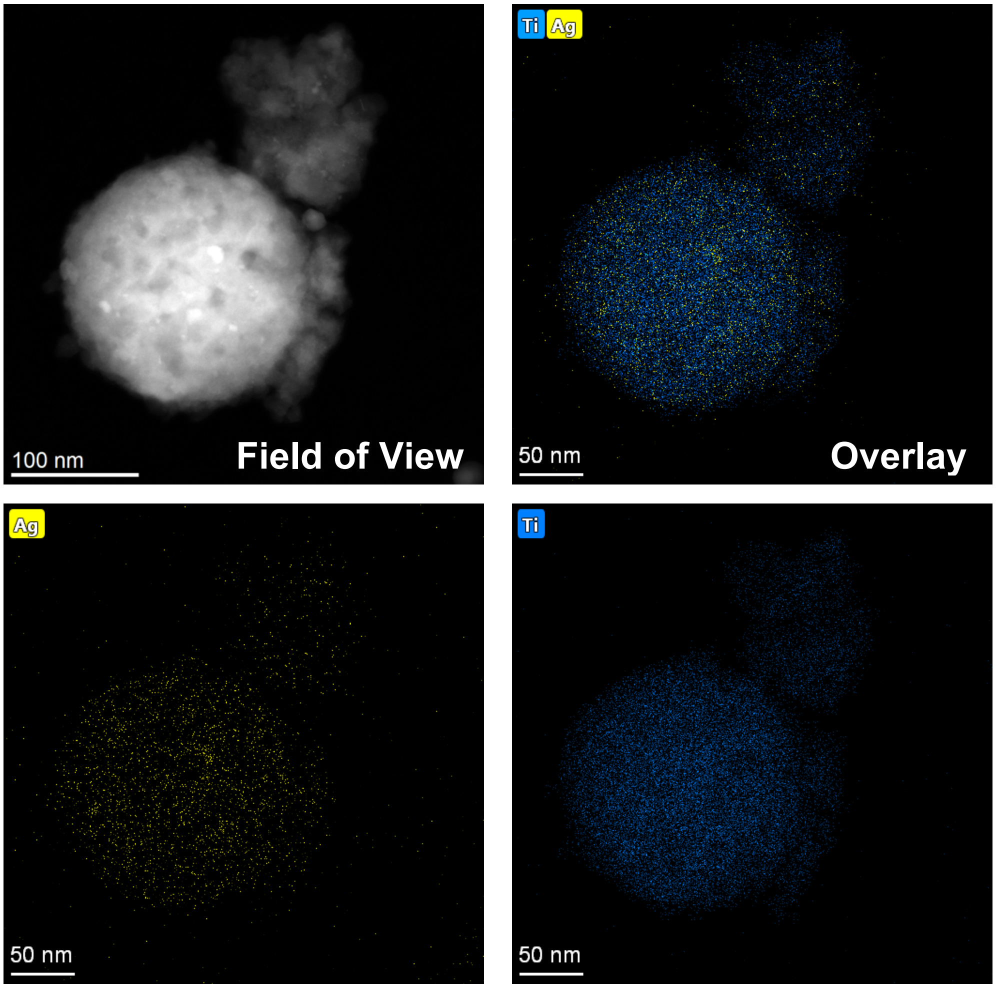

Figure 5.4 *- TEM and XEDS characterization of fresh 2 wt. % Ag-TiO_2 (E) catalyst. Field of view used to collect the map and constituent elemental signals (Ag - yellow, Ti - blue). The nanospheres of TiO_2 appear on the order of 100-150 nm in diameter. Ag nanoparticles on the order of 2-5 nm appear to be dispersed inside the encapsulating TiO_2 nanospheres.*

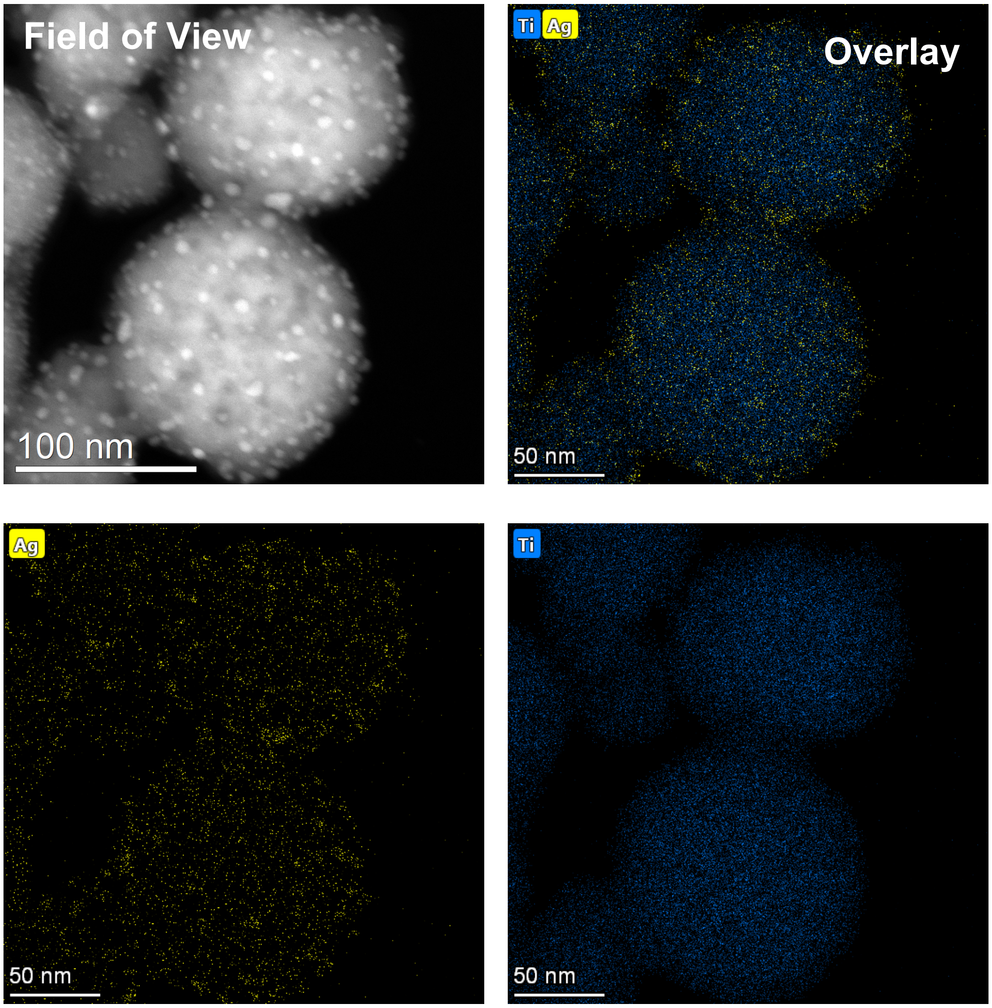

Figure 5.5 *- TEM and XEDS characterization of fresh 2 wt. % Ag-TiO_2 (ES) catalyst. Field of view used to collect the map and constituent elemental signals (Ag - yellow, Ti - blue). The nanospheres of TiO_2 appear on the order of 75-100 nm in diameter. Ag nanoparticles on the order of 2-5 nm appear to be dispersed inside the encapsulating TiO_2 nanospheres.*

The surface areas and average pore size distribution of encapsulated Ag-TiO_2 catalysts are reported in Table 5.1. The average pore size of Ag-TiO_2 (E) is 24.2 nm. Nitrogen adsorption-desorption isotherms shown in Figure 5.6 indicate that Ag-TiO_2 (E) exhibits a type II isotherm. This suggests that the majority of the pores in TiO_2 support are macroporous in nature. As mentioned earlier, calcination of the amorphous catalyst effectively removes the surfactants. However, this process results in collapse and closure of interconnected pores within the encapsulating TiO_2 support. Thus, we see that Ag-TiO_2 (E) has a considerably smaller surface area of 18.68 m^2/g. In contrast, Ag-TiO_2 (I), and Ag-TiO_2 (ES) samples exhibit type IV isotherms with a characteristic hysteresis loop, indicating the existence of mesoporous structures. TiO_2 support in Ag-TiO_2 (I) and Ag-TiO_2 (ES) were both subjected to solvothermal treatment process prior to calcination. As mentioned earlier, this pretreatment using an ethanol and water solution at temperatures higher than the critical point helps in dissolution of surfactant while keeping the interconnected mesoporous network of the TiO_2 intact. Thus, we observe a smaller average pore size and significantly higher surface area (Table 5.1). These observations support that the solvothermal treatment, along with removing the surfactants, assists in the formation of interpenetrating nanocrystals of TiO_2 arranged to obtain a large number of mesopores that interconnect instead of mesopores that combine during dry thermal treatment to form macropores.

Table 5.1 *- Summary of surface area, average pore size, and average crystallite size of TiO_2 support.*

	Ag loading (wt. %)	**BET S.A (m^2/g)**		**Avg. pore size (nm)**		**Avg. TiO_2 crystallite size (nm)**	
Sample	–	Fresh	Aged	Fresh	Aged	Fresh	Aged
Ag-TiO_2 (ES)	1.87	111.5	97.6	6.9	9.1	11.3	14.4
Ag-TiO_2 (E)	1.94	18.68	8.1	24.2	39.6	13.3	27.5
Ag-TiO_2 (I)	2.06	93.6	33.5	6.9	16.1	19.1	23.1

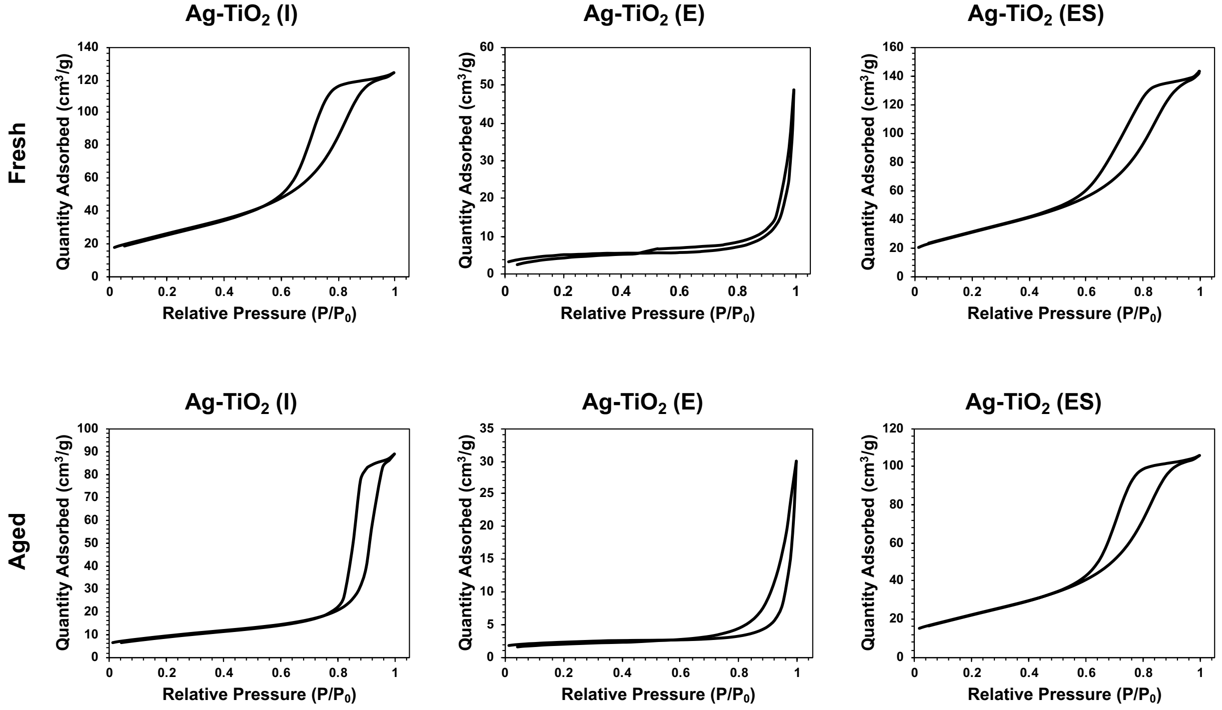

Figure 5.6 *- Nitrogen adsorption and desorption isotherms of fresh and aged Ag-TiO₂ catalysts.*

The polycrystalline nature of the TiO_2 support is visible in all three catalyst samples in Figure 5.7. After calcination, TiO_2 exists in its anatase phase with strong expressions of the {101} facet, as confirmed by XRD analysis. The XRD patterns of fresh TiO_2 nanospheres, Ag-TiO_2 (ES), Ag-TiO_2 (E), and Ag-TiO_2 (I) post calcination are shown in Figure 5.8 (a). All samples displayed similar characteristic diffraction peaks corresponding to the anatase structure of titanium dioxide (JCPDS card no. 21-1272). Furthermore, no distinct characteristic Ag diffraction peaks were observed in any of the fresh catalysts due to the low Ag loading, relatively small nanoparticle size, and high dispersion, as seen in the TEM images. The average TiO_2 crystallite sizes in all three catalyst samples calculated by the Debye-Scherrer equation are reported in Table 1.

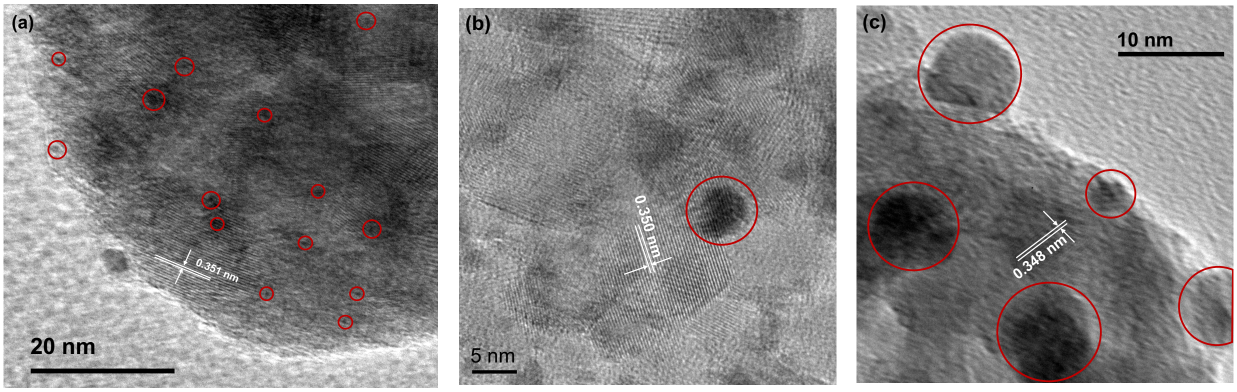

__Figure 5.7__ - HRTEM image of the three different catalyst morphologies (Ag-TiO$_2$ (ES) (a), Ag-TiO$_2$ (E) (b), and Ag-TiO$_2$ (I) (c)) indicating the polycrystalline nature of TiO$_2$ support. The dark contrast areas highlighted by the red circles indicate the Ag nanoparticles.

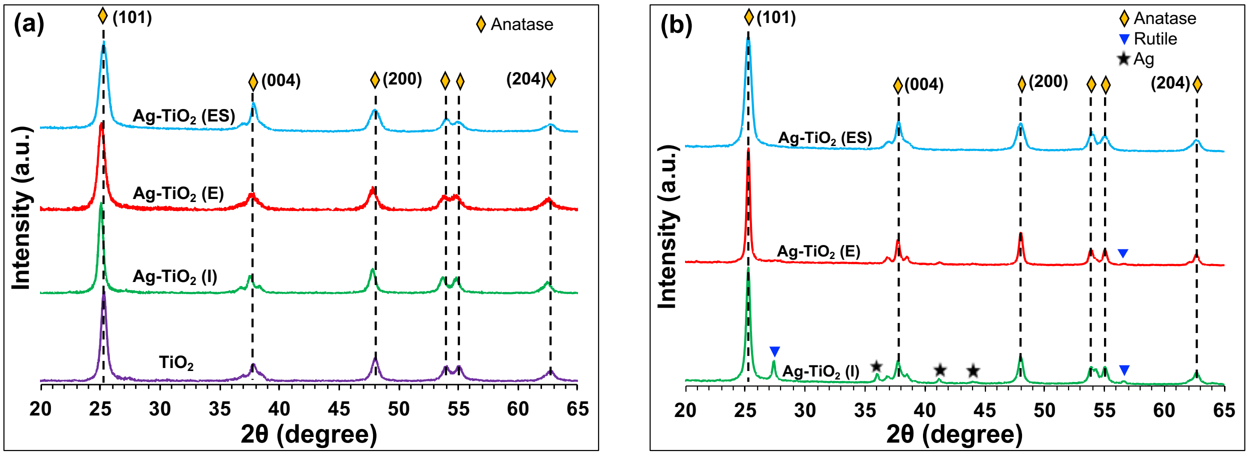

__Figure 5.8__ - XRD patterns of the fresh Ag-TiO$_2$ (a) and aged Ag-TiO$_2$ (b) catalyst samples. Patterns have been normalized to their respective background signal.

As TEM and XEDS analyses examine morphology in a more localized region, x-ray photoelectron spectroscopy (XPS) analysis of the samples was conducted to probe the surface of the sample better and to demonstrate silver encapsulation in the bulk of the sample. The normalized high-resolution XPS spectra of the characteristic Ag 3d region of the three Ag-TiO$_2$ catalyst morphologies are shown in Figure 5.9 (a) - (c). The low signal of Ag with respect to the background in Figure 5.9 (b) and (c) indicates an encapsulation of Ag by TiO$_2$ nanospheres in Ag-TiO$_2$ (E) and Ag-TiO$_2$ (ES) catalysts. In contrast, Ag-TiO$_2$ (I) exhibits much more intense characteristic Ag peaks relative to the background (Figure 5.9 (a)), which confirms that most Ag nanoparticles are retained on the surface of the nanospheres post impregnation.

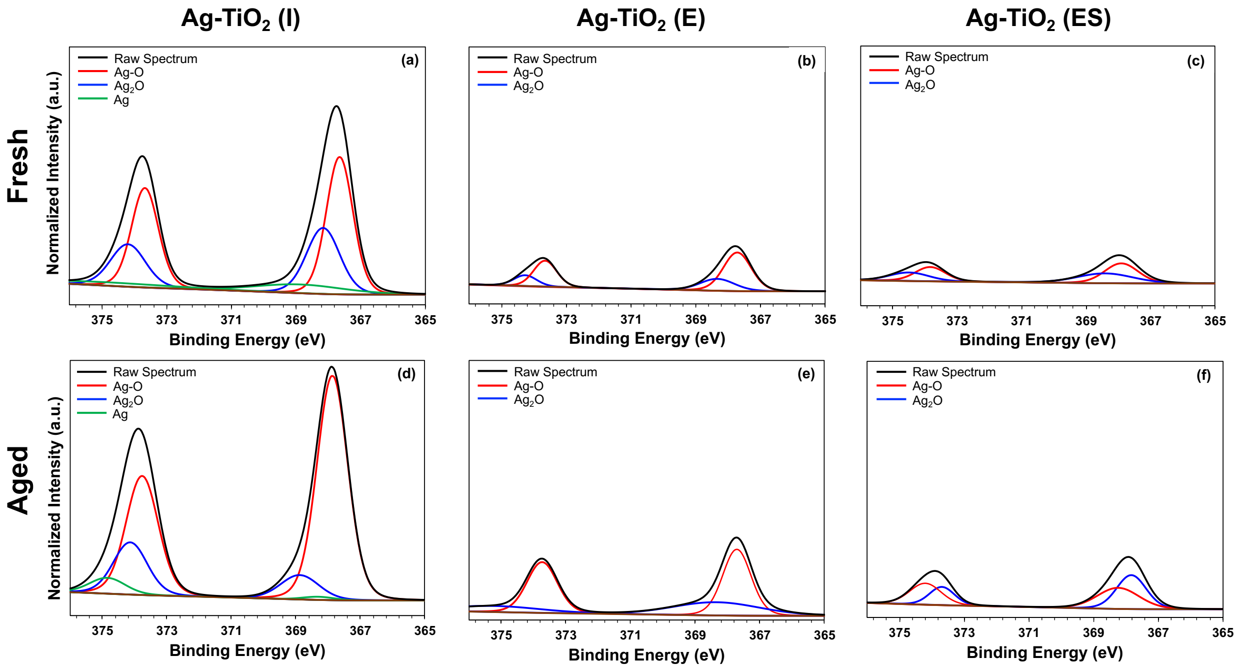

Figure 5.9 *- Normalized and deconvoluted XPS spectra in the Ag 3d scan region for fresh Ag-*TiO_2 *(a - c), and aged Ag-*TiO_2 *(d - f) catalysts.*

The binding energy of Ag ($3d_{5/2}$) is known to be 368.3 eV [11]. However, we observed a slight shift towards a lower value (367.8 eV) in all three catalyst samples. This negative shift in the binding energy of oxidized Ag compounds could have been caused due to extra-atomic relaxation and lattice potential effects. The charge "relaxation" or "dynamic screening" that occurs during the creation of photoelectrons can result in the manifestation of such shifts. This behavior overcompensates the dominant electrostatic initial state effect caused by the high electronegativity of the oxygen atom. These shifts are in agreement with earlier reports in the literature indicating the formation of oxidized Ag species [12–14]. Upon deconvoluting the peaks, we see that Ag-TiO_2 (E) and Ag-TiO_2 (ES) samples predominantly have Ag-O species and trace amounts of Ag_2O.

Although we observed similar trends in the characteristic Ag peaks in Ag-TiO_2 (I) samples, we also see trace amounts of elemental Ag.

The similarity between the TiO_2 nanosphere support morphologies in the three different catalyst systems allows us to more readily compare how encapsulation and solvothermal treatments affect the long-term stability of the catalysts.

5.3.2. Catalytic performance of the fresh catalysts

The oxidation of n-butanol was used to evaluate the catalytic activities of the samples, and the conversion values of n-butanol at different temperatures are shown in Figure 5.10. In general, the conversion began at ~ 90 °C for all the samples. Both encapsulated catalytic systems (Ag-TiO_2 (ES) and Ag-TiO_2 (E)) exhibited better catalytic activity than the conventionally supported Ag-TiO_2 (I) samples.

Fresh Ag-TiO_2 (ES) catalysts exhibited the best catalytic activity amongst all three catalytic systems, as evidenced by their having the lowest temperature required to reach 90% conversion of n-butanol (T_{90} ~ 200 °C), followed by Ag-TiO_2 (E), which exhibited a T_{90} ~ 210 °C. In comparison, the fresh surface impregnated Ag-TiO_2 (I) catalyst exhibited a higher T_{90} of ~ 220 °C. As confirmed by TEM characterization, encapsulating Ag in TiO_2 nanospheres effectively reduces the particle size and facilitates a fairly uniform size distribution of the Ag nanoparticles. This increases the number of active sites available for oxidation, thereby decreasing T_{90}. Additionally, encapsulation provides a three-dimensional interfacial contact between the Ag nanostructures and TiO_2, which maximizes the abundance of metal–support interactions and increases the number of sites that form Ag-TiO_2 interfaces, which are known to favor VOC oxidation due to the reducible nature of the TiO_2 support [15–18].

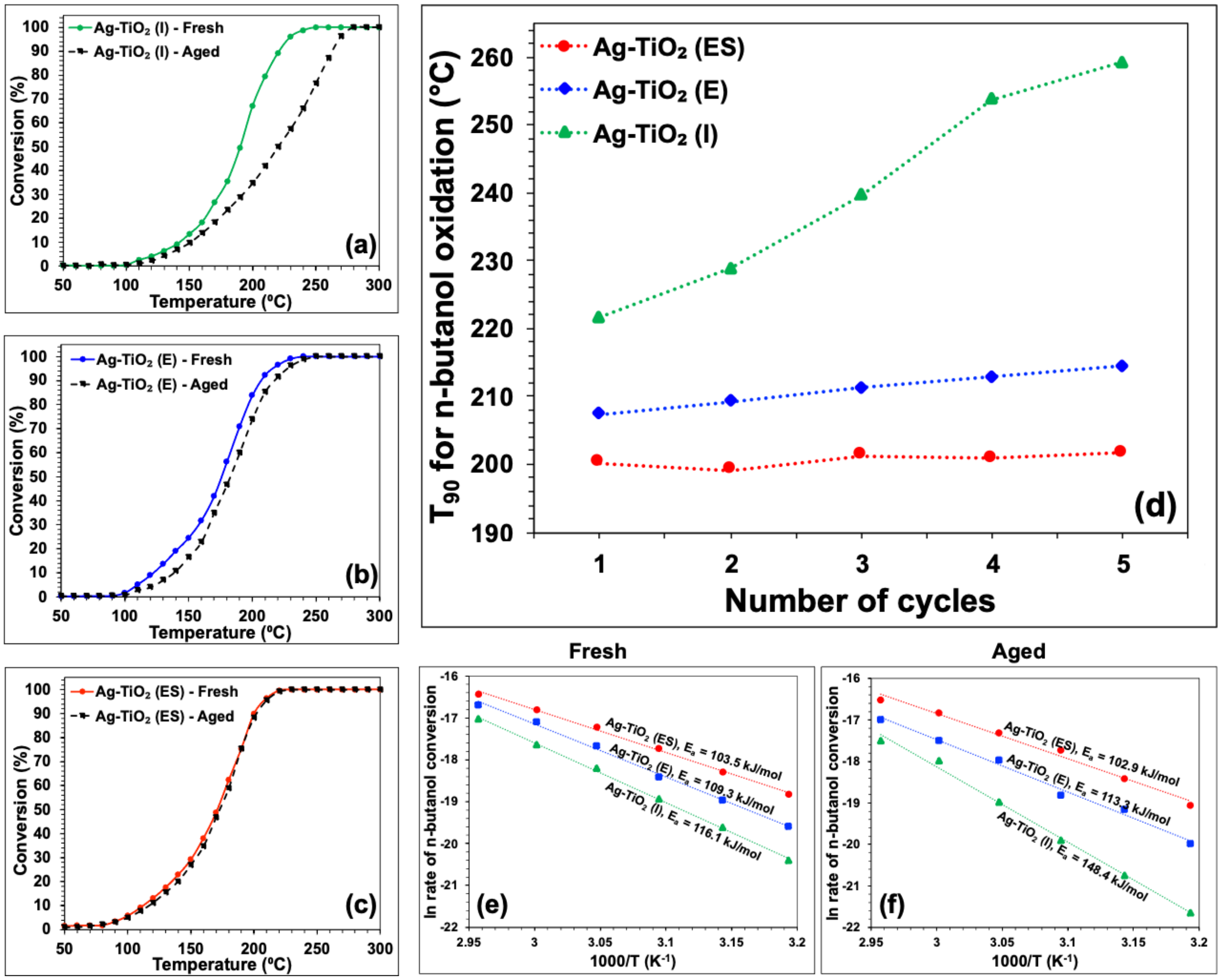

Figure 5.10 *- n-butanol oxidation profiles for fresh and ex-situ aged Ag-TiO_2 (I) (a), Ag-TiO_2 (E) (b), Ag-TiO_2 (ES) (c) catalysts, T_{90} of Ag-TiO_2 catalysts as a function aging cycle (d), and Arrhenius plots for fresh and ex-situ aged Ag-TiO_2 catalysts (e) and (f).*

The total conversion and the selectivity toward each reaction's various by-products as a function of temperature are shown in Figure 5.11. The reaction products detected for the oxidation of n-butanol were butene, isobutane, propane, carbon dioxide, and water. In encapsulated catalytic systems, at low temperatures (< 150 °C) where the overall conversion was low, the reaction was more selective towards the dehydration of n-butanol, producing butene and water. As the reaction temperature increased, a concurrent growth in the percent yield of butene and CO_2 was observed. When reactor temperatures reached ~ 200 °C and 220 °C for the Ag-TiO_2 (ES) and Ag-TiO_2 (E), respectively, the percent yield of butene decreased as the yield of CO_2 continued to grow. At temperatures between 220 - 260 °C, small amounts of propanol and isobutane were formed, possibly by the isomerization and alkylation of butene [19].

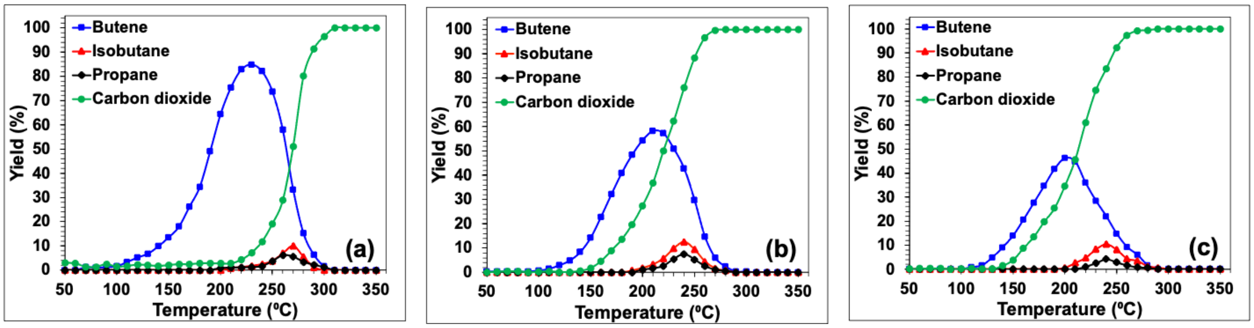

Figure 5.11 *- Products obtained during the n-butanol oxidation reaction over fresh Ag-TiO_2 (I) (a), Ag-TiO_2 (E) (b), and Ag-TiO_2 (ES) (c) catalysts under dry reaction conditions.*

During the catalytic reaction over Ag-TiO_2 (I), we observed a substantial increase in the selectivity towards butene (up to 80%) at temperatures up to 200 °C. In contrast to the encapsulated catalysts, which exhibited the concurrent formation of butene and CO_2, the Ag-TiO_2 (I) did not begin to form CO_2 until it had reached its maximum butene yield. As the reaction temperature increased, the selectivity then shifted towards CO_2 and away from butene. This appreciable offset in the temperature-dependent yield of CO_2 suggests that the differences in initial catalyst morphology have directly affected the way temperature influences the reaction pathways for n-butanol oxidation and subsequently the by-product distribution.

While further study is warranted, it appears that the dissimilarity between the product formation during the oxidation of n-butanol is due to variations in the dominant reaction mechanisms that occur over these two distinct catalyst morphologies. Figure 5.12 illustrates the dominant reaction mechanisms and the hypothetical reaction pathways for n-butanol oxidation over the surface impregnated Ag-TiO_2 catalyst and encapsulated Ag-TiO_2 catalysts.

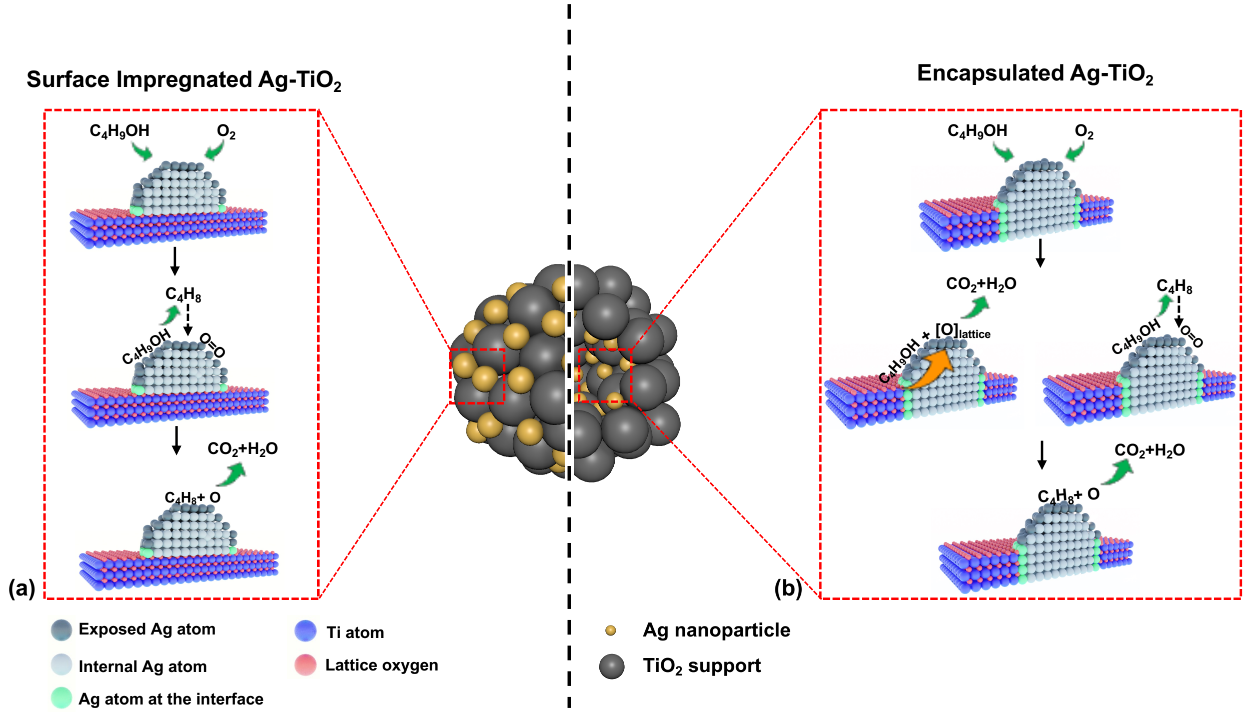

***Figure 5.12** - Schematic representation of complete oxidation of n-butanol oxidation, through Langmuir-Hinshelwood catalytic mechanism over surface impregnated Ag-TiO_2 catalysts (a), and interface-mediated Mars van Krevelen catalytic mechanism over encapsulated Ag-TiO_2 catalysts (b).*

It is possible that on the surface of the impregnated catalyst, the reaction mostly proceeds through a Langmuir–Hinshelwood mechanism. Here, both reactants, n-butanol and oxygen must adsorb on the Ag nanoclusters, and the diatomic oxygen bond needs to be cleaved for the oxidation reaction to proceed [20]. Therefore, at lower reaction temperatures, where the dissociative adsorption of gas-phase oxygen is less likely, the decomposition pathway can favor dehydration, which would produce butene from n-butanol. Similar mechanisms have been proposed for VOC oxidation on surface impregnated catalysts [21–25]. As the reaction temperature increases, butene readsorbs on the surface of Ag nanoclusters, concurrent with the dissociative adsorption of diatomic oxygen and the observation of complete oxidation of n-butanol to CO_2 and H_2O. Contrary to this, in encapsulated catalysts, due to the enhanced metal-support interaction that increases the proximity of lattice oxygen to silver nanoparticles, lattice oxygen from the TiO_2 support can more readily participate in the oxidation reaction through a Mars-van Krevelen (MvK) oxidation mechanism, which favors the formation of CO_2 at relatively lower temperatures [26].

The appreciable variance in the temperature required to achieve complete oxidation of n-butanol to CO_2 with 100% selectivity for the Ag-TiO_2 (ES) (270 °C), Ag-TiO_2 (E) (280 °C), and Ag-TiO_2 (I) (310 °C) catalysts emphasizes the role that catalyst morphology plays in directing reaction pathways and overall catalytic performance.

5.3.3. Effect of thermal aging on catalyst morphology and activity

In industrial applications, promising catalytic materials should have not only high catalytic activity but also exhibit excellent stability and durability. In most applications, coke or carbonaceous deposits that accumulate on the catalysts are removed by regenerating the catalyst at high temperatures (400 - 600 °C) under surplus oxygen [27,28]. However, these conditions may lead to thermal sintering of active metal, thereby decreasing the catalyst activity during its prolonged usage [29]. As such, the three Ag-TiO_2 catalysts were aged at 550 °C for 10 hours to examine how the initial morphology can be used to offset the effects of thermal sintering.

Aging Ag-TiO_2 (I) catalysts resulted in substantial changes in the active site and support morphology, along with appreciable differences in catalytic behavior. Figure 5.13 shows significant agglomeration of the initially dispersed Ag nanoclusters. We observed that Ag particles grew as much as four times from 5-10 nm to 40-50 nm in diameter.

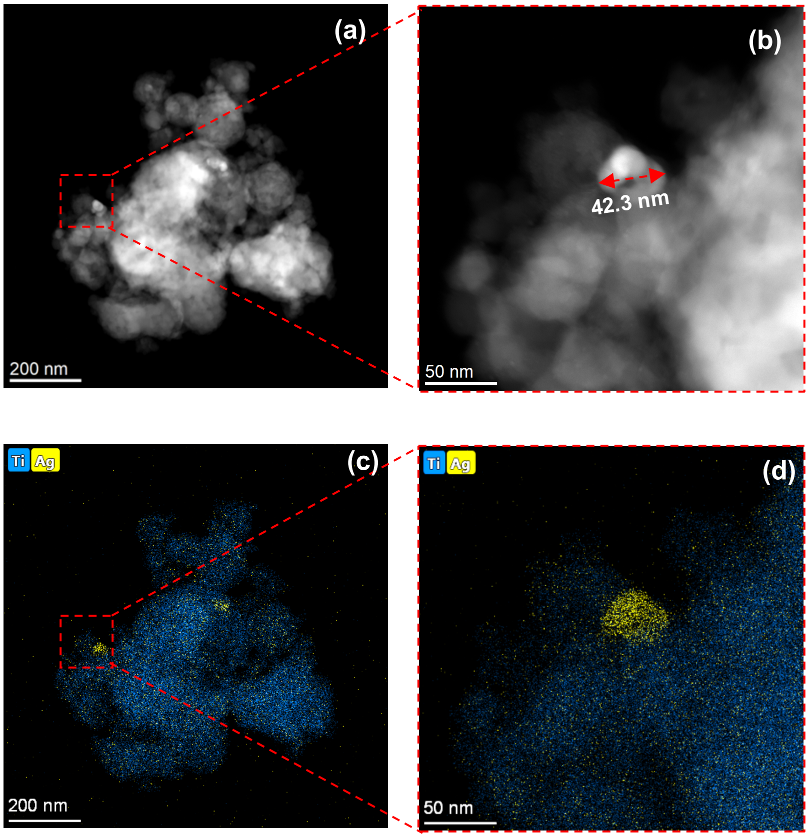

Figure 5.13 *- STEM and XEDS images of Ag-TiO_2 (I) catalyst subjected to ex-situ high-temperature aging (550 °C for 10 hours). TiO_2 support and the active metal (Ag) both agglomerate when the catalyst is subjected to high-temperature aging (550 °C for 10 hours). The magnified image (b) of the highlighted area in (a) is shown to demonstrate the sintering of Ag as a result of aging. Images (c) and (d) represent the corresponding XEDS maps.*

The concurrent increase in the Ag signal intensity, relative to the background, depicted in the XPS spectra of Ag-TiO_2 (I) samples after aging indicates the occurrence of agglomeration in the bulk of the sample (Figure 5.9 (d)). Furthermore, the appearance of bulk Ag and rutile TiO_2 peaks in the corresponding XRD patterns (Figure 5.8 (b)), which were absent in the patterns of the fresh Ag-TiO_2 (I) catalyst, confirm the substantial active metal sintering and changes in the support morphology that result from aging at 550 °C. Presence of distorted octahedral units in the anatase phase of TiO_2 is known to have a high degree of lattice oxygen anion (O^{2-}) displacement. As a result, the lattice oxygen in the anatase phase is more readily accessible to gas phase components, making it more active than the rutile phase [30,31]. Consequently, the complete oxidation of n-butanol over the Ag-TiO_2 (I) catalyst shifted to higher temperatures, accompanied by a T_{90} that increased by nearly 50 °C (Figure 5.10 (a)) to a value of 270 °C. All these changes conclusively state that the surface impregnated Ag-TiO_2 (I) morphology is prone to active metal sintering and support phase changes at elevated temperatures, which readily impedes VOC oxidation efficacy over time.

In contrast, encapsulating the Ag nanoparticles by TiO_2 nanospheres impeded active metal sintering at high temperatures. In Ag-TiO_2 (E) catalysts, high dispersion and relatively uniform size distribution of Ag nanoparticles remained largely unaltered (Figure 5.14 (a) and (b)). A small growth in the photoelectron signal intensity with characteristic Ag 3d binding energies was also detected (Figure 5.9 (b) and (c)). Although further study is warranted, we believe that this could be due to the further increased dispersion or migration of Ag towards the outer perimeter of the TiO_2 encapsulation due to *ex-situ* aging. Evidence of this increased dispersion can be observed by TEM analysis (Figure 5.14 (b)). While the XPS and TEM characterization suggest that a high dispersion of Ag may remain after aging, we observed that a near 10 °C increase in the temperature required to achieve 90% conversion of n-butanol (Figure 5.10 (b)). This increase in T_{90} can be attributed to the growth of TiO_2 crystallites, as their average size nearly doubled from 13.3 nm to 27.5 nm, as confirmed by XRD analysis. As the crystallites grew, we observed a significant decrease in the BET surface area and the average pore diameter of the catalyst (Table 5.1). As such, the thermally induced restructuring of the TiO_2 support adversely affects the internal pore structure of the catalyst. This restructuring may prevent active sites from participating in the oxidation reaction, resulting in an increased T_{90}. Many researchers have shown similar behaviors in encapsulated catalyst morphologies where the agglomeration of active metal was prevented, but the support's average crystallite size grew [32–35].

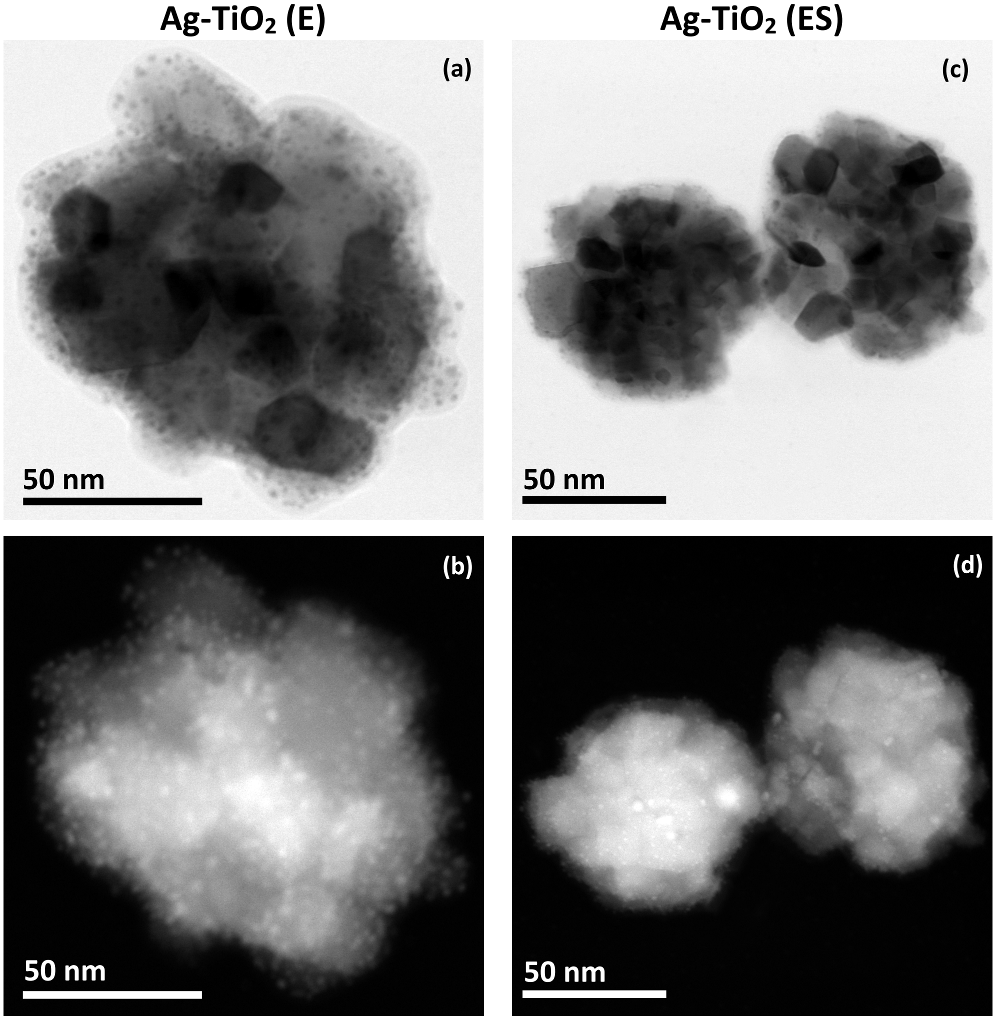

Figure 5.14 *- Bright field and High-angle annular dark-field (HAADF) images of Ag-TiO_2 (E) (a, b) and Ag-TiO_2 (ES) (c, d) catalysts subjected to ex-situ high-temperature aging (550 °C for 10 hours). The bright white dots dispersed throughout the TiO_2 nanosphere correspond to encapsulated Ag nanoparticles.*

While encapsulation alone improved thermal stability, high-temperature *ex-situ* aging had little to no effect on the Ag-TiO_2 (ES) catalysts. The Ag nanoparticles remained in the 2-5 nm diameter range, matching the fresh Ag-TiO_2 (ES) catalysts (Figure 5.14 (c) and (d)). Furthermore, unlike the Ag-TiO_2 (E) and Ag-TiO_2 (I) catalysts, the average size of the TiO_2 support crystallites increased only slightly from 11.3 nm to 14.4 nm after aging, indicating a higher thermal stability of the support. The high temperatures used in solvothermal syntheses can significantly promote the reconstruction of metal nanocrystals resulting in a thermodynamically favored product [36].

Additionally, the pore size and the BET surface area of Ag-TiO_2 (ES) catalysts remained largely unaltered after aging. The retention of the porosity and uniform, highly dispersed Ag species in Ag-TiO_2 (ES) suggests that the mesoporous structure of solvothermally-treated TiO_2 supports facilitates facile reactant access to the active sites and impedes active metal sintering [36,37]. Moreover, first-principles studies have previously demonstrated that the grain boundaries and step sites of anatase TiO_2 with {101} facets have excellent affinity for trapping noble metals [38–40]. The excelling packing of TiO_2 support through solvothermal treatment and the high occurrence of {101} faceted TiO_2 crystallites in Ag-TiO_2 (ES), as evidenced by XRD analysis, work simultaneously to effectively anchor the Ag nanoparticles within the encapsulating TiO_2 shell, which enhances their stability at high temperatures.

It is interesting to note that both encapsulated catalyst systems showed no evidence of TiO_2 phase transformation from anatase to rutile due to aging. It has been previously demonstrated that the presence of Ag^0 in a TiO_2 matrix accelerates the phase transformation process in TiO_2 from anatase to rutile [41]. Deconvolution of the XPS spectra shows no evidence of Ag^0 being present in both fresh and aged encapsulated catalysts. Furthermore, the steric hindrance effect produced by the high dispersion of Ag nanoparticles in the encapsulating TiO_2 support may have also contributed to inhibiting the phase transition [42]. Overall, these observations demonstrate the outstanding resistance the Ag-TiO_2 (ES) catalysts have to thermal sintering. This is ultimately demonstrated by the n-butanol oxidation data shown in Figure 5.10 (c), where we observe an identical light-off profile and T_{90} for both fresh and aged Ag-TiO_2 (ES) catalysts.

Figure 5.10 (d) shows the T_{90} of Ag-TiO_2 catalysts after five 550 °C aging cycles. The encapsulated catalysts, Ag-TiO_2 (E) and Ag-TiO_2 (ES), exhibited excellent stability throughout five aging cycles. However, similar to *ex-situ* aging in the muffle furnace, Ag-TiO_2 (I) catalysts suffered from significant Ag sintering resulting in an increased T_{90} after each cycle, raising the T_{90} for n-butanol conversion from 220 °C to 260 °C over the five cycles.

Table 5.2 *- Summary of activation energy and turnover frequency for n-butanol oxidation of fresh and aged Ag-TiO_2 catalysts.*

	Activation energy (kJ/mol)		**Turnover frequency for n-butanol conversion at 90 °C* (s^{-1}) x 10^{-4}**	
Sample	Fresh	Aged	Fresh	Aged
Ag-TiO_2 (ES)	103.5	102.9	5.35	5.24
Ag-TiO_2 (E)	109.3	113.2	0.54	0.47
Ag-TiO_2 (I)	116.1	148.4	0.23	0.09

*Turnover frequency has been normalized by the mmol of Ag present in the catalyst used

Arrhenius experiments were conducted on the fresh and aged catalysts to investigate if changes in the catalyst morphology and average active metal particle size of the active metal influenced the intrinsic catalytic activity (see Figure 5.10 (e) and (f) and Table 5.2). The apparent activation energy of the encapsulated catalysts remained mostly unchanged after aging. In contrast, the Ag-TiO_2 (I) catalyst exhibited a 32.3 kJ/mol increase in apparent activation energy. Furthermore, we examined the turnover frequency (TOF) of n-butanol decomposition before and after aging (Table 5.2). We determined the rate of n-butanol decomposition at a conversion < 10% (90 °C) to ensure a purely kinetic regime and normalized the rate by the Ag content present in the catalysts. The TOF of Ag-TiO_2 (I) decreased from 2.22 x 10^{-5} s^{-1} to 9.90 10^{-6} s^{-1} after aging at 550 °C. In contrast, the TOF for the Ag-TiO_2 (E) and Ag-TiO_2 (ES) remained relatively stable. These results further reiterate the role of encapsulating active metal species in maintaining the activity of the catalyst under high-temperature aging conditions.

5.3.4. Influence of water on oxidation efficacy

In most practical scenarios, water is often present in the flue gases emitted from various industries and is also a product of VOC catalytic oxidation [24]. In general, low relative humidity in the gaseous stream increases the generation of ·OH radicals and hydrogen atoms, facilitating better oxygen transfer [43]. However, as the relative humidity of the reaction environment further increases, water coverage on the catalyst surface grows, which decreases the number of active sites available for adsorbing n-butanol and oxygen molecules. This competitive adsorption of water decreases the overall reaction efficiency. Additionally, side reactions facilitated by the presence of water vapor, such as dihydroxylation and hydration, can also affect the product formation. Therefore, understanding the role of water in the catalytic oxidation of n-butanol helps refine the reaction engineering of industrial VOC oxidation processes. The oxidation of n-butanol in the presence of 3% water vapor is shown in Figure 5.15. In all three catalytic systems, the competitive adsorption between water and n-butanol increased the T_{90}. Ag-TiO_2 (I) catalysts showed the most significant increase in the T_{90} among the tested samples. Conversion of n-butanol began at ~ 180 °C. As confirmed by TEM analysis, the size of the active metal nanoclusters is much larger in Ag-TiO_2 (I) when compared to the encapsulated catalysts. This results in a reduced availability of sites that can adsorb reactants and subsequently carry out the reactions. This decrease in available sites amplifies the detrimental effects of water-facilitated, competitive adsorption, significantly increases the T_{90} by nearly 50 °C compared to when the same reaction was run under dry conditions.

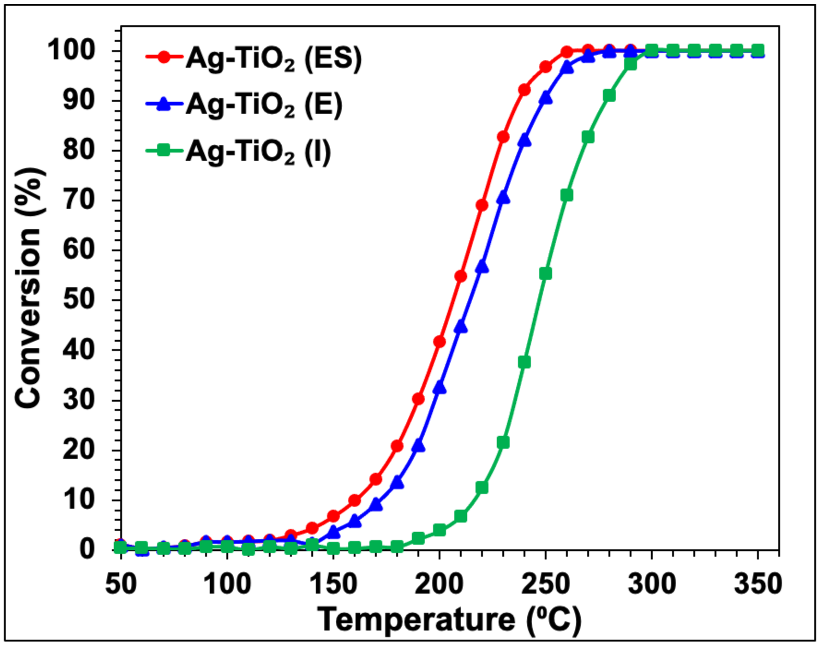

Figure 5.15 *- n-butanol oxidation profiles for fresh Ag-TiO_2 (I), Ag-TiO_2 (E), and Ag-TiO_2 (ES) catalysts in the presence of 3% water vapor in the reaction feed.*

At reaction temperatures lower than 200 °C, selectivity towards butene was higher (Figure 5.16). However, unlike dry oxidation of n-butanol, we observed CO_2 being formed at relatively lower temperatures (210 °C), well before the butene yield reached its maximum. This can be attributed to steam reforming [44]. As the reaction temperature crossed 250 °C, butene formation started to drop while the selectivity towards CO_2 increased. Furthermore, between 230 °C to 310 °C, we observed small amounts of butanone along with isobutane and propane. Overall, complete oxidation of n-butanol to CO_2 with 100% selectivity was achieved at 330 °C.

In contrast, it appeared that encapsulating the Ag provided some stability against the detrimental effects of water vapor in the gas feed. The encapsulated catalysts, Ag-TiO_2 (E) and

Ag-TiO$_2$ (ES), exhibited a less profound increase in the T$_{90}$ in the presence of water (~ 40 °C) than the surface impregnated catalysts. In addition to changes in the T$_{90}$ for n-butanol oxidation, we also observed changes in the selectivity-temperature relationship when water was present in the feed. For encapsulated catalysts, Ag-TiO$_2$ (E) and Ag-TiO$_2$ (ES), n-butanol conversion began at ~ 140 °C. Total conversion together with selectivity towards each reaction pathway at a given temperature is shown in Figure 5.16.

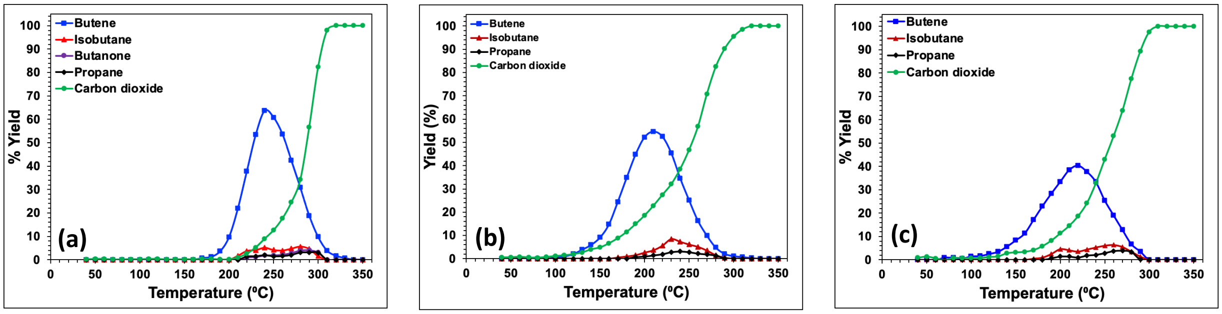

Figure 5.16 *- Products obtained during the n-butanol oxidation reaction over fresh Ag-TiO$_2$ (I) (a), Ag-TiO$_2$ (E) (b), and Ag-TiO$_2$ (ES) (c) catalysts in the presence of 3% water vapor in the reaction feed.*

Compared to dry oxidation, the presence of water vapor in the feed stream had no significant effect on the percentage yield or the number of products formed except for their delay in formation. Due to the competitive adsorption between n-butanol, oxygen, and water over active sites, at temperatures below 200 °C dehydration of n-butanol was dominant, producing butene and water. As the reaction temperature increases, the adsorptive lifetime of water molecules becomes significantly shorter. Thus, as the reaction temperature rose above 230 °C, selectivity towards butene started to drop as the yield of CO$_2$ began to grow. Similar to dry oxidation results, between 220 °C – 300 °C, small amounts of isobutane and propane were formed. In the presence of water vapor, we saw that the temperature required to achieve complete conversion of n-butanol to carbon dioxide with 100% selectivity was increased by nearly 30 °C, from 270 °C to 300 °C on Ag-TiO_2 (ES) and 280°C to 310 °C on Ag-TiO_2 (E).

5.3.5. Effect of saturating the catalyst surface with hydroxyl ions

While the constant co-feeding of water vapor detrimentally affected the product distribution and the overall conversion of n-butanol on Ag-TiO_2 catalysts, water vapor is an unavoidable component in many industrial effluent gas streams. As such, we sought to investigate means of changing the way we expose the catalyst to water in order to improve, instead of hinder, catalytic activity. Previous studies have demonstrated that the hydrophilicity and amphotericity of polycrystalline TiO_2 supports facilitate strong water adsorption, which can be used to improve catalytic activity [45,46]. Consequently, we investigated saturating the catalyst with water vapor before the reaction to increase the abundance of water molecules adsorbed to the surface of the TiO_2 support.

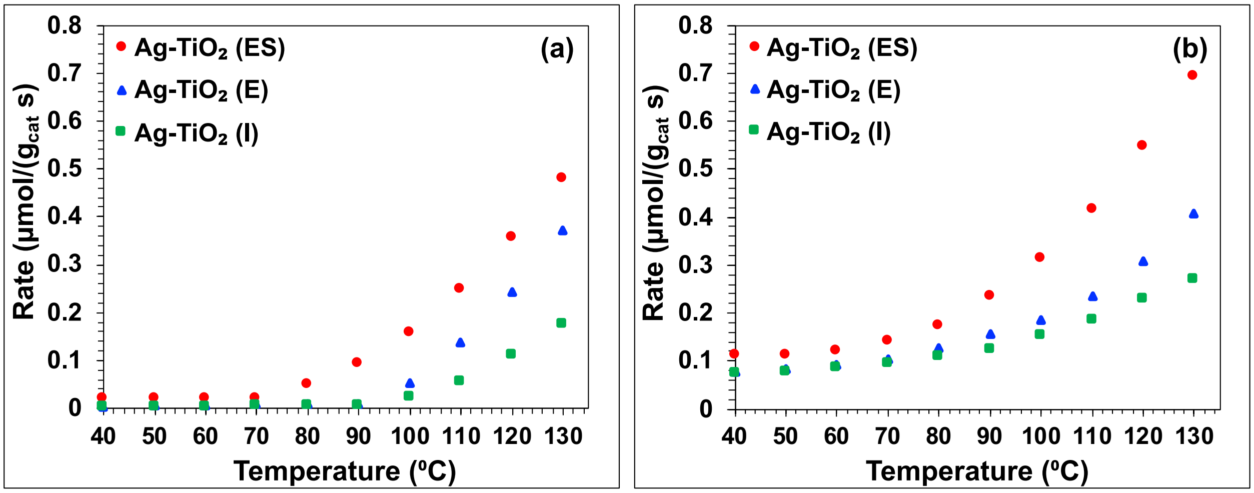

Figure 5.17 - The rate of n-butanol conversion over different Ag-TiO_2 catalysts; under dry oxidation conditions (a), and oxidation carried out after saturating the catalyst surface with hydroxyl ions (b).

Figure 5.17 compares the appreciable increase in reaction rate due to saturating the catalyst surface with water vapor before beginning the oxidation reaction in contrast to dry oxidation conditions. For instance, at 40 °C, we see that the rate of n-butanol conversion over Ag-TiO_2 (ES) was 0.0192 μmol g_{cat}^{-1} s^{-1}. By saturating the catalyst surface with water vapor, the reaction rate increased almost to 0.1124 μmol g_{cat}^{-1} s^{-1}. The rate enhancement decreased as a function of temperature from about sixfold to about twofold at 100 °C. As the reaction temperature increased, the lifetime of the ·O-H group begins to shorten. Thus at higher temperatures (150 °C and above), we observed little to no changes in the n-butanol conversion (Figure 5.18).

Under atmospheric pressure and room temperature conditions, water is known to adsorb on the {101} facets of the TiO_2 crystallites and form a monolayer of two oppositely oriented, weakly and strongly hydrogen-bonded sub-ensembles of ·O-H groups [45]. Among the three catalysts, Ag-TiO_2 (ES) has the smallest average TiO_2 crystallite size and, consequently, the highest surface area capable of supporting sub-ensembles of ·O-H groups per given volume of TiO_2. These ·O-H groups can improve the adsorption and transport of oxygen on TiO_2, which is essential for fast turnover and high conversion in oxidation reactions. Therefore, we see a more prominent rate enhancement on Ag-TiO_2 (ES) compared to the two other catalyst morphologies. Although Ag-TiO_2 (E) has good active metal dispersion, the comparatively larger crystallite size and the lower surface area of the TiO_2 support, resulting from direct calcination, could lower the abundance of ·O-H groups on the catalyst surface. Hence, the rate enhancement was not as significant.

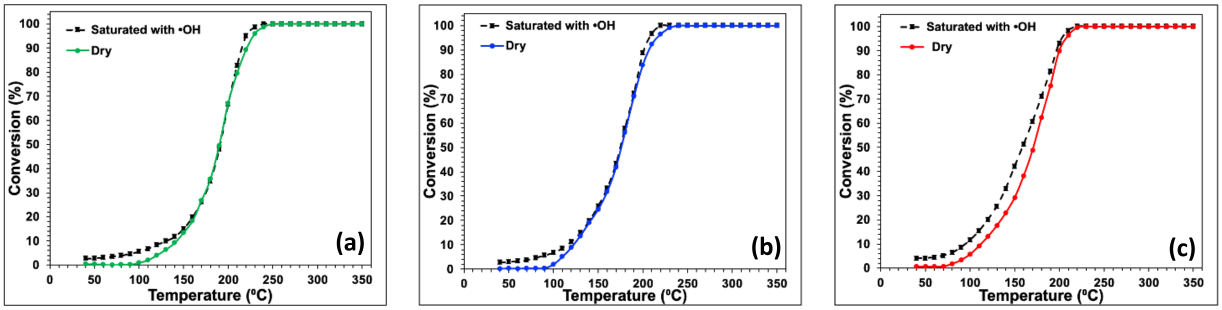

***Figure 5.18** - Comparison between the n-butanol oxidation profiles over Ag-TiO_2 (I) (a), Ag-TiO_2 (E) (b), and Ag-TiO_2 (ES) (c) catalysts. Solid line indicates the reaction carried out under dry conditions and the dotted line indicates the reaction carried out after saturating the surface of the catalyst by hydroxyl groups.*

The activity of the Ag-TiO_2 (I) catalyst shows a less pronounced enhancement of n-butanol oxidation upon pre-exposure to water vapor. As seen in TEM and XEDS characterization, Ag-TiO_2 (I) catalysts consist of Ag nanoparticles decorated over the surface of TiO_2 nanospheres. Silver nanoparticles are known to be hydrophobic in nature. Perhaps, the extreme hydrophobicity of Ag nanoparticles dispersed on the surface of TiO_2 nanosphere could hinder the interaction of the catalyst surface with water and limit the formation of abundant ·O-H groups that would be needed for improving the oxidation rate. These observations suggest that by periodically saturating the surface of the encapsulated catalysts with water vapor in the absence of reactants, we can sustain the rate enhancement and effectively carry out n-butanol oxidation at much lower temperatures than under dry oxidation conditions.

In recent years, feasibility of complete catalytic oxidation of n-butanol has been investigated using various catalysts. So far, to the best of our knowledge, no previous work has been reported where silver based catalysts were used for the oxidation of n-butanol. While platinum, palladium and rhodium based catalysts perform superior to the silver based catalysts reported in this work, the significant cost different between these active metals and silver makes it a noteworthy choice, especially, in an encapsulated morphology.

5.4. Conclusion

This chapter outlines a promising strategy to encapsulate active metal species in a porous reducible metal oxide support while maintaining a high metal dispersion. We demonstrate that tailoring the support morphology and overall catalyst architecture can provide substantial resistance to active metal sintering in industrially-motivated conditions while enhancing the catalytic activity. Unlike aging of surface impregnated Ag-TiO_2 (I) catalysts, which resulted in Ag agglomeration and a T_{90} increase in agreement with a typical sintering behaviour, encapsulated Ag-TiO_2 catalysts showed remarkable stability associated with the sinter-resistance properties of the final composite. In summary, we show that encapsulating the active metal can be used to improve low-temperature activity and thermal stability of the catalyst in the following ways:

- Encapsulation facilitates the production of highly uniform, dispersed, and small active metal sites.
- Following the encapsulation synthesis approach, solvothermal treatment helps anchor the active metal in the tortuous porous structure of the metal oxide support, thereby preventing sintering under high-temperature aging conditions.
- Encapsulation creates an abundance of Ag-TiO_2 interfacial sites, which changes the selectivity and product distribution to favor complete oxidation of n-butanol to CO_2 at relatively lower temperatures.

These factors synergistically come together to provide substantial stability and enhanced activity for solvothermally treated, encapsulated Ag-TiO_2 catalysts in carrying out VOC oxidation for a prolonged period. Furthermore, we delineate an alternative approach to constructively utilize the water vapor present in many industrial effluent gas streams to improve the rate of VOC oxidation by exposing the catalyst surface to water vapor before beginning the reaction. The stark contrast of these observations with conventional sintering suggests that encapsulation along with a solvothermal treatment can be a promising catalyst design strategy in applications where high-temperature degradation is a significant challenge.

5.5. References

(1) Guo, Y.; Wen, M.; Li, G.; An, T. Recent Advances in VOC Elimination by Catalytic Oxidation Technology onto Various Nanoparticles Catalysts: A Critical Review. *Applied Catalysis B: Environmental* **2021**, *281*, 119447. https://doi.org/https://doi.org/10.1016/j.apcatb.2020.119447.

(2) Su, C.; Liu, L.; Zhang, M.; Zhang, Y.; Shao, C. Fabrication of Ag/TiO2 Nanoheterostructures with Visible Light Photocatalytic Function via a Solvothermal Approach. *CrystEngComm* **2012**, *14* (11), 3989–3999. https://doi.org/10.1039/C2CE25161B.

(3) Chen, Y.; Fan, Z.; Zhang, Z.; Niu, W.; Li, C.; Yang, N.; Chen, B.; Zhang, H. Two-Dimensional Metal Nanomaterials: Synthesis, Properties, and Applications. *Chemical Reviews* **2018**, *118* (13), 6409–6455. https://doi.org/10.1021/acs.chemrev.7b00727.

(4) Ma, H.; Zheng, W.; Yan, X.; Li, S.; Zhang, K.; Liu, G.; Jiang, L. Polydopamine-Induced Fabrication of Ag-TiO2 Hollow Nanospheres and Their Application in Visible-Light Photocatalysis. *Colloids and Surfaces A: Physicochemical and Engineering Aspects* **2020**, *586*, 124283. https://doi.org/https://doi.org/10.1016/j.colsurfa.2019.124283.

(5) Zhang, N.; Shao, Q.; Pi, Y.; Guo, J.; Huang, X. Solvent-Mediated Shape Tuning of Well-Defined Rhodium Nanocrystals for Efficient Electrochemical Water Splitting. *Chemistry of Materials* **2017**, *29* (11), 5009–5015. https://doi.org/10.1021/acs.chemmater.7b01588.

(6) Sasikala, S. P.; Poulin, P.; Aymonier, C. Advances in Subcritical Hydro-/Solvothermal Processing of Graphene Materials. *Advanced Materials* **2017**, *29* (22), 1605473. https://doi.org/https://doi.org/10.1002/adma.201605473.

(7) Sui, G.; Li, J.; Du, L.; Zhuang, Y.; Zhang, Y.; Zou, Y.; Li, B. Preparation and Characterization of G-C3N4/Ag–TiO2 Ternary Hollowsphere Nanoheterojunction Catalyst with High Visible Light Photocatalytic Performance. *Journal of Alloys and Compounds* **2020**, *823*, 153851. https://doi.org/https://doi.org/10.1016/j.jallcom.2020.153851.

(8) Xu, B.; Wang, X. Solvothermal Synthesis of Monodisperse Nanocrystals. *Dalton Transactions* **2012**, *41* (16), 4719–4725. https://doi.org/10.1039/C2DT11842D.

(9) Nunes, D.; Pimentel, A.; Santos, L.; Barquinha, P.; Pereira, L.; Fortunato, E.; Martins, R. 2 - Synthesis, Design, and Morphology of Metal Oxide Nanostructures. In *Metal Oxides*; Nunes, D., Pimentel, A., Santos, L., Barquinha, P., Pereira, L., Fortunato, E., Martins, R. B. T.-M. O. N., Eds.; Elsevier, 2019; pp 21–57. https://doi.org/https://doi.org/10.1016/B978-0-12-811512-1.00002-3.

(10) Li, Z.-Q.; Ding, Y.; Mo, L.-E.; Hu, L.-H.; Wu, J.-H.; Dai, S.-Y. Fine Tuning of Nanocrystal and Pore Sizes of TiO2 Submicrospheres toward High Performance Dye-Sensitized Solar Cells. *ACS Applied Materials & Interfaces* **2015**, *7* (40), 22277–22283. https://doi.org/10.1021/acsami.5b06556.

(11) Albiter, E.; Valenzuela, M. A.; Alfaro, S.; Valverde-Aguilar, G.; Martínez-Pallares, F. M. Photocatalytic Deposition of Ag Nanoparticles on TiO2: Metal Precursor Effect on the Structural and Photoactivity Properties. *Journal of Saudi Chemical Society* **2015**, *19* (5), 563–573. https://doi.org/https://doi.org/10.1016/j.jscs.2015.05.009.

(12) Weaver, J. F.; Hoflund, G. B. Surface Characterization Study of the Thermal Decomposition of Ag2O. *Chemistry of Materials* **1994**, *6* (10), 1693–1699. https://doi.org/10.1021/cm00046a022.

(13) Al-Hada, M.; Gregoratti, L.; Amati, M.; Neeb, M. Pristine and Oxidised Ag-Nanoparticles on Free-Standing Graphene as Explored by X-Ray Photoelectron and Auger Spectroscopy. *Surface Science* **2020**, *693*, 121533. https://doi.org/https://doi.org/10.1016/j.susc.2019.121533.

(14) Weaver, J. F.; Hoflund, G. B. Surface Characterization Study of the Thermal Decomposition of AgO. *The Journal of Physical Chemistry* **1994**, *98* (34), 8519–8524. https://doi.org/10.1021/j100085a035.

(15) Liu, H.; Deng, L.; Sun, C.; Li, J.; Zhu, Z. Titanium Dioxide Encapsulation of Supported Ag Nanoparticles on the Porous Silica Bead for Increased Photocatalytic Activity. *Applied Surface Science* **2015**, *326*, 82–90. https://doi.org/https://doi.org/10.1016/j.apsusc.2014.11.110.

(16) Gao, C.; Lyu, F.; Yin, Y. Encapsulated Metal Nanoparticles for Catalysis. *Chemical Reviews* **2020**. https://doi.org/10.1021/acs.chemrev.0c00237.

(17) Zhang, J.; Wang, B.; Nikolla, E.; Medlin, J. W. Directing Reaction Pathways through Controlled Reactant Binding at Pd–TiO2 Interfaces. *Angewandte Chemie International Edition* **2017**, *56* (23), 6594–6598. https://doi.org/10.1002/anie.201703669.

(18) Tang, H.; Su, Y.; Zhang, B.; Lee, A. F.; Isaacs, M. A.; Wilson, K.; Li, L.; Ren, Y.; Huang, J.; Haruta, M.; Qiao, B.; Liu, X.; Jin, C.; Su, D.; Wang, J.; Zhang, T. Classical Strong Metal–Support Interactions between Gold Nanoparticles and Titanium Dioxide. *Science Advances* **2017**, *3* (10), e1700231. https://doi.org/10.1126/sciadv.1700231.

(19) de Klerk, A. Isomerization of 1-Butene to Isobutene at Low Temperature. *Industrial & Engineering Chemistry Research* **2004**, *43* (20), 6325–6330. https://doi.org/10.1021/ie049585m.

(20) Lee, J. E.; Ok, Y. S.; Tsang, D. C. W.; Song, J.; Jung, S.-C.; Park, Y.-K. Recent Advances in Volatile Organic Compounds Abatement by Catalysis and Catalytic Hybrid Processes: A Critical Review. *Science of The Total Environment* **2020**, *719*, 137405. https://doi.org/https://doi.org/10.1016/j.scitotenv.2020.137405.

(21) Huang, H.; Xu, Y.; Feng, Q.; Leung, D. Y. C. Low Temperature Catalytic Oxidation of Volatile Organic Compounds: A Review. *Catalysis Science & Technology* **2015**, *5* (5), 2649–2669. https://doi.org/10.1039/C4CY01733A.

(22) Kamal, M. S.; Razzak, S. A.; Hossain, M. M. Catalytic Oxidation of Volatile Organic Compounds (VOCs) – A Review. *Atmospheric Environment* **2016**, *140*, 117–134. https://doi.org/https://doi.org/10.1016/j.atmosenv.2016.05.031.

(23) Mallat, T.; Baiker, A. Oxidation of Alcohols with Molecular Oxygen on Solid Catalysts. *Chemical Reviews* **2004**, *104* (6), 3037–3058. https://doi.org/10.1021/cr0200116.

(24) Liotta, L. F. Catalytic Oxidation of Volatile Organic Compounds on Supported Noble Metals. *Applied Catalysis B: Environmental* **2010**, *100* (3), 403–412. https://doi.org/https://doi.org/10.1016/j.apcatb.2010.08.023.

(25) Makarova, M. A.; Paukshtis, E. A.; Thomas, J. M.; Williams, C.; Zamaraev, K. I. Dehydration of N-Butanol on Zeolite H-ZSM-5 and Amorphous Aluminosilicate: Detailed Mechanistic Study and the Effect of Pore Confinement. *Journal of Catalysis* **1994**, *149* (1), 36–51. https://doi.org/https://doi.org/10.1006/jcat.1994.1270.

(26) Ruiz Puigdollers, A.; Schlexer, P.; Tosoni, S.; Pacchioni, G. Increasing Oxide Reducibility: The Role of Metal/Oxide Interfaces in the Formation of Oxygen Vacancies. *ACS Catalysis* **2017**, *7* (10), 6493–6513. https://doi.org/10.1021/acscatal.7b01913.

(27) Liao, Y.; Jia, L.; Chen, R.; Gu, O.; Sakurai, M.; Kameyama, H.; Zhou, L.; Ma, H.; Guo, Y. Charcoal-Supported Catalyst with Enhanced Thermal-Stability for the Catalytic Combustion of Volatile Organic Compounds. *Applied Catalysis A: General* **2016**, *522*, 32–39. https://doi.org/https://doi.org/10.1016/j.apcata.2016.04.028.

(28) Okal, J.; Zawadzki, M. Catalytic Combustion of Butane on Ru/γ-Al2O3 Catalysts. *Applied Catalysis B: Environmental* **2009**, *89* (1), 22–32. https://doi.org/https://doi.org/10.1016/j.apcatb.2008.11.024.

(29) de Rivas, B.; López-Fonseca, R.; Sampedro, C.; Gutiérrez-Ortiz, J. I. Catalytic Behaviour of Thermally Aged Ce/Zr Mixed Oxides for the Purification of Chlorinated VOC-Containing Gas Streams. *Applied Catalysis B: Environmental* **2009**, *90* (3), 545–555. https://doi.org/https://doi.org/10.1016/j.apcatb.2009.04.017.

(30) Padayachee, D.; Mahomed, A. S.; Singh, S.; Friedrich, H. B. Effect of the TiO2 Anatase/Rutile Ratio and Interface for the Oxidative Activation of n-Octane. *ACS Catalysis* **2020**, *10* (3), 2211–2220. https://doi.org/10.1021/acscatal.9b04004.

(31) Landmann, M.; Rauls, E.; Schmidt, W. G. The Electronic Structure and Optical Response of Rutile, Anatase and Brookite TiO2. *Journal of Physics: Condensed Matter* **2012**, *24* (19), 195503. https://doi.org/10.1088/0953-8984/24/19/195503.

(32) Joo, S. H.; Park, J. Y.; Tsung, C.-K.; Yamada, Y.; Yang, P.; Somorjai, G. A. Thermally Stable Pt/Mesoporous Silica Core–Shell Nanocatalysts for High-Temperature Reactions. *Nature Materials* **2009**, *8* (2), 126–131. https://doi.org/10.1038/nmat2329.

(33) Cargnello, M.; Jaén, J. J. D.; Garrido, J. C. H.; Bakhmutsky, K.; Montini, T.; Gámez, J. J. C.; Gorte, R. J.; Fornasiero, P. Exceptional Activity for Methane Combustion over Modular Pd@CeO2 Subunits on Functionalized Al2O3. *Science* **2012**, *337* (6095), 713 – 717. https://doi.org/10.1126/science.1222887.

(34) Dick, K.; Dhanasekaran, T.; Zhang, Z.; Meisel, D. Size-Dependent Melting of Silica-Encapsulated Gold Nanoparticles. *Journal of the American Chemical Society* **2002**, *124* (10), 2312–2317. https://doi.org/10.1021/ja017281a.

(35) O'Neill, B. J.; Jackson, D. H. K.; Crisci, A. J.; Farberow, C. A.; Shi, F.; Alba-Rubio, A. C.; Lu, J.; Dietrich, P. J.; Gu, X.; Marshall, C. L.; Stair, P. C.; Elam, J. W.; Miller, J. T.; Ribeiro, F. H.; Voyles, P. M.; Greeley, J.; Mavrikakis, M.; Scott, S. L.; Kuech, T. F.; Dumesic, J. A. Stabilization of Copper Catalysts for Liquid-Phase Reactions by Atomic Layer Deposition. *Angewandte Chemie International Edition* **2013**, *52* (51), 13808–13812. https://doi.org/https://doi.org/10.1002/anie.201308245.

(36) Bore, M. T.; Pham, H. N.; Switzer, E. E.; Ward, T. L.; Fukuoka, A.; Datye, A. K. The Role of Pore Size and Structure on the Thermal Stability of Gold Nanoparticles within Mesoporous Silica. *The Journal of Physical Chemistry B* **2005**, *109* (7), 2873–2880. https://doi.org/10.1021/jp045917p.

(37) Ortel, E.; Sokolov, S.; Zielke, C.; Lauermann, I.; Selve, S.; Weh, K.; Paul, B.; Polte, J.; Kraehnert, R. Supported Mesoporous and Hierarchical Porous Pd/TiO2 Catalytic Coatings with Controlled Particle Size and Pore Structure. *Chemistry of Materials* **2012**, *24* (20), 3828–3838. https://doi.org/10.1021/cm301081w.

(38) Han, F.; Zhou, Z.; Zhang, X.; Huang, Z.; Li, M.; Guo, L. First-Principles Study on Stability and HER Activity of Noble Metal Single Atoms on TiO2: The Effect of Loading Density. *The Journal of Physical Chemistry C* **2018**, *122* (5), 2546–2553. https://doi.org/10.1021/acs.jpcc.7b11486.

(39) Setvin, M.; Hao, X.; Daniel, B.; Pavelec, J.; Novotny, Z.; Parkinson, G. S.; Schmid, M.; Kresse, G.; Franchini, C.; Diebold, U. Charge Trapping at the Step Edges of TiO2 Anatase (101). *Angewandte Chemie International Edition* **2014**, *53* (18), 4714–4716. https://doi.org/https://doi.org/10.1002/anie.201309796.

(40) Iyemperumal, S. K.; Pham, T. D.; Bauer, J.; Deskins, N. A. Quantifying Support Interactions and Reactivity Trends of Single Metal Atom Catalysts over TiO2. *The Journal of Physical Chemistry C* **2018**, *122* (44), 25274–25289. https://doi.org/10.1021/acs.jpcc.8b05611.

(41) García-Serrano, J.; Gómez-Hernández, E.; Ocampo-Fernández, M.; Pal, U. Effect of Ag Doping on the Crystallization and Phase Transition of TiO2 Nanoparticles. *Current Applied Physics* **2009**, *9* (5), 1097–1105. https://doi.org/https://doi.org/10.1016/j.cap.2008.12.008.

(42) Mosquera, A. A.; Albella, J. M.; Navarro, V.; Bhattacharyya, D.; Endrino, J. L. Effect of Silver on the Phase Transition and Wettability of Titanium Oxide Films. *Scientific Reports* **2016**, *6* (1), 32171. https://doi.org/10.1038/srep32171.

(43) Sapi, A.; Liu, F.; Cai, X.; Thompson, C. M.; Wang, H.; An, K.; Krier, J. M.; Somorjai, G. A. Comparing the Catalytic Oxidation of Ethanol at the Solid–Gas and Solid–Liquid Interfaces over Size-Controlled Pt Nanoparticles: Striking Differences in Kinetics and Mechanism. *Nano Letters* **2014**, *14* (11), 6727–6730. https://doi.org/10.1021/nl5035545.

(44) Jeong, H.; Kang, M. Hydrogen Production from Butane Steam Reforming over Ni/Ag Loaded MgAl2O4 Catalyst. *Applied Catalysis B: Environmental* **2010**, *95* (3), 446–455. https://doi.org/https://doi.org/10.1016/j.apcatb.2010.01.026.

(45) Zhao, Z.; Li, Z.; Zou, Z. Structure and Properties of Water on the Anatase TiO2(101) Surface: From Single-Molecule Adsorption to Interface Formation. *The Journal of Physical Chemistry C* **2012**, *116* (20), 11054–11061. https://doi.org/10.1021/jp301468c.

(46) Saavedra, J.; Whittaker, T.; Chen, Z.; Pursell, C. J.; Rioux, R. M.; Chandler, B. D. Controlling Activity and Selectivity Using Water in the Au-Catalysed Preferential Oxidation of CO in H2. *Nature Chemistry* **2016**, *8* (6), 584–589. https://doi.org/10.1038/nchem.2494.

Chapter 6

Visible-light Enhanced Catalytic Oxidation of VOCs Over Ag-TiO_2 Core@Shell Catalysts

6.1. Introduction

Catalytic oxidation reactions are a critical part of the modern-day chemical industry. Often, the rates of these reactions are limited by one elementary chemical step, referred to as the rate-limiting step [1]. For example, as discussed in Chapter Five, the rate of n-butanol oxidation over Ag-TiO_2 catalyst is limited by dissociative adsorption of molecular oxygen on Ag nanoparticles. Therefore, thermal energy is supplemented to drive most of the catalytic oxidation reactions, resulting in a significant consumption of dwindling reserves of fossil fuels [2,3]. However, concerns over the long-term availability and environmental consequences of fossil fuels have motivated a substantial amount of research and development in the field of technologies that utilize the energy abundantly available in sunlight and gave rise to the field of "photo-thermal catalysis" [4–7]. Photo-thermal catalytic reactions can synergistically use the energy from light and heat to overcome the energetic barrier posed by the rate limiting step and can enhance reaction rates, even under moderate operating conditions [8,9]. Researchers have shown that by engineering multifunctional nanostructures with specific lattice vibrational energy, phonon density, bandgap energies, and trap sites, it is possible to utilize the energy present in UV, visible, and infrared radiations synchronously with thermal energy to activate reactants on the catalyst's surface [10–17].

For example, a semiconductor, upon absorption of a photon with equal or higher energy than the bandgap, can generate electron-hole pairs. This is referred to as photoexcitation [18]. Eventually, these charge carriers can migrate to the semiconductor surface and be transferred to adsorbed molecules, thereby initiating reduction or oxidation processes [19–22]. However, the efficiency of this process remains insufficiently low, mainly due to fast charge carrier recombination and low absorption and utilization of the solar spectrum by traditional wide bandgap semiconductors [18]. Another example is plasmon-mediated catalysis using metal nanoparticles [12]. Some metals nanoparticles display unique and interesting optical and electrical properties. This property can be explained by Mie theory [23].

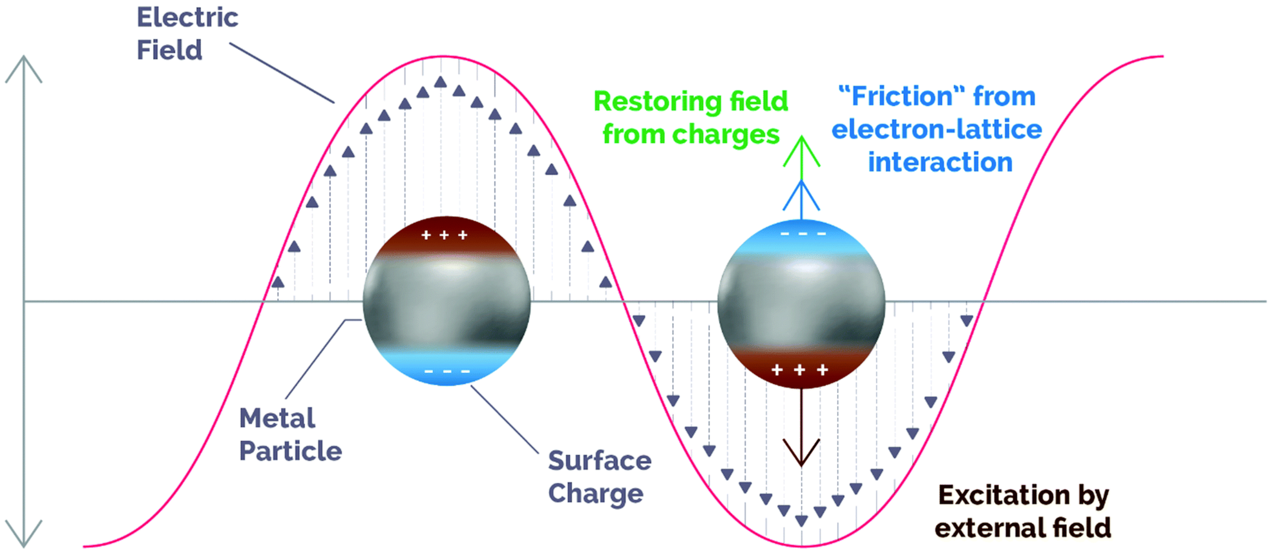

Figure 6.1 *- Schematic illustration of the dynamics of an excited plasmonic nanoparticle. The motion of carriers follows the changes induced by the incoming electromagnetic field (brown), while a restoring force is generated by the out-of-equilibrium surface charges (green) and the ionic network produces damping due to electronic collisions (blue). Adapted with permission from ref. 9. Copyright Royal Society of Chemistry (2020).*

According to this theory, free electrons in the conduction band of metal nanoparticles can move when guided by external incident irradiation (Figure 6.1). This motion is dampened by inelastic electron collisions and the restoring force on the electron cloud created by the accumulation of surface charges. Under resonant conditions, both the incident electromagnetic wave and the resonant frequency of conduction electrons are in phase, thus maximizing the electric field in so-called “hot spots or hot electrons” on the surface of plasmonic nanoparticles [23,24]. Apart from the enhanced electric field, other relevant properties of localized surface plasmonic resonance (LSPR) arise from the different relaxation processes that occur within plasmonic structures. After excitation, the energy stored in surface plasmons can decay through several pathways, either radiative (as re-emitted photons) or non-radiative (electron-hole pair excitations and electron-electron collisions) [9,25]. In sum, the synergistic combination of hot carrier generation, local heating effect, and optical near-field enhancement that arise from LSPR drives plasmon-enhanced photo-thermal catalysis [26].

Nanocrystals of Au, Ag, Cu with wide light absorption ranges can photo generate “hot electrons” when oscillations of the conduction electrons are excited under the light [27]. Compared to the direct photoexcitation in semiconductors, the hot electrons produced by non-radiative decay of localized surface plasmons are much more energetic than the typical intensity of traditional photocatalysis [28]. When these metals are in contact with a semiconductor, a Schottky barrier around the interface is created. It promotes electron transfer and suppresses the combination of charge carriers. These are different from traditional co-catalyst-loaded semiconductor systems. For example, plasmonic metal-semiconductor systems such as Au-TiO_2 can reach a theoretical incident photo-to-current conversion efficiency (IPCE) of around 26%, which is much higher than the traditional photocatalytic IPCE of around 1%, serving as an up-and-coming candidate for solar energy exploitation [29]. In addition to the above-mentioned photoexcited plasmonic effects, the thermal catalytic effect cannot be ignored as these plasmonic metals have been widely used as supported noble metal catalysts in a wide range of thermal catalytic reactions. For example, Zheng and co-workers prepared Au-modified CeO_2 samples with various Au loading amounts (0.25-1 wt. %) and particle sizes ranging from 3 - 20 nm. They evaluated the surface plasmon resonance photoabsorption, charge separation, resonant energy transfer, and surface catalysis in the aerobic oxidation of propylene reaction [30]. Their results revealed that photoexcitation and surface catalysis presented opposite correlation on Au nanoparticle size and co-determined the final photocatalytic performance. Hence, finding optimal active metal particle sizes that maximize the balance between the plasmonic and catalytic roles over metallic nanostructures would be ideal for the further rational design of efficient plasmonic metal-semiconductor systems.

Building on the advancements made in the field of metal-semiconductor catalytic systems, we demonstrate a methodology of increasing the metal-semiconductor interfaces by encapsulating silver nanoparticles in porous TiO_2 shell (Ag@TiO_2 catalysts) to obtaining a core@shell like catalyst morphology. We evaluate the morphology and the visible light absorption capability of the catalyst via transmission electron microscopy and UV-Visible spectroscopy. While the encapsulation morphology provides excellent thermal stability to the catalyst, our results indicate that the Ag@TiO_2 catalysts also show outstanding absorption of visible light through the creation of resonant surface plasmons. Catalytic oxidation of n-butanol was used to probe the VOC oxidation efficacy of Ag@TiO_2 catalysts. Our studies indicate that Ag@TiO_2 catalysts can drive catalytic oxidation reactions of VOCs at significantly lower temperatures than those associated with conventional thermal oxidation processes by concurrently utilizing thermal and energy and low-intensity photon flux (similar to solar intensity).

6.2. Experimental

6.2.1. Materials

The ionic surfactant hexadecyltrimethylammonium bromide (CTAB, ≥ 98%), the metal precursors silver nitrate ($AgNO_3$, ACS reagent ≥ 99.0%) and titanium (IV) isopropoxide (TTIP, 99.999% trace metals basis) and hydrazine (anhydrous, 98%) were all purchased from Sigma-Aldrich. All the synthesis were carried out in deionized water and anhydrous ethanol.

6.2.2. Synthesis of $Ag@TiO_2$ catalysts

The synthesis of $Ag@TiO_2$ core@shell catalysts was carried out using an ionic surfactant mediated one-pot, two-step process. In a typical synthesis, 0.0073 g of 20 mL of CTAB was added to a beaker containing 20 mL of deionized. The solution was stirred for 10 minutes to ensure the dissolution of CTAB. To this mixture, 0.5 mL aqueous hydrazine solution (100 mM) was added, and the mixture was stirred for an additional 1 minute at room temperature. Thereafter, 0.5 mL of $AgNO_3$ aqueous solution (50 mM) was added to this mixture and stirred for an additional 10 minutes at room temperature. With the addition of $AgNO_3$ aqueous solution, the mixture turns orangish-yellow, indicating the formation of Ag nanoparticles. Next, through a dropwise addition of 32 mL of 1mM ethanolic TTIP solution, a TiO_2 shell was formed around the Ag nanoparticles. After the dropwise addition of ethanolic TTIP solution, the contents in the beaker were stirred for an additional 1 hour. The final $Ag@TiO_2$ core@shell catalysts were collected via centrifugation at 4000 rpm for 25 minutes and dried at 70 °C for 12 hours. Post drying, $Ag@TiO_2$ core@shell catalysts were calcined at 550 °C for 3 hours in a muffle furnace to remove any residual surfactant. After calcination, the catalysts were subjected to characterization and catalytic experiments.

6.2.3. Catalyst characterization

Characterization of the samples was done using a total of five different techniques: Thermogravimetric analysis (TGA), Brunauer – Emmett – Teller derived N_2 physisorption surface analysis (BET), Ultraviolet-Visible (UV-Vis) spectroscopy, transmission electron microscopy (TEM), X-ray powder diffraction (XRD).

In-situ thermal decomposition studies were carried out using TGA (TA Instrument Q 500). Roughly 15 mg of catalyst sample was placed in the TGA instrument and heated from 25 °C to 600 °C at a rate of 5 °C /min under the flow of air. The airflow in the TGA system was diluted by balance N_2 gas, lowering the actual O_2 concentration to 16 %. An integrated gas sorption apparatus (Micromeritics ASAP 2020) was used to determine the textural properties of the synthesized catalysts. The catalyst samples were degassed for 24 hours under vacuum at 350 °C, and nitrogen adsorption and desorption experiments were carried out at 77 K. The BET equation in the relative pressure (P/P_0) range from 0.06 to 0.32 was used to calculate the surface area from the isotherm data. The median pore width and the micropore size distribution were obtained from the Horvath-Kawazoe model using slit pore geometry and the BJH adsorption model.

UV-Vis spectroscopy was used to confirm the formation of Ag nanoparticles and the subsequent encapsulation of the TiO_2 shell around Ag nanoparticles. Roughly 25 mg of sample were ground into a fine powder and dispersed in 10 mL of anhydrous ethanol. Next, the solution was sonicated for 10 minutes to form a suspension. About 2 mL of the suspension was transferred to the quartz cuvette with path length 1 cm, followed by the addition of 5 mL of ethanol. UV-vis measurements were carried out in a double-slit Xenon lamp-based UV-vis spectrophotometer

(Evolution 350, Thermo Scientific). Vision Pro v4.20 software connected with the UV-vis spectrophotometer was used to obtain absorbance data for each wavelength between 190 - 1100 nm, with a bandwidth of 4 nm at a scan speed of 600 nm/min. The baseline for each UV-Vis spectrum measurement was a blank anhydrous ethanoic solution.

Before centrifugation, nearly 50 μL of synthesized Ag@TiO_2 core@shell nanoparticles were dispersed in 2 mL ethanol and ultrasonicated for 10 minutes to break up agglomerates. These nanoparticles were then deposited on carbon films supported on copper grids by adding the suspension drop-wise and allowing the ethanol to evaporate. The encapsulation and dispersion of Ag@TiO_2 core@shell catalysts were confirmed by standard bright field TEM using a Jeol 2010F Analytical Electron Microscope equipped with a zirconated tungsten (100) thermal field emission tip at 200 kV.

The XRD patterns of the samples were recorded on a Rigaku 600 Miniflex X-ray diffractometer instrument with Cu Kα radiation (λ=1.5406 Å). The wide-angle 2θ was scanned from 15 to 90° with a step size of 0.01 for all the measurements.

6.2.4. Thermal and photo-thermal VOC oxidation experiments

Similar to the protocol reported in Chapter Five, oxidation of n-butanol was used as the probe reaction to evaluate the catalytic activity Ag@TiO_2. The gaseous feed used for the catalytic tests was composed of 1000 ppmv of n-butanol in dry air. The required concentration of n-butanol was generated by bubbling an accurate amount of dry air through a saturator containing n-butanol. The outlet flow from the saturator was mixed with a second stream of dry air to obtain 0.1% of n-butanol feed at the reactor inlet.

VOC oxidation reactions were carried in a reactor system (depicted in Figure 6.2), consisting of a custom-designed quartz tube with an inline plate zone, a custom milled firebrick to allow simultaneous thermal insulation and visible light access reactor bed, temperature-controlled heat plate. The custom quartz reactor apparatus was fabricated by United Silica and had 0.25 in tubes (O.D.) at each end, a 1 mm x 1 in x 1 in plate zone and tapered 1 in transition zones. The top of the flat plate reactor was insulated with quartz wool with a small opening exactly above plate zone to minimize the vertical heat dissipation.

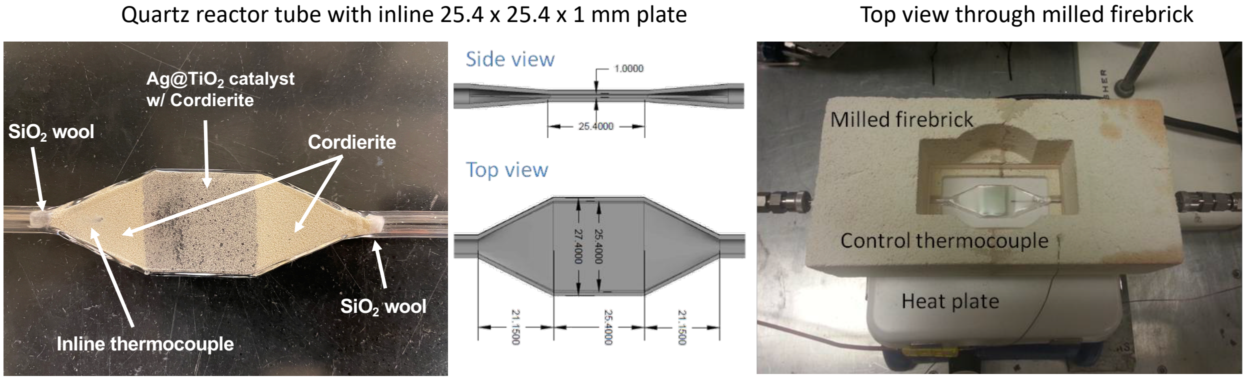
Quartz reactor tube with inline 25.4 x 25.4 x 1 mm plate

Top view through milled firebrick

Figure 6.2 *- Photo-thermal reactor used to carryout VOC oxidation experiments.*

Prior to loading the catalyst, the reactor was first thoroughly rinsed with deionized water and ethanol and then dried with a stream of air. A plug of quartz wool was inserted at the downstream end. Then 300 mg of 35-60 mesh cordierite powder (previously calcined at 800°C for 4 hours) was added. Next, 50 mg of $Ag@TiO_2$ catalyst (pressed into pellets and sieved to particles between 60 and 80 mesh), diluted with 300 mg of cordierite powder (also sieved to particles between 60−80 mesh, calcined at 800°C for 4 hours) was carefully loaded into the reactor. This was followed by adding another 300 mg of 35-60 mesh cordierite powder and finally an upstream plug of quartz wool. With each addition of powder, the reactor tube was shaken until the powder's upstream face was even and perpendicular to the reactor axis. A thermocouple was inserted in the reactor, embedded in the catalyst bed, to measure the exact reaction temperature.

Temperature-dependent thermal and photo-thermal experiments were carried out to evaluate the efficacy of Ag@TiO_2 catalysts for VOC oxidation. The flowrate of the n-butanol and Air mixture entering to the reactor was maintained constant at 100 mL/min. Measurements were taken at 10 °C intervals between 30 °C and 350 °C. At each temperature, the catalyst was allowed 15 minutes to reach a steady state under dark conditions, followed by 15 minutes of visible light illumination, followed by 15 minutes in the dark to assure that the rate returned to the initial value obtained in the dark. A Dolan-Jenner DC950 Halogen lamp, equipped with UV and IR cut-off filter that produces 250 mW/cm^2 at the catalyst surface, was used as the visible light source in all the experiments. The reaction products were analysed by a gas chromatograph (Varian 450-GC). The conversion of n-butanol ($X_{C_4H_{10}O}$) was calculated according to the equation:

$$X_{n-butanol}(\%) = \left[\frac{[C_4H_{10}O]_{in} - [C_4H_{10}O]_{out}}{[C_4H_{10}O]_{in}}\right] \times 100$$

where $[\mathrm{C_4H_{10}O}]_{\mathrm{in}}$ and $[\mathrm{C_4H_{10}O}]_{\mathrm{out}}$ are the n-butanol concentration in the feed gas and the outlet gas, respectively.

6.3. Results and discussion

6.3.1. Catalyst characterization

Figure 6.3 provides the representative TEM characterization of Ag nanoparticles and Ag@TiO_2 core@shell catalysts. The size of the Ag nanoparticles was in the order of 8-12 nm. As shown in 6.3 (c) and (d), addition of TTIP and its subsequent sol-gel hydrolysis results in the formation of porous TiO_2 envelope around Ag nanoparticles. The overall size of Ag@TiO_2 core@shell catalysts varied between 25-30 nm (avg. shell thickness between 5-7nm). Furthermore, no noticeable signs of scattered TiO_2 nanocrystals with missing cores were observed, indicating the high efficacy of obtaining core@shell morphologies.

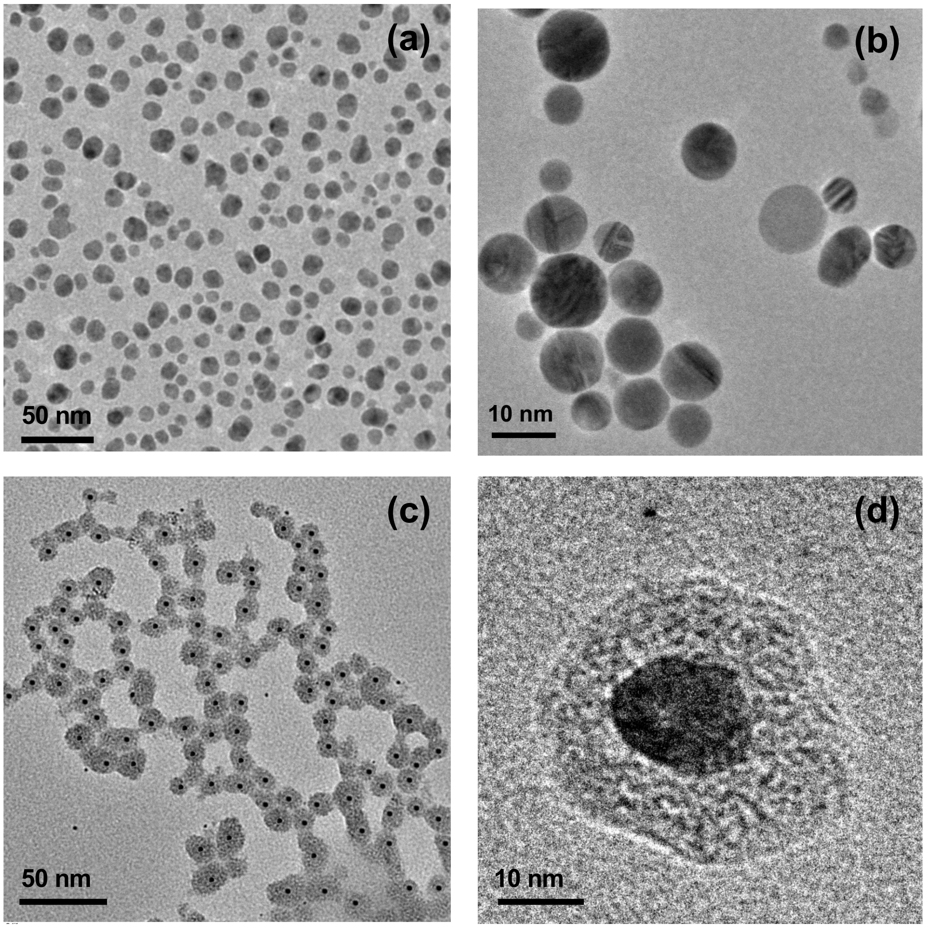

Figure 6.3 *- TEM images of Ag nanoparticles (a, b), and Ag@TiO_2 core@shell catalysts (c, d).*

Thermal decomposition of the Ag@TiO_2 catalysts prior to calcination and the associated surfactant removal is represented in Figure 6.4 (a). The gradual weight loss between 100 to 450 °C can be attributed to the removal of surfactants. Oxidation of the amorphous precursor with an inorganic/organic hybrid spherical structure can lead to a small incremental weight change at about 520 °C. Therefore, removal of CTAB and crystallization of the TiO_2 support can be best achieved by a calcination treatment at 550 °C.

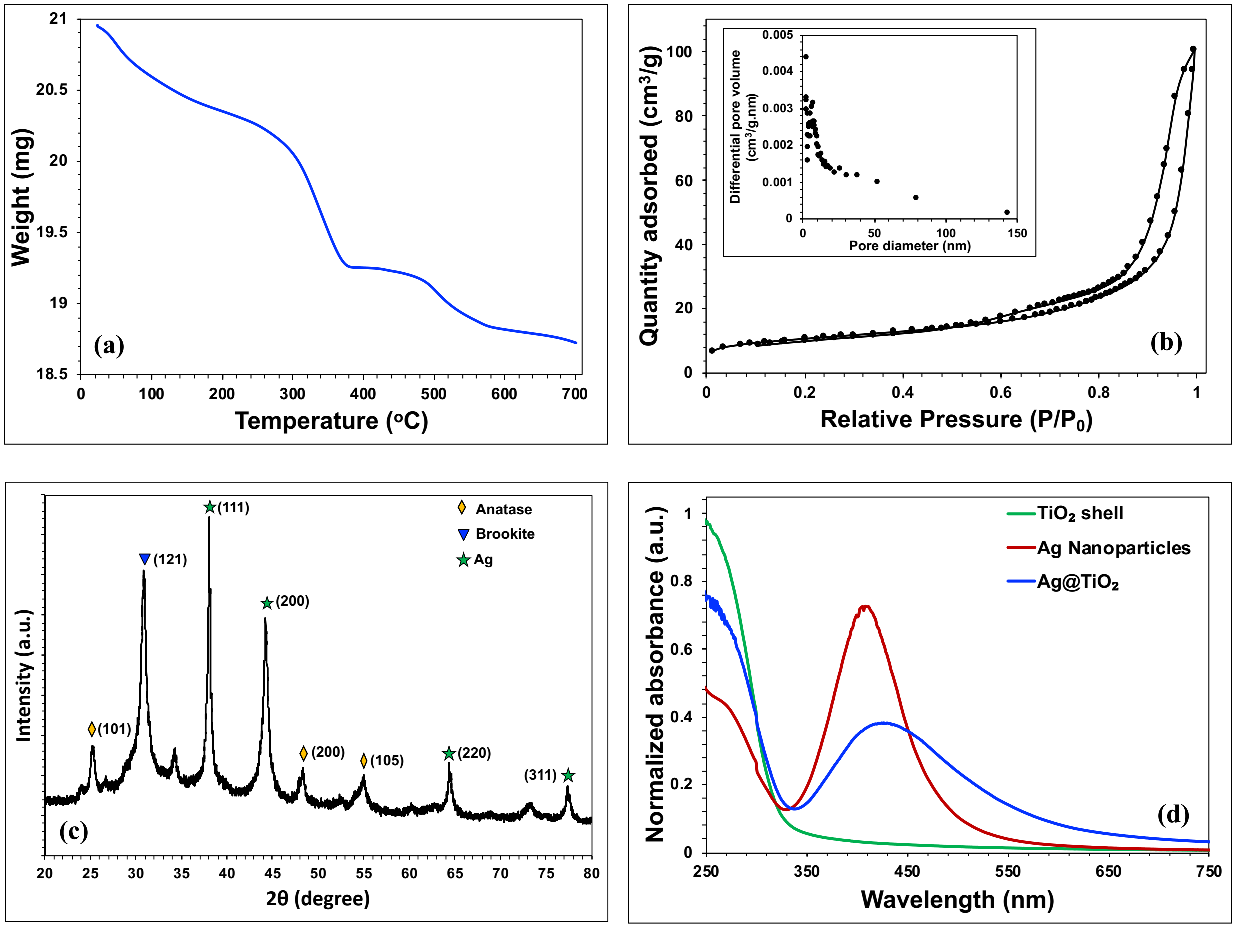

Figure 6.4 *- Analytical characterization of Ag@TiO_2 nanoparticles; Thermal decomposition profile Ag@TiO_2 nanoparticles after synthesis prior to calcination (a), nitrogen sorption isotherm of Ag@TiO_2 catalysts (b), XRD pattern of Ag@TiO_2 catalyst after calcination (c), and UV-Vis absorption spectrum of TiO_2, Ag, and Ag@TiO_2 nanoparticles (d).*

As the prepared Ag@TiO_2 core@shell nanoparticles were intended to be used for catalytic oxidation of VOCs, the accessibility of active site (Ag core) is a very important factor. Therefore, the porosity of the encapsulating shell and the overall available surface area of the material was evaluated by N_2 physisorption. The isotherm results (Figure 6.4 (b)) as well as pore size distribution indicate that the TiO_2 shell contains predominantly mesoporous structures with an average pore size of 17.7 nm and total available average surface area of 56.3 m^2/g.

The post synthesis calcination at 550 °C results in removal of surfactant and crystallization of the encapsulating TiO_2 shell. The XRD analysis showed the presence of polycrystalline Ag and TiO_2 nanoparticles. The diffraction peaks of the Ag core NPs appeared at 38.1°, 44.2°, 64.5°, and 77.4°, which corresponded to the (111), (200), (220), and (311) planes of the face centered cubic Ag crystal structure, respectively (COD 9008459). This result indicates that metallic Ag NPs are stable in Ag@TiO_2 even after the calcination at 550 °C. On the other hand, the pattern of the TiO_2 shell was a mixture of anatase and brookite phases, with peaks at 25.3°, 30.9°, 48.3°, and 55.1°, corresponding to (101), (004), (200), and (105) lattice planes of TiO_2, respectively. The average particle size of TiO_2 crystals was calculated using the Debye-Scherrer equation and was found to be 3.2 nm.

UV-Vis absorption spectra of TiO_2 shell, Ag nanoparticles, and Ag@TiO_2 core@shell catalysts are shown in Figure 6.4 (d). Contrary to the TiO_2 shell, which showed maximum absorption at wavelengths less than 250 nm, the maximum absorption wavelength of Ag nanoparticles and Ag@TiO_2 core@shell were around 400-440 nm, resulting from the localized surface plasmon resonance (LSPR) of Ag nanoparticles [31,32]. LSPR originates from the collective oscillation of electrons at the surface of silver nanoparticles. The SPR peak location can be modified mainly by changing the size and shape of the nanoparticles and the change in the dielectric environment surrounding the nanoparticles [8,33]. The results in Figure 6.4 (c) show that the LSPR peak of Ag@TiO_2 core@shell nanoparticles red-shift (from 412 nm for the Ag nanoparticles) to a higher wavelength (435-440 nm in Ag@TiO_2 core@shell nanoparticles). This absorption shift is caused by a high refractive index of the TiO_2 shell and strongly suggests a complete coverage of Ag nanoparticles with titania.

6.3.2. Thermal and photo-thermal catalytic oxidation of VOC

Figure 6.5 (a) compares the steady-state thermal and photo-thermal oxidation profiles of n-butanol at different temperatures. We observed that the n-butanol conversion began at ~ 100 °C during thermal oxidation. Subsequently, with the increase in the thermal input, the percentage conversion of n-butanol increased, finally reaching T_{90} at 230 °C. In comparison, under photo-thermal oxidation conditions, we observed n-butanol conversion beginning at temperatures as low as 30 °C. In the presence of visible light illumination, the overall conversion of n-butanol was relatively higher at each temperature compared to plain thermal oxidation, achieving T_{90} at 190 °C. Two sets of control experiments, n-butanol oxidation over plain TiO_2 and photodegradation of n-butanol in the absence of catalysts, were carried out to understand the importance of Ag core in photo-thermal n-butanol oxidation. As expected, oxidation over plain TiO_2 and photodegradation experiments in the absence of catalyst showed no evidence of n-butanol conversion Figure 6.5 (a).

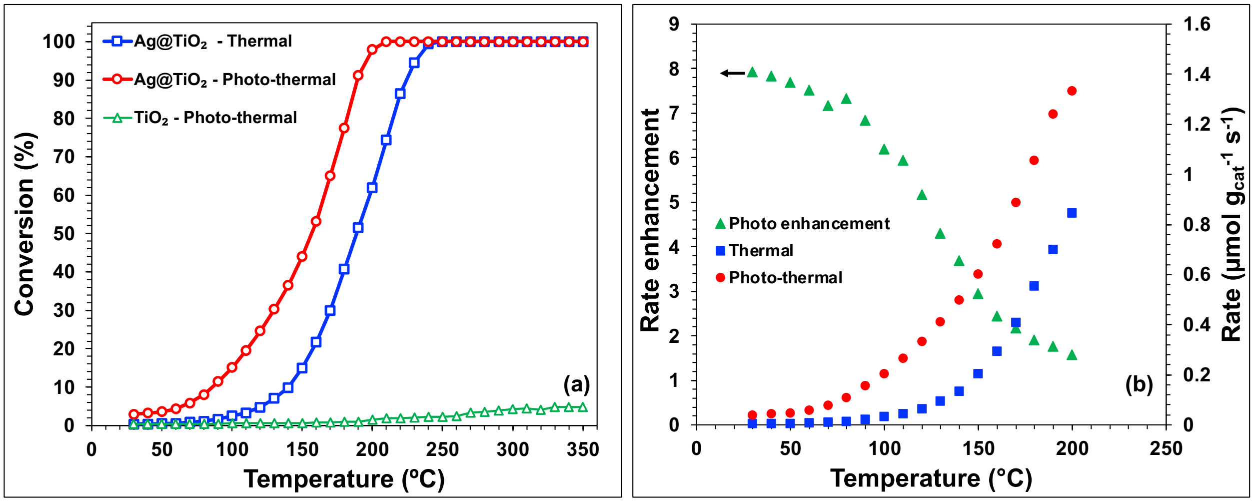

Figure 6.5 *- Visible light enhanced n-butanol oxidation reaction; n-butanol oxidation profiles over Ag@*TiO_2 *catalysts in the in the dark and with visible illumination (a) and Rate enhancement of n-butanol oxidation (left axis, green triangles) under visible illumination.*

Figure 6.5 (b) shows the measured reaction rate in the thermal (no light) and photothermal (light on) process as a function of operational temperature. The figure also shows the rate enhancement, calculated as the photothermal rate divided by thermal rate as a function of temperature. The rate enhancement decreased as the reaction temperature increased from about eight-fold at lower temperatures (< 70°C) to about two-fold at higher temperatures (> 160 °C). Overall, the visible light illumination had a remarkable effect on enhancing the VOC oxidation activity. We observed that illuminated Ag@TiO_2 core@shell catalysts achieved reaction rates comparable to those obtained only a thermal energy input (light off) but temperatures up to 30 °C lower.

As seen from Figure 6.4 (d), the LSPR of Ag nanoparticles enables Ag@TiO_2 core@shell catalysts to absorb light in the visible spectrum. In other words, silver interacts with visible light through the formation of resonant surface plasmons. In an oxidative environment, the surface plasmons could possibly interact with adsorbates on the surface of the Ag core by promoting the transfer of energetic electrons to the unoccupied adsorbate states. These transfers can occur either directly through the process of chemical interface damping or indirectly via the decay of plasmons into energetic electrons followed by the scattering of these electrons from unpopulated adsorbate states [5,9,13,24]. Hence, the plasmon-relaxation processes result in inducing photoactivity. As such, the photon fields could induce direct photoexcitation of adsorbates and change the rates of reaction through uncatalyzed photoreactions [6,7]. Furthermore, local heating of nanoparticles increases the reaction rate because of the Arrhenius dependence of rate constants on temperature. The transfer of energetic electrons to adsorbates could lead to electron-induced surface reactions that increase the overall reaction rates [9,25,34]. Several studies have reported that the transfer of energetic electrons to adsorbate is responsible for the observed enhancement in the rates of oxidation reactions on silver nanostructures [11,12,35,36].

6.4. Conclusion

This chapter demonstrates an effective strategy of encapsulating plasmonic silver nanoparticles in a thermally stable porous TiO_2 shell. The encapsulation helps in broadening and maximizing the wavelengths that can be absorbed by silver nanoparticles. Gas phase VOC oxidation carried out in flat plate reactor indicate that that $Ag@TiO_2$ core@shell catalysts characterized by the resonant formation of surface plasmons, can yield chemically useful energetic electrons when irradiated with continuous-wave low-intensity visible light. These electrons can be used in tandem with thermal energy to completely decompose n-butanol at viable rates at significantly reduced temperatures compared to those of pure thermal processes.

6.5. References

(1) Thomas, J. M.; Thomas, W. J. *Principles and Practice of Heterogeneous Catalysis*; John Wiley & Sons, 2014.

(2) Zhao, Y.; Gao, W.; Li, S.; Williams, G. R.; Mahadi, A. H.; Ma, D. Solar- versus Thermal-Driven Catalysis for Energy Conversion. *Joule* **2019**, *3* (4), 920–937. https://doi.org/https://doi.org/10.1016/j.joule.2019.03.003.

(3) Wittstock, A.; Zielasek, V.; Biener, J.; Friend, C. M.; Bäumer, M. Nanoporous Gold Catalysts for Selective Gas-Phase Oxidative Coupling of Methanol at Low Temperature. *Science* **2010**, *327* (5963), 319 – 322. https://doi.org/10.1126/science.1183591.

(4) Zimmerman, J. B.; Anastas, P. T.; Erythropel, H. C.; Leitner, W. Designing for a Green Chemistry Future. *Science* **2020**, *367* (6476), 397 – 400. https://doi.org/10.1126/science.aay3060.

(5) Watanabe, K.; Menzel, D.; Nilius, N.; Freund, H.-J. Photochemistry on Metal Nanoparticles. *Chemical Reviews* **2006**, *106* (10), 4301–4320. https://doi.org/10.1021/cr050167g.

(6) Brus, L. Noble Metal Nanocrystals: Plasmon Electron Transfer Photochemistry and Single-Molecule Raman Spectroscopy. *Accounts of Chemical Research* **2008**, *41* (12), 1742–1749. https://doi.org/10.1021/ar800121r.

(7) Jain, P. K.; Huang, X.; El-Sayed, I. H.; El-Sayed, M. A. Noble Metals on the Nanoscale: Optical and Photothermal Properties and Some Applications in Imaging, Sensing, Biology, and Medicine. *Accounts of Chemical Research* **2008**, *41* (12), 1578–1586. https://doi.org/10.1021/ar7002804.

(8) Kelly, K. L.; Coronado, E.; Zhao, L. L.; Schatz, G. C. The Optical Properties of Metal Nanoparticles: The Influence of Size, Shape, and Dielectric Environment. *The Journal of Physical Chemistry B* **2003**, *107* (3), 668–677. https://doi.org/10.1021/jp026731y.

(9) Mateo, D.; Cerrillo, J. L.; Durini, S.; Gascon, J. Fundamentals and Applications of Photo-Thermal Catalysis. *Chemical Society Reviews* **2021**, *50* (3), 2173–2210. https://doi.org/10.1039/D0CS00357C.

(10) Shi, Y.; Lyu, Z.; Zhao, M.; Chen, R.; Nguyen, Q. N.; Xia, Y. Noble-Metal Nanocrystals with Controlled Shapes for Catalytic and Electrocatalytic Applications. *Chemical Reviews* **2021**, *121* (2), 649–735. https://doi.org/10.1021/acs.chemrev.0c00454.

(11) Ji, W.; Shen, T.; Kong, J.; Rui, Z.; Tong, Y. Synergistic Performance between Visible-Light Photocatalysis and Thermocatalysis for VOCs Oxidation over Robust Ag/F-Codoped SrTiO3. *Industrial & Engineering Chemistry Research* **2018**, *57* (38), 12766–12773. https://doi.org/10.1021/acs.iecr.8b02873.

(12) Christopher, P.; Xin, H.; Linic, S. Visible-Light-Enhanced Catalytic Oxidation Reactions on Plasmonic Silver Nanostructures. *Nature Chemistry* **2011**, *3* (6), 467–472. https://doi.org/10.1038/nchem.1032.

(13) Mulugeta, D.; Kim, K. H.; Watanabe, K.; Menzel, D.; Freund, H.-J. Size Effects in Thermal and Photochemistry of (NO) 2 on Ag Nanoparticles. *Physical review letters* **2008**, *101* (14), 146103.

(14) Pustovalov, V. K. Theoretical Study of Heating of Spherical Nanoparticle in Media by Short Laser Pulses. *Chemical Physics* **2005**, *308* (1), 103–108. https://doi.org/https://doi.org/10.1016/j.chemphys.2004.08.005.

(15) Govorov, A. O.; Zhang, W.; Skeini, T.; Richardson, H.; Lee, J.; Kotov, N. A. Gold Nanoparticle Ensembles as Heaters and Actuators: Melting and Collective Plasmon Resonances. *Nanoscale Research Letters* **2006**, *1* (1), 84. https://doi.org/10.1007/s11671-006-9015-7.

(16) Liu, N.; Chen, X.; Zhang, J.; Schwank, J. W. DRIFTS Study of Photo-Assisted Catalytic CO+NO Redox Reaction over CuO/CeO2-TiO2. *Catalysis Today* **2015**, *258*, 139–147. https://doi.org/https://doi.org/10.1016/j.cattod.2015.04.022.

(17) Westrich, T. A.; Dahlberg, K. A.; Kaviany, M.; Schwank, J. W. High-Temperature Photocatalytic Ethylene Oxidation over TiO2. *The Journal of Physical Chemistry C* **2011**, *115* (33), 16537–16543. https://doi.org/10.1021/jp204405h.

(18) Schneider, J.; Matsuoka, M.; Takeuchi, M.; Zhang, J.; Horiuchi, Y.; Anpo, M.; Bahnemann, D. W. Understanding TiO2 Photocatalysis: Mechanisms and Materials. *Chemical Reviews* **2014**, *114* (19), 9919–9986. https://doi.org/10.1021/cr5001892.

(19) FUJISHIMA, A.; HONDA, K. Electrochemical Photolysis of Water at a Semiconductor Electrode. *Nature* **1972**, *238* (5358), 37–38. https://doi.org/10.1038/238037a0.

(20) Xiao, C.; Wang, H.; Zhang, L.; Sun, S.; Wang, W. Enhanced Photocatalytic Nitrogen Fixation on MoO2/BiOCl Composite. *ChemCatChem* **2019**, *11* (24), 6467–6472. https://doi.org/https://doi.org/10.1002/cctc.201901635.

(21) Paik, T.; Cargnello, M.; Gordon, T. R.; Zhang, S.; Yun, H.; Lee, J. D.; Woo, H. Y.; Oh, S. J.; Kagan, C. R.; Fornasiero, P.; Murray, C. B. Photocatalytic Hydrogen Evolution from Substoichiometric Colloidal WO3–x Nanowires. *ACS Energy Letters* **2018**, *3* (8), 1904–1910. https://doi.org/10.1021/acsenergylett.8b00925.

(22) Liu, H.; Wu, P.; Li, H.; Chen, Z.; Wang, L.; Zeng, X.; Zhu, Y.; Jiang, Y.; Liao, X.; Haynes, B. S.; Ye, J.; Stampfl, C.; Huang, J. Unravelling the Effects of Layered Supports on Ru Nanoparticles for Enhancing N2 Reduction in Photocatalytic Ammonia Synthesis. *Applied Catalysis B: Environmental* **2019**, *259*, 118026. https://doi.org/https://doi.org/10.1016/j.apcatb.2019.118026.

(23) Mie, G. Beiträge Zur Optik Trüber Medien, Speziell Kolloidaler Metallösungen. *Annalen der Physik* **1908**, *330* (3), 377–445. https://doi.org/https://doi.org/10.1002/andp.19083300302.

(24) Linic, S.; Chavez, S.; Elias, R. Flow and Extraction of Energy and Charge Carriers in Hybrid Plasmonic Nanostructures. *Nature Materials* **2021**, *20* (7), 916–924. https://doi.org/10.1038/s41563-020-00858-4.

(25) Baffou, G.; Cichos, F.; Quidant, R. Applications and Challenges of Thermoplasmonics. *Nature Materials* **2020**, *19* (9), 946–958. https://doi.org/10.1038/s41563-020-0740-6.

(26) Brongersma, M. L.; Halas, N. J.; Nordlander, P. Plasmon-Induced Hot Carrier Science and Technology. *Nature Nanotechnology* **2015**, *10* (1), 25–34. https://doi.org/10.1038/nnano.2014.311.

(27) Yin, Z.; Wang, Y.; Song, C.; Zheng, L.; Ma, N.; Liu, X.; Li, S.; Lin, L.; Li, M.; Xu, Y.; Li, W.; Hu, G.; Fang, Z.; Ma, D. Hybrid Au–Ag Nanostructures for Enhanced Plasmon-Driven Catalytic Selective Hydrogenation through Visible Light Irradiation and Surface-Enhanced Raman Scattering. *Journal of the American Chemical Society* **2018**, *140* (3), 864–867. https://doi.org/10.1021/jacs.7b11293.

(28) Zhou, L.; Swearer, D. F.; Zhang, C.; Robatjazi, H.; Zhao, H.; Henderson, L.; Dong, L.; Christopher, P.; Carter, E. A.; Nordlander, P.; Halas, N. J. Quantifying Hot Carrier and Thermal Contributions in Plasmonic Photocatalysis. *Science* **2018**, *362* (6410), 69 – 72. https://doi.org/10.1126/science.aat6967.

(29) Tian, Y.; Tatsuma, T. Mechanisms and Applications of Plasmon-Induced Charge Separation at TiO2 Films Loaded with Gold Nanoparticles. *Journal of the American Chemical Society* **2005**, *127* (20), 7632–7637. https://doi.org/10.1021/ja042192u.

(30) Jiang, D.; Wang, W.; Sun, S.; Zhang, L.; Zheng, Y. Equilibrating the Plasmonic and Catalytic Roles of Metallic Nanostructures in Photocatalytic Oxidation over Au-Modified CeO2. *ACS Catalysis* **2015**, *5* (2), 613–621. https://doi.org/10.1021/cs501633q.

(31) Jensen, T. R.; Malinsky, M. D.; Haynes, C. L.; van Duyne, R. P. Nanosphere Lithography: Tunable Localized Surface Plasmon Resonance Spectra of Silver Nanoparticles. *The Journal of Physical Chemistry B* **2000**, *104* (45), 10549–10556. https://doi.org/10.1021/jp002435e.

(32) Mock, J. J.; Barbic, M.; Smith, D. R.; Schultz, D. A.; Schultz, S. Shape Effects in Plasmon Resonance of Individual Colloidal Silver Nanoparticles. *The Journal of Chemical Physics* **2002**, *116* (15), 6755–6759. https://doi.org/10.1063/1.1462610.

(33) Sakai, H.; Kanda, T.; Shibata, H.; Ohkubo, T.; Abe, M. Preparation of Highly Dispersed Core/Shell-Type Titania Nanocapsules Containing a Single Ag Nanoparticle. *Journal of the American Chemical Society* **2006**, *128* (15), 4944–4945. https://doi.org/10.1021/ja058083c.

(34) Albiter, E.; Valenzuela, M. A.; Alfaro, S.; Valverde-Aguilar, G.; Martínez-Pallares, F. M. Photocatalytic Deposition of Ag Nanoparticles on TiO2: Metal Precursor Effect on the Structural and Photoactivity Properties. *Journal of Saudi Chemical Society* **2015**, *19* (5), 563–573. https://doi.org/https://doi.org/10.1016/j.jscs.2015.05.009.

(35) Xu, P.; Lu, W.; Zhang, J.; Zhang, L. Efficient Hydrolysis of Ammonia Borane for Hydrogen Evolution Catalyzed by Plasmonic Ag@Pd Core–Shell Nanocubes. *ACS Sustainable Chemistry & Engineering* **2020**, *8* (33), 12366–12377. https://doi.org/10.1021/acssuschemeng.0c02276.

(36) Baffou, G.; Quidant, R.; García de Abajo, F. J. Nanoscale Control of Optical Heating in Complex Plasmonic Systems. *ACS Nano* **2010**, *4* (2), 709–716. https://doi.org/10.1021/nn901144d.

Chapter 7

Conclusions and Future Directions

7.1. Conclusion

Rapid industrialization and urbanization have contributed to a substantial increase in the emission of volatile organic compounds (VOCs) in recent years [1,2]. Detrimental health impacts of VOCs and their increasingly stringent environmental regulations warrant continuous research to develop more effective, economical, and sustainable technologies to mitigate emissions of these pollutants. The findings presented in this dissertation address some of the pressing limitations of the industrial VOC abatement processes in an economical and sustainable way.

The first phase of this research started with understanding and addressing the phenomenon of heel accumulation in the micropores of the beaded activated carbon (BAC), the adsorbent used to capture VOCs during the automotive painting process. Unearthing the factors responsible for heel formation and the mechanistic understanding of their accumulation led to developing a simple surface modification method that impedes heel formation in BAC. BAC. Analytical and mechanistic studies presented in Chapter 2 demonstrated how acid surface modification could be used to limit heel formation without compromising the structural integrity of BAC. In an effort to improve the efficacy of the industrial VOC abatement technique, we further explored feasible methods of regenerating the spent BAC. This effort resulted in the invention of a unique solvent-based regeneration technique. The lab-scale studies presented in Chapter 3 demonstrated that the organic solvent, dimethyl sulfoxide (DMSO), can be effectively used to recover the adsorption capacity of the spent BAC without compromising its structural integrity. Building on the same, the chapter also proposed a way to incorporate the solvent-based regeneration technique *in-situ*. While the surface modification technique can enhance the operational and functional life of the BAC, implementing an *in-situ* solvent-based regeneration technique can avoid the intermittent operational shutdowns and also curtail the transportation and adsorbent replacement costs. These stark advantages make the solvent-based regeneration approach considerably superior to conventional thermal regeneration. Combined, surface modification and *in-situ* solvent-based regeneration can make the VOC pre-concentrator unit more efficient, economical, and sustainable.

The second phase of this research investigated the feasibility of using energy-efficient catalytic oxidation to decompose or destroy VOCs into H_2O and CO_2 as an alternative to the commonly used thermal incinerator. As such, Chapters 4 and 5 provide a detailed roadmap to the synthesis of a novel catalyst architecture of encapsulating catalytically active noble metals in a porous reducible TiO_2 support. Through comparisons with conventional surface-impregnated catalysts, which suffer from significant sintering and deactivation at high operational temperatures, we demonstrated that encapsulation helps maintain a uniform metal particle distribution (2−5 nm) and promotes metal-support interactions by maximizing interfacial sites, thereby improving activity and stability. In addition, we discovered that subjecting the encapsulated catalyst to a post-synthesis solvothermal treatment step anchors the active metal more strongly to the support, which helps maintain superior activity under repeated aging cycles. Above all, the results from Chapters

4 and 5 showed that encapsulation provides excellent thermal stability to the catalyst, prevents agglomeration of active metal, and preserves the catalytic activity of the material.

Finally, we sought to push the boundaries of catalytic reactions used to oxidize VOC molecules via concurrent utilization of thermal energy and visible light to bring down the overall energy requirement of the VOC abatement. By encapsulating plasmonic silver nanostructures in a porous TiO_2 shell resembling a core@shell morphology, we created a multifunctional material capable of generating energetic electrons upon visible light illumination. Photo-thermal reaction studies presented in Chapter 6 demonstrated that these electrons could be used in tandem with thermal energy to completely decompose VOC molecules at viable rates at significantly reduced temperatures compared to those of pure thermal processes. Overall, the work presented in this dissertation provides a concrete framework to develop and implement an efficient, economical, and sustainable technology for the abatement of VOCs produced in industrial settings.

7.2. Future directions

Several avenues open up naturally following the work delineated in this dissertation. The following section discusses some of the exciting new possibilities that emerge from the findings presented in this dissertation.

7.2.1. Optimizing the vapor-phase solvent-based adsorbent regeneration

DMSO vapor proved to be very effective in removing the heel accumulated in the pore structures of BAC compared to the corresponding liquid phase regeneration [3]. Modeling efforts on possible mass transport limitations in pore structures could provide meaningful insight in understanding the bottlenecks and definite differences between regeneration mechanisms or lack thereof. Additionally, a systematic study to optimize and scale up the regeneration process could be carried out following the computational mechanistic studies. The regeneration studies reported in Chapter 3 were carried out at 290 °C and under a flow rate of 200 mL/min of nitrogen and DMSO mixture, generating around 800 ppmv of DMSO flow continuously for a span of 12 hours. While this set-up resulted in recovering nearly 82% of the adsorption capacity of BAC, regeneration carried out at 400 °C proved unsuccessful in surface area recovery. As such, the efficiency of vapor-phase regeneration as a function of temperature, DMSO concentration, and regeneration time is not very well understood. Understanding and optimizing these parameters would help in scaling up the regeneration process in an effective manner.

7.2.2. Evaluating the thermal stability of noble-metal encapsulated catalysts

Catalytic oxidation and aging studies presented in Chapters 4 and 5 demonstrated that the metal encapsulated catalyst morphology exhibits superior catalytic performance than their corresponding surface impregnated counterparts. Specifically, our synthesis increases the abundance of the {101} faceted crystals of encapsulating TiO_2 support, which anchors the metal nanoparticles to the support and providing excellent thermal stability to the catalyst [4–7]. Leveraging these aspects, further studies were carried out to investigate the stability of Ag encapsulated TiO_2 catalysts at temperatures as high as 800 °C. Preliminary results from microscopic characterization indicate that while the encapsulating TiO_2 support undergoes restructuring, the high dispersion and particle size of Ag nanoparticles (active metal) remain unchanged (Figure 7.1). The absence of active metal sintering indicates that the overall catalytic activity of Ag encapsulated TiO_2 catalysts may remain unaltered even after being exposed to temperatures as high as 800 °C.

From a practical standpoint this unique discovery is highly encouraging, as it can provide a generalizable method of preparing thermally stable noble metal catalysts. Many industrially relevant reactions such as catalytic reforming of methane, water-gas shift reaction, automotive emission catalysis occur at extremely high temperatures [8]. Among all these reactions, the catalytically active metal undergoes substantial agglomeration as they are being exposed to high reaction temperatures, loosing catalytic activity over the long run. Leveraging the synthesis protocol reported in Chapter 4, a systematic study can be carried out under distinctive reaction atmospheres and with different active metal combinations to evaluate the thermal stability and reactions mechanisms of encapsulated catalysts.

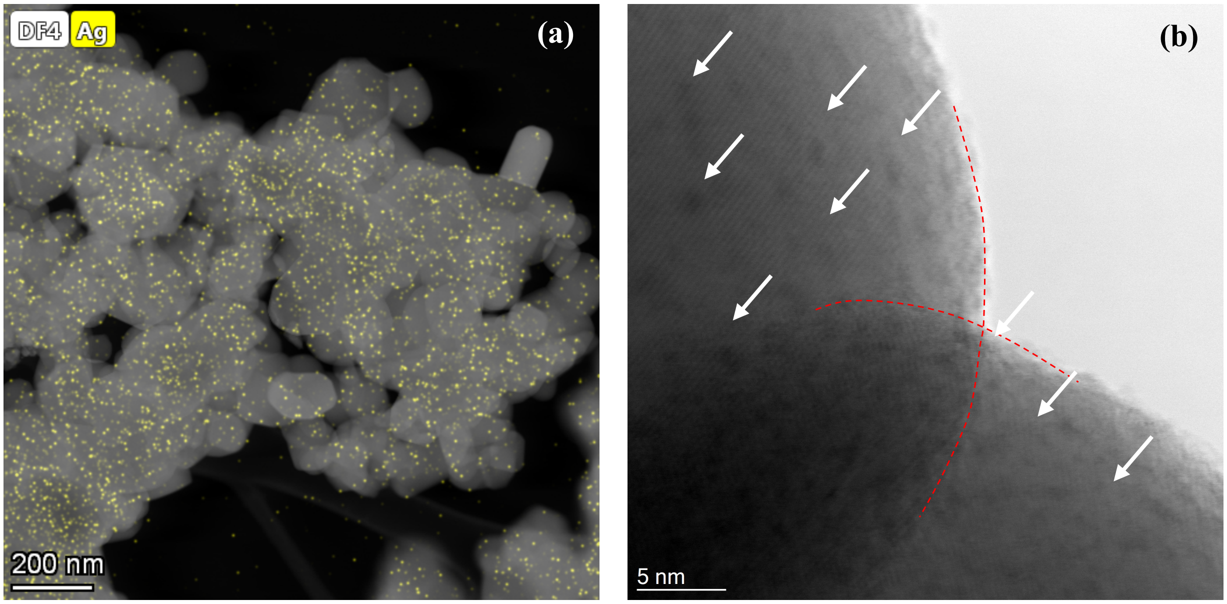

Figure 7.1 *- X-ray dispersive spectroscopic (a), and Transmission electron microscopy (b) characterization of Ag encapsulated* TiO_2 *catalysts aged at 800 °C for 4 hours under air. Some Ag nanoclusters are highlighted by arrows in (b).*

7.2.3. Visible-light enhanced reactions over bimetallic encapsulated catalysts

The fascinating encapsulation morphologies presented in this dissertation can also be modified to obtain a thermally stable bimetallic hybrid catalysts that can utilize visible light to synthesize ammonia under much milder reaction conditions than what is currently possible in large-scale thermo-catalytic industries. For instance, preliminary synthesis efforts to make Ru and Ag nanoparticles encapsulated in TiO_2 nanosphere proved to be successful using the recipe presented in Chapter 4. Alternatively, leveraging the core@shell synthesis reported in Chapter 6, a bimetallic hybrid catalyst could be synthesized using Ru and Ag via a combination of surfactant mediated approach and incipient wet impregnation. A schematic illustration of these bimetallic catalyst systems is presented in Figure 7.2. Studies have shown that synergistic photo-thermal activation can also be applied to dissociating molecular nitrogen, directly influencing the rate-determining step for ammonia synthesis [9]. As such, through photo-thermal catalytic approach, the localized surface plasmonic resonance and associated hot electron generation capability of silver nanostructures could be leveraged to drive modular renewable ammonia synthesis over bimetallic Ru/Ag@TiO_2 hybrid catalysts. In sum, encapsulation approach provides exciting new avenues to synthesize sinter resistant multifunctional catalysts.

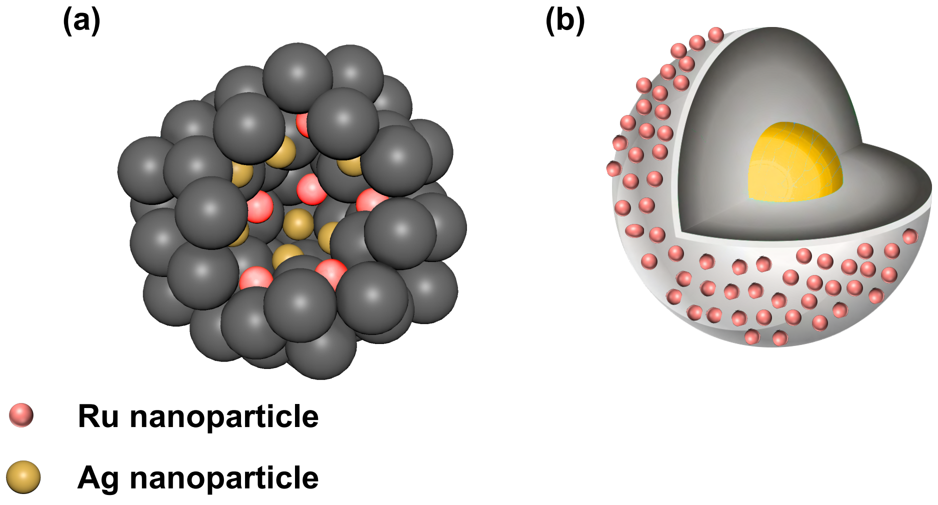

Figure 7.2 *- Schematic illustration of proposed bimetallic Ag-Ru encapsulated TiO_2 catalyst (a), and bimetallic hybrid Ru/Ag@TiO_2 catalyst (b).*

7.3. References

(1) McDonald, B. C.; de Gouw, J. A.; Gilman, J. B.; Jathar, S. H.; Akherati, A.; Cappa, C. D.; Jimenez, J. L.; Lee-Taylor, J.; Hayes, P. L.; McKeen, S. A.; Cui, Y. Y.; Kim, S.-W.; Gentner, D. R.; Isaacman-VanWertz, G.; Goldstein, A. H.; Harley, R. A.; Frost, G. J.; Roberts, J. M.; Ryerson, T. B.; Trainer, M. Volatile Chemical Products Emerging as Largest Petrochemical Source of Urban Organic Emissions. *Science* **2018**, *359* (6377), 760 LP – 764. https://doi.org/10.1126/science.aaq0524.

(2) Lewis, A. C. The Changing Face of Urban Air Pollution. *Science* **2018**, *359* (6377), 744 LP – 745. https://doi.org/10.1126/science.aar4925.

(3) Ohtani, H.; Ellwood, K. R. J.; Venkat, M.; Bhat, A.; Schwank, J. Recovery of Adsorption Capacity of Beaded Activated Carbon Using Gas-Phase Organic Solvents. Google Patents March 19, 2020.

(4) Bhat, A.; Hill, A. J.; Fisher, G. B.; Schwank, J. W. Improving the Thermal Stability and N-Butanol Oxidation Activity of Ag-TiO2 Catalysts by Controlling the Catalyst Architecture and Reaction Conditions. *Applied Catalysis B: Environmental* **2021**, 120476. https://doi.org/https://doi.org/10.1016/j.apcatb.2021.120476.

(5) Setvin, M.; Hao, X.; Daniel, B.; Pavelec, J.; Novotny, Z.; Parkinson, G. S.; Schmid, M.; Kresse, G.; Franchini, C.; Diebold, U. Charge Trapping at the Step Edges of TiO2 Anatase (101). *Angewandte Chemie International Edition* **2014**, *53* (18), 4714–4716. https://doi.org/https://doi.org/10.1002/anie.201309796.

(6) Han, F.; Zhou, Z.; Zhang, X.; Huang, Z.; Li, M.; Guo, L. First-Principles Study on Stability and HER Activity of Noble Metal Single Atoms on TiO2: The Effect of Loading Density. *The Journal of Physical Chemistry C* **2018**, *122* (5), 2546–2553. https://doi.org/10.1021/acs.jpcc.7b11486.

(7) Iyemperumal, S. K.; Pham, T. D.; Bauer, J.; Deskins, N. A. Quantifying Support Interactions and Reactivity Trends of Single Metal Atom Catalysts over TiO2. *The Journal of Physical Chemistry C* **2018**, *122* (44), 25274–25289. https://doi.org/10.1021/acs.jpcc.8b05611.

(8) Dai, Y.; Lu, P.; Cao, Z.; Campbell, C. T.; Xia, Y. The Physical Chemistry and Materials Science behind Sinter-Resistant Catalysts. *Chemical Society Reviews* **2018**, *47* (12), 4314–4331. https://doi.org/10.1039/C7CS00650K.

(9) Bloh, J. Z. Intensification of Heterogeneous Photocatalytic Reactions Without Efficiency Losses: The Importance of Surface Catalysis. *Catalysis Letters* **2021**. https://doi.org/10.1007/s10562-021-03573-0.